New concept of an advanced spin polarization detector based on a Lamb-shift polarimeter and possible applications

Von der Fakultät für Mathematik und Naturwissenschaften der RWTH Aachen University zur Erlangung des akademischen Grades eines Doktors der Naturwissenschaften genehmigte Dissertation

vorgelegt von

Nicolas, Faatz, M.Sc.

aus

Trier

Berichter: Prof. Dr. Jörg Pretz
Prof. Dr. Christoph Hanhart

Tag der mündlichen Prüfung: 23. Juli 2026

Diese Dissertation ist auf den Internetseiten der Universitätsbibliothek verfügbar.

Abstract

Since the 1980's Lamb-shift polarimeters (LSPs) have been utilized as a low energy polarimeter to measure the degrees of nuclear polarization in molecular, atomic and ionic beams consisting of hydrogen and its isotopes. Its operating principle is based on the production of metastable atomic states followed by selective quenching of the different nuclear polarization states. The development started in 1968 with theoretical studies and experimental realization of a nuclear spin filter by McKibben et al. as a key component. Over the years LSPs have been successfully employed in several experiments, e.g. the ANKE spectrometer located at COSY/Jülich. In contrast to its success the method has limitations since only half of the atomic spin states can be selected. In addition, only systems composed of hydrogen or its isotopes can be analyzed. This work presents theoretical models based on the implementation of the density operator formalism to overcome these limitations. Future experimental realizations can be used for several different experiments addressing parity violation, dark matter research or even the preparation of polarized nuclear fuel for energy production via nuclear fusion. In addition, motivated by the growing interest in polarized helium-3 experiments, a new detector concept for helium-3 ions based on the Lamb-shift polarimeter is presented. This approach enables a realization of a low-energy polarimeter suitable of verifying the nuclear polarization created by potential future polarized helium-3 ion sources.

Zusammenfassung

Seit den 80er-Jahren wurden Lambshift-Polarimeter als Niederenergie-Polarimeter verwendet, um die nukleare Polarisation von Molekül-, Atom- und Ionenstrahlen, welche aus Wasserstoff und dessen Isotopen zusammengestellt sind, zu messen. Die Funktionsweise des Polarimeters basiert dabei auf der Produktion von metastabilen Atomzuständen und deren Seperation durch selektive Abregung. Im Jahr 1968 wurde der erste Grundstein zur Entwicklung von McKibben et al. durch die theoretische Entwicklung und experimentellen Realisierung des "nuclear spin filter" gelegt, welcher Hauptbestandteil des Polarimeters ist. Über die Jahre wurde es erfolgreich in verschiedensten Experimenten, z. B. beim polarisierten internen Target am ANKE-Experiment, eingesetzt. Entgegen seiner erfolgreichen Historie ist das Lambshift-Polarimeter limitiert, da es nur die Hälfte der atomaren Spinzustände selektieren kann. Hinzu kommt, dass nur Systeme, welche aus Wasserstoff oder seinen Isotopen zusammengestellt sind, bisher erfolgreich detektiert werden können. Daher präsentiert diese Arbeit theoretische Modelle basierend auf der Implementierung des quantenmechanischen Dichteoperator-Formalismus um diese Limitation zu überwinden. Eine zukünftige experimentelle Realisierung kann für einige verschiedene Experimente genutzt werden. Diese addresieren die Paritätsverletzung, Erforschung dunkler Materie und sogar die Verifizierung von polarisiertem Treibstoff zur Energiegewinnung durch Kernfusion. Zusätzlich wird ein neues Konzept für ein Detektorsystem für Helium-3, basierend auf dem Lambshift-Polarimeter, präsentiert, welches motiviert ist durch den Anstieg des Interesses an polarisierten Helium-3 Experimenten. Dieses Konzept ermöglicht die Realisierung eines Niederenergie-Polarimeters zur Messung der Kernspin-Polarisation von potentiell zukünftigen Helium-3 Ionenquellen.

Contents

Abstract iii

Zusammenfassung v

List of Figures ix

List of Tables xiii

List of Abbreviations xv

Introduction 1

1 Motivation 3
- 1.1 Bound beta decay . . . 3
- 1.2 Parity violation . . . 5
- 1.3 Dark matter and axions . . . 7
- 1.4 Helium-3 sources . . . 8
- 1.5 Polarized nuclear fusion . . . 9

2 General theory 13
- 2.1 One electron atomic system . . . 13
- 2.2 Further corrections . . . 17
  - 2.2.1 Fine structure . . . 17
  - 2.2.2 Lamb-shift . . . 19
  - 2.2.3 Hyperfine structure . . . 20
- 2.3 Dirac equation for one electron atomic system . . . 22
- 2.4 Atomic interaction with external fields . . . 27
  - 2.4.1 Stark effect . . . 27
  - 2.4.2 Landé g-factor . . . 29
  - 2.4.3 Breit-Rabi diagram . . . 30
  - 2.4.4 Lifetime . . . 32
- 2.5 Density operator . . . 32
  - 2.5.1 The Lindblad master equation . . . 34
- 2.6 Electromagnetic waves in a cylindrical cavity . . . 36

3 Derivation of the formalism 43
- 3.1 Hydrogen . . . 43
- 3.2 Deuterium . . . 52
- 3.3 Tritium . . . 63
- 3.4 Single ionized helium-3 . . . 64
- 3.5 The applied Lindblad master equation . . . 67

4 Nuclear spin filter **69**
4.1 The old spin filter . . . 69
4.1.1 The entropy of the system . . . 89
4.2 2nd generation spin filter . . . 92
4.3 Spin filter for single ionized helium-3 . . . 107
4.3.1 Mechanical dynamics . . . 107
4.3.2 Relativistic approach . . . 109
4.3.3 Spin dynamics . . . 112

5 Lamb-shift polarimeter for helium-3 **117**
5.1 Wien filter . . . 117
5.2 Interaction region . . . 119
5.3 Quenching region . . . 121

6 Possible applications **129**
6.1 TUM set-up for BoB . . . 129
6.2 Set-up for parity violation in metastable hydrogen . . . 132
6.3 Set-up for probing dark matter axions . . . 133
6.4 Set-up for using a helium-3 LSP . . . 133
6.5 Set-up to produce nuclear polarized fuel for nuclear fusion . . . 134
6.6 Spin filter as spin polarized beam source . . . 135

Summary and Conclusion **137**

7 Appendix **139**
A Spherical harmonics . . . 140
B Derivations for the general theory chapter . . . 141
C Electric multipole expansion . . . 143
C.1 Monopole . . . 144
C.2 Dipole . . . 145
C.3 Quadrupole . . . 145
D Coupling constants . . . 152
E Derivation of the differential equation for the Lorentz force . . . 160
F Proof of the variation method theorem . . . 161
G Complementary material on the Bessel function of the first kind . . . 162
H Drawings and additional simulations . . . 163
I Relativistic Simulations . . . 164

Bibliography **166**

Acknowledgements **181**

Declaration of Authorship **181**

List of Figures

1.1 Relative differential cross-section for the double polarized deuterium tritium/helium-3 fusion. . . . 11

2.1 Sketch of a cylindrical cavity. . . . 36

3.1 Breit-Rabi diagrams for excited hydrogen states with $n = 2$. . . . 50
3.2 Lifetime evolution of excited hydrogen states in the presence of external fields. . . . 51
3.3 Breit-Rabi diagrams for excited deuterium states with $n = 2$. . . . 62
3.4 Lifetime evolution of excited deuterium states in the presence of external fields. . . . 62
3.5 Breit-Rabi diagrams for excited tritium states with $n = 2$. . . . 63
3.6 Lifetime evolution of excited tritium states in the presence of external fields. . . . 64
3.7 Breit-Rabi diagram for the metastable $2S_{1/2}$ and short-living $2P_{1/2}$ set of single ionized helium-3. . . . 66
3.8 Lifetime evolution of ionic metastable helium-3 states in the presence of external field. . . . 67

4.1 Nuclear spin filter drawings along the beam line. . . . 71
4.2 Nuclear spin filter measurements. . . . 72
4.3 Nuclear spin filter measurements with analysis. . . . 73
4.4 Time evolution of the old nuclear spin filter system and comparing the influence of the magnetic radio frequency part. . . . 75
4.5 Simulation of an unpolarized beam in the old nuclear spin filter for one frequency. . . . 76
4.6 Simulation of an unpolarized beam in the old nuclear spin filter for one frequency with larger static electric field. . . . 77
4.7 Simulation of an unpolarized beam in the old nuclear spin filter for one frequency with larger radio frequency power. . . . 78
4.8 Nuclear spin filter measurements part one. . . . 79
4.9 Nuclear spin filter measurements part two. . . . 79
4.10 Nuclear spin filter measurements part three. . . . 80
4.11 Simulation for metastable hydrogen atoms in the old spin filter for a different frequency. . . . 81
4.12 Bessel functions of the first kind. . . . 82
4.13 Lorentz distribution for the frequency spectrum in a cylindrical cavity. . . . 82
4.14 Measurement of the Lorentz distribution of a cylindrical cavity. . . . 83
4.15 Residual graph for the frequency measurement based on a Lorentz distribution. . . . 84
4.16 Simulation for metastable hydrogen atoms in the old spin filter for a frequency band. 85
4.17 Simulation for metastable hydrogen atoms in the old spin filter for a frequency band part two. . . . 86
4.18 Simulation for metastable deuterium atoms in the old spin filter. . . . 87
4.19 Simulation for metastable tritium atoms in the old spin filter. . . . 88
4.20 Comparison of a simulation with a measurement. . . . 89
4.21 Complete numerical spin filter simulations. . . . 91
4.22 Complete numerical spin filter simulations part two. . . . 91

4.23 Numerical calculations of the entropy. 92
4.24 Numerical calculations of the entropy part two. 92
4.25 Picture of the cavity of an already existing spin filter. 94
4.26 Design of a new cavity type for larger Q-values. 95
4.27 Frequency band for the 2nd generation nuclear spin filter. 96
4.28 New generation nuclear spin filter simulations. 97
4.29 New generation nuclear spin filter simulations part two. 97
4.30 New generation nuclear spin filter simulations for deuterium. 98
4.31 New generation nuclear spin filter simulations part three. 98
4.32 Simulations for the new generation nuclear spin filter for the α peaks. 99
4.33 New generation nuclear spin filter simulations for tritium. 99
4.34 Simulations for the new generation nuclear spin filter with a frequency band. 100
4.35 Design for the second generation nuclear spin filter part one. 101
4.36 Design for the second generation nuclear spin filter part two. 102
4.37 Design for the second generation nuclear spin filter part three. 103
4.38 Design for the second generation nuclear spin filter part four. 104
4.39 Design for the second generation nuclear spin filter part five. 105
4.40 Design for the second generation nuclear spin filter part six. 106
4.41 Position trajectories comparing the influence of the radio frequency in a classical treatment. 108
4.42 Position trajectories comparing relativistic and classical treatment. 112
4.43 Frequency band of the singly ionized helium-3 nuclear spin filter. 113
4.44 Spin filter for helium-3 part one. 114
4.45 Spin filter for helium-3 part two. 114
4.46 Spin filter for helium-3 part three. 115
4.47 Spin filter for helium-3 part four. 115
4.48 Spin filter for helium-3 part five. 116

5.1 Experimental setup of an LSP. 117
5.2 Wien filter mass spectrum for single ionized helium-4 ions. 119
5.3 Argon cell drawings cut through the beam line. 121
5.4 Experimental setup for the test of a CCD camera. 122
5.5 Measurement with the CCD camera in the quenching region. 123
5.6 Measurement with the CCD camera in the quenching region part two. 123
5.7 Measurement with the CCD camera in the quenching region part three. 124
5.8 Measurement with the CCD camera in the quenching region part four. 124
5.9 Measurement with the CCD camera in the quenching region part five. 125
5.10 Measurement with the CCD camera in the quenching region part six. 125
5.11 Measurement with the CCD camera in the quenching region part seven. 126
5.12 Measurement with the CCD camera in the quenching region part eight. 126
5.13 Measurement with the CCD camera in the quenching region part nine. 127
5.14 Transmission probability of a 1.2 μm thick aluminium layer. 127

6.1 Possible experimental setup for the BoB experiment. 130
6.2 Experimental setup for the H^- measurement. 130
6.3 Grid system to apply the counter field for the H^- measurement. 131
6.4 Detection of H^- due to a Spin filter measurement. 131
6.5 Possible setup for the parity violation experiment. 133
6.6 Possible setup for the dark matter axion experiment. 133
6.7 Possible setup for measuring the nuclear polarization of helium-3 sources. 134
6.8 Possible setup to probe the production of nuclear polarized fuel for nuclear fusion. . 135

7.1 Design for the second generation nuclear spin filter. 164
7.2 Further nuclear spin filter simulations. 164

List of Tables

1.1 BoB possible spin configurations. 5
1.2 Possible transitions due to weak interaction in the hydrogen atom. 6
1.3 Possible transitions due to weak interaction in the deuterium atom. 6
1.4 The magnetic field values for the resonance of the axions. 8

3.1 Parameters for the hydrogen states. 50
3.2 Parameters for the deuterium states. 61
3.3 Parameters for the tritium states. 63
3.4 Parameters for the single ionized helium-3 states. 66

4.1 Fit parameters for the subtraction of the background. 71
4.2 Fit parameters for the peak structures of the nuclear spin filter signal. 71
4.3 Experimental settings for the nuclear spin filter. 80
4.4 Results of the Lorentz fit for the frequency spectrum of a cylindrical cavity. 84
4.5 Parameters for numerical simulations of the old nuclear spin filter system. 85
4.6 Parameters of the complete spin filter simulations. 93
4.7 Different cavity modes for the upgraded nuclear spin filter. 96
4.8 Parameters for numerical simulations of the 2nd generation nuclear spin filter system. 100
4.9 Parameters for the simulations of the beam dynamics. 109
4.10 Different cavity modes for the nuclear spin filter of singly ionized helium-3. 113
4.11 Parameters for numerical simulations of the spin filter for singly ionized helium-3. . 116

5.1 Settings of the measurements of the CCD camera. 128

6.1 Settings of the measurement for the H^- spin filter curve. 132

7.1 Roots of the Bessel function of the first kind. 162
7.2 Roots of the derivative of the Bessel function of the first kind. 163
7.3 Parameters of the simulations in the appendix. 165

List of Abbreviations

PHELIX **P**etawatt **H**och-**E**nergie **L**aser für Schwer**i**onenen**x**perimente

POLIS **Pol**arized-**i**on **s**ource

OPPIS **O**ptically **p**umped **p**olarized **i**on **s**ource

eRHIC **E**lectron-**r**elativistic **h**eavy **i**on **c**ollider

RHIC **R**elativistic **h**eavy **i**on **c**ollider

ANKE **A**pparatus for studies of **n**ucleon and **k**aon **e**jectiles

COSY **Co**oler **sy**nchrotron

MAC-E **M**agnetic **a**diabatic **c**ollimation combined with an **e**lectrostatic filter

CERN **C**onseil **e**uropéen pour la **r**echerche **n**ucléaire

MEOP **M**etastability **e**xchange **o**ptical **p**umping

ABS **A**tomic **b**eam **s**ource

LSP **L**amb-**s**hift **p**olarimeter

BNL **B**rookhaven **N**ational **L**aboratory

FZJ **F**orschungs**z**entrum **J**ülich

BoB **Bo**und **b**eta decay

ESR **E**xperimentier**s**peicher**r**ing

GSI **G**esellschaft für **S**chwer**i**onenforschung

V-A **V**ector minus **a**xial vector theory

QCD **Q**uantum **c**hromo**d**ynamics

DOE **D**epartment **o**f **e**nergy

EIC **E**lectron-**i**on **c**ollider

MRI **M**agnetic **r**esonance **i**maging

EDM **E**lectric **d**ipole **m**oment

SNO **S**udbury **n**eutrino **o**bservatory

QED **Q**uantum **e**lectro**d**ynamics

HFS **H**yper**f**ine **s**plitting

PMT **P**hoto**m**ultiplier **t**ube

CCD **C**harged-**c**oupled **d**evice

ECR **E**lectron **c**yclotron **r**esonance

TUM **T**echnische **U**niversität **M**ünchen

SF **S**pin **f**ilter

Dy **Dy**sprosium

Ho **Ho**lmium

SM **S**tandard **m**odel

QM **Q**uantum **m**echanics

FS **F**ine **s**plitting

TM **T**ransverse **m**agnetic waves

TE **T**ransverse **e**lectric waves

BS **B**asis **s**tep

IH **I**nductive **h**ypothesis

IS **I**nductive **s**tep

Introduction

Since the discovery of the quantum mechanical spin by Stern and Gerlach in 1922 [1], experimental efforts have been turned towards its manipulation. This led to the new field of polarization physics, in which an ensemble of particles in the presence of a defining quantization axis, e.g. an external magnetic field, has in average a preferred spin direction. First sources of polarized particles, partially based on the Stern-Gerlach method, were introduced to produce highly nuclear polarized hydrogen and deuteron beams. These sources are called atomic beam sources (ABS) [2, 3]. To verify the polarization values new detector systems have been developed. One of them is the Lamb-shift polarimeter (LSP) [4, 5]. In 1968 the corresponding foundation has been established by McKibben et al. in the development of the nuclear spin filter (SF) [6], which is a main device of the LSP. In 1986 Belov et al. continued the development of an LSP by utilizing the charge exchange reaction for a polarized proton beam inside a sodium oven as well as employing a photomultiplier to detect the incoming Ly-α photons during the quench process [7]. Not until 1993 Lemieux et al. first combined all components together to produce the first measured Ly-α spectra for a polarized proton as well as deuteron beam [8]. In this case they utilized cesium instead of sodium for the charge exchange process. From there on different groups successfully implemented an LSP in their experiments as a low energy polarimeter. Kremers et al. [9] implemented an LSP to measure the nuclear polarization of protons and deuteron beams produced by the polarized-ion source (POLIS). At the Brookhaven National Laboratory (BNL) the LSP is used at the optically pumped polarized ion source (OPPIS) for the preparation of the nuclear polarized H^- beam at the relativistic heavy ion collider (RHIC) [10]. Moreover, the LSP has been used to measure the nuclear polarization of the internal gas target at ANKE [11]. And finally the LSP is utilized in the experiment investigating the double polarized $d-d$ fusion reaction, where the goal is to measure the spin-correlation parameters of the fusion reaction [12]

$$\begin{aligned} d + d &\rightarrow {}^3\mathrm{He} + n, \\ d + d &\rightarrow t + p. \end{aligned} \tag{1}$$

Even though the LSP has a successful history, its analyzation of the single hyperfine states is limited as only half of the spin states are individually resolvable. Therefore, this thesis addresses a theoretical model to overcome the boundaries and to lay a path for an experimental realization to identify all hyperfine states separately. In Ch. 1 several experiments are summarized, which would benefit from such an upgraded LSP. Subsequently, in Ch. 2 the necessary theory is laid-out to model quantum mechanically hydrogen-like systems. Moreover, the necessary theoretically framework for this thesis is established in Ch. 3. The nuclear spin filter is introduced in Ch. 4. Measurements validate the numerical simulations for the already existing device in Sec. 4.1, while Sec. 4.2 comprises the upgrade of the nuclear spin filter and its modelling. Furthermore, the LSP is restricted to atomic, molecular and ionic systems composed of hydrogen and its isotopes. This has been demonstrated experimentally by Engels et al. through detecting the nuclear polarization in H_2 and D_2 molecules [13], in HD molecules [14] and even for H_3^+ by El-Kordy et al. [15]. Thus, in Sec. 4.3 a model for a SF based on singly ionized helium-3 is presented. Finally, in Ch. 5 a framework is introduced, which opens the door for an LSP-like detector based on helium-3 ions. Finally, concluding remarks and possible future investigations are summarized in Ch. 6.6.

Chapter 1

Motivation

Since many years the LSP has been successfully implemented in the internal gas jet target at the apparatus for studies of nucleon and kaon ejectiles (ANKE) [16], where it verified the nuclear polarization of the polarized gas jet created by an ABS [3]. This was one important experiment at the cooler synchrotron (COSY) [11], which was dedicated to determine fundamental high energy physics with polarized beams and targets at the Forschungszentrum Jülich (FZJ). Moreover, the work with the LSP led to new understandings, which result in the possibilities to measure the nuclear polarization of molecules, as explained in the introduction. Furthermore, in [17] it has been recently shown that an LSP [5, 4] can be used to verify the nuclear polarization of the polarized H^-/D^- source [18], which provided COSY with its beams. Therefore, the LSP has a thriving time at storage rings and particle accelerators but this chapter is dedicated to experiments, which do not need large energies but still require an upgraded LSP to validate their results.

1.1 Bound beta decay

Unstable atoms or ions undergo radioactive actions to bring their nucleus into a stable form. One of the three main processes is called $\beta^{\mp}$-decay and describes the transformation either of a neutron n into a proton p or vice versa. In general, the β^- process is preferred as the neutron is slightly heavier than the proton $m_n/m_p = 1.00137841946 \pm 40$ [19]. The neutron decays in a three-body process to

$$n \rightarrow p + e^- + \bar{\nu}_e, \tag{1.1}$$

with e^- being the electron and $\bar{\nu}_e$ an anti-electron neutrino. This reaction takes place due to the weak force, which is allowed to change the flavour of quarks. For free neutrons this process is theoretically well understood and even calculated to the second order correction [20], which is in agreement with the experimental data [21].
In rare cases the electron does not gain enough energy to escape from the attractive central electrostatic potential created by the nucleus and is recaptured. These cases are called bound beta decays (BoB) and have first been theoretically predicted by Daudel, Jean and Lecoin [22]. The probability to observe bound beta decays rises with an increasing binding energy, which is maximized for fully ionized ions. The first measurement validating the theory was conducted at the Experimentierspeicherring (ESR) at Gesellschaft für Schwerionenforschung (GSI) in Darmstadt [23]. Here, the reaction of dysprosium $^{163}_{66}Dy^{66+}$ into holmium $^{163}_{67}Ho^{66+}$

$$^{163}_{66}Dy^{66+} \rightarrow {}^{163}_{67}Ho^{66+} + \bar{\nu}_e, \tag{1.2}$$

was observed. A bunch of $^{163}_{66}Dy^{66+}$ ions was introduced in the ESR storage ring for a period of up to 80 minutes. The accumulated $^{163}_{67}Ho^{66+}$ ions, created in bound beta decays, followed the same trajectory as their mass to charge ratio is nearly equal. In a final detection process a gas jet was sent perpendicular to the ion beam to ionize the remaining electron of the $^{163}_{67}Ho^{66+}$ ions.

$^{163}_{67}\mathrm{Ho}^{67+}$ ions, now following a different trajectory, have been counted and thereby identified.
To investigate further limits onto the scalar and tensor coupling constants of the weak interaction [24] as well as the possible existence of right-handed anti-neutrinos [25] a group around Schott [26, 27, 28] suggests directly investigating the bound beta decay of free neutrons into hydrogen atoms and anti-electron neutrinos via

$$n \rightarrow \mathrm{H} + \bar{\nu}_e, \tag{1.3}$$

which has not been observed yet. Its challenge is due to the low branching ratio of $4 \cdot 10^{-6}$ [29, 30] in comparison to the three-body decay. Because of the short range of the weak interaction the formation of S-orbitals is preferred as these allow to find the electron with a high probability in the centre where the nucleus is situated. Correspondingly, it is expected to obtain 83.2 % ground state hydrogen atoms $\left(1S_{1/2}\right)$ as well as 10.4 % metastable ones $\left(2S_{1/2}\right)$. To investigate the key aspects of the weak interaction it is necessary to determine the spin dynamics of the educts. This task is achievable by measuring the occupation numbers of the hyperfine substates of the metastable hydrogen atoms in a constant homogeneous external magnetic field B which eliminates the necessity of having polarized neutrons. Assuming only left-handed weak interaction currents, the transition probabilities p_i are obtained in [24] and summarized in the Tab. 1.1. The resulting Breit-Rabi states, here in the Paschen-Back area, are defined later in Sec. 3.1. Here, especially the β_3 state with electron and proton spin antiparallel to the external fields is of special interest because it is forbidden due to the current standard model theory. Subsequently, the development of a device, which is capable of separating the Breit-Rabi states, is one of the main goals for this thesis.
The idea of a possible experimental realization for this project starts with an intense neutron source delivering a large amount of free neutrons, which have a lifetime of
$\tau = 877.75 \pm 0.28_{stat.} + 0.22/-0.16_{syst.}$ s [31]. A beam tube behind the chamber, in which the neutrons decay, serves as a guiding direction for the educts. In this area a magnetic homogeneous field along the beam axis is applied, which establishes a quantization axis and therefore, defines the single Breit-Rabi states. Next to it, a spin filter [32, 6] is placed. Its purpose is to select one of the four Breit-Rabi states by quenching the remaining substates back into the ground state. The already known type of spin filter, described in detail in Sec. 4.1, is only able to filter the two α states separately but does not work for the important β states. In the next step, a rotation of the external magnetic field follows. From there on it points perpendicularly towards the beam direction to deflect all protons and electrons produced in the three-body process. Then the remaining unharmed metastable hydrogen atoms enter an argon-cell in which they react to H^- ions [33, 34]. A magnetic adiabatic collimation combined with an electrostatic filter (MAC-E) [35] distinguishes the different kinetic energies of the H^- ions produced out of metastable or ground state hydrogen atoms. The difference of 10 eV in their kinetic energy is caused by the binding energy of the first electron of the hydrogen atom created in the bound beta decay. Correspondingly, only H^- ions produced by metastable hydrogen atoms pass the MAC-E filter and are detected afterwards.

Table 1.1: The transition probabilities for the six possible bound beta decays by following the vector minus axial vector (V-A) theory are presented. Correspondingly, the resulting metastable Breit-Rabi states in the Paschen-Back area are presented here. Their definitions are introduced later in Sec. 3.1.

	n	p	e^-	$\bar{\nu}_e$	p_i [%]	BR state at $B \geq B_c$
1	$\uparrow$	$\uparrow$	$\uparrow$	$\downarrow$	0.622 ± 0.011	α_1
2	$\uparrow$	$\uparrow$	$\downarrow$	$\uparrow$	0	β_4
3	$\uparrow$	$\downarrow$	$\uparrow$	$\uparrow$	0	α_2
4	$\downarrow$	$\downarrow$	$\downarrow$	$\uparrow$	0	β_3
5	$\downarrow$	$\downarrow$	$\uparrow$	$\downarrow$	44.14 ± 0.05	α_2
6	$\downarrow$	$\uparrow$	$\downarrow$	$\downarrow$	55.24 ± 0.04	β_4

1.2 Parity violation

The parity based on its operator Π acting onto a wave function $\psi(\vec{x})$ and mirroring the sign of its positional argument

$$\Pi\psi(\vec{x}) = \psi(-\vec{x}), \tag{1.4}$$

is conserved for electromagnetic interactions [36]. In contrast, the weak interaction challenged the fundamental law of parity conservation. The first hint to this was found in the $\tau-\theta$ puzzle [37, 38] where two different decay channels for the K^+ meson into pions π

$$\begin{aligned} K^+ &\rightarrow \pi^+ + \pi^0, \\ K^+ &\rightarrow \pi^+ + \pi^+ + \pi^-, \end{aligned} \tag{1.5}$$

were found. The action of Π onto a pion-wave function leads to [38]

$$\Pi\psi_\pi(\vec{x}) = -\psi_\pi(\vec{x}), \tag{1.6}$$

for a pion with an even angular momentum. Consequently, the final K^+ states result in different parities, which was the first hint that parity is violated here. At the time the scientist instead considered the particles (named τ and θ), which are responsible for the distinct decay channels, to be different from each other, even though the data was showing no discrepancy in properties, like their mass. A few years later, Lee and Yang doubted that the parity is conserved under weak interaction and proposed experiments to test their statement [39]. The first direct experimental observation was conducted by Wu et al. [40]. In this experiment they took advantage of the possibility to polarize ${}^{60}_{27}\mathrm{Co}$ in low magnetic fields [41]. The cobalt isotope decays via a β^--decay into an excited nickel ${}^{60}_{28}\mathrm{Ni}^*$ nucleus

$${}^{60}_{27}\mathrm{Co} \rightarrow {}^{60}_{28}\mathrm{Ni}^* + e^- + \bar{\nu}_e. \tag{1.7}$$

The ${}^{60}_{27}\mathrm{Co}$ is a spin five particle with a positive parity, while the ${}^{60}_{28}\mathrm{Ni}^*$ nucleon is a spin four particle also with positive parity. The ${}^{60}_{27}\mathrm{Co}$ was then polarized so that the state $|I = 5, m_I = 5\rangle$ was prepared. Consequently, the nickel nucleus, produced in the β^--decay, had to be in the state $|I = 4, m_I = 4\rangle$, while the electron and the anti-electron neutrino needed to be in $|S = 1/2, m_s = 1/2\rangle$ to conserve the spin. Lee and Yang calculated [39] the angular intensity distribution for a β-decay process

$$I(\theta)\, d\theta = c\,(1 + \alpha\cos(\theta))\sin(\theta)\, d\theta, \tag{1.8}$$

with θ being the angle between the spin projection of the original ${}^{60}_{27}\mathrm{Co}$ nucleus and the electron momentum. Here c is some normalization constant. Only in the presence of parity violation one

Table 1.2: The transition probabilities from the metastable $2S_{1/2}$ hydrogen set to the short-living $2P_{1/2}$ states due to the weak force and in the presence of an external homogenous magnetic field B are shown. The corresponding coupling constants are evaluated at the energy crossing points. The definitions of the Breit-Rabi states are introduced later in Sec. 3.1.

	Matrix element for hydrogen	Crossing point B [mT]	Nucleon-electron coupling constants
1	$\langle e_2\|V\|\beta_4\rangle$	54.6	$-2C_{2P}$
2	$\langle f_4\|V\|\beta_4\rangle$	109.8	$C_{1P} + 1.1C_{2P}$
3	$\langle f_3\|V\|\beta_3\rangle$	116.3	$C_{1P} - C_{2P}$

gets $\alpha \neq 0$. Thus, any asymmetry in $I(\theta)d\theta$ would correspond to a parity violation. In the Wu experiment a detector was placed under the $^{60}_{27}$Co sample and by reversing the quantization axis of the external magnetic field the asymmetry was observed. Up to today, the accepted status in physics is that there are only left-handed neutrinos as well as right-handed anti-neutrinos as already described in Sec. 1.1. Moreover, a handful of experiments are being conducted to verify and measure the interaction strength of weak interactions [42, 43] with high accuracy. One important proposal is the investigation of parity violation in hydrogen and deuterium atoms, respectively [44]. External electric fields perform dipole transitions with $\Delta l \pm 1$, which is explained in Sec. 2.4.1, between the metastable $2S_{1/2}$ and the short-living $2P_{1/2}$ set. The parity of hydrogen-like wave functions, introduced in Sec. 2.1, is given by

$$\Pi\Psi_{n,l,m}(\vec{x}) = (-1)^l \Psi_{n,l,m}(\vec{x}), \tag{1.9}$$

which is explained in more detail in [45]. Consequently, in the absence of external electric fields these transitions are only possible due to the parity violating weak interaction, since spontaneous γ emissions are highly suppressed as the transition probability is proportional to the energy difference of the initial and final state [46]. Thus, the lifetime of the $2S_{1/2}$ set only due to electric dipole transitions to the $2P_{1/2}$ is estimated to be around 20 years [46]. Dunford and Holt provide [44] the possible transitions due to the parity violating nucleon-electron neutral weak current interaction, which can be seen in Tab. 1.2 and Tab. 1.3. Weak transitions in a bound state would therefore cover the area around near zero momentum transfer. An additional reason for conducting the experiment is that, without major difficulties, four different coupling constants could be measured. Moreover, the hydrogen atom is the only bound system, which can be calculated analytically with high precision. To perform such an experiment a complete spin filter helps to select each hyperfine state individually, where its development is the aim of this thesis.

Table 1.3: The transition probabilities from the metastable $2S_{1/2}$ deuterium set to the short-living $2P_{1/2}$ states due to the weak force and in the presence of an external homogenous magnetic field B are shown. The corresponding coupling constants are evaluated at the energy crossing points. The definitions of the Breit-Rabi states are introduced later in Sec. 3.2.

	Matrix element for deuterium	Crossing point B [mT]	Nucleon-electron coupling constants
1	$\langle e_2\|V\|\beta_6\rangle$	55.5	$-\sqrt{2}C_{2D}$
2	$\langle e_3\|V\|\beta_5\rangle$	57.0	$-\sqrt{2}C_{2D}$
3	$\langle f_6\|V\|\beta_6\rangle$	111.7	$C_{1D} + C_{2D}$
4	$\langle f_5\|V\|\beta_5\rangle$	113.1	C_{1D}
5	$\langle f_4\|V\|\beta_4\rangle$	114.6	$C_{1D} - C_{2D}$

1.3 Dark matter and axions

The influence of invisible matter on objects due to their gravitational force was stated first in 1846. During this time the trajectory of Uranus was disturbed, and an eighth, yet unidentified planet was held responsible [47]. Shortly after, Le Verrier's calculation was confirmed with its discovery performed by Galle [48]. This was the unveiling of the planet Neptune. Nevertheless, this was the first time in history that the presence of an unobserved mass was demonstrated to have an influence on a visible planet.
It nearly took another century before the next experimental puzzle was observed. Only the introduction of dark matter could explain the unexpected velocities of single galaxies within the Coma galaxy cluster observed by Zwicky in 1933 [49]. In 1970 Rubin and Ford observed differing rotational speeds at larger radii for visible spiral galaxies than theoretically expected by the amount of the visible matter [50]. Therefore, a large dark matter density outside of these visible spiral galaxies was held responsible for this difference. Many years later, more evidence of possible existing dark matter were observed in the famous bullet cluster event [51]. Two galaxy clusters collided with each other and three different observation tools were used to determine the mass distribution. First, stars of single galaxies were observed by their bright visible light. Their movement was nearly unperturbed because of their large density. In contrast, gas clouds, observed via X-rays, which are less dense consequently interfered with each other. These clouds heated up and were distorted in such a way that they could not follow their original cluster trajectory. The total mass distribution was then determined by the method of microlensing. It showed a much larger amount of matter than the visible light, which was placed in the middle of the two galaxy clusters. Consequently, the dark matter, responsible for the larger mass distribution, needed to be much denser than gas clouds and in addition it is non-baryonic.
This triggered the development of many theoretical models including new not yet observed particles being considered as dark matter candidates. One of those is the quantum chromodynamics (QCD) axion [52]. To restrict the mass range of the axion particle Yang and Dong now suggest the observation of the new interaction of these axions in the hydrogen hyperfine states [53]. The advantage of this is that the binding energies can be varied by applying an external homogenous magnetic field. In addition, different transitions can be observed at the same time. Moreover, the detection process would be simplified by determining only the final spin states instead of the energy difference, which is tiny. Furthermore, the direct coupling of the axion field to both the proton and the electron could be determined individually. Yang and Dong suggest two different scenarios of their creations, one before and one after the cosmological inflation, which consequently changes the axion mass. The first one, called classical scenario, would correspond to an axion mass of $m_a \approx 10^{-5}\ \mathrm{eV}/c^2$ whereas $m_a \leq 10^{-7}\ \mathrm{eV}/c^2$ is represented by the anthropic model. The corresponding transitions in the hyperfine splitting can be seen in Tab. 1.4 for the resonance condition. Subsequently, the oscillation time of the axion is expressed as

$$\tau = \frac{2\pi h}{m_a c^2}, \tag{1.10}$$

which is much shorter than the lifetime of both the ground state and metastable atom for both scenarios.
To perform such an experiment a fully polarized hydrogen beam is needed. Yang and Dong suggest to use an atomic beam source [3] to produce a polarized ground state beam. The detection process could be realized via an improved Lamb-shift polarimeter [4, 5]. Moreover, an indirect observation could be also achieved by investigating the metastable hydrogen states. Hence, an improved spin filter can be utilized to create the beam polarization as well as being used for the detection process as part of the LSP. Consequently, in both scenarios an improved spin filter, as addressed in this thesis, would be necessary to scan a wider mass range for the axion search.

Table 1.4: The magnetic field values at which the energy gap for a transition equals to the mass m_a of the two different types of axions are shown. At these field values the resonance condition is given. The magnetic field values are given for the ground state $1S_{1/2}$ and for the metastable atoms $2S_{1/2}$ respectively. The definitions of the hydrogen Breit-Rabi states are introduced later in Sec. 2.4.3 and Sec. 3.1.

	$E_{\beta_4} \leftrightarrow E_{\alpha_1}$	$E_{\alpha_2} \leftrightarrow E_{\alpha_1}$
$1S_{1/2}$	10^{-5} eV at 50 mT	10^{-7} eV at 1.76 mT
$2S_{1/2}$	10^{-5} eV at 82.6 mT	10^{-7} eV at 2.05 mT

1.4 Helium-3 sources

Since 2003 the Brookhaven national laboratory (BNL) has been investigating collisions of polarized high energy proton beams at the relativistic heavy ion collider (RHIC) to gain more knowledge of the proton structure [54]. In 2020 the department of energy (DOE) chose the site of BNL to build the new electron-ion collider (EIC) [55], in remembrance of the earlier storage ring, also called eRHIC. In addition to the polarized electrons, a polarized helium-3 (^{3}He) source will be added to the repertoire [56]. The reason for using polarized helium-3 lies in its neutron-like nuclear structure and its efficient methods of optical pumping to polarize it. Firstly, it is used in medicine as a contrast agent to perform magnetic resonance imaging (MRI) of the lung [57]. Its advantage lies in the much higher polarization value which can last for weeks. Subsequently, optical pumping methods to polarize helium-3 are used to create a nuclear polarized neutron beam. The neutrons, with anti-parallel spins in comparison to the polarization of the helium-3 atoms, are stopped by the spin-dependent reaction [58]

$$n + {}^3\mathrm{He} \rightarrow {}^4\mathrm{He}^* \rightarrow t + p, \tag{1.11}$$

since the spins of the neutron and helium-3 must combine to zero to meet the spin of helium-4. Thus, the neutrons with parallel spins pass the helium-3 gas unharmed. Moreover, experiments have been conducted to use high energy lasers to accelerate ions out of polarized and unpolarized gas jets and therefore realizing high energy polarized sources [59, 60]. As a future project the study of polarized nuclear fusion, in which the helium-3 plays a major role, is addressed in [61]. More information regarding the fusion process is provided in the next section 1.5. Subsequently, the search for the electric dipole moment (EDM), as a consequence of CP violating processes beyond the standard model (SM), which would thereby explain the inequality of observed matter versus anti-matter, is also addressed for the helium-3 [62, 63]. Furthermore, the polarized helium-3, which is a spin 1/2 particle, is often used as an ideal substitute for polarized neutrons [64, 65]. Its advantage is that as an ion it can be forced onto orbits and thereby stored in a storage ring. In addition, beside the proton and deuteron, it has one of the simplest nucleus, which makes it suitable for validating the SM [66, 67].
Consequently, detector systems are needed to verify the nuclear polarization of helium-3 beams and gas targets. As previously mentioned the LSP has a successful history in validating nuclear polarization of hydrogen and H^- beams at COSY, therefore, this thesis addresses the possibility to extend this feature also to helium-3. Similarly such an LSP could be used to determine the helium-3 nuclear polarization of low energy sources at pre-acceleration stage with a life analysis as well as for polarized gas jet targets of a planned ABS for helium-3 [68].

1.5 Polarized nuclear fusion

In 1920 Eddington first suggested that the possible energy source of stars could be due to nuclear fusion [69]. This statement was highly controversial as it was believed that the necessary energy to overcome the Coulomb barrier is too large to realize possible fusion processes. In other words the classical picture of the nuclear fusion reaction needed a higher temperature than the sun can provide. Just a few years later, after the introduction of the Schrödinger equation, the quantum tunnelling effect was discovered [70]. This meant that a lower temperature for nuclear fusion is sufficient to overcome the Coulomb barrier. Shortly after the discovery of the quantum tunnelling effect, Atkinson and Houtermans raised the question of abundant elements in the sun [71]. Moreover, von Weizsäcker and Bethe separately formulated the CNO cycle in which protons fuse to helium-4 [72, 73, 74, 75]. Today many different branches of the CNO cycle are known where for low solar temperatures the most abundant is stated as [76]

$$\begin{aligned} {}^{12}_{6}\mathrm{C} + p &\rightarrow {}^{13}_{7}\mathrm{N} + \gamma, \\ {}^{13}_{7}\mathrm{N} &\rightarrow {}^{13}_{6}\mathrm{C} + e^{+} + \nu_e, \\ {}^{13}_{6}\mathrm{C} + p &\rightarrow {}^{14}_{7}\mathrm{N} + \gamma, \\ {}^{14}_{7}\mathrm{N} + p &\rightarrow {}^{15}_{8}\mathrm{O} + \gamma, \\ {}^{15}_{8}\mathrm{O} &\rightarrow {}^{15}_{7}\mathrm{N} + e^{+} + \nu_e, \\ {}^{15}_{7}\mathrm{N} + p &\rightarrow {}^{12}_{6}\mathrm{C} + {}^{4}_{2}\mathrm{He}. \end{aligned} \tag{1.12}$$

In addition, Bethe developed the first steps towards the pp-chain [74, 75], which is the dominant process in our sun [76]

$$\begin{aligned} p + p &\rightarrow d + e^{+} + \nu_e, \\ d + p &\rightarrow {}^{3}_{2}\mathrm{He} + \gamma, \\ {}^{3}_{2}\mathrm{He} + {}^{3}_{2}\mathrm{He} &\rightarrow {}^{4}_{2}\mathrm{He} + 2p. \end{aligned} \tag{1.13}$$

This is because the fusion products need to overcome a lower Coulomb barrier as compared to heavier elements, given in the CNO cycle. Regarding the pp-chain, different branches, including heavier elements, are also possible. For stars similar to the sun these branches are less probable due to the fact that heavier elements have a larger Coulomb barrier. For his contributions Bethe was awarded with the Nobel Prize in 1967 [77]. To verify these fusion theories it is necessary to observe the only particle which escapes the dense star, which are the created neutrinos. The first conducted experiment to observe solar neutrinos from the pp-chain is the famous homestake experiment [78] for which Davis Jr. received a part of the Nobel Prize in 2002 [79]. They took advantage of a β^- decay due to a neutrino capture

$${}^{37}_{17}\mathrm{Cl} + \nu_e \rightarrow {}^{37}_{18}\mathrm{Ar} + e^{-}. \tag{1.14}$$

To run this reaction the captured neutrino needed to have an energy of at least 0.814 MeV [78]. The only energetically significant neutrinos produced in the sun originated from the less common branches of the pp-chain. Nevertheless, the counted amount of solar neutrinos deviated highly from the theoretically predicted value. The neutrino puzzle was solved by the proof of the neutrino oscillations by the sudbury neutrino observatory (SNO) [80] and super-kamiokande [81] collaboration. For their major contribution in physics the directors were honored with the Nobel Prize in 2015 [82]. The final experimental evidence for the correctness of von Weizsäcker's and Bethe's theory was accomplished by the Borexino group measuring the first neutrinos created in the CNO cycle [83] after having verified, in a comprehensive measurement, the pp-chain [84].
Nuclear fusion, as a natural source of energy, triggered the development of artificial fusion to generate a save and sustainable source of energy for humanity. To increase the efficiency of the

fusion reactions Goldhaber first introduced the idea of using polarized fuel [85]. Consequently, the question arose if the polarization would survive long enough in the plasma to undergo a fusion reaction. This was theoretically investigated by Kulsrud et al. [86]. The corresponding result was that most of the polarization should survive unless the outer conditions of a tokamak would be too extreme, e.g. a cold plasma could lead to molecular hydrogen recombinations. Experimental plans for its verification are on their way incorporating laser induced nuclear polarized fusion at the Petawatt Hoch-Energie Laser für Schwerionenexperimente (PHELIX) at GSI [87] and magnetic confined plasma in the DIII-D tokamak at San Diego [88].
Three generations of reaction types are proposed

$$\begin{aligned} d + t &\rightarrow {}^{4}_{2}\mathrm{He}\,(3.5\ \mathrm{MeV}) + n\,(14.1\ \mathrm{MeV})\,, \\ d + d &\rightarrow {}^{3}_{2}\mathrm{He}\,(0.82\ \mathrm{MeV}) + n\,(2.45\ \mathrm{MeV})\,, \\ &\rightarrow t\,(1.01\ \mathrm{MeV}) + p\,(3.02\ \mathrm{MeV})\,, \\ d + {}^{3}_{2}\mathrm{He} &\rightarrow {}^{4}_{2}\mathrm{He}\,(3.6\ \mathrm{MeV}) + p\,(14.7\ \mathrm{MeV})\,, \end{aligned} \tag{1.15}$$

each with its own advantages and disadvantages [89]. The reason for using these reactions instead of the first channel of the pp-chain is due to larger energy gain and their still low Coulomb barrier. While the first and second reaction include neutrons in their educts the third is neutron free. Nevertheless, deuterium is needed as product, which means that the second reaction can happen simultaneously. As an uncharged particle the neutrons cannot be confined within the plasma and will damage the surface of the tokamak over time. Polarized fuel can be used to enlarge the total cross section σ of the reactants as well as controlling the trajectory of the educts by the differential cross section $d\sigma/d\Omega$, which reduces the wall area damaged by neutrons. Consequently, only certain parts of the wall are damaged and would need to be replaced, when the damage taken becomes too severe. Moreover, only certain parts of the wall would be harmed and in order to compensate the damage, extra shielding and cooling can be applied. The cross section for the first and third kind is theoretically [86, 90] well known and experimentally verified [91, 92]. In the case that both particle's spin are aligned with an external homogenous magnetic field in z-direction, the differential cross section is expressed as [88]

$$\frac{d\sigma}{d\Omega} = \frac{\sigma_0}{4\pi}\left[1 - \frac{1}{2}p_z^D p_z^F + \frac{3}{2}p_z^D p_z^F \sin^2(\theta) + \frac{1}{4}p_{zz}\left(1 - 3\cos^2(\theta)\right)\right]. \tag{1.16}$$

Here p_z^D is the vector polarization of the deuterium d, defined in Eq. (2.128), whereas p_z^F is the vector polarization for the tritium t or helium-3 ^{3}He, respectively. The deuterium tensor polarization is characterized by p_{zz} and is defined in Eq. 2.129. Moreover, θ is the angle between the trajectory of the ejectile with the quantization axis in the centre of mass frame [89]. The cross section for an unpolarized nuclear fusion σ_0 is only dependent on the energy of the products and is otherwise constant [93]. Therefore, at low fusion energies of about several keV the differential cross section is independent of the scattering angle θ within the centre of mass frame. Three different cases of a fully double-polarized fusion process exist. In the first one both particle spins are parallel to each other, e.g. for the spin 1/2 particle $m_I = 1/2$ and the deuterium $m_I = 1$. In the second one the deuterium state is in the $m_I = 0$ state, while in the third one the spins are antiparallel, e.g. $m_I = 1/2$ and for the deuterium $m_I = -1$. Consequently, the differential cross

section for the single cases are given by

$$\begin{aligned}
&\text{I:} \quad p_z^D = p_z^F = p_{zz} = 1, \\
&\quad \frac{d\sigma}{d\Omega} = \frac{\sigma_0}{4\pi}\frac{9}{4}\sin^2(\theta), \\
&\text{II:} \quad p_z^D = 0,\ p_z^F = 1,\ p_{zz} = -2, \\
&\quad \frac{d\sigma}{d\Omega} = \frac{\sigma_0}{4\pi}\left(\frac{1}{2} + \frac{3}{2}\cos^2(\theta)\right), \\
&\text{III:} \quad p_z^D = -1,\ p_z^F = p_{zz} = 1, \\
&\quad \frac{d\sigma}{d\Omega} = \frac{\sigma_0}{4\pi}\left(\frac{1}{4} + \frac{3}{4}\cos^2(\theta)\right),
\end{aligned} \tag{1.17}$$

and are displayed in Fig. 1.1.

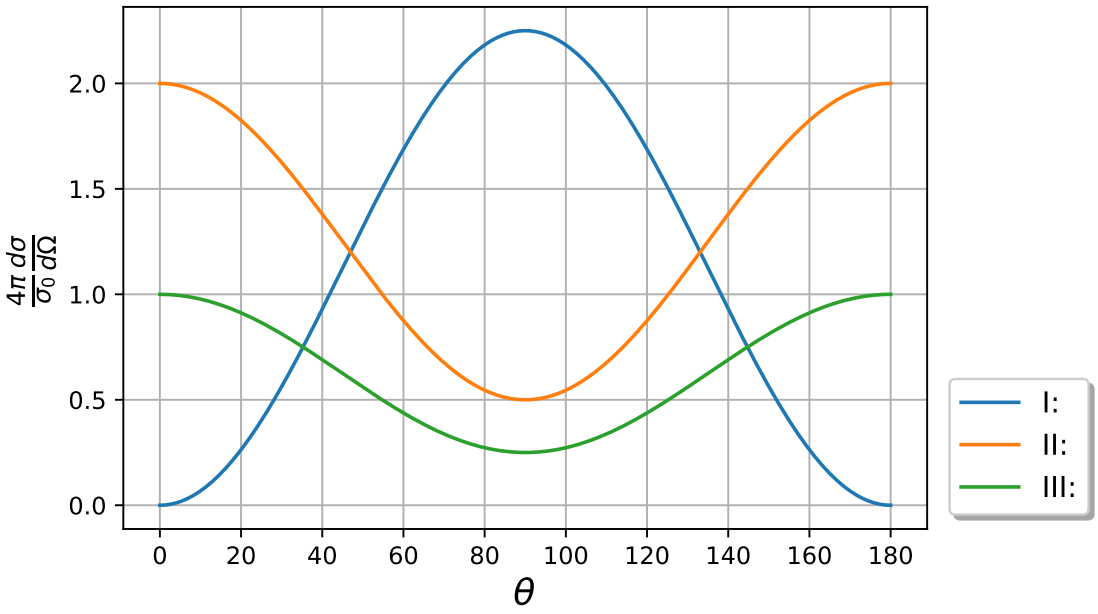

Figure 1.1: The relative differential cross-section of the three different cases for the double polarized deuterium tritium/helium-3 fusion reaction are displayed as function of θ in the centre of mass frame.

In contrast to this, the total cross section

$$\sigma = \int_0^{2\pi} d\varphi \int_0^{\pi} d\theta \, \frac{d\sigma}{d\Omega}, \tag{1.18}$$

for the polarized cases is

$$\begin{aligned}
&\text{I:} \quad \sigma = \frac{3\sigma_0}{2}, \\
&\text{II:} \quad \sigma = \sigma_0, \\
&\text{III:} \quad \sigma = \frac{\sigma_0}{2}.
\end{aligned} \tag{1.19}$$

Consequently, a large energy gain can be achieved by polarizing the fusion products as explained in case I. Therefore, the research for a high intensity source yielding a large polarization value is under investigation. Rakitzis raises the idea to resolve this problem by using an infrared laser to polarize the rotational angular momentum of dedicated molecules [94] and then to transfer the

polarization to the nucleus via the hyperfine beat [95, 96, 97]. The molecule, then confined in a strong magnetic field, could be dissociated, if atoms are involved, which should not enter the plasma of the tokamak. In a next step a special magnetic field configuration could be included to enhance the polarization value [98, 99]. In a final step an LSP would be applied to verify the nuclear polarization [4, 5]. Also the complete spin filter, discussed in this thesis, could improve the measurements. Finally, Parisi and Diallo explain that the nuclear fusion efficiency based on spin polarized fuel is much more relevant, as the power to run the reactor remains equal, and therefore the electric power outcome is largely increased [100]. Before the development of an upgraded nuclear spin filter, the necessary theory needs to be introduced. In addition, the current expertise lacks of a full understanding of the spin dynamics inside the nuclear spin filter. Therefore, the general theory is applied to model and explain the influence of different parameters on the experimental outcome of such measurements.

Chapter 2

General theory

This chapter covers the theory, necessary to perform later calculations and numerical simulations. First the quantum mechanical description of hydrogen-like systems including fine and hyperfine corrections is covered. Next, the density operator and its time evolution is addressed. The chapter then concludes in describing cylindrical cavities based on classical electrodynamics.

2.1 One electron atomic system

In this section, the two-body problem of an electron inside a central electrostatic potential of an atomic nucleus is investigated. Thereby, the spin as degree of freedom is ignored for now. The Hamiltonian describing the two-body problem is expressed as [45]

$$H = \frac{|\vec{p}_e|^2}{2m_e} + \frac{|\vec{p}_N|^2}{2m_N} + V\left(|\vec{r}_e - \vec{r}_N|\right), \tag{2.1}$$

where the index e describes the variables of the electron, whereas N indicates those of the nucleus. In addition, m represents the mass, while $\vec{p}$ characterizes the momentum and $\vec{r}$ the position vector. To simplify the problem, the centre-of-momentum frame is used, in which two new radii and momenta can be defined as follows

$$\begin{aligned} \vec{R} &= \frac{m_e\vec{r}_e + m_N\vec{r}_N}{m_e + m_N}, \\ \vec{r} &= \vec{r}_e - \vec{r}_N, \\ \vec{P} &= \vec{p}_e + \vec{p}_N, \\ \vec{p} &= \frac{m_N\vec{p}_e - m_e\vec{p}_N}{m_e + m_N}. \end{aligned} \tag{2.2}$$

The Hamilton operator is separable as there is no cross term connecting $\vec{R}$ with $\vec{r}$ which leads to a separable wave function

$$F(\vec{R},\vec{r}) = \tilde{f}\left(\vec{R}\right) \otimes f\left(\vec{r}\right). \tag{2.3}$$

This becomes clear after the calculation in Eq. 2.6 is performed. Subsequently, due to the chain and product rules the following expressions can be stated

$$\begin{aligned} \vec{\nabla}_e F\left(\vec{R},\vec{r}\right) &= \vec{\nabla}_R F\left(\vec{R},\vec{r}\right)\frac{\partial R}{\partial r_e} + \vec{\nabla}_r F\left(\vec{R},\vec{r}\right)\frac{\partial r}{\partial r_e} = \vec{\nabla}_R F\left(\vec{R},\vec{r}\right)\frac{m_e}{m_e + m_N} + \vec{\nabla}_r F\left(\vec{R},\vec{r}\right), \\ \vec{\nabla}_N F\left(\vec{R},\vec{r}\right) &= \vec{\nabla}_R F\left(\vec{R},\vec{r}\right)\frac{\partial R}{\partial r_N} + \vec{\nabla}_r F\left(\vec{R},\vec{r}\right)\frac{\partial r}{\partial r_N} = \vec{\nabla}_R F\left(\vec{R},\vec{r}\right)\frac{m_N}{m_e + m_N} - \vec{\nabla}_r F\left(\vec{R},\vec{r}\right). \end{aligned} \tag{2.4}$$

Consequently, the two new momenta fulfill the following relation in position space

$$\begin{aligned}\vec{P} &= -i\hbar\left(\vec{\nabla}_e + \vec{\nabla}_N\right) = -i\hbar\left(\vec{\nabla}_R\frac{m_e}{m_e+m_N} + \vec{\nabla}_r + \vec{\nabla}_R\frac{m_N}{m_e+m_N} - \vec{\nabla}_r\right) = -i\hbar\vec{\nabla}_R,\\ \vec{p} &= -\frac{i\hbar}{m_e+m_N}\left(m_N\vec{\nabla}_e - m_e\vec{\nabla}_N\right)\\ &= -\frac{i\hbar}{m_e+m_N}\left(m_N\left[\vec{\nabla}_R\frac{m_e}{m_e+m_N} + \vec{\nabla}_r\right] - m_e\left[\vec{\nabla}_R\frac{m_N}{m_e+m_N} - \vec{\nabla}_r\right]\right) = -i\hbar\vec{\nabla}_r.\end{aligned} \tag{2.5}$$

Reinserting both momenta into the Hamiltonian Eq. (2.1) leads to

$$\begin{aligned}H &= \frac{p_e^2}{2m_e} + \frac{p_N^2}{2m_N} + V(r)\\ &= \underbrace{\frac{P^2}{2(m_e+m_N)}}_{=H_1\left(\vec{P},\vec{R}\right)} + \underbrace{\frac{p^2(m_e+m_N)}{2m_em_N} + V(r)}_{=H_2(\vec{p},\vec{r})}.\end{aligned} \tag{2.6}$$

The first Hamiltonian $H_1\left(\vec{P},\vec{R}\right)$ describes the movement of the centre of mass system, while the second one $H_2(\vec{p},\vec{r})$ explains the binding relation of the electron to the nucleus. From here on, the derivation follows the steps given in [46] to obtain the eigensolution of $H_2(\vec{p},\vec{r})$. First, the reduced mass $\left({}^{m_e+m_N}/_{m_em_N}\right)^{-1}$ is approximated by m_e, as the nucleus is much heavier than the electron. Moreover, the electrostatic interaction is given by the Coulomb potential $V(|\vec{r}|) = -{}^{Ze^2}/_{4\pi\varepsilon_0 r}$. Therefore, the Hamiltonian takes the following form

$$H = \frac{p^2}{2m_e} - \frac{Ze^2}{4\pi\varepsilon_0 r}, \tag{2.7}$$

where Z is the nuclear charge number, e the elementary charge and ε_0 the vacuum electric permittivity. In the next step, the time-independent eigenproblem $H\psi = E\psi$ of the Hamiltonian is investigated in spherical coordinates in the position Hilbert space

$$\left(-\frac{\hbar^2}{2m_e}\left[\frac{2}{r}\frac{\partial}{\partial r} + \frac{\partial^2}{\partial r^2} + \frac{\cos(\theta)}{r^2\sin(\theta)}\frac{\partial}{\partial\theta} + \frac{1}{r^2}\frac{\partial^2}{\partial\theta^2} + \frac{1}{r^2\sin^2(\theta)}\frac{\partial^2}{\partial\varphi^2}\right] - \frac{Ze^2}{4\pi\varepsilon_0 r}\right)\psi(\vec{r}) = E\psi(\vec{r}). \tag{2.8}$$

Moreover, the solution for the eigenfunctions is, due to the separation of variables, a function composed of a radial-dependent function and one for the angles $\psi(\vec{r}) = R(r)Y(\theta,\varphi)$. The angular dependencies are determined by the spherical harmonics $Y_{l,m}(\theta,\varphi)$, which are defined by

$$\begin{aligned}&\left[\frac{\cos(\theta)}{\sin(\theta)}\frac{\partial}{\partial\theta} + \frac{\partial^2}{\partial\theta^2} + \frac{1}{\sin^2(\theta)}\frac{\partial^2}{\partial\varphi^2}\right]Y_{l,m}(\theta,\varphi) = -l(l+1)Y_{l,m}(\theta,\varphi)\\ &\text{with:}\quad l\in\mathbb{N}_0\quad\text{and}\quad m\in\mathbb{Z}.\\ &\text{In addition:}\quad m = -l,-l+1,...,l-1,l.\end{aligned} \tag{2.9}$$

Thus, the spherical harmonics are related to the orbital angular momentum operator by

$$\begin{aligned}-\frac{\vec{L}^2}{\hbar^2} &= \frac{\cos(\theta)}{\sin(\theta)}\frac{\partial}{\partial\theta} + \frac{\partial^2}{\partial\theta^2} + \frac{1}{\sin^2(\theta)}\frac{\partial^2}{\partial\varphi^2}\\ \text{and}\quad L_zY_{l,m}(\theta,\varphi) &= \hbar mY_{l,m}(\theta,\varphi).\end{aligned} \tag{2.10}$$

Subsequently, the differential equation for the radial function is now given by

$$\left(-\frac{\hbar^2}{2m_e}\left[\frac{2}{r}\frac{\partial}{\partial r} + \frac{\partial^2}{\partial r^2} - \frac{l(l+1)}{r^2}\right] - \frac{Ze^2}{4\pi\varepsilon_0 r} - E\right)R(r) = 0. \tag{2.11}$$

To find the solution of Eq. (2.11) for $r \to \infty$ the following ansatz is chosen

$$R(r) = e^{-\lambda r} f(r), \tag{2.12}$$

with a function $f(r)$, which evolves slowly in the limit $r \to \infty$ such that

$$\left.\frac{\partial f(r)}{\partial r}\right|_{r\to\infty} = 0. \tag{2.13}$$

The reason is that the eigenfunction is an element of the Hilbert space of square-integrable functions $L^2\left(\mathbb{R}^3\right)$ and therefore normalizable via the scalar product [101]

$$\begin{aligned} \langle\psi|\phi\rangle &= \int_{-\infty}^{\infty} \psi(x)^* \phi(x)\, dx \\ \text{and} \quad \langle\psi|\psi\rangle &= \int_{-\infty}^{\infty} |\psi(x)|^2 dx < \infty. \end{aligned} \tag{2.14}$$

To determine the exponent λ those assumptions are plugged into Eq. (2.11). The differential equation then takes the following form for the limit $r \to \infty$

$$\begin{aligned} -\frac{\hbar^2}{2m_e}\frac{\partial^2 R(r)}{\partial r^2} - ER(r) &= \left(-\frac{\hbar^2\lambda^2}{2m_e} - E\right) R(r) = 0, \\ \Rightarrow \quad \lambda &= \pm\sqrt{-\frac{2m_e E}{\hbar^2}} = \tilde{E}, \end{aligned} \tag{2.15}$$

while only the positive solution is valid, as otherwise the wave function would diverge for $r \to \infty$. In addition, $\lambda \in \mathbb{R}$ as the bound system for the Coulomb potential demands $E < 0$. Inserting the ansatz back into the differential equation Eq. (2.11) without any restrictions for r, it leads to the new differential equation for $f(r)$

$$\begin{aligned} &\frac{\partial^2 f(r)}{\partial r^2} + 2\left(\frac{1}{r} - \tilde{E}\right)\frac{\partial f(r)}{\partial r} + \left\{2\left[\frac{\tilde{Z} - \tilde{E}}{r}\right] - \frac{l(l+1)}{r^2}\right\} f(r) = 0 \\ \text{with:} \quad &\tilde{Z} = \frac{m_e Z e^2}{4\pi\varepsilon_0\hbar^2}. \end{aligned} \tag{2.16}$$

As a next ansatz, a power series is chosen

$$f(r) = r^\beta \sum_{\alpha=0}^{\infty} a_\alpha r^\alpha. \tag{2.17}$$

The following relation is obtained by inserting it back into the differential equation Eq. (2.16) for $f(r)$

$$\sum_{\alpha=0}^{\infty} a_\alpha \left\{\left[(\beta+\alpha)(\beta+\alpha+1) - l(l+1)\right] r^{\beta+\alpha-2} + \left[-2\tilde{E}(\beta+\alpha+1) + 2\tilde{Z}\right] r^{\beta+\alpha-1}\right\} = 0. \tag{2.18}$$

Consequently, to obtain more insight into $f(r)$ the technique of equating coefficients is used. From the power $r^{\beta-2}$, the next expression is obtained

$$\begin{aligned} &\beta(\beta+1) - l(l+1) = 0, \\ \Rightarrow \quad &\beta = l \quad \text{or} \quad \beta = -(l+1), \end{aligned} \tag{2.19}$$

while only the first solution is physically valid as the wavefunction needs to be normalizable. For the second solution $f(r)|_{r=0}$ diverges, which can be easily seen by looking at the first power

$\alpha = 0$ in Eq. (2.17). Returning to the method of equating coefficients, a recursive formula for the coefficient a_α is obtained

$$\begin{aligned} & a_\alpha \left[(l+\alpha)(l+\alpha+1) - l(l+1)\right] = -\left[-2\tilde{E}(l+\alpha-1+1) + 2\tilde{Z}\right] a_{\alpha-1}, \\ \Rightarrow \quad & a_\alpha = \frac{2\tilde{E}(l+\alpha) - 2\tilde{Z}}{(l+\alpha)(l+\alpha+1) - l(l+1)} a_{\alpha-1}. \end{aligned} \tag{2.20}$$

At some point, the series needs to end as otherwise for large α the function $R(r)$ is not normalizable

$$\begin{aligned} & a_\alpha = \frac{\left(2\tilde{E} - {}^{2\tilde{Z}}/_{l+\alpha}\right) a_{\alpha-1}}{l+\alpha+1-{}^{l(l+1)}/_{l+\alpha}} \underset{\alpha\to\infty}{\approx} \frac{\left(2\tilde{E}\right)^\alpha a_0}{(l+\alpha+1)!}, \\ \Rightarrow \quad & f(r) = r^l \sum_{\alpha=0}^{\infty} a_\alpha r^\alpha \underset{\alpha\to\infty}{\approx} r^l e^{2\tilde{E}r}, \\ \Rightarrow \quad & R(r) = e^{-2\tilde{E}r} f(r) \underset{\alpha\to\infty}{\approx} e^{\tilde{E}r}. \end{aligned} \tag{2.21}$$

Thus, the first vanishing coefficient is chosen to be $a_{n-l} = 0$. Consequently, the recursive formula gives an expression for the energy

$$\begin{aligned} & 0 = \frac{2\tilde{E}(l+n-l) - 2\tilde{Z}}{(l+n-l)(l+n-l+1) - l(l+1)} a_{n-l-1}, \\ \Rightarrow \quad & \tilde{E} = \frac{\tilde{Z}}{n} \quad \text{and} \quad n \neq l \quad \text{with} \quad n \in \mathbb{N}, \end{aligned} \tag{2.22}$$

to ensure that the energy stays negative and the denominator does not diverge. In addition to the previous restrictions, it is found that

$$n > l. \tag{2.23}$$

The reason is that α is restricted to positive values or zero and therefore a_{n-l}, as the break up condition, must have a positive α. Finally, the entire normalized radial eigenfunction, as defined in Eq. (2.14), and the corresponding eigenenergies are

$$\begin{aligned} E_n &= -\frac{Z^2 m_e e^4}{2(4\pi\varepsilon_0)^2 \hbar^2 n^2}, \\ R_{n,l}(r) &= \sqrt{\left(\frac{2Z}{na_0}\right)^3 \frac{(n-l-1)!}{2n(n+l)!}} e^{-\frac{Zr}{na_0}} \left(\frac{2Zr}{na_0}\right)^l L_{n-l-1}^{2l+1}\left(\frac{2Zr}{na_0}\right), \end{aligned} \tag{2.24}$$

with $a_0 = \frac{4\pi\varepsilon_0\hbar^2}{m_e e^2}$ being the Bohr radius, a constant independent of the normalization parameter introduced in Eq. (2.17), and $L_n^k(x)$ are the associated Laguerre polynomials [102]. Therefore, the entire wave functions are stated as

$$\Psi_{n,l,m}(r,\theta,\varphi) = \sqrt{\left(\frac{2Z}{na_0}\right)^3 \frac{(n-l-1)!}{2n(n+l)!}} e^{-\frac{Zr}{na_0}} \left(\frac{2Zr}{na_0}\right)^l L_{n-l-1}^{2l+1}\left(\frac{2Zr}{na_0}\right) Y_{l,m}(\theta,\varphi). \tag{2.25}$$

Concluding, the energy E_n is only dependent on the main quantum number n, resulting in a degeneracy for all states with the same main quantum number. This degeneracy will be partially lifted by taking further corrections on the Coulomb potential into account.

2.2 Further corrections

Even though the solutions for an atomic bound electron system is very accurate to experimental results, small deviations occur, which are then corrected by perturbation theory.

2.2.1 Fine structure

The fine structure includes three different effects. The first one is known under the name Darwin term and describes a small variation in the electrostatic potential due to rapid changes in the electron trajectory caused by quantum mechanical oscillations, also known under the name Zitterbewegung [103]. A more detailed motivation and more information for the Hamiltonian are provided in [104]. The Hamiltonian describing this effect is expressed as

$$H_{Dar} = \frac{Z\alpha\hbar^3}{8m_e^2 c} 4\pi\delta^3(\vec{r}), \tag{2.26}$$

with $\alpha = \frac{e^2}{4\pi\varepsilon_0\hbar c}$ being the fine-structure constant, c symbolizing the speed of light and $\delta(x)$ the delta distribution. The Darwin term vanishes for almost all wave functions due to the fact that $\Psi_{n,l,m}(r,\theta,\varphi) \sim r^l$, except for those where $l = 0$. Therefore, the Darwin term is only relevant for S-orbitals. Subsequently, calculating the first order energy correction leads to

$$\begin{aligned} E_{Dar} &= \langle\Psi_{n,l,m}|H_{Dar}|\Psi_{n,l,m}\rangle = \langle\Psi_{n,0,0}|H_{Dar}|\Psi_{n,0,0}\rangle \\ &= \frac{Z\alpha\hbar^3}{8m_e^2 c}\int_0^\infty dr\int_0^{2\pi} d\varphi\int_0^\pi d\theta\,\frac{r^2\sin(\theta)\,4\pi}{r^2\sin(\theta)}|R_{n,0}(r)|^2\underbrace{|Y_{0,0}|^2}_{=1/4\pi}\delta(r)\,\delta(\theta)\,\delta(\varphi) \\ &= \frac{2nE_n^2}{m_e c^2}. \end{aligned} \tag{2.27}$$

In the derivation the following relation is used

$$\frac{1}{n}L_{n-1}^1(0) = 1. \tag{2.28}$$

The proof is shown in App. B. The second effect is based on relativistic corrections due to possible large electron speeds. Consequently, the kinetic energy term needs to be adjusted to be valid for a relativistic regime, too. The first order correction is

$$H_{rel} = -\frac{|\vec{p}|^4}{8m_e^3 c^2}. \tag{2.29}$$

With the help of the unperturbed Hamiltonian it is possible to get a simple relation for the operator p^4 [105]

$$\begin{aligned} & H^{(0)}|\Psi_{n,l,m}\rangle = \left(\frac{p^2}{2m_e} + V(r)\right)|\Psi_{n,l,m}\rangle, \\ \Rightarrow\quad & \langle\Psi_{n',l',m'}|p^2|\Psi_{n,l,m}\rangle = 2m_e\left(E_n\delta_{n,n'}\delta_{l,l'}\delta_{m,m'} - \langle\Psi_{n',l',m'}|V(r)|\Psi_{n,l,m}\rangle\right). \end{aligned} \tag{2.30}$$

Due to this, the matrix element for p^4 is stated as

$$\begin{aligned} &\langle\Psi_{n',l',m'}|p^4|\Psi_{n,l,m}\rangle = \langle\Psi_{n',l',m'}|\left[2m_e\left(E_n\mathbb{1} - V(r)\right)\right]^2|\Psi_{n,l,m}\rangle \\ &= 4m_e^2\left(E_n^2\delta_{n,n'}\delta_{l,l'}\delta_{m,m'} - 2E_n\langle\Psi_{n',l',m'}|V(r)|\Psi_{n,l,m}\rangle + \langle\Psi_{n',l',m'}|V^2(r)|\Psi_{n,l,m}\rangle\right). \end{aligned} \tag{2.31}$$

Consequently, the matrix elements are to be calculated

$$\begin{aligned} \langle\Psi_{n',l',m'}|V(r)|\Psi_{n,l,m}\rangle &= -\frac{Ze^2}{4\pi\varepsilon_0}\int_0^\infty dr\int_0^{2\pi} d\varphi\int_0^\pi d\theta\, r\sin(\theta)\,R_{n,l}^* Y_{l,m}^* R_{n',l'}Y_{l',m'} \\ &= -\frac{Ze^2}{4\pi\varepsilon_0}\int_0^\infty dr\, r R_{n,l}^* R_{n',l'}\delta_{l,l'}\delta_{m,m'}. \end{aligned} \tag{2.32}$$

Here it is visible that l and m are fixed. Moreover, the first order perturbed energy is obtained by

$$\langle \Psi_{n,l,m} | H_{rel} | \Psi_{n,l,m} \rangle . \tag{2.33}$$

Therefore, the average values of r^{-1} and r^{-2} are calculated in App. B as

$$\begin{aligned} \left\langle \frac{1}{r} \right\rangle &= \frac{Z}{a_0 n^2}, \\ \left\langle \frac{1}{r^2} \right\rangle &= \frac{Z^2}{a_0^2 n^3 \left(l + 1/2\right)}. \end{aligned} \tag{2.34}$$

Consequently, the first order energy correction for the relativistic part is

$$E_{rel} = -\frac{4m_e^2}{8m_e^3 c^2} \left(E_n^2 + \frac{2E_n Z^2 e^2}{4\pi\varepsilon_0 a_0 n^2} + \frac{Z^4 e^4}{16\pi^2 \varepsilon_0^2 a_0^2 n^3 \left(l + 1/2\right)} \right) = -\frac{E_n^2}{2m_e c^2} \left(\frac{4n}{l + 1/2} - 3 \right). \tag{2.35}$$

The final part of the fine structure correction is called spin-orbit coupling and is caused by the magnetic moment due to the electron spin interacting with the magnetic moment created by the orbital motion around the nucleus. The corresponding Hamiltonian is expressed as [104]

$$H_{SO} = \frac{Ze^2}{4\pi\varepsilon_0} \frac{g_s - 1}{2m_e^2 c^2} \frac{\vec{L} \cdot \vec{S}}{r^3}, \tag{2.36}$$

with g_s being the electron g-factor, while $\vec{L}$ is the orbital angular momentum operator and $\vec{S}$ the spin operator, respectively. Separating the angular dependencies from the radial ones, leads us to calculate the expectation values of $\vec{L} \cdot \vec{S}$ and r^{-3}. Starting with the angular part

$$\begin{aligned} \left\langle \vec{L} \cdot \vec{S} \right\rangle &= \frac{1}{2} \left[\left(\left\langle \vec{L} \right\rangle + \left\langle \vec{S} \right\rangle \right)^2 - \left\langle \vec{S} \right\rangle^2 - \left\langle \vec{L} \right\rangle^2 \right] = \frac{1}{2} \left(\left\langle \vec{J} \right\rangle^2 - \left\langle \vec{S} \right\rangle^2 - \left\langle \vec{L} \right\rangle^2 \right) \\ &= \frac{\hbar^2}{2} \left[j\left(j+1\right) - l\left(l+1\right) - s\left(s+1\right) \right], \end{aligned} \tag{2.37}$$

where in the last steps it is used that $\vec{L}$ and $\vec{S}$ commute as they act on different Hilbert spaces. Here, the total angular momentum operator for the electron $\vec{J} = \vec{L} \otimes \mathbb{1} + \mathbb{1} \otimes \vec{S}$ is introduced. Kramers relation [101] is used, to avoid calculating complex radial integrals and to obtain the average value of r^{-3}

$$\frac{s+1}{n^2} \left\langle r^s \right\rangle - \left(2s+1\right) \frac{a_0}{Z} \left\langle r^{s-1} \right\rangle + \frac{s}{4} \left[\left(2l+1\right)^2 - s^2 \right] \frac{a_0^2}{Z^2} \left\langle r^{s-2} \right\rangle = 0. \tag{2.38}$$

Setting $s = -1$ results in

$$\left\langle r^{-3} \right\rangle = \frac{4 \left\langle r^{-2} \right\rangle Z}{\left[\left(2l+1\right)^2 - 1 \right] a_0} = \frac{Z^3}{a_0^3 n^3 l \left(l+1\right) \left(l + 1/2\right)}. \tag{2.39}$$

Subsequently, the energy correction for the spin-orbit coupling is

$$\left\langle H_{SO} \right\rangle = \frac{E_n^2 n \left(g_s - 1\right) \left[j\left(j+1\right) - l\left(l+1\right) - s\left(s+1\right) \right]}{m_e c^2 l \left(l+1\right) \left(l + 1/2\right)}. \tag{2.40}$$

2.2.2 Lamb-shift

The Lamb-shift, one of the most prominent effects due to quantum electrodynamics (QED) and first discovered by Lamb and Retherford [106], is introduced in this section. It originates from the interaction of an electron with virtual photons created by electromagnetic fields. Due to the fact that there are an infinite amount of Feynman diagrams each of higher order, the renormalization needs to be used to find an appropriate cut-off. In this section a simple derivation for the Lamb-shift is given based on [107]. A more complete derivation using quantum field theory is displayed in [108]. The starting point for the derivation is that the electron orbit is distorted by fluctuations of the electromagnetic fields produced by the nucleus. Therefore, the orbit is adjusted by

$$\vec{r} \to \vec{r} + \delta\vec{r}, \tag{2.41}$$

with $\delta\vec{r}$ being a very small correction. Correspondingly, the central potential, which depends on the radius, is adjusted too

$$V(\vec{r}) \to V\left(\vec{r} + \delta\vec{r}\right). \tag{2.42}$$

Expanding this potential in a Taylor series around $\delta\vec{r} = \vec{0}$ the following expression is obtained

$$V\left(\vec{r} + \delta\vec{r}\right) = V\left(\vec{r}\right) + \vec{\nabla}V\left(\vec{r}\right) \cdot \delta\vec{r} + \frac{1}{2}\left(\delta\vec{r} \cdot \vec{\nabla}\right)^2 V\left(\vec{r}\right). \tag{2.43}$$

Assuming an isotropic perturbation the second term vanishes for the expectation value. In addition, only the energy change matters

$$\left\langle V\left(\vec{r} + \delta\vec{r}\right)\right\rangle - \left\langle V\left(\vec{r}\right)\right\rangle = \left\langle \frac{1}{2}\left(\delta\vec{r} \cdot \vec{\nabla}\right)^2 V\left(\vec{r}\right)\right\rangle. \tag{2.44}$$

As the correction of the orbit $\delta\vec{r}$ is due to vacuum fluctuations $\mathscr{H}_{\mathrm{Vac}}$ while the undisturbed trajectories are given by the central potential $\mathscr{H}_{\mathrm{Atom}}$ it is assumed that they are independent from each other. In addition, due to the vacuum isotropy all components of $\delta\vec{r}$ are equal to each other ($\delta r = \delta x = \delta y = \delta z$). Consequently, it is possible to write

$$\begin{aligned}
\left\langle V\left(\vec{r} + \delta\vec{r}\right)\right\rangle - \left\langle V\left(\vec{r}\right)\right\rangle &= \frac{1}{2}\left\langle \frac{1}{3}3\left(\delta r\right)^2\right\rangle_{\mathrm{Vac}} \left\langle \vec{\nabla}^2 V\left(\vec{r}\right)\right\rangle_{\mathrm{Atom}} \\
&= \frac{1}{6}\left\langle \left(\delta\vec{r}\right)^2\right\rangle_{\mathrm{Vac}} \left\langle \vec{\nabla}^2 V\left(\vec{r}\right)\right\rangle_{\mathrm{Atom}} \\
&= \frac{1}{6}\left\langle \left(\delta\vec{r}\right)^2\right\rangle_{\mathrm{Vac}} \left\langle \vec{\nabla}^2 \frac{-e^2}{4\pi\varepsilon_0 r}\right\rangle_{\mathrm{Atom}} \\
&= \frac{1}{6}\left\langle \left(\delta\vec{r}\right)^2\right\rangle_{\mathrm{Vac}} \left\langle \frac{e^2}{\varepsilon_0}\delta\left(\vec{r}\right)\right\rangle_{\mathrm{Atom}},
\end{aligned} \tag{2.45}$$

where the latter $\delta\left(\vec{r}\right)$ is a delta distribution. Next, it is necessary to focus on the first term concerning the vacuum fluctuation. Assuming that the dominant part is caused by the electric field component, it is possible to characterize it with the help of the second quantization for a mode k by

$$\vec{E}_k(t) = \varepsilon_k\left(a_k e^{-i\omega_k t + i\vec{k}\cdot\vec{r}} + a_k^\dagger e^{i\omega_k t - i\vec{k}\cdot\vec{r}}\right) \quad \text{with} \quad \varepsilon_k = \sqrt{\frac{\hbar c k}{2\varepsilon_0 V}}. \tag{2.46}$$

V represents the investigated volume, while ω_k is the angular frequency for the corresponding wave number k. In addition, a_k symbolizes the annihilation operator for the mode k, while $a_k^\dagger$ represents the creation operator, respectively. Moreover, the corresponding fluctuations are time-dependent according to

$$\delta\vec{r}\left(t\right) = \delta\vec{r}\left(t = 0\right)\left(e^{-i\omega_k t} + e^{i\omega_k t}\right). \tag{2.47}$$

Consequently, the classical equation of motion results in

$$\begin{aligned} m_e \frac{d^2 \delta\vec{r}\,(t)}{dt^2} &= -\underbrace{\omega_k^2}_{=c^2k^2}\, m_e \delta\vec{r}\,(t=0)\left(e^{-i\omega_k t} + e^{i\omega_k t}\right) = -e\vec{E}_k, \\ \Rightarrow \quad \delta\vec{r}\,(t) &= \frac{e}{m_e c^2 k^2}\vec{E}_k. \end{aligned} \tag{2.48}$$

To calculate the average displacement it is necessary to sum over all possible modes which are created from the starting vacuum state $|0\rangle$

$$\begin{aligned} \left\langle (\delta\vec{r})^2 \right\rangle_{\text{Vac}} &= \sum_k \left(\frac{e}{m_e c^2 k^2}\right)^2 \left\langle 0 \middle| \left(\vec{E}_k\right)^2 \middle| 0 \right\rangle \\ &= \sum_k \left(\frac{e\varepsilon_k}{m_e c^2 k^2}\right)^2 \left[\left\langle 0 \middle| a_k a_k e^{-2i\omega_k t + 2i\vec{k}\cdot\vec{r}} \middle| 0 \right\rangle + \left\langle 0 \middle| a_k a_k^\dagger \middle| 0 \right\rangle \right. \\ &\left. + \left\langle 0 \middle| a_k^\dagger a_k \middle| 0 \right\rangle + \left\langle 0 \middle| a_k^\dagger a_k^\dagger e^{2i\omega_k t - 2i\vec{k}\cdot\vec{r}} \middle| 0 \right\rangle \right] \\ &= \sum_k \left(\frac{e\varepsilon_k}{m_e c^2 k^2}\right)^2 \\ &= \frac{V}{(2\pi)^3} \int g_s d^3k \left(\frac{e\varepsilon_k}{m_e c^2 k^2}\right)^2 \\ &= \frac{g_s V}{2\pi^2} \int_0^\infty dk\, k^2 \frac{e^2}{m_e^2 c^4} \frac{\hbar c}{2\varepsilon_0 V} \frac{1}{k^3} \\ &= \frac{g_s}{4\varepsilon_0 \pi^2} \left(\frac{e^2}{\hbar c}\right) \left(\frac{\hbar}{m_e c}\right)^2 \int_0^\infty \frac{dk}{k}, \end{aligned} \tag{2.49}$$

with $g_s = 2$ being the polarization modes of photons. This integral diverges logarithmically. Correspondingly, it is necessary to find an appropriate cut-off. The lower bound can be replaced by assuming that the modes need to be large enough to reach the Bohr radius $k_{lower} \approx \frac{\pi}{a_0}$. In contrast to this the upper bound is restricted by the Compton wavelength $k_{upper} \approx \frac{m_e c}{\hbar}$. Therefore, the result of the vacuum fluctuation is

$$\begin{aligned} \left\langle (\delta\vec{r})^2 \right\rangle_{\text{Vac}} &= \frac{1}{2\varepsilon_0 \pi^2} \left(\frac{e^2}{\hbar c}\right) \left(\frac{\hbar}{m_e c}\right)^2 \left[\ln\left(\frac{m_e c}{\hbar}\right) - \ln\left(\frac{\pi}{a_0}\right)\right] \\ &= \frac{1}{2\varepsilon_0 \pi^2} \left(\frac{e^2}{\hbar c}\right) \left(\frac{\hbar}{m_e c}\right)^2 \ln\left(\frac{4\varepsilon_0 \hbar c}{e^2}\right). \end{aligned} \tag{2.50}$$

Finally, the energy correction due to the Lamb-shift is in a good approximation stated as

$$E_{Lamb} = \frac{1}{6} \left\langle (\delta\vec{r})^2 \right\rangle_{\text{Vac}} \left\langle \frac{e^2}{\varepsilon_0} \delta(\vec{r}) \right\rangle_{\text{Atom}} = \frac{1}{6} \frac{1}{2\varepsilon_0 \pi^2} \left(\frac{e^2}{\hbar c}\right) \left(\frac{\hbar}{m_e c}\right)^2 \ln\left(\frac{4\varepsilon_0 \hbar c}{e^2}\right) \left\langle \frac{e^2}{\varepsilon_0} \delta(\vec{r}) \right\rangle_{\text{Atom}}. \tag{2.51}$$

2.2.3 Hyperfine structure

So far the energy corrections are due to processes involving only the electron and its interaction to the central potential of a perfect spherical object. In contrast the hyperfine interaction takes the nuclear spin and its magnetic moment, as well as possible non-spherical structure of the nucleus into account. Therefore, the deviation of certain nuclei from the ideal spherical shape results in the emergence of intrinsic electric quadrupole and magnetic octupole moments [109, 110]. The derivation for the electrical quadrupole is available in App. C. In the following the magnetic dipole as first order correction is introduced. It interplays with the electron and is therefore given by the following Hamiltonian [104, 46]

$$H_{HF} = \frac{\mu_0}{4\pi} \frac{2\mu_B \mu_k g_I}{\hbar^2} \left[\frac{8\pi}{3} \vec{S}\cdot\vec{I}\,\delta(\vec{r}) - \frac{\vec{S}\cdot\vec{I}}{r^3} + \frac{3\left(\vec{S}\cdot\vec{r}\right)\left(\vec{I}\cdot\vec{r}\right)}{r^5} + \frac{\vec{L}\cdot\vec{I}}{r^3}\right], \tag{2.52}$$

where $\vec{I}$ is the nuclear spin angular momentum and g_I its nuclear g-factor. In addition, $\mu_k = e\hbar/2m_p$ represents the nuclear magneton, while $\mu_B = e\hbar/2m_e$ is the Bohr magneton, respectively. Finally, μ_0 symbolizes the magnetic vacuum permeability. From here the steps of [46] are followed. The first term in the Hamiltonian is, as previously mentioned for the Darwin correction, unequal zero only for S-orbitals, meaning $l = 0$. As the energy difference between two states of the same orbit is much smaller than jumping into a new orbit the energy correction for a fixed main quantum number n and orbital angular momentum number l is addressed here. This simplifies the Hamiltonian immensely. First, the derivation starts with some states with $l \neq 0$. To reformulate the second and third term in the Hamiltonian the following relation is used

$$\begin{aligned}\left(\vec{S}\cdot\vec{I}\right)r^2 - 3\left(\vec{S}\cdot\vec{r}\right)\left(\vec{I}\cdot\vec{r}\right) &= \sum_{i,j=1}^{3} S_i I_j \left(r^2\delta_{i,j} - 3x_i x_j\right) \\ &= -\frac{\left\langle r^2\right\rangle}{(2l+3)(2l-1)\hbar^2}\left[2\vec{L}^2\left(\vec{S}\cdot\vec{I}\right) - 3\left(\vec{S}\cdot\vec{L}\right)\left(\vec{I}\cdot\vec{L}\right) - 3\left(\vec{I}\cdot\vec{L}\right)\left(\vec{S}\cdot\vec{L}\right)\right].\end{aligned} \tag{2.53}$$

To prove this relation it would be necessary to compute all possible combinations of expectation values, which is obtainable in App. C. Subsequently, by inserting Eq. (2.53) into Eq. (2.52) the next relation is obtained

$$H_{HF}|_{l\neq 0} = \frac{\mu_0}{4\pi}\frac{2\mu_B\mu_k g_I}{\hbar^4\left\langle r^3\right\rangle}\left[\frac{2\vec{L}^2\left(\vec{S}\cdot\vec{I}\right) - 3\left(\vec{S}\cdot\vec{L}\right)\left(\vec{I}\cdot\vec{L}\right) - 3\left(\vec{I}\cdot\vec{L}\right)\left(\vec{S}\cdot\vec{L}\right)}{(2l+3)(2l-1)} + \vec{L}\cdot\vec{I}\right]. \tag{2.54}$$

In the next step the following relations are utilized

$$\begin{aligned}\vec{S} &= \frac{\left\langle\vec{S}\cdot\vec{J}\right\rangle}{\left\langle\vec{J}^2\right\rangle}\vec{J} = \frac{j(j+1) - l(l+1) + s(s+1)}{2j(j+1)}\vec{J}, \\ \vec{L} &= \frac{\left\langle\vec{L}\cdot\vec{J}\right\rangle}{\left\langle\vec{J}^2\right\rangle}\vec{J} = \frac{j(j+1) + l(l+1) - s(s+1)}{2j(j+1)}\vec{J}.\end{aligned} \tag{2.55}$$

The proof can be found in App. B. Continuing with implementing Eq. (2.55) into the Hamiltonian of Eq. (2.54) the next expression is obtained

$$H_{HF}|_{l\neq 0} = \frac{\mu_0}{4\pi}\frac{2\mu_B\mu_k g_I}{\hbar^2\left\langle r^3\right\rangle}\frac{l(l+1)}{j(j+1)}\vec{I}\cdot\vec{J}. \tag{2.56}$$

Using the result of Eq. (2.39) the Hamiltonian transforms to

$$\begin{aligned}H_{HF}|_{l\neq 0} &= \frac{\mu_0}{4\pi}\frac{e^2 g_I Z^3}{2a_0^3 m_e m_p n^3 j(j+1)(l+1/2)}\vec{I}\cdot\vec{J} \\ &= A\frac{\vec{I}\cdot\vec{J}}{\hbar^2}.\end{aligned} \tag{2.57}$$

In the derivation for Eq. (2.56) the assumption, that $l \neq 0$, was never exactly needed. Consequently, the same derivation can be applied for $l = 0$. Moreover, the Hamiltonian of Eq. (2.56) vanishes for $l = 0$ and therefore only the first term of Eq. (2.52) remains. To show that Eq. (2.56) vanishes, the expectation value of $\left\langle r^{-3}\right\rangle$ for $l = 0$

$$\begin{aligned}\left\langle r^{-3}\right\rangle &= \int_0^\infty dr\int_0^{2\pi} d\varphi\int_0^\pi d\theta\,\frac{\sin(\theta)}{r}\left(\frac{2Z}{na_0}\right)^3\frac{(n-1)!}{2nn!}e^{-2Zr/na_0}\left[L_{n-1}^1\left(\frac{2Zr}{na_0}\right)\right]^2|Y_{0,0}|^2 \\ &= \left(\frac{2Z}{na_0}\right)^3\frac{(n-1)!}{2nn!}\int_0^\infty dx\,\frac{e^{-x}}{x}\left[L_{n-1}^1(x)\right]^2,\end{aligned} \tag{2.58}$$

is addressed. The integral diverges for $x = 0$. To understand the result of the integral better, the associated Laguerre polynomial is investigated

$$L^1_{n-1}(x) = \frac{e^x x^{-1}}{(n-1)!}\frac{d^{n-1}}{dx^{n-1}}\left(e^{-x}x^n\right) = \frac{(-1)^{n-1}x^{n-1}}{(n-1)!} + \frac{(-1)^{n-2}nx^{n-2}}{(n-1)!} + \ldots - \frac{xn!}{2\,(n-1)!} + \frac{n!}{(n-1)!}. \quad (2.59)$$

In order to prevent that the last term of the associated Laguerre polynomial diverges for the integral, a small part of the radius at the centre is deduced by $\varepsilon \to 0$ which results in

$$\lim_{\varepsilon\to 0}\int_\varepsilon^\infty dx\,\frac{e^{-x}}{x} = \lim_{\varepsilon\to 0}\Gamma\left(0,\varepsilon\right). \quad (2.60)$$

Thus, $\left\langle r^{-3}\right\rangle$ for $l = 0$ is a large but finite number, such that Eq. (2.56) goes to zero for $l = 0$. Consequently, due to the first term of Eq. (2.52), the resultant Hamiltonian for $l = 0$ is stated as

$$\begin{aligned} H_{HF}|_{l=0} &= \frac{\mu_0}{4\pi}\frac{2\mu_B\mu_k g_I}{\hbar^2}\frac{8\pi}{3}\vec{I}\cdot\vec{S}\delta\left(\vec{r}\right) \\ &= \frac{4\mu_0\mu_B\mu_k g_I}{3\hbar^2}|R_{n,0}(r=0)|^2|Y_{0,0}|^2\vec{I}\cdot\vec{S} \\ &= \frac{\mu_0\mu_B\mu_k g_I}{3\pi\hbar^2}|R_{n,0}(r=0)|^2\vec{I}\cdot\vec{S} \\ &= \tilde{A}\frac{\vec{I}\cdot\vec{S}}{\hbar^2}. \end{aligned} \quad (2.61)$$

2.3 Dirac equation for one electron atomic system

The Dirac equation describes relativistic spin 1/2 particles. Allows for a complete derivation of wave functions as well as eigenenergies for a central Coulomb potential. The derivation follows the steps stated at [111]. First, the Hamiltonian is expressed as

$$H_{\text{Dirac}} = c\vec{\alpha}\cdot\vec{p} + \beta m_e c^2 - \frac{Ze^2}{4\pi\varepsilon_0 r}\mathbb{1}, \quad (2.62)$$

with

$$\beta = \begin{pmatrix}\mathbb{1} & \underline{0}\\ \underline{0} & -\mathbb{1}\end{pmatrix}, \quad \alpha_i = \begin{pmatrix}\underline{0} & \sigma_i\\ \sigma_i & \underline{0}\end{pmatrix}, \quad (2.63)$$

$\in \mathbb{C}^{4x4}$, introducing the spin 1/2 dynamics into the equation by the Pauli matrices σ_i, which are connected to the spin-1/2 operator by $\vec{S} = \frac{\hbar}{2}\vec{\sigma}$. Consequently, the orbital angular momentum $\vec{L}$ is no longer sufficient to describe the rotational dynamics due to the spin-orbit coupling. Instead, $|\vec{J}|^2$, J_z and the spin-orbit coupling $\vec{S}\cdot\vec{L}$ share the same eigenbasis. The four-vectorial wavefunctions also called spinors are split up into a pair of two dimensional wavefunctions

$$\Psi(\vec{r}) = \begin{pmatrix}\psi_1\left(\vec{r}\right)\\ \psi_2\left(\vec{r}\right)\end{pmatrix}. \quad (2.64)$$

With the introduced Hamiltonian from Eq. (2.62) and the defined spinor the eigenequation

$$H\Psi(\vec{r}) = E\Psi(\vec{r}), \quad (2.65)$$

can be split into two coupled equations

$$\begin{aligned} \left(E - m_e c^2 + \frac{Ze^2}{4\pi\varepsilon_0 r}\right)\psi_1\left(\vec{r}\right) - c\left(\vec{\sigma}\cdot\vec{p}\right)\psi_2\left(\vec{r}\right) = 0, \\ \left(E + m_e c^2 + \frac{Ze^2}{4\pi\varepsilon_0 r}\right)\psi_2\left(\vec{r}\right) - c\left(\vec{\sigma}\cdot\vec{p}\right)\psi_1\left(\vec{r}\right) = 0. \end{aligned} \quad (2.66)$$

First, the angular part and next the radial segment is addressed. Only the last term, including the Pauli matrices, has angular components, as it is visible in Eq. (2.66). Therefore, this part is addressed first

$$\begin{aligned}\vec{\sigma}\cdot\vec{p} &\overset{\text{use I}}{=} \frac{1}{r^2}\left(\vec{\sigma}\cdot\vec{r}\right)^2\left(\vec{\sigma}\cdot\vec{p}\right) \overset{\text{use II}}{=} \frac{1}{r^2}\left(\vec{\sigma}\cdot\vec{r}\right)\left[\vec{r}\cdot\vec{p}+i\vec{\sigma}\cdot\left(\vec{r}\times\vec{p}\right)\right]\\ &= \left(\vec{\sigma}\cdot\hat{e}_r\right)\left[\hat{e}_r\cdot\vec{p}+i\vec{\sigma}\cdot\frac{\vec{L}}{r}\right]\\ &= i\left(\vec{\sigma}\cdot\hat{e}_r\right)\left[-\hbar\frac{\partial}{\partial r}+\frac{2\vec{S}\cdot\vec{L}}{\hbar r}\right],\end{aligned} \tag{2.67}$$

where the following properties are used

$$\begin{aligned}&\text{I:}\quad \left(\vec{\sigma}\cdot\vec{a}\right)^2 = |\vec{a}|^2,\\ &\text{II:}\quad \left(\vec{\sigma}\cdot\vec{a}\right)\left(\vec{\sigma}\cdot\vec{b}\right) = \vec{a}\cdot\vec{b}+i\vec{\sigma}\cdot\left(\vec{a}\times\vec{b}\right).\end{aligned} \tag{2.68}$$

Subsequently, the ansatz for the two wave functions is chosen as

$$\begin{aligned}\psi_1 &= u\left(r\right)\chi^{j,m_j}_{l=j\mp1/2},\\ \psi_2 &= -iv\left(r\right)\chi^{j,m_j}_{l=j\pm1/2},\end{aligned} \tag{2.69}$$

with

$$\chi^{j,m_j}_{l=j\mp1/2} = \frac{1}{\sqrt{2l+1}}\begin{pmatrix}\pm\sqrt{l\pm m_j+1/2}\,Y_{l,m_j-1/2}\\ \sqrt{l\mp m_j+1/2}\,Y_{l,m_j+1/2}\end{pmatrix}. \tag{2.70}$$

Consequently, it is possible to realize that there are two solutions, which only differ in their ordering of χ^{j,m_j}_l. First, it is shown that

$$\begin{aligned}\left(\vec{\sigma}\cdot\hat{e}_r\right)\chi^{j,m_j}_{l=j\mp1/2} &= \left(\cos\left(\varphi\right)\sin\left(\theta\right)\sigma_x+\sin\left(\varphi\right)\sin\left(\theta\right)\sigma_y+\cos\left(\theta\right)\sigma_z\right)\chi^{j,m_j}_{l=j\mp1/2}\\ &= \begin{pmatrix}\cos\left(\theta\right) & e^{-i\varphi}\sin\left(\theta\right)\\ e^{i\varphi}\sin\left(\theta\right) & -\cos\left(\theta\right)\end{pmatrix}\chi^{j,m_j}_{l=j\mp1/2}\\ &= -\chi^{j,m_j}_{l=j\pm1/2}.\end{aligned} \tag{2.71}$$

To perform this calculation the definition for χ^{j,m_j}_l from Eq. (2.70) and the properties for the spherical harmonics from [46] are used

$$\begin{aligned}\cos\left(\theta\right)Y_{l,m} &= \sqrt{\frac{\left(l+m+1\right)\left(l-m+1\right)}{\left(2l+1\right)\left(2l+3\right)}}Y_{l+1,m}+\sqrt{\frac{\left(l+m\right)\left(l-m\right)}{\left(2l+1\right)\left(2l-1\right)}}Y_{l-1,m},\\ \sin\left(\theta\right)e^{-i\varphi}Y_{l,m} &= \sqrt{\frac{\left(l-m+1\right)\left(l-m+2\right)}{\left(2l+1\right)\left(2l+3\right)}}Y_{l+1,m-1}-\sqrt{\frac{\left(l+m\right)\left(l+m-1\right)}{\left(2l+1\right)\left(2l-1\right)}}Y_{l-1,m-1},\\ \sin\left(\theta\right)e^{i\varphi}Y_{l,m} &= -\sqrt{\frac{\left(l+m+1\right)\left(l+m+2\right)}{\left(2l+1\right)\left(2l+3\right)}}Y_{l+1,m+1}+\sqrt{\frac{\left(l-m\right)\left(l-m-1\right)}{\left(2l+1\right)\left(2l-1\right)}}Y_{l-1,m+1}.\end{aligned} \tag{2.72}$$

It is important to notice that the two books have a different convention in defining the spherical harmonics, which differ by a sign. The proof that the change in sign accomplishes the relations in Eq. (2.72) is stated in App. A. With this result the angular part of Eq. (2.67) can be expressed as

$$\begin{aligned}&i\left(\vec{\sigma}\cdot\hat{e}_r\right)\left[-\hbar\frac{\partial}{\partial r}+\frac{2\vec{S}\cdot\vec{L}}{\hbar r}\right]\chi^{j,m_j}_{l=j\mp1/2} = -i\left[-\hbar\frac{\partial}{\partial r}+\frac{\mu\left(j,l\right)}{\hbar r}\right]\chi^{j,m_j}_{l=j\pm1/2}\\ &\text{with}\quad \mu\left(j,l\right) = \begin{cases}-j-3/2 = -\left(\lambda+1\right) & ,\text{if } l=j+1/2\\ j-1/2 = \left(\lambda-1\right) & ,\text{if } l=j-1/2\end{cases}\\ &\text{and}\quad \lambda = j+1/2.\end{aligned} \tag{2.73}$$

Next, the radial part is addressed. Therefore, the last term, including the Pauli matrices, from Eq. (2.66) is replaced with the result obtained in Eq. (2.73)

$$\begin{aligned}
&\left(\varepsilon - \frac{c}{\hbar} + \frac{Z\alpha}{x}\right) u(x) - \frac{\partial}{\partial x} v(x) - \frac{\lambda+1}{x} v(x) = 0, \\
&\left(\varepsilon + \frac{c}{\hbar} + \frac{Z\alpha}{x}\right) v(x) + \frac{\partial}{\partial x} u(x) - \frac{\lambda-1}{x} u(x) = 0 \\
&\text{with} \quad \varepsilon = \frac{E}{m_e c\hbar}, \quad x = m_e r, \quad \alpha = \frac{e^2}{4\pi\varepsilon_0 \hbar c},
\end{aligned} \tag{2.74}$$

for the first solution of the ansatz defined in Eq. (2.69). However, the difference between the two ansätze of Eq. (2.69) inserted in Eq. (2.74) differ only in redefining $\lambda \to -\lambda$. Therefore, only the first solution of the ansatz is chosen. Consequently, the same steps as in Ch. 2.1 are performed to obtain a result. Thus, the equations are evaluated at $x \to \infty$

$$\begin{aligned}
\left(\varepsilon - \frac{c}{\hbar}\right) u(x) - \frac{\partial v(x)}{\partial x} = 0, \\
\left(\varepsilon + \frac{c}{\hbar}\right) v(x) + \frac{\partial u(x)}{\partial x} = 0.
\end{aligned} \tag{2.75}$$

By differentiating the first of the two equations the following results are obtained

$$\frac{\partial u(x)}{\partial x} = \frac{\partial^2 v(x)}{\partial x^2} \frac{1}{\varepsilon - c/\hbar}. \tag{2.76}$$

Subsequently, inserting it into the second equation leads to

$$\begin{aligned}
&\left(\varepsilon + \frac{c}{\hbar}\right) v(x) + \frac{\partial^2 v(x)}{\partial x^2} \frac{1}{\varepsilon - c/\hbar} = 0, \\
\Rightarrow \quad &\frac{\partial^2 v(x)}{\partial x^2} = \left(\frac{c^2}{\hbar^2} - \varepsilon^2\right) v(x).
\end{aligned} \tag{2.77}$$

The only physical reasonable solution is

$$v(x)|_{x\to\infty} = e^{-\sqrt{c^2/\hbar^2 - \varepsilon^2}\, x}, \tag{2.78}$$

as a positive exponential function would diverge. By ignoring normalization for now, $u(x)$ takes the same form due to Eq. (2.75)

$$u(x)|_{x\to\infty} = e^{-\sqrt{c^2/\hbar^2 - \varepsilon^2}\, x}. \tag{2.79}$$

Moreover, as an ansatz a power series is chosen to address the coupled differential equations Eq. (2.74) at any position x for both $u(x)$ and $v(x)$

$$\begin{aligned}
u(x) &= e^{-\sqrt{c^2/\hbar - \varepsilon^2}\, x} x^\nu \sum_{i=0}^{\infty} a_i x^i, \\
v(x) &= e^{-\sqrt{c^2/\hbar - \varepsilon^2}\, x} x^\nu \sum_{i=0}^{\infty} b_i x^i.
\end{aligned} \tag{2.80}$$

Inserting these back into Eq. (2.74) leads to

$$\begin{aligned}
&\sum_{i=0}^{\infty} x^\nu \left[\left(\varepsilon - \frac{c}{\hbar}\right) a_i x^i + Z\alpha a_i x^{i-1} + \sqrt{\frac{c^2}{\hbar^2} - \varepsilon^2}\, b_i x^i - \nu b_i x^{i-1} - b_i i x^{i-1} - (\lambda+1)\, b_i x^{i-1}\right] = 0, \\
&\sum_{i=0}^{\infty} x^\nu \left[\left(\varepsilon + \frac{c}{\hbar}\right) b_i x^i + Z\alpha b_i x^{i-1} - \sqrt{\frac{c^2}{\hbar^2} - \varepsilon^2}\, a_i x^i + \nu a_i x^{i-1} + a_i i x^{i-1} - (\lambda-1)\, a_i x^{i-1}\right] = 0.
\end{aligned} \tag{2.81}$$

Subsequently, the technique of equating coefficients is used for $i-1$ at the lowest order of the power series $i = 0$ to determine ν. Consequently, $\nu - 1$ is the first order of the polynomial. Therefore, Eq. (2.81) is reduced to

$$\begin{aligned} Z\alpha a_0 - (\nu + \lambda + 1)\, b_0 &= 0, \\ Z\alpha b_0 + (\nu - \lambda + 1)\, a_0 &= 0. \end{aligned} \tag{2.82}$$

One of these two coefficients a_0 and b_0 will be fixed due to normalization and the second is related to the first of the two equations from Eq. (2.82) by

$$b_0 = \frac{Z\alpha}{\nu + \lambda + 1} a_0. \tag{2.83}$$

The only possible solution for the coupled system from Eq. (2.82) is stated when the determinate of the following linear system

$$\begin{pmatrix} Z\alpha & -(\nu + \lambda + 1) \\ \nu - \lambda + 1 & Z\alpha \end{pmatrix} \begin{pmatrix} a_0 \\ b_0 \end{pmatrix} = \vec{0}, \tag{2.84}$$

vanishes as a complete power series is required. Consequently, this results in

$$\begin{aligned} & (Z\alpha)^2 + (\nu - \lambda + 1)(\nu + \lambda + 1) = (Z\alpha)^2 + \nu^2 + 2\nu - \lambda^2 + 1 = 0, \\ \Rightarrow \quad & \nu = \pm\sqrt{\lambda^2 - (Z\alpha)^2} - 1, \end{aligned} \tag{2.85}$$

for ν. The only physical solution is the one with the positive square root as the solution would diverge otherwise at $r \to 0$. Subsequently, using the method of equating coefficients on Eq.(2.81) leads to

$$\begin{aligned} \left(\varepsilon - \frac{c}{\hbar}\right) a_{i-1} + \sqrt{\frac{c^2}{\hbar^2} - \varepsilon^2}\, b_{i-1} + Z\alpha a_i - (\nu + i + \lambda + 1)\, b_i &= 0, \\ \left(\frac{c}{\hbar} + \varepsilon\right) b_{i-1} - \sqrt{\frac{c^2}{\hbar^2} - \varepsilon^2}\, a_{i-1} + Z\alpha b_i - (-\nu - i + \lambda - 1)\, a_i &= 0. \end{aligned} \tag{2.86}$$

Moreover, multiplying the first equation of Eq. (2.86) by $\sqrt{\frac{c}{\hbar} + \varepsilon}$, the second with $\sqrt{\frac{c}{\hbar} - \varepsilon}$ and then subtracting the first from the second results in

$$\begin{aligned} & \left(\frac{c}{\hbar} + \varepsilon\right)\sqrt{\frac{c}{\hbar} - \varepsilon}\, b_{i-1} + Z\alpha\sqrt{\frac{c}{\hbar} - \varepsilon}\, b_i - \sqrt{\frac{c^2}{\hbar^2} - \varepsilon^2}\sqrt{\frac{c}{\hbar} - \varepsilon}\, a_{i-1} \\ & - (-\nu - i + \lambda - 1)\sqrt{\frac{c}{\hbar} - \varepsilon}\, a_i + \left(\frac{c}{\hbar} - \varepsilon\right)\sqrt{\frac{c}{\hbar} + \varepsilon}\, a_{i-1} - Z\alpha\sqrt{\frac{c}{\hbar} + \varepsilon}\, a_i \\ & - \sqrt{\frac{c^2}{\hbar^2} - \varepsilon^2}\sqrt{\frac{c}{\hbar} + \varepsilon}\, b_{i-1} + (\nu + i + \lambda + 1)\sqrt{\frac{c}{\hbar} + \varepsilon}\, b_i = 0, \\ \Rightarrow \quad & a_i\left(Z\alpha\sqrt{\frac{c}{\hbar} + \varepsilon} + (-\nu - i + \lambda - 1)\sqrt{\frac{c}{\hbar} - \varepsilon}\right) = b_i\left((\nu + i + \lambda + 1)\sqrt{\frac{c}{\hbar} + \varepsilon} + Z\alpha\sqrt{\frac{c}{\hbar} - \varepsilon}\right), \\ \Rightarrow \quad & \frac{b_i}{a_i} = \frac{Z\alpha\sqrt{c/\hbar + \varepsilon} + (-\nu - i + \lambda - 1)\sqrt{c/\hbar - \varepsilon}}{(\nu + i + \lambda + 1)\sqrt{c/\hbar + \varepsilon} + Z\alpha\sqrt{c/\hbar - \varepsilon}}. \end{aligned} \tag{2.87}$$

It is necessary for the series to end at a certain point, due to the same argument as in Sec. 2.1. The breaking point is at

$$a_{\tilde{n}+1} = b_{\tilde{n}+1} = 0. \tag{2.88}$$

Consequently, Eq. (2.86) for $i = \tilde{n}+1$ turns to

$$\begin{aligned}
\left(\frac{c}{\hbar}-\varepsilon\right)a_{\tilde{n}} &= \sqrt{\frac{c^2}{\hbar^2}-\varepsilon^2}\,b_{\tilde{n}},\\
\left(\frac{c}{\hbar}+\varepsilon\right)b_{\tilde{n}} &= \sqrt{\frac{c^2}{\hbar^2}-\varepsilon^2}\,a_{\tilde{n}},\\
\Rightarrow\quad \frac{b_{\tilde{n}}}{a_{\tilde{n}}} &= \sqrt{\frac{c/\hbar-\varepsilon}{c/\hbar+\varepsilon}}.
\end{aligned} \tag{2.89}$$

Subsequently, Eq. (2.87) is solved for the eigenenergies ε

$$\begin{aligned}
\frac{\sqrt{c/\hbar-\varepsilon}}{\sqrt{c/\hbar+\varepsilon}} &= \frac{Z\alpha\sqrt{c/\hbar+\varepsilon}+\sqrt{c/\hbar-\varepsilon}\,(-\nu-\tilde{n}+\lambda-1)}{Z\alpha\sqrt{c/\hbar-\varepsilon}+\sqrt{c/\hbar+\varepsilon}\,(\nu+\tilde{n}+\lambda+1)},\\
\Rightarrow\quad Z\alpha\left(\frac{c}{\hbar}-\varepsilon\right)+\sqrt{\frac{c^2}{\hbar^2}-\varepsilon^2}\,(\nu+\tilde{n}+\lambda+1) &= Z\alpha\left(\frac{c}{\hbar}+\varepsilon\right)+\sqrt{\frac{c^2}{\hbar^2}-\varepsilon^2}\,(-\nu-\tilde{n}+\lambda-1),\\
\Rightarrow\quad Z\alpha\varepsilon &= \sqrt{\frac{c^2}{\hbar^2}-\varepsilon^2}\,(\nu+\tilde{n}+1),\\
\Rightarrow\quad Z^2\alpha^2\varepsilon^2 &= \left(\frac{c^2}{\hbar^2}-\varepsilon^2\right)(\nu+\tilde{n}+1)^2,\\
\Rightarrow\quad \varepsilon &= \pm\frac{c}{\hbar}\frac{1}{\sqrt{1+\frac{Z^2\alpha^2}{(\nu+\tilde{n}+1)^2}}}.
\end{aligned} \tag{2.90}$$

Using the definitions of Eq. (2.74) and the result for ν Eq. (2.85) with the solution of λ in Eq. (2.73) the energies are obtained

$$E = \frac{m_e c^2}{\sqrt{1+\frac{Z^2\alpha^2}{\left(\sqrt{(j+1/2)^2-Z^2\alpha^2}+\tilde{n}\right)^2}}}, \tag{2.91}$$

where the positive energy solution for a matter particle is used. By performing a Taylor expansion for $(Z\alpha)^2$ at zero the non-relativistic results are reproduced

$$\begin{aligned}
&\text{Zeroth order:}\quad m_e c^2,\\
&\text{First order:}\quad -\frac{\left[\tilde{n}\,(j+1/2)+(j+1/2)^2\right]Z^2\alpha^2 m_e c^2}{2\,(\underbrace{j+1/2+\tilde{n}}_{=n})^3\,(j+1/2)} = -\frac{Z^2\alpha^2 m_e c^2}{2n^2},\\
&\text{Second order:}\quad \frac{1}{2}\left[-\frac{3\left(\tilde{n}\,(j+1/2)+(j+1/2)^2\right)}{4\,(j+1/2+\tilde{n})^4\,(j+1/2)^2}+\frac{\tilde{n}}{4\,(j+1/2+\tilde{n})^3\,(j+1/2)^2}\right.\\
&\qquad\left.-\frac{\tilde{n}\,(j+1/2)+(j+1/2)^2}{4\,(j+1/2+\tilde{n})^3\,(j+1/2)^3}+\frac{3\left(\tilde{n}\,(j+1/2)+(j+1/2)^2\right)}{4\,(j+1/2+\tilde{n})^5\,(j+1/2)}\right]Z^4\alpha^4 m_e c^2\\
&\qquad = \frac{1}{2}\left[\frac{-4n+3\,(j+1/2)}{4n^4\,(j+1/2)}\right]Z^4\alpha^4 m_e c^2,\\
&\Rightarrow\quad E = \underbrace{m_e c^2}_{\text{Rest mass}}+\underbrace{E_n}_{\text{Bohr}}+\underbrace{\frac{E_n Z^2\alpha^2}{n}\left(\frac{1}{j+1/2}-\frac{3}{4n}\right)}_{\text{Fine splitting}}.
\end{aligned} \tag{2.92}$$

In particular, for $g_s = 2$, the fine splitting is recovered as introduced in Sec. 2.2.1.

2.4 Atomic interaction with external fields

In the presence of external electromagnetic fields further corrections to the eigenfunctions and eigenenergies are necessary.

2.4.1 Stark effect

As previously seen, the electric potential of the nucleus interacts with the electron which results into dedicated orbitals. External electric fields cause perturbations to those trajectories. The first order in its interaction is introduced by the electric dipole interaction also known as the Stark effect [112]. More detailed information on this topic are stated in [104, 46]. The corresponding Hamiltonian is

$$H_{Stark} = e\vec{r} \cdot \vec{E}, \tag{2.93}$$

with $\vec{E}$ being the external electric field vector. The potential is treated again with the help of perturbation theory. Therefore, the first two orders in energy corrections are expressed by

$$\begin{aligned} &\text{First order:} && E_1 = \langle \Psi_{n,l,m} | H_{Stark} | \Psi_{n,l,m} \rangle , \\ &\text{Second order:} && E_2 = \sum_{\tilde{n} \neq n, \tilde{l}, \tilde{m}} \frac{| \langle \Psi_{\tilde{n},\tilde{l},\tilde{m}} | H_{Stark} | \Psi_{n,l,m} \rangle |^2}{E_n - E_{\tilde{n}}}, \end{aligned} \tag{2.94}$$

for a non-degenerate system. In Sec. 2.1 the hydrogen system and its unperturbed Hamiltonian is introduced as a degenerate system, as the eigenenergies only depend on the main quantum number n, but not on l and m. Correspondingly, the ground state is the only one which can be treated as non-degenerate. Moreover, the first energy correction vanishes for the ground state. For convenience and without loss of generality the quantization axis is chosen along the electric field $\vec{E} = \varepsilon_z \hat{e}_z$. Consequently, the first order energy corrections is stated as

$$\begin{aligned} \langle \Psi_{1,0,0} | H_{Stark} | \Psi_{1,0,0} \rangle &= \int_0^\infty dr \int_0^{2\pi} d\varphi \int_0^\pi d\theta \, r^2 \sin(\theta) \, er\varepsilon_z \cos(\theta) \, |\Psi_{1,0,0}|^2 = 0 \\ \text{because} \quad & \int_0^\pi d\theta \, \sin(\theta) \cos(\theta) = 0. \end{aligned} \tag{2.95}$$

Moreover, all diagonal matrix elements vanish, which can be proven with the help of the parity operator

$$\begin{aligned} \langle \Psi_{n,l,m} | e\vec{E} \cdot \vec{r} | \Psi_{n,l,m} \rangle &= (-1)^{2l} \langle \Psi_{n,l,m} | e\vec{E} \cdot \vec{r} | \Psi_{n,l,m} \rangle \\ &= \langle \Psi_{n,l,m} | \Pi e\vec{E} \cdot \vec{r} \Pi | \Psi_{n,l,m} \rangle = - \langle \Psi_{n,l,m} | e\vec{E} \cdot \vec{r} | \Psi_{n,l,m} \rangle = 0. \end{aligned} \tag{2.96}$$

Therefore, the set of states with $n = 2$ are the first to have a linear dependency in the electric field for their energy corrections. Due to their degeneracy the degenerate subspace needs to be diagonalized to find the perturbed eigenenergies and eigenstates. In the case of an electric field pointing into z-direction the only non-vanishing matrix element is

$$\begin{aligned} \langle \Psi_{2,0,0} | H_{Stark} | \Psi_{2,1,0} \rangle &= \int_0^\infty dr \int_0^{2\pi} d\varphi \int_0^\pi d\theta \, r^4 \sin(\theta) \, \frac{e\varepsilon_z Z^4}{32 a_0^4 \pi} \left(-\frac{Zr}{a_0} + 2 \right) e^{-Zr/a_0} \cos^2(\theta) \\ &= \frac{e\varepsilon_z Z^4}{24 a_0^4} \int_0^\infty dr \, r^4 \left(-\frac{Zr}{a_0} + 2 \right) e^{-Zr/a_0} \\ &= -\frac{3 e \varepsilon_z a_0}{Z} \\ &\coloneqq \delta_z. \end{aligned} \tag{2.97}$$

It is important to note that the energy correction is linear in the external electric field flux. Moreover, the Hamiltonian of the subspace is represented in the $|n,l,m_l\rangle$ basis by

$$H_{Stark} \coloneqq \begin{array}{c} \\ \langle 2,0,0| \\ \langle 2,1,0| \\ \langle 2,1,1| \\ \langle 2,1,-1| \end{array} \begin{array}{c} \begin{array}{cccc} |2,0,0\rangle & |2,1,0\rangle & |2,1,1\rangle & |2,1,-1\rangle \end{array} \\ \begin{pmatrix} 0 & \delta_z & 0 & 0 \\ \delta_z & 0 & 0 & 0 \\ 0 & 0 & 0 & 0 \\ 0 & 0 & 0 & 0 \end{pmatrix} \end{array}. \tag{2.98}$$

The corresponding eigenstates to the eigenenergies $E_{1,2} = \pm\delta_z$ are then expressed by

$$\begin{aligned} |v_1\rangle &= \frac{1}{\sqrt{2}}\left(|2,0,0\rangle + |2,1,0\rangle\right), \\ |v_2\rangle &= \frac{1}{\sqrt{2}}\left(|2,0,0\rangle - |2,1,0\rangle\right). \end{aligned} \tag{2.99}$$

Similarly an external electric field pointing in x-direction $\vec{E} = \varepsilon_x \hat{e}_x$ can be assumed. In this case the only non-vanishing matrix elements are

$$\begin{aligned} &\langle \Psi_{2,0,0}|H_{Stark}|\Psi_{2,1,\pm1}\rangle = \int_0^\infty dr \int_0^{2\pi} d\varphi \int_0^\pi d\theta\, r^3 \sin(\theta)\, e\varepsilon_x \Psi^*_{2,0,0}\Psi_{2,1,\pm1} \\ &= \mp \int_0^\infty dr \int_0^{2\pi} d\varphi \int_0^\pi d\theta\, r^4 \sin^3(\theta)\cos(\varphi)\, \frac{\sqrt{2}e\varepsilon_x Z^4}{64\pi a_0^4}\left(-\frac{Zr}{a_0}+2\right)e^{-Zr/a_0}e^{\pm i\varphi} \\ &= \mp \frac{\sqrt{2}e\varepsilon_x Z^4}{48 a_0^4}\int_0^\infty dr\, r^4\left(-\frac{Zr}{a_0}+2\right)e^{-Zr/a_0} \\ &= \pm \frac{3e\varepsilon_x a_0}{\sqrt{2}Z} \\ &\coloneqq \delta. \end{aligned} \tag{2.100}$$

Consequently, the Stark Hamiltonian can be expressed as

$$H_{Stark} \coloneqq \begin{array}{c} \\ \langle 2,0,0| \\ \langle 2,1,0| \\ \langle 2,1,1| \\ \langle 2,1,-1| \end{array} \begin{array}{c} \begin{array}{cccc} |2,0,0\rangle & |2,1,0\rangle & |2,1,1\rangle & |2,1,-1\rangle \end{array} \\ \begin{pmatrix} 0 & 0 & \delta & -\delta \\ 0 & 0 & 0 & 0 \\ \delta & 0 & 0 & 0 \\ -\delta & 0 & 0 & 0 \end{pmatrix} \end{array}. \tag{2.101}$$

As expected the same energy splitting $E_{1,2} = \pm\sqrt{2}\delta$ is obtained but now with a different set of eigenstates

$$\begin{aligned} |v_1\rangle &= \frac{1}{\sqrt{2}}\left(|2,1,1\rangle + |2,1,-1\rangle\right), \\ |v_2\rangle &= \frac{1}{\sqrt{2}}\left[|2,0,0\rangle + \frac{1}{\sqrt{2}}\left(|2,1,1\rangle - |2,1,-1\rangle\right)\right], \\ |v_2\rangle &= \frac{1}{\sqrt{2}}\left[|2,0,0\rangle + \frac{1}{\sqrt{2}}\left(|2,1,-1\rangle - |2,1,1\rangle\right)\right]. \end{aligned} \tag{2.102}$$

Subsequently, the second order correction is discussed. A general derivation in parabolic coordinates was derived by Epstein [113] and Bethe [46]. Assuming the external electric field is pointing

in z-direction then the matrix element is derived by

$$\begin{aligned}
&\langle \tilde{n}, \tilde{l}, \tilde{m}|z|n, l, m\rangle = \int_0^\infty dr \int_0^{2\pi} d\varphi \int_0^\pi d\theta\, r^3 \sin(\theta)\cos(\theta)\, R_{\tilde{n},\tilde{l}} R_{n,l} Y^*_{\tilde{l},\tilde{m}} Y_{l,m} \\
&= \frac{1}{2\pi}\int_0^\infty dr \int_0^{2\pi} d\varphi \int_0^\pi d\theta\, r^3 \sin(\theta)\cos(\theta)\, R_{\tilde{n},\tilde{l}} R_{n,l} (-1)^{m-\tilde{m}} \mathcal{P}_{\tilde{l},\tilde{m}} \mathcal{P}_{l,m} e^{i(m-\tilde{m})\varphi} \\
&= \int_0^\infty dr \int_0^{2\pi} d\varphi \int_0^\pi d\theta \frac{r^3}{2\pi} \sin(\theta)\, R_{\tilde{n},\tilde{l}} R_{n,l} (-1)^{m-\tilde{m}} \mathcal{P}_{\tilde{l},\tilde{m}} e^{i(m-\tilde{m})\varphi} \\
&\left[\sqrt{\frac{(l+m+1)(l-m+1)}{(2l+1)(2l+3)}}\mathcal{P}_{l+1,m} + \sqrt{\frac{(l+m)(l-m)}{(2l+1)(2l-1)}}\mathcal{P}_{l-1,m}\right],
\end{aligned} \tag{2.103}$$

where $\mathcal{P}_{l,m}$ is again the normalized Legendre polynomial and the following relation is used from [46]

$$\cos(\theta)\,\mathcal{P}_{l,m} = \sqrt{\frac{(l+m+1)(l-m+1)}{(2l+1)(2l+3)}}\mathcal{P}_{l+1,m} + \sqrt{\frac{(l+m)(l-m)}{(2l+1)(2l-1)}}\mathcal{P}_{l-1,m}. \tag{2.104}$$

Thereby, selection rules for l and m can be extracted from the matrix element as the Legendre polynomial satisfy a normalization relation, which is stated in Eq. (7.28). Consequently, the matrix element vanishes for all situations except $\tilde{l} = l \pm 1$ and $\tilde{m} = m$. Moreover, the energy correction simplifies to

$$E_2 = \sum_{\tilde{n}\neq n}\sum_{\tilde{l}=l\pm1} \frac{|\langle \Psi_{\tilde{n},\tilde{l},m}|H_{Stark}|\Psi_{n,l,m}\rangle|^2}{E_n - E_{\tilde{n}}}. \tag{2.105}$$

The energy correction goes with the square of the electric field flux due to the fact that the matrix element is squared. Consequently, the higher order correction becomes more important for large external electric fields. In case of $n = 2$ the quadratic term reaches large energy corrections for values $\varepsilon_z/Z^2 > 1\,\mathrm{GV/m}$. In addition, Epstein and Bethe provide a system of coupled differential equations, originating from the entire non-relativistic hydrogen-like atom in the presence of an static external electric field, addressed in parabolic coordinates, which results in simpler treatments for higher order corrections [113, 46].

2.4.2 Landé g-factor

Before addressing the interaction of external magnetic fields it is important to introduce the Landé g-factor, g_j. The derivation is based on [104, 109]. It is convenient to comprise the magnetic moments of the spin $\vec{\mu}_s$ and the magnetic moment of the orbital angular momentum $\vec{\mu}_l$ into one for the total angular momentum of the electron $\vec{\mu}_j$. The individual magnetic moments are defined as follows

$$\begin{aligned}
\vec{\mu}_s &= g_s \mu_B \frac{\vec{S}}{\hbar}, \\
\vec{\mu}_l &= g_l \mu_B \frac{\vec{L}}{\hbar},
\end{aligned} \tag{2.106}$$

where $\mu_B = e\hbar/2m_e$ represents the Bohr magneton. To determine the Landé g-factor the next relation has to be fullfilled

$$\begin{aligned}
g_s\mu_B\frac{\vec{S}}{\hbar} + g_l\mu_B\frac{\vec{L}}{\hbar} &\stackrel{!}{=} g_j\mu_B\frac{\vec{J}}{\hbar}, \\
\Rightarrow g_s\vec{S} + g_l\vec{L} &\stackrel{!}{=} g_j\vec{J}.
\end{aligned} \tag{2.107}$$

For the next step it is necessary to multiply from the left side with $\vec{J}$

$$g_s\vec{J}\cdot\vec{S} + g_l\vec{J}\cdot\vec{L} = g_j|\vec{J}|^2. \tag{2.108}$$

In Eq. (2.108) it is clear that $\vec{J}\cdot\vec{L}$, $\vec{J}\cdot\vec{S}$ and $|\vec{J}|^2$ share the same eigenbasis. In the next step the expression $\vec{J}\cdot\vec{L}$ is replaced by

$$\begin{aligned} |\vec{S}|^2 &= \left(\vec{J}-\vec{L}\right)^2 = |\vec{J}|^2 + |\vec{L}|^2 \underbrace{-2\vec{J}\cdot\vec{L}}_{\text{as } [J_i,L_i]=0}, \\ \Rightarrow \vec{J}\cdot\vec{L} &= \frac{1}{2}\left(|\vec{J}|^2 + |\vec{L}|^2 - |\vec{S}|^2\right). \end{aligned} \tag{2.109}$$

Analogously for $\vec{J}\cdot\vec{S}$

$$\vec{J}\cdot\vec{S} = \frac{1}{2}\left(|\vec{J}|^2 + |\vec{S}|^2 - |\vec{L}|^2\right). \tag{2.110}$$

Subsequently, with the replacements Eq. 2.108 takes the following form

$$g_s\frac{1}{2}\left(|\vec{J}|^2 + |\vec{S}|^2 - |\vec{L}|^2\right) + g_l\frac{1}{2}\left(|\vec{J}|^2 + |\vec{L}|^2 - |\vec{S}|^2\right) = g_j|\vec{J}|^2. \tag{2.111}$$

Consequently, g_j is determined by calculating the expectation value of Eq. 2.111

$$g_j = \frac{1}{2}\frac{g_s\left[j\left(j+1\right)+s\left(s+1\right)-l\left(l+1\right)\right]+g_l\left[j\left(j+1\right)-s\left(s+1\right)+l\left(l+1\right)\right]}{j\left(j+1\right)}. \tag{2.112}$$

The g-factors have been determined experimentally with high precision, yielding $g_s \approx 2.002$ [114] and $g_l = 1$ [115]. While the Dirac theory sets $g_s = 2$, the observed discrepancy has been resolved due QED calculations [116, 117].

2.4.3 Breit-Rabi diagram

In this section previous results from Ch. 2.2.3, treating the hyperfine splitting, are combined with interactions of external magnetic fields $\vec{B}$ with the atom [104]. The corresponding Hamiltonian is expressed as

$$H_{BR} = A\frac{\vec{I}\cdot\vec{J}}{\hbar^2} + \left(g_j\mu_B\frac{\vec{J}}{\hbar} - g_I\mu_k\frac{\vec{I}}{\hbar}\right)\cdot\vec{B}. \tag{2.113}$$

$\mu_B = {e\hbar}/{2m_e}$ is the Bohr magneton while $\mu_k = {e\hbar}/{2m_p}$ stands for the nuclear magneton. Subsequently, g_j is the Landé g-factor, defined in Sec. 2.4.2, and g_I the nuclear g-factor. Restricting the influence of the magnetic field to the interaction caused by this Hamiltonian result in splittings inside a set of states without changing angular quantum number l or the main quantum number n. By assuming a homogenous constant magnetic field in z-direction, $\vec{B} = B_z\hat{e}_z$, the so-called Breit-Rabi diagram is found, which depends on the set of states and the corresponding atom. It displays the evolution of the eigenenergies as function of the external magnetic field flux.
As an example the Hamiltonian is applied for the hydrogen ground state. Therefore, the nucleus is spin ${1}/{2}$ and the total angular momentum of the electron is reduced to the spin of the electron $\vec{S}$, which is also a spin 1/2 particle. In addition, the hyperfine splitting constant A for the hydrogen ground state has been measured to ${A}/{h} \approx 1.42$ GHz [118]. Moreover, the Landé g-factor reduces to the spin g-factor $g_s \approx 2.002$ [114] while the nuclear g-factor for the proton is $g_I \approx 5.586$ [119].
There are two advantageous representations to calculate the matrix elements. The first is the coupled representation $|n,l,m_l,s,m_s,F,m_F\rangle \coloneqq |F,m_F\rangle$ and the second is the uncoupled one $|n,j,m_j,I,m_I\rangle \coloneqq |m_j,m_I\rangle$. By using the coupled basis the Hamiltonian can be expressed as

$$H_{BR} \coloneqq \begin{array}{c} \\ \langle 1,1| \\ \langle 1,0| \\ \langle 1,-1| \\ \langle 0,0| \end{array} \begin{array}{c} \begin{array}{cccc} |1,1\rangle & |1,0\rangle & |1,-1\rangle & |0,0\rangle \end{array} \\ \begin{pmatrix} \frac{A}{4}+\frac{1}{2}(g_s\mu_B-g_I\mu_k)B_z & 0 & 0 & 0 \\ 0 & \frac{A}{4} & 0 & \frac{1}{2}(g_s\mu_B+g_I\mu_k)B_z \\ 0 & 0 & \frac{A}{4}-\frac{1}{2}(g_s\mu_B-g_I\mu_k)B_z & 0 \\ 0 & \frac{1}{2}(g_s\mu_B+g_I\mu_k)B_z & 0 & -\frac{3A}{4} \end{pmatrix} \end{array}. \tag{2.114}$$

Consequently, the eigenenergies and eigenstates evolve to

$$\begin{aligned}
E_{a_1} &= \frac{A}{4} + \frac{1}{2}\left(g_s\mu_B - g_I\mu_k\right)B_z, \\
|a_1\rangle &= |1,1\rangle, \\
E_{a_2} &= -\frac{A}{4} + \frac{1}{2}\sqrt{A^2 + \left(g_s\mu_B + g_I\mu_k\right)^2 B_z^2}, \\
|a_2\rangle &= \frac{1}{\sqrt{1 + \left(\frac{(g_s\mu_B + g_I\mu_k)B_z}{A + \sqrt{A^2 + (g_s\mu_B + g_I\mu_k)^2 B_z^2}}\right)^2}} \left(\frac{\left(g_s\mu_B + g_I\mu_k\right)B_z}{A + \sqrt{A^2 + \left(g_s\mu_B + g_I\mu_k\right)^2 B_z^2}}|0,0\rangle + |1,0\rangle\right), \\
E_{b_3} &= \frac{A}{4} - \frac{1}{2}\left(g_s\mu_B - g_I\mu_k\right)B_z, \\
|b_3\rangle &= |1,-1\rangle, \\
E_{b_4} &= -\frac{A}{4} - \frac{1}{2}\sqrt{A^2 + \left(g_s\mu_B + g_I\mu_k\right)^2 B_z^2}, \\
|b_4\rangle &= \frac{1}{\sqrt{1 + \left(\frac{A - \sqrt{A^2 + (g_s\mu_B + g_I\mu_k)^2 B_z^2}}{(g_s\mu_B + g_I\mu_k)B_z}\right)^2}} \left(|0,0\rangle + \frac{A - \sqrt{A^2 + \left(g_s\mu_B + g_I\mu_k\right)^2 B_z^2}}{\left(g_s\mu_B + g_I\mu_k\right)B_z}|1,0\rangle\right).
\end{aligned} \tag{2.115}$$

Next, the extreme cases of the external magnetic fields are addressed. Starting with $B_z \to 0$ the eigenstates are stated as

$$\begin{aligned}
|a_1\rangle &= |F = 1, m_F = 1\rangle, \\
|a_2\rangle &= |F = 1, m_F = 0\rangle, \\
|b_3\rangle &= |F = 1, m_F = -1\rangle, \\
|b_4\rangle &= |F = 0, m_F = 0\rangle,
\end{aligned} \tag{2.116}$$

while for the limit $B_z \gg |B_c|$

$$\begin{aligned}
|a_1\rangle &= |m_S = \pm 1/2, m_I = \pm 1/2\rangle, \\
|a_2\rangle &= |m_S = \pm 1/2, m_I = \mp 1/2\rangle, \\
|b_3\rangle &= |m_S = \mp 1/2, m_I = \mp 1/2\rangle, \\
|b_4\rangle &= \mp\,|m_S = \mp 1/2, m_I = \pm 1/2\rangle.
\end{aligned} \tag{2.117}$$

The upper sign is for positive magnetic field fluxes, while the lower sign is valid for negative ones. Per definition this lower bound is the so-called critical field value $B_c = \frac{A}{g_j\mu_B - g_I\mu_k}$ [120]. This means that every magnetic field above this limit is well represented by the uncoupled representation, while fields below this value follow the coupled basis. This is well understandable as the external magnetic field couples to the intrinsic magnetic moments individually and once its interaction is stronger than the electron-nucleon coupling, the electron and nuclear spins decouple from each other. Therefore, depending on the outer condition of the magnetic field one of these two representations is a better approximation than the other. For the sake of completeness as the problem is treated by perturbation theory the magnetic field is still restricted to a small finite number in comparison to the magnetic field produced by the atomic dynamics but is still large enough that the electron and nuclear spins decouple. In case of the hydrogen ground state this value is reached at $B_c \approx 50$ mT.

2.4.4 Lifetime

Up to this point, this chapter has addressed different physical phenomena, which adjusted the original eigensytem of the atom. In this section the focus lies in the lifetime of excited electronic states within an atomic or ionic system and how to model it. Thereby, the derivation and the motivation follow [36]. Here the corresponding potential for a decay is expressed as

$$V_{\text{life}} = -i\frac{\hbar}{2\tau}, \tag{2.118}$$

with τ being the lifetime of an excited state. To show that this potential is appropriate it is inserted into the Schrödinger equation and it is sought for an exponential radiative decay

$$\begin{aligned} & i\hbar\frac{\partial}{\partial t}\left|\psi_n(t)\right\rangle = \left(H(t) + V_{life}\right)\left|\psi_n(t)\right\rangle, \\ \Rightarrow \quad & \left|\psi_n(t)\right\rangle = e^{-i/\hbar\left(\int_0^t H(t')dt' + V_{life}t\right)}\left|\psi_n(t=0)\right\rangle, \\ \Rightarrow \quad & \left\langle\psi_n(t)\middle|\psi_n(t)\right\rangle = e^{-t/\tau}. \end{aligned} \tag{2.119}$$

In addition, the lifetime of excited states can be manipulated by external fields. This is investigated in Ch. 3 and used later for selective quenching processes in Ch. 4.

2.5 Density operator

The general ideas of this section are based on [36]. At any given time, each natural system should be describable by only one state $|\psi\rangle$, which contains all the information about each particle's position and momentum. States which fulfill this condition are called pure states and contain all the necessary information about the system. Unfortunately, natural systems often are too complex or unknown so that a variety of different states $|\psi_i\rangle$ might describe this system. As some might be more probable than others, each of them is weighted by its probability p_i to describe the entire system correctly. A state of this set is called a non-pure state. The operator projecting this behaviour is called density operator ρ and can be written as

$$\rho = \sum_i p_i \left|\psi_i\right\rangle\left\langle\psi_i\right|. \tag{2.120}$$

The probabilities are $p_i \in \mathbb{R}_+$ and fulfill $\sum_i p_i = 1$. Consequently, the density operator has three important characteristics

$$\begin{aligned} & \rho = \rho^\dagger && \text{(hermitian)}, \\ & \langle\phi|\rho|\phi\rangle \geq 0, \ \forall\,|\phi\rangle && \text{(semidefinite)}, \\ & \mathrm{Tr}\,(\rho) = 1. \end{aligned} \tag{2.121}$$

The first and second property is proven in one step

$$\langle\phi|\rho^\dagger|\phi\rangle = \sum_i p_i^* \langle\phi|\psi_i\rangle^* \langle\psi_i|\phi\rangle^* = \sum_i p_i \langle\psi_i|\phi\rangle\langle\phi|\psi_i\rangle = \langle\phi|\rho|\phi\rangle = \sum_i p_i |\langle\psi_i|\phi\rangle|^2 \geq 0. \tag{2.122}$$

The third statement can be proven with the help of the trace of an arbitrary operator B with an arbitrary orthonormal basis $|a\rangle$, which can be expressed as

$$\mathrm{Tr}\,(B) = \sum_a \langle a|B|a\rangle. \tag{2.123}$$

For the density operator this results in

$$\begin{aligned} \mathrm{Tr}\,(\rho) &= \sum_a \langle a|\rho|a\rangle = \sum_a \sum_i p_i \langle a|\psi_i\rangle\langle\psi_i|a\rangle \\ &= \sum_i p_i \langle\psi_i| \underbrace{\left(\sum_a |a\rangle\langle a|\right)}_{=\mathbb{1}} |\psi_i\rangle = \sum_i p_i \langle\psi_i|\psi_i\rangle = \sum_i p_i = 1. \end{aligned} \tag{2.124}$$

Another property to distinguish pure from non-pure states is stated as

$$\begin{aligned} &\mathrm{Tr}\left(\rho^2\right) = 1 \qquad \text{(pure state)},\\ &\mathrm{Tr}\left(\rho^2\right) < 1 \qquad \text{(non-pure state)}. \end{aligned} \tag{2.125}$$

The proof follows as

$$\begin{aligned} \text{For a pure state:} \qquad & \mathrm{Tr}\left(\rho^2\right) = \sum_a \langle a| \left(|\psi\rangle \langle\psi|\psi\rangle \langle\psi|\right) |a\rangle = \langle\psi| \left(\sum_a |a\rangle \langle a|\right) |\psi\rangle = 1,\\ \text{For a non-pure state:} \qquad & \mathrm{Tr}\left(\rho^2\right) = \sum_a \langle a| \left(\sum_{i,j} p_i p_j |\psi_i\rangle \underbrace{\langle\psi_i|\psi_j\rangle}_{=\delta_{i,j}} \langle\psi_j|\right) |a\rangle\\ & \qquad = \sum_i p_i^2 \langle\psi_i| \left(\sum_a |a\rangle \langle a|\right) |\psi_i\rangle = \sum_i p_i^2 < 1. \end{aligned} \tag{2.126}$$

In addition, the expectation value of an arbitrary operator B can be calculated via

$$\langle B\rangle = \mathrm{Tr}(\rho B) = \sum_a \sum_i p_i \langle a|\psi_i\rangle \langle\psi_i|B|a\rangle = \sum_i p_i \langle\psi_i| B \left(\sum_a |a\rangle \langle a|\right) |\psi_i\rangle = \sum_i p_i \langle\psi_i|B|\psi_i\rangle . \tag{2.127}$$

Important examples are the definition of the vector polarization [121]

$$\begin{aligned} p_z &= \frac{1}{s\hbar} \langle S_z\rangle = \frac{1}{s\hbar} \mathrm{Tr}\left(\rho S_z\right) = \frac{1}{s\hbar} \sum_{m_s'=-s}^{s} \langle m_s'| \left(\sum_{m_s=-s}^{s} p_{m_s} |m_s\rangle \langle m_s| S_z\right) |m_s'\rangle\\ &= \frac{1}{s\hbar} \sum_{m_s',m_s=-s}^{s} p_{m_s} \delta_{m_s',m_s} \langle m_s|S_z|m_s'\rangle = \sum_{m_s=-s}^{s} \frac{p_{m_s} m_s}{s}, \end{aligned} \tag{2.128}$$

and the tensor polarization for spin 1 particles [121]

$$p_{zz} = \frac{1}{\hbar} \langle S_{zz}\rangle = \frac{1}{\hbar} \mathrm{Tr}\left(\rho S_{zz}\right) = \frac{1}{\hbar^2} \mathrm{Tr}\left(\rho \left[3S_z S_z - 2\hbar \mathbb{1}\right]\right) = p_1 + p_{-1} - 2p_0. \tag{2.129}$$

The relations satisfied by the density operator highlight its descriptive power once it is determined. Thus, a maximum statistical knowledge of a given system is established. To get access to the system at any given time it is important to investigate its time evolution. In quantum mechanics (QM) the time evolution of any state is given by the Schrödinger equation

$$\begin{aligned} i\hbar \frac{\partial}{\partial t} |\psi\rangle &= H |\psi\rangle ,\\ -i\hbar \frac{\partial}{\partial t} \langle\psi| &= \langle\psi| H. \end{aligned} \tag{2.130}$$

Subsequently, the time evolution for the density operator is expressed by the von Neumann equation

$$\begin{aligned} \frac{\partial}{\partial t}\rho &= \sum_i p_i \left[\left(\frac{\partial}{\partial t} |\psi_i\rangle\right) \langle\psi_i| + |\psi_i\rangle \left(\frac{\partial}{\partial t} \langle\psi_i|\right)\right]\\ &= -\frac{i}{\hbar} \sum_i p_i \left[H |\psi_i\rangle \langle\psi_i| - |\psi_i\rangle \langle\psi_i| H\right]\\ &= -\frac{i}{\hbar} \left[H, \rho\right], \end{aligned} \tag{2.131}$$

where the last line contains the commutator $[A, B] = AB - BA$. So far the density matrix formalism has been studied on an unique isolated system. Next, the formalism is extended towards two

subsystems A and B. With the assumption, to have a pure state $|\psi\rangle$ of the entire system $A \cup B$, it is possible to write this state as a linear combination of two sets of orthonormal bases, one from each Hilbert space $\mathscr{H}_A$ and $\mathscr{H}_B$

$$|\psi\rangle = \sum_{i,j} c_{i,j} \underbrace{|a_i\rangle \otimes |b_j\rangle}_{:=|a_i,b_j\rangle}. \tag{2.132}$$

Moreover, the evaluation of an operator $C = C_A \otimes \mathbb{1}_B$ acting only on the subsystem A motivates the definition for the reduced density matrix ρ_A

$$\begin{aligned}
\mathrm{Tr}\left(\rho C\right) &= \sum_{i,j} \langle a_i, b_j| \left(\rho C\right) |a_i, b_j\rangle \\
&= \sum_{i,j} \sum_{i',j'} \sum_{i'',j''} c_{i',j'} c^*_{i'',j''} \langle a_i, b_j|a_{i'}, b_{j'}\rangle \underbrace{\langle a_{i''}, b_{j''}|C|a_i, b_j\rangle}_{=\langle a_{i''}|C_A|a_i\rangle \delta_{b_{j''},b_j}} \\
&= \sum_{i,j} \sum_{i',i''} \langle a_i|c_{i',j} c^*_{i'',j}|a_{i'}\rangle \langle a_{i''}|C_A|a_i\rangle \\
&= \sum_{i} \langle a_i| \Bigg(\underbrace{\sum_{i',i'',j} c_{i',j} c^*_{i'',j} |a_{i'}\rangle \langle a_{i''}|}_{=\rho_A} \Bigg) C_A |a_i\rangle .
\end{aligned} \tag{2.133}$$

Due to its form it is accessible by

$$\rho_A = \mathrm{Tr}_B\left(\rho\right), \tag{2.134}$$

with $\mathrm{Tr}_B\left(C\right) = \sum_j \langle b_j|C|b_j\rangle$ being only the trace over the basis for system B.

2.5.1 The Lindblad master equation

In this section the time evolution of the reduced density operator, governed by the Lindblad master equation [122], is addressed. A motivation for its derivation is performed by following the steps of article [123]. The starting assumptions are that first the density operator $\rho_A\left(t'\right)$ depends only linear on $\rho_A\left(t\right)$ for $t' > t$ and secondly it varies only based on one specific time rather than a time period. Due to these assumptions it is possible to write

$$\rho_{A_{i,j}}\left(t'\right) = \sum_{l,m=1}^{N} X_{i,l,j,m} \rho_{A_{l,m}}, \tag{2.135}$$

for a N dimensional Hilbertspace. In this case $X_{i,l,j,m}$ are arbitrary N^4 dimensional complex operators, which might depend on the time. Due to the fact that the density operator is hermitian it is clear that

$$\begin{aligned}
\rho^*_{A_{j,i}}\left(t'\right) = \sum_{l,m=1}^{N} X^*_{j,m,i,l} \rho_{A_{l,m}}\left(t\right) = \sum_{l,m=1}^{N} X_{i,l,j,m} \rho_{A_{l,m}}\left(t\right) = \rho_{A_{i,j}}\left(t'\right), \\
\Rightarrow \quad \sum_{j,m=1}^{N} \left(X^*_{j,m,i,l} - X_{i,l,j,m}\right) \rho_{A_{l,m}}\left(t\right) = 0.
\end{aligned} \tag{2.136}$$

Consequently, due to the last line X is also hermitian and therefore diagonalizable. Thus, it has an eigenequation with corresponding eigenvalues λ and eigenvectors v and can be expressed by them as

$$X_{i,l,j,m} = \sum_{\alpha=1}^{N^2} \lambda^\alpha v^\alpha_{i,l} v^{*\alpha}_{j,m}. \tag{2.137}$$

Moreover, the reduced density operator is expressed as

$$\rho_A\left(t'\right) = \sum_{\alpha=1}^{N^2} \lambda^\alpha v^\alpha \rho_A\left(t\right) v^{\dagger\alpha}. \tag{2.138}$$

By using the trace property of the density operator it is found that

$$\begin{aligned} \mathrm{Tr}_A\left(\rho_A\left(t'\right)\right) = 1 = \mathrm{Tr}_A\left(\sum_{\alpha=1}^{N^2} \lambda^\alpha v^\alpha \rho_A\left(t\right) v^{\dagger\alpha}\right) = \mathrm{Tr}_A\Bigg(\underbrace{\sum_{\alpha=1}^{N^2} \lambda^\alpha v^{\dagger\alpha} v^\alpha}_{\stackrel{!}{=}\mathbb{1}} \rho_A\left(t\right)\Bigg), \\ \Rightarrow \quad \sum_{\alpha=1}^{N^2} \lambda^\alpha v^{\dagger\alpha} v^\alpha = \mathbb{1}. \end{aligned} \tag{2.139}$$

Using the fact that the eigenvectors span an orthonormal basis

$$\sum_{i,l}^{N} v_{i,l}^\alpha v_{i,l}^{*\beta} = \mathrm{Tr}_A\left(v^\alpha v^{\dagger\beta}\right) = \delta_{\alpha,\beta}, \tag{2.140}$$

a restriction for the eigenvalues is obtained

$$\mathrm{Tr}_A\left(\sum_{\alpha=1}^{N^2} \lambda^\alpha v^{\dagger\alpha} v^\alpha\right) = \sum_{\alpha=1}^{N^2} \lambda^\alpha \mathrm{Tr}_A\left(v^{\dagger\alpha} v^\alpha\right) = \sum_{\alpha=1}^{N^2} \lambda^\alpha = N = \mathrm{Tr}_A\left(\mathbb{1}\right). \tag{2.141}$$

Subsequently, as a starting point the eigenproblem at the time $t' = t$ is investigated. Due to Eq. (2.138) and the orthonormal condition of the eigenbasis Eq. (2.140) it is recognized that all eigenvectors need to be zero except for one which equals to the unitary. Without loss of generality it is chosen

$$v^{N^2} = \frac{1}{\sqrt{N}}\mathbb{1}, \tag{2.142}$$

and the corresponding eigenvalue is given due to Eq. (2.141)

$$\lambda^{N^2} = N. \tag{2.143}$$

In the next step, a small amount of time $t' = t + dt$ is added, which varies the last results slightly by

$$\begin{aligned} \lambda^{N^2} &= N\left(1 - c^{N^2} dt\right) \qquad \lambda^\alpha = c^\alpha dt, \quad \text{for}\, \alpha \neq N^2, \\ v^{N^2} &= \frac{1}{\sqrt{N}}\left(1 + Y dt\right) \qquad v^\alpha \neq 0, \quad \text{for}\, \alpha \neq N^2. \end{aligned} \tag{2.144}$$

Inserting these into Eq. (2.138) leads to

$$\begin{aligned} \rho_A\left(t + dt\right) &= \left(1 - c^{N^2} dt\right)\left(1 + Y dt\right) \rho_A(t) \left(1 + Y^\dagger dt\right) + dt \sum_{\alpha=1}^{N^2-1} c^\alpha v^\alpha \rho_A(t) v^{\dagger\alpha} \\ &= \rho_A(t) - c^{N^2} dt \rho_A(t) + Y dt \rho_A(t) + \rho_A(t) Y^\dagger dt + dt \sum_{\alpha=1}^{N^2-1} c^\alpha v^\alpha \rho_A(t) v^{\dagger\alpha}, \\ \Rightarrow \quad \lim_{dt\to 0} \frac{\rho_A\left(t + dt\right) - \rho_A\left(t\right)}{dt} &= \frac{d\rho_A(t)}{dt} \\ &= -c^{N^2} \rho_A(t) + Y \rho_A(t) + \rho_A(t) Y^\dagger + \sum_{\alpha=1}^{N^2-1} c^\alpha v^\alpha \rho_A(t) v^{\dagger\alpha}, \end{aligned} \tag{2.145}$$

where terms of higher order in dt are neglected. Inserting also the result of Eq. (2.144) into Eq. (2.139) gives

$$\begin{aligned} \mathbb{1} &= \left(1 - c^{N^2} dt\right)\left(1 + Y^\dagger dt\right)(1 + Y dt) + dt \sum_{\alpha=1}^{N^2-1} c^\alpha v^{\dagger\alpha} v^\alpha, \\ \Rightarrow \quad c^{N^2}\mathbb{1} &= Y^\dagger + Y + \sum_{\alpha=1}^{N^2-1} c^\alpha v^{\dagger\alpha} v^\alpha. \end{aligned} \tag{2.146}$$

Substituting $c^{N^2}\rho_A(t) = \frac{1}{2}\left(c^{N^2}\rho_A(t) + \rho_A(t)c^{N^2}\right)$ in Eq. (2.145) with the last result from Eq. (2.146) results in

$$\frac{d\rho_A(t)}{dt} = \left[\frac{1}{2}\left(Y - Y^\dagger\right), \rho_A(t)\right] - \frac{1}{2}\sum_{\alpha=1}^{N^2-1} c^\alpha \left(v^{\dagger\alpha} v^\alpha \rho_A(t) + \rho_A(t) v^{\dagger\alpha} v^\alpha - 2v^\alpha \rho_A(t) v^{\dagger\alpha}\right). \tag{2.147}$$

Replacing $-i/\hbar H = \frac{1}{2}\left(Y - Y^\dagger\right)$ and $L^\alpha = \sqrt{c^\alpha} v^\alpha$ the Lindblad equation is obtained

$$\frac{d\rho_A(t)}{dt} = -\frac{i}{\hbar}\left[H, \rho_A(t)\right] - \frac{1}{2}\sum_{\alpha=1}^{N^2-1}\left(L^{\dagger\alpha} L^\alpha \rho_A(t) + \rho_A(t) L^{\dagger\alpha} L^\alpha - 2L^\alpha \rho_A(t) L^{\dagger\alpha}\right). \tag{2.148}$$

In general the operators L and $L^\dagger$ are some kind of creation and annihilation operators describing the dissipation into the bigger system B.

2.6 Electromagnetic waves in a cylindrical cavity

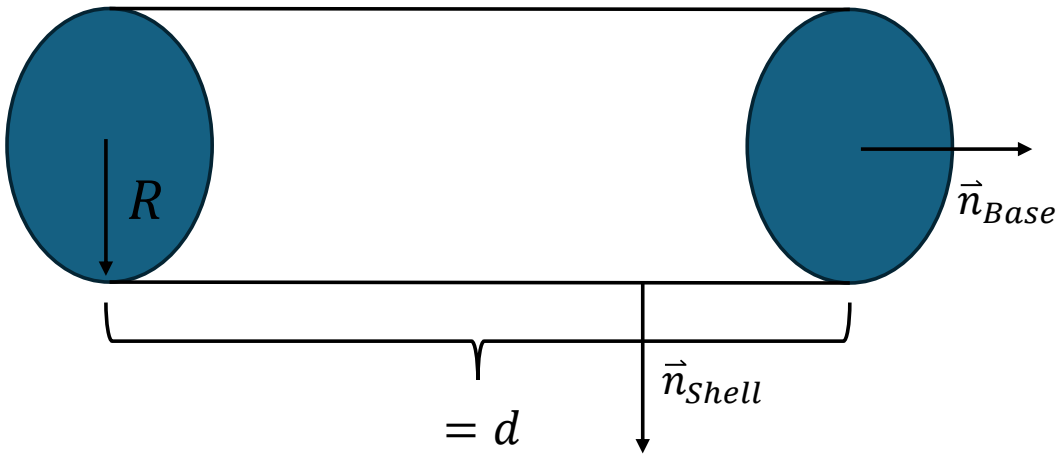

Figure 2.1: A sketch of a cylindrically shaped cavity with a radius R for the base area and a height d of the shell surface is shown.

In this section the electromagnetic modes of a cylindrical shaped cavity are introduced. The derivation is based on [124]. The cavity has a radius R of its base area and a height d, which is visible in the sketch Fig. 2.1. The surface is assumed to be a perfect metal with infinite conductivity and the inside containing an ideal vacuum, meaning there are no charge densities $\tilde{\rho}$ nor any charged currents $\vec{j}$. Consequently, this is a source free environment. Moreover, it can be assumed that the fields introduced in the system will evolve in an harmonic manner in time meaning

$$\begin{aligned} \vec{E}(x, y, z, t) &= \vec{E}(x, y, z) e^{-i\omega t}, \\ \vec{B}(x, y, z, t) &= \vec{B}(x, y, z) e^{-i\omega t}. \end{aligned} \tag{2.149}$$

Taking these assumptions into account, the Maxwell equations simplify to

$$\begin{aligned}\vec{\nabla}\times\vec{E} &= i\omega\vec{B},\\ \vec{\nabla}\times\vec{B} &= -i\mu_0\varepsilon_0\omega\vec{E},\\ \vec{\nabla}\cdot\vec{E} &= 0,\\ \vec{\nabla}\cdot\vec{B} &= 0.\end{aligned} \tag{2.150}$$

Consequently, the wave equations are obtained by taking the curl operator of the first Maxwell equation

$$\begin{aligned}&\vec{\nabla}\times\left(\vec{\nabla}\times\vec{E}\right) - i\omega\vec{\nabla}\times\vec{B} = \vec{\nabla}\underbrace{\left(\vec{\nabla}\cdot\vec{E}\right)}_{=0} - \vec{\nabla}^2\vec{E} - \mu_0\varepsilon_0\omega^2\vec{E} = 0,\\ \Rightarrow\quad &\left(\vec{\nabla}^2 + \mu_0\varepsilon_0\omega^2\right)\vec{E} = \vec{0},\end{aligned} \tag{2.151}$$

and second part of Eq. (2.150)

$$\begin{aligned}&\vec{\nabla}\times\left(\vec{\nabla}\times\vec{B}\right) + i\mu_0\varepsilon_0\omega\vec{\nabla}\times\vec{E} = \vec{\nabla}\underbrace{\left(\vec{\nabla}\cdot\vec{B}\right)}_{=0} - \vec{\nabla}^2\vec{B} - \mu_0\varepsilon_0\omega^2\vec{B} = 0,\\ \Rightarrow\quad &\left(\vec{\nabla}^2 + \mu_0\varepsilon_0\omega^2\right)\vec{B} = \vec{0}.\end{aligned} \tag{2.152}$$

In the further part of the derivation it will be advantageous to split the fields into transverse and longitudinal components. Therefore, the coordinate system is chosen so that the z-component, describing the longitudinal one, goes through the centre of the base of the cylinder. The transverse component then includes the remaining x and y components

$$\begin{aligned}\vec{E}_{trans} &= E_x\hat{e}_x + E_y\hat{e}_y,\\ \vec{B}_{trans} &= B_x\hat{e}_x + B_y\hat{e}_y.\end{aligned} \tag{2.153}$$

Consequently, the Maxwell equations from Eq. (2.150) can be split up into six new equations. Starting with the first equation from Eq. (2.150)

$$\begin{aligned}&\vec{\nabla}\times\vec{E} - i\omega\vec{B} = \vec{\nabla}\times\left(E_z\hat{e}_z + \vec{E}_{trans}\right) - i\omega\left(B_z\hat{e}_z + \vec{B}_{trans}\right)\\ &= \frac{\partial E_z}{\partial y}\hat{e}_x - \frac{\partial E_z}{\partial x}\hat{e}_y - \frac{\partial E_y}{\partial z}\hat{e}_x + \frac{\partial E_x}{\partial z}\hat{e}_y + \left(\frac{\partial E_y}{\partial x} - \frac{\partial E_x}{\partial y}\right)\hat{e}_z - i\omega B_z\hat{e}_z - i\omega B_x\hat{e}_x - i\omega B_y\hat{e}_y = \vec{0}\end{aligned} \tag{2.154}$$

The equation corresponding to the z-component reads

$$\begin{aligned}&\left(\frac{\partial E_y}{\partial x} - \frac{\partial E_x}{\partial y}\right) - i\omega B_z = 0,\\ \Rightarrow\quad &\hat{e}_z\cdot\left(\vec{\nabla}_{trans}\times\vec{E}_{trans}\right) = i\omega B_z,\end{aligned} \tag{2.155}$$

with $\vec{\nabla}_{trans} = \frac{\partial}{\partial x}\hat{e}_x + \frac{\partial}{\partial y}\hat{e}_y$. The equations from the x and y components can be unified to

$$\frac{\partial\vec{E}_{trans}}{\partial z} + i\omega\hat{e}_z\times\vec{B}_{trans} = \vec{\nabla}_{trans}E_z. \tag{2.156}$$

A similar result for the second Maxwell equation from Eq. (2.150) is obtained

$$\begin{aligned}&\frac{\partial\vec{B}_{trans}}{\partial z} - i\mu_0\varepsilon_0\omega\hat{e}_z\times\vec{E}_{trans} = \vec{\nabla}_{trans}B_z,\\ &\hat{e}_z\cdot\left(\vec{\nabla}_{trans}\times\vec{B}_{trans}\right) = -i\mu_0\varepsilon_0\omega E_z.\end{aligned} \tag{2.157}$$

Finally, the third and fourth Maxwell equation can be rewritten to

$$\begin{aligned}\vec{\nabla}_{trans} \cdot \vec{E}_{trans} &= -\frac{\partial E_z}{\partial z},\\ \vec{\nabla}_{trans} \cdot \vec{B}_{trans} &= -\frac{\partial B_z}{\partial z}.\end{aligned} \tag{2.158}$$

In addition to the prior assumptions, the fields are restricted regarding the dependencies on the z position variable, as standing waves will build up inside the cavity. Consequently, the fields need to be proportional to one of the harmonic functions sine or cosine, which will be determined via the boundary conditions at the surfaces. Moreover, only two different types of electromagnetic waves can coexist in such a cavity. These are transverse magnetic (TM) and transverse electric waves (TE). First the TM modes are addressed. For an ideal TM mode the magnetic z-component is zero, $B_z = 0$. In addition, the two boundary conditions

$$\begin{aligned}\vec{n} \times \vec{E}|_S &= \vec{0},\\ \vec{n} \cdot \vec{B}|_S &= 0,\end{aligned} \tag{2.159}$$

need to be satisfied, where $\vec{n}$ is the normal vector characterized by pointing perpendicular away from the plane surface and directed towards the outside. The boundary condition for the base area can be utilized to

$$\begin{aligned}&\hat{e}_z \times \vec{E}|_{z=0,d} = E_x \hat{e}_y - E_y \hat{e}_x|_{z=0,d} = \vec{0},\\ &E_x|_{z=0,d} = E_y|_{z=0,d} = 0,\\ \Rightarrow\quad &\vec{E}_{trans}|_{z=0,d} = \vec{0}.\end{aligned} \tag{2.160}$$

Therefore, the transverse electric field components are restricted to

$$\vec{E}_{trans}(x,y,z) = \vec{E}_{trans}(x,y)\sin(kz) \quad \text{with:} \quad k = \frac{p\pi}{d}, \quad p \in \mathbb{N}_0. \tag{2.161}$$

Continuing with the boundary conditions on the shell surface leads to

$$\begin{aligned}&\hat{e}_r \times \vec{E}|_{r=R} = E_\varphi \hat{e}_z - E_z \hat{e}_\varphi|_{r=R} = \vec{0},\\ \Rightarrow\quad &E_\varphi|_{r=R} = E_z|_{r=R} = 0.\end{aligned} \tag{2.162}$$

Next, Eq. (2.157) can be transformed to

$$\vec{B}_{trans} = \int i\mu_0\varepsilon_0\omega \hat{e}_z \times \vec{E}_{trans} dz, \tag{2.163}$$

as the B_z component vanishes. Using this and inserting it into Eq. (2.156) leads to

$$\begin{aligned}&\frac{\partial \vec{E}_{trans}}{\partial z} + i\omega \hat{e}_z \times \left(\int i\mu_0\varepsilon_0\omega \hat{e}_z \times \vec{E}_{trans} dz \right) = \vec{\nabla}_{trans} E_z,\\ \Rightarrow\quad &k\vec{E}_{trans}(x,y,t)\cos(kz) - \frac{\mu_0\varepsilon_0\omega^2}{k}\vec{E}_{trans}(x,y,t)\cos(kz) = \vec{\nabla}_{trans} E_z,\\ \Rightarrow\quad &E_z = E_z(x,y,t)\cos(kz) \quad \text{and} \quad \vec{E}_{trans}(x,y,t) = -\frac{k\vec{\nabla}_{trans} E_z(x,y,t)}{\mu_0\varepsilon_0\omega^2 - k^2},\\ \Rightarrow\quad &\vec{E}_{trans} = -\frac{k\vec{\nabla}_{trans} E_z(x,y,t)}{\mu_0\varepsilon_0\omega^2 - k^2}\sin(kz).\end{aligned} \tag{2.164}$$

Consequently, by inserting the final result back into Eq. (2.163) one obtains

$$\vec{B}_{trans} = \frac{i\mu_0\varepsilon_0\omega}{\mu_0\varepsilon_0\omega^2 - k^2}\cos(kz)\hat{e}_z \times \vec{\nabla}_{trans} E_z(x,y,t). \tag{2.165}$$

The only remaining part is encoded in the $E_z(x,y,t)$ component. The time dependency is known due to the above assumption that the fields evolve with $e^{-i\omega t}$ in time. Subsequently, the x and y dependencies are resolved by taking the wave equation Eq. (2.151) and the boundary condition Eq. (2.162) into account. Therefore, the wave equation transforms to

$$\left(\vec{\nabla}^2_{trans} + \frac{\partial^2}{\partial z^2} + \mu_0\varepsilon_0\omega^2\right)\vec{E} = \left(\vec{\nabla}^2_{trans} - k^2 + \mu_0\varepsilon_0\omega^2\right)\vec{E} = \vec{0}. \tag{2.166}$$

Concentrating only on the E_z-component and transforming the equation into polar coordinates results in

$$\left(\frac{1}{r}\frac{\partial}{\partial r}\left(r\frac{\partial}{\partial r}\right) + \frac{1}{r^2}\frac{\partial^2}{\partial\varphi^2}\underbrace{-k^2 + \mu_0\varepsilon_0\omega^2}_{=\gamma^2}\right)E_z = 0. \tag{2.167}$$

Choosing the following ansatz

$$E_z(r,\varphi,z,t) = E_z(z,t)f(r)e^{-im\varphi}, \tag{2.168}$$

leads to

$$\begin{aligned}&\left(\frac{\partial^2 f(r)}{\partial r^2} + \frac{1}{r}\frac{\partial f(r)}{\partial r} - \frac{m^2}{r^2}f(r) + \gamma^2 f(r)\right)E_z(z,t)e^{-im\varphi} = 0,\\ \Rightarrow\quad & r^2\frac{\partial^2 f(r)}{\partial r^2} + r\frac{\partial f(r)}{r} + \left(r^2\gamma^2 - m^2\right)f(r) = 0.\end{aligned} \tag{2.169}$$

This equation is known as Bessel's differential equation and its solution are Bessel functions of the first kind

$$J_m(x) = \sum_{l=0}^{\infty}\frac{(-1)^l}{l!\Gamma(l+m+1)}\left(\frac{x}{2}\right)^{2l+m}, \tag{2.170}$$

with $\Gamma(n)$ being the Gamma function. The boundary condition from Eq. (2.162) determines the argument of the Bessel function, which provides the solution for E_z

$$E_z = E_0 J_m\left(\underbrace{\frac{x_{m,n}r}{R}}_{=\gamma r}\right)e^{-im\varphi}e^{-i\omega t}\cos\left(\frac{p\pi z}{d}\right), \tag{2.171}$$

where $x_{m,n}$ is the n-th root of $J_m(x)$. The solution is a discrete number of Bessel functions as

$$\begin{aligned}m &\in \mathbb{N}_0,\\ n &\in \mathbb{N},\end{aligned} \tag{2.172}$$

which results in a discrete spectrum of frequencies, which are called modes. To be more specific the resonance frequencies are given by

$$\begin{aligned}\gamma^2 = \frac{x^2_{m,n}}{R^2} &= \mu_0\varepsilon_0\omega^2 - \frac{p^2\pi^2}{d^2},\\ \Rightarrow\quad \omega_{m,n,p} &= \frac{1}{\sqrt{\mu_0\varepsilon_0}}\sqrt{\frac{x^2_{m,n}}{R^2} + \frac{p^2\pi^2}{d^2}}.\end{aligned} \tag{2.173}$$

Once the E_z-component is obtained, the transverse magnetic and electric components can be derived via Eq. (2.164) and Eq. (2.165). Therefore, the derivative of the Bessel function from Eq. (2.170) needs to be determined

$$\begin{aligned}\frac{\partial}{\partial x}J_m(x) &= \frac{1}{2}\sum_{l=0}^{\infty}\frac{(-1)^l(2l+m)}{l!\Gamma(l+m+1)}\left(\frac{x}{2}\right)^{2l+m-1}\\ &= \frac{1}{2}\left(J_{m-1}(x) - J_{m+1}(x)\right).\end{aligned} \tag{2.174}$$

The full calculation is stated in App. G. Consequently, the fields for the TM modes are given by

$$\begin{aligned}
E_r &= -\frac{k x_{m,n} E_0}{2R\left(\mu_0\varepsilon_0\omega^2 - k^2\right)} \sin(kz)\, e^{-im\varphi} e^{-i\omega t} \left[J_{m-1}\left(\frac{x_{m,n} r}{R}\right) - J_{m+1}\left(\frac{x_{m,n} r}{R}\right)\right], \\
E_\varphi &= \frac{imkE_0}{r\left(\mu_0\varepsilon_0\omega^2 - k^2\right)} \sin(kz)\, e^{-im\varphi} e^{-i\omega t} J_m\left(\frac{x_{m,n} r}{R}\right), \\
E_z &= E_0 J_m\left(\frac{x_{m,n} r}{R}\right) e^{-im\varphi} e^{-i\omega t} \cos(kz), \\
B_r &= -\frac{\mu_0\varepsilon_0\omega m E_0}{r\left(\mu_0\varepsilon_0\omega^2 - k^2\right)} \cos(kz)\, e^{-im\varphi} e^{-i\omega t} J_m\left(\frac{x_{m,n} r}{R}\right), \\
B_\varphi &= \frac{i\mu_0\varepsilon_0\omega x_{m,n} E_0}{2R\left(\mu_0\varepsilon_0\omega^2 - k^2\right)} \cos(kz)\, e^{-im\varphi} e^{-i\omega t} \left[J_{m-1}\left(\frac{x_{m,n} r}{R}\right) - J_{m+1}\left(\frac{x_{m,n} r}{R}\right)\right], \\
B_z &= 0.
\end{aligned} \tag{2.175}$$

The two field components E_φ and B_r need to be investigated in the limit $r \to 0$ to show that they do not diverge for any m. Starting with

$$\begin{aligned}
&\frac{1}{r} \text{ it is finite for } r \in (0, \infty). \\
&\text{Next, the case } m = 0 \text{ is invested:} \\
&\frac{m}{r} = 0 \text{ and } J_0(0) = 1 \\
&\text{especially in the limit } r \to 0. \text{ Next one investigates the case } m \in \mathbb{N} \text{ for } r \to 0: \\
&\lim_{r\to 0} \frac{J_m(r)}{r} = \text{"0"} \cdot \text{"}\infty\text{"}.
\end{aligned} \tag{2.176}$$

Using l'Hôpital's rule:

$$\lim_{r\to 0} \frac{J_m(r)}{r} = \lim_{r\to 0} \frac{dJ_m(r)}{dr} \frac{1}{dr/dr} = \lim_{r\to 0} \frac{1}{2}\left(J_{m-1}(r) - J_{m+1}(r)\right) = \begin{cases} \frac{1}{2} & \text{, if } m = 1 \\ 0 & \text{, else} \end{cases}.$$

Next, the TE modes can be addressed. Those are defined by having no electric z-component ($E_z = 0$). Analogously to the TM modes the fields need to satisfy the same boundary conditions given in Eq. (2.159). Focusing first on the base area the boundary condition for the magnetic field turns into

$$\hat{e}_z \cdot \vec{B}|_{z=0,d} = B_z|_{z=0,d} = 0. \tag{2.177}$$

Consequently, the magnetic z-component is

$$B_z(x, y, z, t) = B_z(x, y, t) \sin(kz) \quad \text{with:} \quad k = \frac{p\pi}{d}, \quad p \in \mathbb{N}_0. \tag{2.178}$$

Moreover, the boundary condition for the shell surface restricts the magnetic field even further

$$\hat{e}_r \cdot \vec{B}|_{r=R} = B_r|_{r=R} = 0. \tag{2.179}$$

Inserting the last result and Eq. (2.162) into Eq. (2.157) leads to

$$\begin{aligned}
&\underbrace{\frac{\partial B_r}{\partial z}|_{r=R}}_{=0} \hat{e}_r + \frac{\partial B_\varphi}{\partial z}|_{r=R} \hat{e}_\varphi - i\mu_0\varepsilon_0\omega \hat{e}_z \times \left(E_r \hat{e}_r + \underbrace{E_\varphi}_{=0} \hat{e}_\varphi\right)|_{r=R} = \frac{\partial B_z}{\partial r}|_{r=R} \hat{e}_r + \frac{1}{r}\frac{\partial B_z}{\partial \varphi}|_{r=R} \hat{e}_\varphi, \\
&\text{Equation for the } \hat{e}_r\text{-component:} \quad \frac{\partial B_z}{\partial r}|_{r=R} = 0, \\
&\text{Equation for the } \hat{e}_\varphi\text{-component:} \quad \frac{\partial B_\varphi}{\partial z}|_{r=R} - i\mu_0\varepsilon_0\omega E_r|_{r=R} = \frac{1}{r}\frac{\partial B_z}{\partial \varphi}|_{r=R}.
\end{aligned} \tag{2.180}$$

Subsequently, transforming Eq. (2.156) results in the following expression

$$\vec{E}_{trans} = -i\omega \int \hat{e}_z \times \vec{B}_{trans} dz. \tag{2.181}$$

Next, inserting the upper relation into Eq. (2.157) leads to

$$\begin{aligned}
&\frac{\partial \vec{B}_{trans}}{\partial z} - i\mu_0\varepsilon_0\omega\hat{e}_z \times (-i\omega) \int \hat{e}_z \times \vec{B}_{trans} dz = \vec{\nabla}_{trans} B_z = \vec{\nabla}_{trans} B_z(x,y,t) \sin(kz), \\
\Rightarrow\quad &\vec{B}_{trans} = \vec{B}_{trans}(x,y,t) \cos(kz), \\
&-k\vec{B}_{trans}(x,y,t) + \frac{\mu_0\varepsilon_0\omega^2}{k}\vec{B}_{trans}(x,y,t) = \vec{\nabla}_{trans} B_z(x,y,t), \\
\Rightarrow\quad &\vec{B}_{trans} = \frac{k\vec{\nabla}_{trans} B_z(x,y,t)}{\mu_0\varepsilon_0\omega^2 - k^2} \cos(kz).
\end{aligned} \tag{2.182}$$

Reinserting this result into the integral expression for the transverse electric field Eq. (2.181) leads to

$$\vec{E}_{trans} = -\frac{i\omega\hat{e}_z \times \vec{\nabla}_{trans} B_z(x,y,t)}{\mu_0\varepsilon_0\omega^2 - k^2} \sin(kz). \tag{2.183}$$

Similar to the derivation for the TM E_z component, B_z is determined to

$$B_z = B_0 J_m\left(\frac{\tilde{x}_{m,n} r}{R}\right) e^{-im\varphi} e^{-i\omega t} \sin(kz), \tag{2.184}$$

with $\tilde{x}_{m,n}$ being the n-th root of $\frac{\partial J_m(x)}{\partial x}$ due to the boundary condition $\frac{\partial B_z}{\partial r}|_{r=R} = 0$ from Eq. (2.180). Subsequently, the fields are given by

$$\begin{aligned}
E_r &= \frac{\omega m B_0}{r(\mu_0\varepsilon_0\omega^2 - k^2)} J_m\left(\frac{\tilde{x}_{m,n} r}{R}\right) e^{-im\varphi} e^{-i\omega t} \sin(kz), \\
E_\varphi &= -\frac{i\omega B_0 \tilde{x}_{m,n}}{2R(\mu_0\varepsilon_0\omega^2 - k^2)} \left[J_{m-1}\left(\frac{\tilde{x}_{m,n} r}{R}\right) - J_{m+1}\left(\frac{\tilde{x}_{m,n} r}{R}\right)\right] e^{-im\varphi} e^{-i\omega t} \sin(kz), \\
E_z &= 0, \\
B_r &= \frac{k\tilde{x}_{m,n} B_0}{2R(\mu_0\varepsilon_0\omega^2 - k^2)} \left[J_{m-1}\left(\frac{\tilde{x}_{m,n} r}{R}\right) - J_{m+1}\left(\frac{\tilde{x}_{m,n} r}{R}\right)\right] e^{-im\varphi} e^{-i\omega t} \cos(kz), \\
B_\varphi &= -\frac{ikmB_0}{r(\mu_0\varepsilon_0\omega^2 - k^2)} J_m\left(\frac{\tilde{x}_{m,n} r}{R}\right) e^{-im\varphi} e^{-i\omega t} \cos(kz), \\
B_z &= B_0 J_m\left(\frac{\tilde{x}_{m,n} r}{R}\right) e^{-im\varphi} e^{-i\omega t} \sin(kz).
\end{aligned} \tag{2.185}$$

These results restrict p for the TE mode even more to

$$p \in \mathbb{N}, \tag{2.186}$$

as for $p = 0$ all fields vanish. Therefore, this is not a valid solution. Likewise, to the TM modes, the resonance frequency is given by

$$\omega_{m,n,p} = \frac{1}{\sqrt{\mu_0\varepsilon_0}} \sqrt{\frac{\tilde{x}_{m,n}^2}{R^2} + \frac{p^2\pi^2}{d^2}}. \tag{2.187}$$

The special case for $r \to 0$ in E_r and B_φ is treated analogue to the TM-modes.
So far a perfect cavity has been assumed, where the entire fields are reflected at the walls. In reality a small fraction of those fields enter the walls and is lost via Ohm's law. Therefore, the remaining fields are damped exponentially over time. The characteristic damping constant is

called Q-value and is defined by the ratio of energy input over energy loss. As the energy of electromagnetic fields U is proportional to the absolute value squared of the fields the fields are given by

$$\begin{aligned}\vec{E}(x,y,z,t) &= \vec{E}(x,y,z)\, e^{-i\omega_{m,n,p}t} e^{-\frac{\omega_{m,n,p}t}{2Q}},\\ \vec{B}(x,y,z,t) &= \vec{B}(x,y,z)\, e^{-i\omega_{m,n,p}t} e^{-\frac{\omega_{m,n,p}t}{2Q}}.\end{aligned} \tag{2.188}$$

Due to the damping the fields get smeared out, which allows a small frequency band around the resonance frequency to enter the cavity. This gets clearer by moving into the frequency space by performing a Fourier transformation

$$\vec{E}(x,y,z,\omega) = \left(\mathcal{F}\vec{E}(x,y,z,t)\right)(\omega) = \frac{1}{\sqrt{2\pi}} \int_0^\infty \vec{E}(x,y,z)\, e^{-i\omega_{m,n,p}t} e^{-\frac{\omega_{m,n,p}t}{2Q}} e^{i\omega t} dt. \tag{2.189}$$

The solution of this integral is

$$\vec{E}(x,y,z,\omega) = -\frac{2Q\vec{E}(x,y,z)\left((2iQ-1)\,\omega_{m,n,p} - 2iQ\omega\right)}{(4Q^2+1)\,\omega_{m,n,p}^2 - 8Q^2\omega\omega_{m,n,p} + 4Q^2\omega^2}. \tag{2.190}$$

Its absolute squared value equals then to

$$|\vec{E}(x,y,z,\omega)| = \frac{|\vec{E}(x,y,z)|}{\left(\omega - \omega_{m,n,p}\right)^2 + \frac{\omega_{m,n,p}^2}{4Q^2}}. \tag{2.191}$$

The solution is a Lorentz distribution and by this the Q-value is connected to the line width Γ at the half maximum of the Lorentz distribution via

$$\Gamma = \frac{\omega_{m,n,p}}{Q}. \tag{2.192}$$

Chapter 3

Derivation of the formalism

The theoretical framework shown in this chapter has been developed during this project. Here, the sets of states are introduced, which are relevant for the numerical simulations performed in this thesis. Moreover, their interactions with external fields are investigated and a final Lindblad master equation is proposed.

3.1 Hydrogen

Hydrogen, composed of one proton circulated by an electron, has the simplest atomic structure. In this thesis the metastable $2S_{1/2}$ states, characterized by $n = 2$, $l = 0$ and $j = s = 1/2$, as well as the short living $2P_{1/2}$ ($n = 2$, $l = 1$, $j = s = 1/2$), and $2P_{3/2}$ set ($n = 2$, $l = 1$, $j = 3/2$, $s = 1/2$) are relevant. The basis $|n, l, m_l, s, m_s\rangle$ leaves the wave functions separable into their orbital wave function $\Psi_{n,l,m}(\vec{r})$ and their spin wave function χ

$$\Phi(\vec{r}) = \Psi_{n,l,m}(\vec{r}) \otimes \chi. \tag{3.1}$$

The corresponding eigenenergy and orbital wave functions from Sec. 2.1 are expressed by

$$\begin{aligned}
E_2 &= -\frac{E_R}{4}, \\
\Psi_{2,0,0}(r,\theta,\varphi) &= \frac{1}{\sqrt{8a_0^3}}\left(-\frac{r}{a_0}+2\right)e^{-\frac{r}{2a_0}}\frac{1}{\sqrt{4\pi}}, \\
\Psi_{2,1,0}(r,\theta,\varphi) &= \frac{1}{\sqrt{24a_0^3}}\left(\frac{r}{a_0}\right)e^{-\frac{r}{2a_0}}\sqrt{\frac{3}{4\pi}}\cos(\theta), \\
\Psi_{2,1,\pm1}(r,\theta,\varphi) &= \mp\frac{1}{\sqrt{24a_0^3}}\left(\frac{r}{a_0}\right)e^{-\frac{r}{2a_0}}\sqrt{\frac{3}{8\pi}}\sin(\theta)\,e^{\pm i\varphi},
\end{aligned} \tag{3.2}$$

with $E_R = m_e e^4/32\pi^2\varepsilon_0^2\hbar^2$ being the Rydberg constant. Subsequently, the corrections due to the fine structure from Sec. 2.2.1 is given for the metastable set by

$$\begin{aligned}
E_{FS} &= -\frac{5}{2}\frac{E_2^2}{m_e c^2}, \\
|j = 1/2, m_j = 1/2\rangle &= |m_l = 0, m_s = 1/2\rangle, \\
|j = 1/2, m_j = -1/2\rangle &= |m_l = 0, m_s = -1/2\rangle.
\end{aligned} \tag{3.3}$$

For the $2P$ sets the vector space is expressed as

$$\mathcal{D}_{l=1} \otimes \mathcal{D}_{s=1/2} = \mathcal{D}_{j=3/2} \oplus \mathcal{D}_{j=1/2}. \tag{3.4}$$

Correspondingly, the corrections for the $2P_{1/2}$ set are displayed by

$$\begin{aligned}
E_{FS} &= -\frac{5}{2}\frac{E_2^2}{m_e c^2}, \\
|j = 1/2, m_j = 1/2\rangle &= \sqrt{\frac{2}{3}}\,|m_l = 1, m_s = -1/2\rangle - \frac{1}{\sqrt{3}}\,|m_l = 0, m_s = 1/2\rangle\,, \\
|j = 1/2, m_j = -1/2\rangle &= \frac{1}{\sqrt{3}}\,|m_l = 0, m_s = -1/2\rangle - \sqrt{\frac{2}{3}}\,|m_l = -1, m_s = 1/2\rangle\,,
\end{aligned} \tag{3.5}$$

with the approximation of $g_s = 2$. Finally for the $2P_{3/2}$ set

$$\begin{aligned}
E_{FS} &= -\frac{1}{2}\frac{E_2^2}{m_e c^2}, \\
|j = 3/2, m_j = 3/2\rangle &= |m_l = 1, m_s = 1/2\rangle\,, \\
|j = 3/2, m_j = 1/2\rangle &= \frac{1}{\sqrt{3}}\,|m_l = 1, m_s = -1/2\rangle + \sqrt{\frac{2}{3}}\,|m_l = 0, m_s = 1/2\rangle\,, \\
|j = 3/2, m_j = -1/2\rangle &= \sqrt{\frac{2}{3}}\,|m_l = 0, m_s = -1/2\rangle + \frac{1}{\sqrt{3}}\,|m_l = -1, m_s = 1/2\rangle\,, \\
|j = 3/2, m_j = -3/2\rangle &= |m_l = -1, m_s = -1/2\rangle\,.
\end{aligned} \tag{3.6}$$

Also here the g-factor was approximated by two. Next follows the Lamb-shift from Sec. 2.2.2 for the metastable case

$$\begin{aligned}
E_{Lamb} &= \frac{1}{6}\frac{1}{2\varepsilon_0\pi^2}\left(\frac{e^2}{\hbar c}\right)\left(\frac{\hbar}{m_e c}\right)^2 \ln\left(\frac{4\varepsilon_0\hbar c}{e^2}\right)\frac{e^2}{\varepsilon_0}|\Psi_{2,0,0}\,(r = 0, \theta = 0, \varphi = 0)\,|^2 \\
&= \frac{1}{6}\frac{1}{2\varepsilon_0\pi^2}\left(\frac{e^2}{\hbar c}\right)\left(\frac{\hbar}{m_e c}\right)^2 \ln\left(\frac{4\varepsilon_0\hbar c}{e^2}\right)\frac{e^2}{\varepsilon_0}\frac{1}{8a_0^3\pi},
\end{aligned} \tag{3.7}$$

and in the cases of the $2P$ sets

$$E_{Lamb} = 0.$$

Subsequently, the hyperfine structure for the metastable hydrogen $2S_{1/2}$ set is investigated first. The proton as well as the electron are spin 1/2 particles. Therefore, the vector space is expressed as

$$\mathcal{D}_{I=1/2} \otimes \mathcal{D}_{s=1/2} = \mathcal{D}_{F=1} \oplus \mathcal{D}_{F=0}. \tag{3.8}$$

Consequently, the relation between the coupled $|F, m_F\rangle$ and uncoupled $|m_j, m_I\rangle$ basis is represented by

$$\begin{aligned}
|F = 1, m_F = 1\rangle &= |m_s = 1/2, m_I = 1/2\rangle\,, \\
|F = 1, m_F = 0\rangle &= \frac{1}{\sqrt{2}}\left(|m_s = 1/2, m_I = -1/2\rangle + |m_s = -1/2, m_I = 1/2\rangle\right), \\
|F = 1, m_F = -1\rangle &= |m_s = -1/2, m_I = -1/2\rangle\,, \\
|F = 0, m_F = 0\rangle &= \frac{1}{\sqrt{2}}\left(|m_s = 1/2, m_I = -1/2\rangle - |m_s = -1/2, m_I = 1/2\rangle\right).
\end{aligned} \tag{3.9}$$

Analogously for the short living $2P_{1/2}$ set the following relation is found

$$\mathcal{D}_{I=1/2} \otimes \mathcal{D}_{j=1/2} = \mathcal{D}_{F=1} \oplus \mathcal{D}_{F=0}. \tag{3.10}$$

with the states expressed by

$$
\begin{aligned}
|F=1, m_F=1\rangle &= |m_j={}^1\!/_2, m_I={}^1\!/_2\rangle \\
&= \sqrt{\frac{2}{3}}\,|m_l=1, m_s=-{}^1\!/_2, m_I={}^1\!/_2\rangle - \frac{1}{\sqrt{3}}\,|m_l=0, m_s={}^1\!/_2, m_I={}^1\!/_2\rangle\,, \\
|F=1, m_F=0\rangle &= \frac{1}{\sqrt{2}}\left(|m_j={}^1\!/_2, m_I=-{}^1\!/_2\rangle + |m_j=-{}^1\!/_2, m_I={}^1\!/_2\rangle\right) \\
&= \frac{1}{\sqrt{3}}\,|m_l=1, m_s=-{}^1\!/_2, m_I=-{}^1\!/_2\rangle - \frac{1}{\sqrt{6}}\,|m_l=0, m_s={}^1\!/_2, m_I=-{}^1\!/_2\rangle \\
&+ \frac{1}{\sqrt{6}}\,|m_l=0, m_s=-{}^1\!/_2, m_I={}^1\!/_2\rangle - \frac{1}{\sqrt{3}}\,|m_l=-1, m_s={}^1\!/_2, m_I={}^1\!/_2\rangle\,, \\
|F=1, m_F=-1\rangle &= |m_j=-{}^1\!/_2, m_I=-{}^1\!/_2\rangle \\
&= \frac{1}{\sqrt{3}}\,|m_l=0, m_s=-{}^1\!/_2, m_I=-{}^1\!/_2\rangle - \sqrt{\frac{2}{3}}\,|m_l=-1, m_s={}^1\!/_2, m_I=-{}^1\!/_2\rangle\,, \\
|F=0, m_F=0\rangle &= \frac{1}{\sqrt{2}}\left(|m_j={}^1\!/_2, m_I=-{}^1\!/_2\rangle - |m_j=-{}^1\!/_2, m_I={}^1\!/_2\rangle\right) \\
&= \frac{1}{\sqrt{3}}\,|m_l=1, m_s=-{}^1\!/_2, m_I=-{}^1\!/_2\rangle - \frac{1}{\sqrt{6}}\,|m_l=0, m_s={}^1\!/_2, m_I=-{}^1\!/_2\rangle \\
&- \frac{1}{\sqrt{6}}\,|m_l=0, m_s=-{}^1\!/_2, m_I={}^1\!/_2\rangle + \frac{1}{\sqrt{3}}\,|m_l=-1, m_s={}^1\!/_2, m_I={}^1\!/_2\rangle\,.
\end{aligned}
\tag{3.11}
$$

The vector space of the third set $2P_{3/2}$ is represented by

$$
\mathcal{D}_{I={}^1\!/_2} \otimes \mathcal{D}_{j={}^3\!/_2} = \mathcal{D}_{F=2} \oplus \mathcal{D}_{F=1}. \tag{3.12}
$$

The corresponding eight states are then

$$
\begin{aligned}
&|F=2,m_F=2\rangle = |m_j={}^3\!/_2, m_I={}^1\!/_2\rangle = |m_l=1, m_s={}^1\!/_2, m_I={}^1\!/_2\rangle\,,\\
&|F=2,m_F=1\rangle = \frac{1}{\sqrt{4}}\,|m_j={}^3\!/_2, m_I=-{}^1\!/_2\rangle + \sqrt{\frac{3}{4}}\,|m_j={}^1\!/_2, m_I={}^1\!/_2\rangle\\
&= \frac{1}{\sqrt{4}}\,|m_l=1, m_s={}^1\!/_2, m_I=-{}^1\!/_2\rangle\\
&+ \sqrt{\frac{3}{4}}\left(\frac{1}{\sqrt{3}}\,|m_l=1, m_s=-{}^1\!/_2, m_I={}^1\!/_2\rangle + \sqrt{\frac{2}{3}}\,|m_l=0, m_s={}^1\!/_2, m_I={}^1\!/_2\rangle\right),\\
&|F=2,m_F=0\rangle = \frac{1}{\sqrt{2}}\left(|m_j={}^1\!/_2, m_I=-{}^1\!/_2\rangle + |m_j=-{}^1\!/_2, m_I={}^1\!/_2\rangle\right)\\
&= \frac{1}{\sqrt{2}}\left(\frac{1}{\sqrt{3}}\,|m_l=1, m_s=-{}^1\!/_2, m_I=-{}^1\!/_2\rangle + \sqrt{\frac{2}{3}}\,|m_l=0, m_s={}^1\!/_2, m_I=-{}^1\!/_2\rangle\right.\\
&\left.+\sqrt{\frac{2}{3}}\,|m_l=0, m_s=-{}^1\!/_2, m_I={}^1\!/_2\rangle + \frac{1}{\sqrt{3}}\,|m_l=-1, m_s={}^1\!/_2, m_I={}^1\!/_2\rangle\right),\\
&|F=2,m_F=-1\rangle = \sqrt{\frac{3}{4}}\,|m_j=-{}^1\!/_2, m_I=-{}^1\!/_2\rangle + \frac{1}{\sqrt{4}}\,|m_j=-{}^3\!/_2, m_I={}^1\!/_2\rangle\\
&= \sqrt{\frac{3}{4}}\left(\sqrt{\frac{2}{3}}\,|m_l=0, m_s=-{}^1\!/_2, m_I=-{}^1\!/_2\rangle + \frac{1}{\sqrt{3}}\,|m_l=-1, m_s={}^1\!/_2, m_I=-{}^1\!/_2\rangle\right)\\
&+ \frac{1}{\sqrt{4}}\,|m_l=-1, m_s=-{}^1\!/_2, m_I={}^1\!/_2\rangle\,,\\
&|F=2,m_F=-2\rangle = |m_j=-{}^3\!/_2, m_I=-{}^1\!/_2\rangle = |m_l=-1, m_s=-{}^1\!/_2, m_I=-{}^1\!/_2\rangle\,,\\
&|F=1,m_F=1\rangle = \sqrt{\frac{3}{4}}\,|m_j={}^3\!/_2, m_I=-{}^1\!/_2\rangle - \frac{1}{\sqrt{4}}\,|m_j={}^1\!/_2, m_I={}^1\!/_2\rangle\\
&= \sqrt{\frac{3}{4}}\,|m_l=1, m_s={}^1\!/_2, m_I=-{}^1\!/_2\rangle\\
&- \frac{1}{\sqrt{4}}\left(\frac{1}{\sqrt{3}}\,|m_l=1, m_s=-{}^1\!/_2, m_I={}^1\!/_2\rangle + \sqrt{\frac{2}{3}}\,|m_l=0, m_s={}^1\!/_2, m_I={}^1\!/_2\rangle\right),\\
&|F=1,m_F=0\rangle = \frac{1}{\sqrt{2}}\left(|m_j={}^1\!/_2, m_I=-{}^1\!/_2\rangle - |m_j=-{}^1\!/_2, m_I={}^1\!/_2\rangle\right)\\
&= \frac{1}{\sqrt{2}}\left(\frac{1}{\sqrt{3}}\,|m_l=1, m_s=-{}^1\!/_2, m_I=-{}^1\!/_2\rangle + \sqrt{\frac{2}{3}}\,|m_l=0, m_s={}^1\!/_2, m_I=-{}^1\!/_2\rangle\right.\\
&\left.-\sqrt{\frac{2}{3}}\,|m_l=0, m_s=-{}^1\!/_2, m_I={}^1\!/_2\rangle - \frac{1}{\sqrt{3}}\,|m_l=-1, m_s={}^1\!/_2, m_I={}^1\!/_2\rangle\right),\\
&|F=1,m_F=-1\rangle = \frac{1}{\sqrt{4}}\,|m_j=-{}^1\!/_2, m_I=-{}^1\!/_2\rangle - \sqrt{\frac{3}{4}}\,|m_j=-{}^3\!/_2, m_I={}^1\!/_2\rangle\\
&= \frac{1}{\sqrt{4}}\left(\sqrt{\frac{2}{3}}\,|m_l=0, m_s=-{}^1\!/_2, m_I=-{}^1\!/_2\rangle + \frac{1}{\sqrt{3}}\,|m_l=-1, m_s={}^1\!/_2, m_I=-{}^1\!/_2\rangle\right)\\
&- \sqrt{\frac{3}{4}}\,|m_l=-1, m_s=-{}^1\!/_2, m_I={}^1\!/_2\rangle\,.
\end{aligned}
\tag{3.13}
$$

The hyperfine constants A from Sec. 2.2.3 are stated as

$$\begin{aligned} A_{2S_{1/2}} &= \frac{\mu_0 \mu_B \mu_k g_I}{3\pi} \frac{1}{2a_0^3}, \\ A_{2P_{1/2}} &= \frac{\mu_0 e^2 g_I \hbar^2}{72\pi m_e m_p a_0^3}, \\ A_{2P_{3/2}} &= \frac{\mu_0 e^2 g_I \hbar^2}{360\pi m_e m_p a_0^3}. \end{aligned} \tag{3.14}$$

Next the eigensystem in the presence of a homogenous constant magnetic field in z-direction $\vec{B} = B_z \hat{e}_z$ is investigated as explained in Sec. 2.4.3. The angular momentum operators $\vec{I}$ and $\vec{J}$ are necessary to calculate the Breit-Rabi system. As the ground state $1S_{1/2}$ quantum numbers do not differ from the ones of the metastable $2S_{1/2}$ and the $2P_{1/2}$ set, the result is analogue to Eq. 2.115. For the metastable $2S_{1/2}$ the Breit-Rabi system takes the following form

$$\begin{aligned} E_{\alpha_1} &= \frac{A_{2S_{1/2}}}{4} + \frac{1}{2}\left(g_s\mu_B - g_I\mu_k\right) B_z, \\ |\alpha_1\rangle &= |F=1, m_F=1\rangle, \\ E_{\alpha_2} &= -\frac{A_{2S_{1/2}}}{4} + \frac{1}{2}\sqrt{A_{2S_{1/2}}^2 + \left(g_s\mu_B + g_I\mu_k\right)^2 B_z^2}, \\ |\alpha_2\rangle &= \frac{1}{\sqrt{1+x^2\left(B_z\right)}}\left(x(B_z)\,|F=0, m_F=0\rangle + |F=1, m_F=0\rangle\right), \\ E_{\beta_3} &= \frac{A_{2S_{1/2}}}{4} - \frac{1}{2}\left(g_s\mu_B - g_I\mu_k\right) B_z, \\ |\beta_3\rangle &= |F=1, m_F=-1\rangle, \\ E_{\beta_4} &= -\frac{A_{2S_{1/2}}}{4} - \frac{1}{2}\sqrt{A_{2S_{1/2}}^2 + \left(g_s\mu_B + g_I\mu_k\right)^2 B_z^2}, \\ |\beta_4\rangle &= \frac{1}{\sqrt{1+\omega^2(B_z)}}\left(|F=0, m_F=0\rangle + \omega(B_z)\,|F=1, m_F=0\rangle\right) \\ \text{with} \quad x(B_z) &= \frac{\left(g_s\mu_B + g_I\mu_k\right) B_z}{A_{2S_{1/2}} + \sqrt{A_{2S_{1/2}}^2 + \left(g_s\mu_B + g_I\mu_k\right)^2 B_z^2}} \\ \text{and} \quad \omega\left(B_z\right) &= \frac{A_{2S_{1/2}} - \sqrt{A_{2S_{1/2}}^2 + \left(g_s\mu_B + g_I\mu_k\right)^2 B_z^2}}{\left(g_s\mu_B + g_I\mu_k\right) B_z}. \end{aligned} \tag{3.15}$$

Analogously for the $2P_{1/2}$ set

$$
\begin{aligned}
E_{e_1} &= \frac{A_{2P_{1/2}}}{4} + \frac{1}{2}\left(g_j\mu_B - g_I\mu_k\right)B_z,\\
|e_1\rangle &= |F=1, m_F=1\rangle,\\
E_{e_2} &= -\frac{A_{2P_{1/2}}}{4} + \frac{1}{2}\sqrt{A^2_{2P_{1/2}} + \left(g_j\mu_B + g_I\mu_k\right)^2 B_z^2},\\
|e_2\rangle &= \frac{1}{\sqrt{1+y^2\left(B_z\right)}}\left(y(B_z)\,|F=0, m_F=0\rangle + |F=1, m_F=0\rangle\right),\\
E_{f_3} &= \frac{A_{2P_{1/2}}}{4} - \frac{1}{2}\left(g_j\mu_B - g_I\mu_k\right)B_z,\\
|f_3\rangle &= |F=1, m_F=-1\rangle,\\
E_{f_4} &= -\frac{A_{2P_{1/2}}}{4} - \frac{1}{2}\sqrt{A^2_{2P_{1/2}} + \left(g_j\mu_B + g_I\mu_k\right)^2 B_z^2},\\
|f_4\rangle &= \frac{1}{\sqrt{1+z^2(B_z)}}\left(|F=0, m_F=0\rangle + z(B_z)\,|F=1, m_F=0\rangle\right)\\
\text{with}\quad y(B_z) &= \frac{\left(g_j\mu_B + g_I\mu_k\right)B_z}{A_{2P_{1/2}} + \sqrt{A^2_{2P_{1/2}} + \left(g_j\mu_B + g_I\mu_k\right)^2 B_z^2}}\\
\text{and}\quad z\left(B_z\right) &= \frac{A_{2P_{1/2}} - \sqrt{A^2_{2P_{1/2}} + \left(g_j\mu_B + g_I\mu_k\right)^2 B_z^2}}{\left(g_j\mu_B + g_I\mu_k\right)B_z}.
\end{aligned}
\tag{3.16}
$$

Furthermore, the Breit-Rabi system in the case of $2P_{3/2}$ is investigated. The eigensystem can be separated into five independent linear systems

$$
\begin{aligned}
&\langle F=2, m_F=2|H_{BR}|F=2, m_F=2\rangle = \frac{3A_{2P_{3/2}}}{4} + \frac{1}{2}\left(3g_j\mu_B - g_I\mu_k\right)B_z,\\
&\qquad\qquad |F=2, m_F=1\rangle \qquad\qquad |F=1, m_F=1\rangle\\
&H_{BR} = \begin{matrix}\langle F=2, m_F=1|\\ \langle F=1, m_F=1|\end{matrix}\begin{pmatrix} \frac{3A_{2P_{3/2}}}{4} + \frac{1}{4}\left(3g_j\mu_B - g_I\mu_k\right)B_z & \frac{\sqrt{3}}{4}\left(g_j\mu_B + g_I\mu_k\right)B_z \\ \frac{\sqrt{3}}{4}\left(g_j\mu_B + g_I\mu_k\right)B_z & -\frac{5A_{2P_{3/2}}}{4} + \frac{1}{4}\left(5g_j\mu_B + g_I\mu_k\right)B_z \end{pmatrix},\\
&\qquad\qquad |F=2, m_F=0\rangle \qquad\qquad |F=1, m_F=0\rangle\\
&H_{BR} = \begin{matrix}\langle F=2, m_F=0|\\ \langle F=1, m_F=0|\end{matrix}\begin{pmatrix} \frac{3A_{2P_{3/2}}}{4} & \frac{1}{2}\left(g_j\mu_B + g_I\mu_k\right)B_z \\ \frac{1}{2}\left(g_j\mu_B + g_I\mu_k\right)B_z & -\frac{5A_{2P_{3/2}}}{4} \end{pmatrix},\\
&\qquad\qquad |F=2, m_F=-1\rangle \qquad\qquad |F=1, m_F=-1\rangle\\
&H_{BR} = \begin{matrix}\langle F=2, m_F=-1|\\ \langle F=1, m_F=-1|\end{matrix}\begin{pmatrix} \frac{3A_{2P_{3/2}}}{4} - \frac{1}{4}\left(3g_j\mu_B - g_I\mu_k\right)B_z & \frac{\sqrt{3}}{4}\left(g_j\mu_B + g_I\mu_k\right)B_z \\ \frac{\sqrt{3}}{4}\left(g_j\mu_B + g_I\mu_k\right)B_z & -\frac{5A_{2P_{3/2}}}{4} - \frac{1}{4}\left(5g_j\mu_B + g_I\mu_k\right)B_z \end{pmatrix},\\
&\langle F=2, m_F=-2|H_{BR}|F=2, m_F=-2\rangle = \frac{3A_{2P_{3/2}}}{4} - \frac{1}{2}\left(3g_j\mu_B - g_I\mu_k\right)B_z.
\end{aligned}
\tag{3.17}
$$

Subsequently, the Breit-Rabi basis is displayed

$$
\begin{aligned}
E_{g_1} &= \frac{3A_{2P_{3/2}}}{4} + \frac{1}{2}\left(3g_j\mu_B - g_I\mu_k\right)B_z,\\
|g_1\rangle &= |F=2, m_F=2\rangle,\\
E_{g_2} &= -\frac{A_{2P_{3/2}}}{4} + g_j\mu_B B_z + \sqrt{A_{2P_{3/2}}^2 - \frac{A_{2P_{3/2}}}{2}\left(g_j\mu_B + g_I\mu_k\right)B_z + \frac{1}{4}\left(g_j\mu_B + g_I\mu_k\right)^2 B_z^2},\\
|g_2\rangle &= \frac{1}{\sqrt{1+\chi_1^2(B_z)}}\left(|F=2, m_F=1\rangle + \chi_1(B_z)\,|F=1, m_F=1\rangle\right),\\
E_{g_3} &= -\frac{A_{2P_{3/2}}}{4} + \sqrt{A_{2P_{3/2}}^2 + \frac{1}{4}\left(g_j\mu_B + g_I\mu_k\right)^2 B_z^2},\\
|g_3\rangle &= \frac{1}{\sqrt{1+\varepsilon_1^2(B_z)}}\left(|F=2, m_F=0\rangle + \varepsilon_1(B_z)\,|F=1, m_F=0\rangle\right),\\
E_{g_4} &= -\frac{A_{2P_{3/2}}}{4} - g_j\mu_B B_z + \sqrt{A_{2P_{3/2}}^2 + \frac{A_{2P_{3/2}}}{2}\left(g_j\mu_B + g_I\mu_k\right)B_z + \frac{1}{4}\left(g_j\mu_B + g_I\mu_k\right)^2 B_z^2},\\
|g_4\rangle &= \frac{1}{\sqrt{1+\kappa_1^2(B_z)}}\left(|F=2, m_F=-1\rangle + \kappa_1(B_z)\,|F=1, m_F=-1\rangle\right),\\
E_{g_5} &= \frac{3A_{2P_{3/2}}}{4} - \frac{1}{2}\left(3g_j\mu_B - g_I\mu_k\right)B_z,\\
|g_5\rangle &= |F=2, m_F=-2\rangle,\\
E_{h_6} &= -\frac{A_{2P_{3/2}}}{4} + g_j\mu_B B_z - \sqrt{A_{2P_{3/2}}^2 - \frac{A_{2P_{3/2}}}{2}\left(g_j\mu_B + g_I\mu_k\right)B_z + \frac{1}{4}\left(g_j\mu_B + g_I\mu_k\right)^2 B_z^2},\\
|h_6\rangle &= \frac{1}{\sqrt{1+\chi_2^2(B_z)}}\left(\chi_2(B_z)\,|F=2, m_F=1\rangle + |F=1, m_F=1\rangle\right),\\
E_{h_7} &= -\frac{A_{2P_{3/2}}}{4} - \sqrt{A_{2P_{3/2}}^2 + \frac{1}{4}\left(g_j\mu_B + g_I\mu_k\right)^2 B_z^2},\\
|h_7\rangle &= \frac{1}{\sqrt{1+\varepsilon_2^2(B_z)}}\left(\varepsilon_2(B_z)\,|F=2, m_F=0\rangle + |F=1, m_F=0\rangle\right),\\
E_{h_8} &= -\frac{A_{2P_{3/2}}}{4} - g_j\mu_B B_z - \sqrt{A_{2P_{3/2}}^2 + \frac{A_{2P_{3/2}}}{2}\left(g_j\mu_B + g_I\mu_k\right)B_z + \frac{1}{4}\left(g_j\mu_B + g_I\mu_k\right)^2 B_z^2},\\
|h_8\rangle &= \frac{1}{\sqrt{1+\kappa_2^2(B_z)}}\left(\kappa_2(B_z)\,|F=2, m_F=-1\rangle + |F=1, m_F=-1\rangle\right)
\end{aligned}
\tag{3.18}
$$

with

$$
\chi_{1/2}(B_z) = \frac{\sqrt{3}}{4}\frac{\left(g_j\mu_B + g_I\mu_k\right)B_z}{\pm A_{2P_{3/2}} \mp \frac{1}{4}\left(g_j\mu_B + g_I\mu_k\right)B_z \pm \sqrt{A_{2P_{3/2}}^2 - \frac{A_{2P_{3/2}}}{2}\left(g_j\mu_B + g_I\mu_k\right)B_z + \frac{1}{4}\left(g_j\mu_B + g_I\mu_k\right)^2 B_z^2}},
$$

$$
\varepsilon_{1/2}(B_z) = \frac{1}{2}\frac{\left(g_j\mu_B + g_I\mu_k\right)B_z}{\pm A_{2P_{3/2}} \pm \sqrt{A_{2P_{3/2}}^2 + \frac{1}{4}\left(g_j\mu_B + g_I\mu_k\right)^2 B_z^2}}
$$

and

$$
\kappa_{1/2}(B_z) = \frac{\sqrt{3}}{4}\frac{\left(g_j\mu_B + g_I\mu_k\right)B_z}{\pm A_{2P_{3/2}} \pm \frac{1}{4}\left(g_j\mu_B + g_I\mu_k\right)B_z \pm \sqrt{A_{2P_{3/2}}^2 + \frac{A_{2P_{3/2}}}{2}\left(g_j\mu_B + g_I\mu_k\right)B_z + \frac{1}{4}\left(g_j\mu_B + g_I\mu_k\right)^2 B_z^2}}.
$$

The Tab. 3.1 summarizes all experimentally measured values of the parameters for the three relevant sets of hydrogen states. The value for the hyperfine splitting constant of the $2P_{3/2}$ set differs from the one stated in [125]. The reason is that the source quotes the entire energy splitting, e.g. $E_{HFS} = E_{g_1}|_{B=0} - E_{h_6}|_{B=0} = 2A_{2P_{3/2}}$. Moreover, the last column contains the different binding energies caused by the Lamb-shift as well as the fine splitting. As the gross energy level due

Table 3.1: The table contains all necessary values and parameters for the hydrogen states. Energy values are displayed in units of frequency as given in the original sources. The values were measured with much higher precision, resulting in uncertainties that are several orders of magnitude smaller. Thus, the uncertainties are omitted.

	g_j[a]	g_I	A [MHz][b]	τ	ΔE [MHz]
$2S_{1/2}$	2.002 [114]	5.586 [119]	177.57 [126]	$\frac{1}{8.23}$ s [127]	
$2P_{1/2}$	0.666	5.586 [119]	59.22 [128]	1.6 ns [129]	1057.84 [130][c]
$2P_{3/2}$	1.334	5.586 [119]	11.83 [125]	1.6 ns [129]	9912.2 [131][d]

a: Based on Ch. 2.4.2
b: Deviations of the values from the sources are explained in the text
c: Corresponds to the Lamb-shift
d: Corresponds to the fine splitting

to Ch. 2.1 is similar for all three sets, the relative zero energy is set at the binding energy of the metastable $2S_{1/2}$ set. The hyperfine splitting is excluded in this setting and will change the energy splitting accordingly. Consequently, the binding of the $2P_{1/2}$ set is increased, relative to the metastable $2S_{1/2}$ set, due to the Lamb-shift, while the fine splitting decreases the binding of the $2P_{3/2}$ set. Subsequently, the Breit-Rabi energies from Eq. (3.15), Eq. (3.16) and Eq. (3.18), in addition to the fine splitting and Lamb-shift, are displayed in Fig. 3.1a and Fig. 3.1b. The eigenenergies are presented as function of the homogenous external magnetic field $\vec{B} = B_z \hat{e}_z$. In Fig. 3.1a energy crossings between different sets are visible, while Fig. 3.1b dissolves the single Breit-Rabi states. The magnetic field value for which states are degenerated will be called Zeeman crossing. Thus, this expression refers only to specific magnetic field values and does not take the actual energy evolution for more complex Hamiltonians into account.

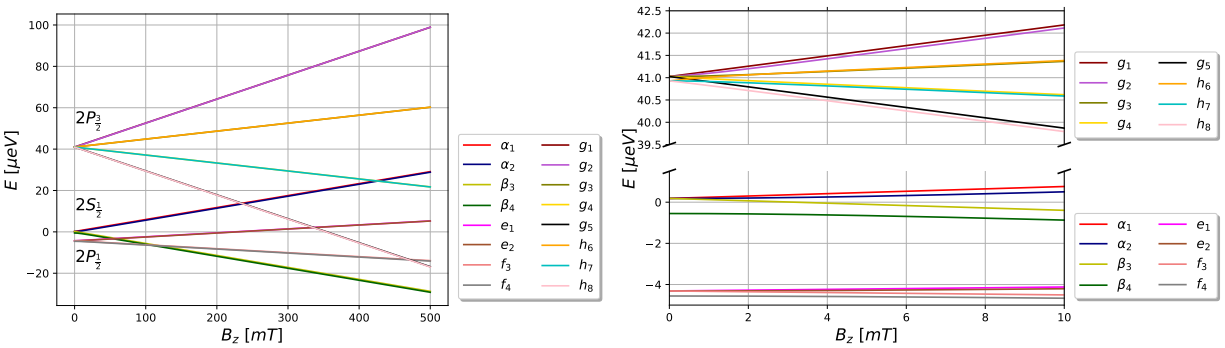

(a) (b)

Figure 3.1: The Breit-Rabi diagram for the excited hydrogen states with $n = 2$ is depicted. The vertical axis describes the binding energy of the single states as function of the external magnetic field given on the horizontal axis. The zero-energy is defined by the binding energy excluding the hyperfine splitting of the metastable $2S_{1/2}$ set at zero magnetic field flux. Consequently, the $2P_{1/2}$ set differs by the Lamb-shift while the fine splitting separates the $2P_{3/2}$ set from the metastable $2S_{1/2}$ hydrogen states. In Fig. 3.1a the evolution for large magnetic field fluxes is displayed while the eigenstates with the same electric quantum number m_j are better visible in Fig. 3.1b.

In the next step, the external electric field is included. A static homogenous external electric field of the form $\vec{E} = E_x \hat{e}_x$ is assumed, which couples the metastable $2S_{1/2}$ set with the two short-living $2P_{1/2}$ and $2P_{3/2}$ sets. The coupling in the $|n, l, m_l, s, m_s\rangle$ basis, based on Eq. (3.1), can be

expressed by

$$\begin{aligned}\langle n,l,m_l,s,m_s|e\vec{r}\cdot\vec{E}|\tilde{n},\tilde{l},\tilde{m}_l,\tilde{s},\tilde{m}_s\rangle &= e\int d^3r\,\Psi_{n,l,m_l}(\vec{r})\,\vec{r}\cdot\vec{E}\Psi_{\tilde{n},\tilde{l},\tilde{m}_l}(\vec{r})\otimes\langle\chi_{s,m_s}|\chi_{\tilde{s},\tilde{m}_s}\rangle \\ &= e\int d^3r\,\Psi_{n,l,m_l}(\vec{r})\,\vec{r}\cdot\vec{E}\Psi_{\tilde{n},\tilde{l},\tilde{m}_l}(\vec{r})\,\delta_{s,\tilde{s}}\delta_{m_s,\tilde{m}_s}.\end{aligned} \tag{3.19}$$

By following Sec. 2.4.1 the orbital part of the matrix element is deduced and the energy correction due to a field flux of $E_x = 10^3\,\mathrm{V/m}$ corresponds to a tiny energy correction of $\delta \approx 0.159\,\mu\mathrm{eV}$. Thus, this interaction leaves the Breit-Rabi basis nearly unperturbed, thereby leaving them still as a good set of eigenstates. Nevertheless, the coupling of the different sets affects the lifetimes of the excited states. In Sec. 2.4.4 the potential is introduced to model lifetimes. Consequently, it is necessary to solve the time independent eigensystem, including the Breit-Rabi Hamiltonian Eq. (2.113), the Stark potential Eq. (2.93) and the lifetime potential from Eq. (2.118), in the Breit-Rabi basis. The coupling constants for the Stark potential are introduced in the App. D. While the real part of the eigenvalues correspond to the new eigenenergies, which are nearly unchanged, the imaginary part equals to

$$\mathrm{Im}\,(\lambda_i) = -\frac{\hbar}{2T_i}, \tag{3.20}$$

with T_i being the new lifetime of the i-th state. Subsequently, the new lifetimes of the three sets of states are displayed in Fig. 3.2 for a static constant electric field flux of $E_x = 10^3\,\mathrm{V/m}$ and as function of the external magnetic field. As previously mentioned the coupling constant from the Stark effect is weak, which results in its stronger influence for decreasing energy difference between the coupled states. The coupling strengths are maximized at Zeeman crossings visible in Fig. 3.1a. Consequently, at these magnetic field values the corresponding lifetimes of the metastable states are heavily reduced and those of the short-living states slightly increased.

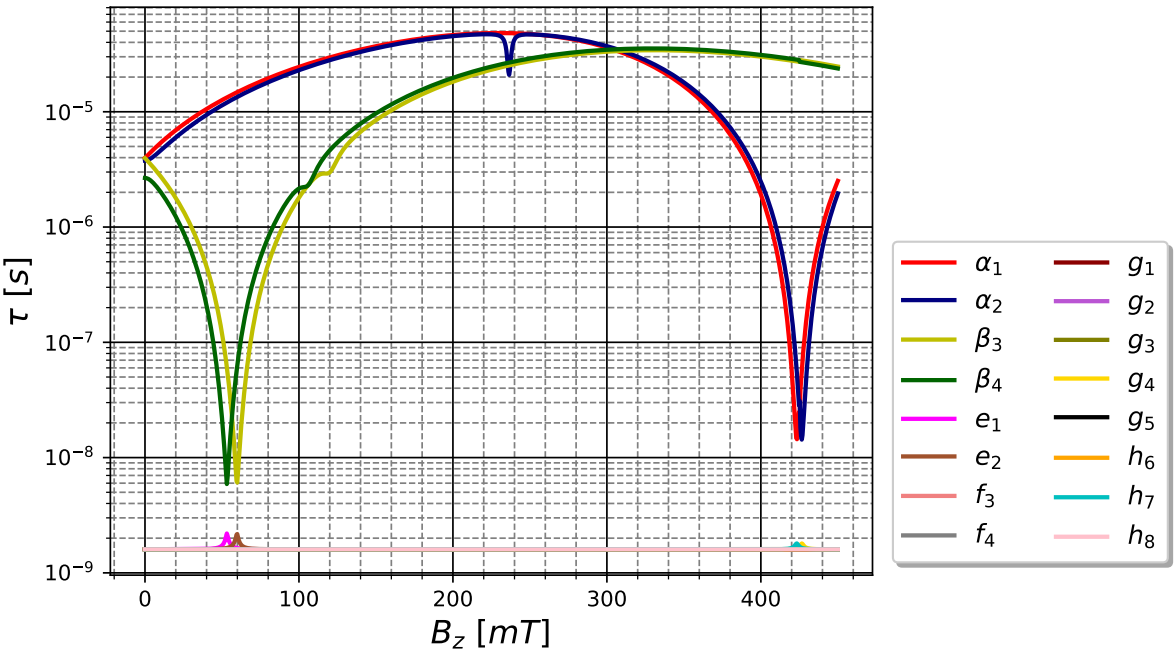

Figure 3.2: The evolution of the lifetimes of metastable hydrogen $2S_{1/2}$ as well as the short-living $2P_{1/2}$ and $2P_{3/2}$ states in the presence of an external electric field $\vec{E} = E_x\hat{e}_x$ and as function of a homogenous magnetic field $\vec{B} = B_z\hat{e}_z$ is displayed. The applied electric field flux is $E_x = 10^3\,\mathrm{V/m}$.

3.2 Deuterium

The deuterium atom is a stable hydrogen isotope carrying an additional neutron in its nucleus. Therefore, the deuteron is a spin 1 particle which differs from the normal hydrogen. Consequently, the binding energy, up to the hyperfine structure, is identical to that of hydrogen and is displayed in Sec. 3.1. Also here the metastable $2S_{1/2}$ as well as the short living $2P_{1/2}$ and $2P_{3/2}$ sets are relevant for the thesis. Subsequently, the vector space for the coupled representation of the metastable $2S_{1/2}$ set is stated as

$$\mathcal{D}_{I=1} \otimes \mathcal{D}_{s=1/2} = \mathcal{D}_{F=3/2} \otimes \mathcal{D}_{F=1/2}. \tag{3.21}$$

Moreover, the states are displayed as

$$\begin{aligned}
|F = 3/2, m_F = 3/2\rangle &= |m_s = 1/2, m_I = 1\rangle\,, \\
|F = 3/2, m_F = 1/2\rangle &= \frac{1}{\sqrt{3}}\,|m_s = -1/2, m_I = 1\rangle + \sqrt{\frac{2}{3}}\,|m_s = 1/2, m_I = 0\rangle\,, \\
|F = 3/2, m_F = -1/2\rangle &= \sqrt{\frac{2}{3}}\,|m_s = -1/2, m_I = 0\rangle + \frac{1}{\sqrt{3}}\,|m_s = 1/2, m_I = -1\rangle\,, \\
|F = 3/2, m_F = -3/2\rangle &= |m_s = -1/2, m_I = -1\rangle\,, \\
|F = 1/2, m_F = 1/2\rangle &= \sqrt{\frac{2}{3}}\,|m_s = -1/2, m_I = 1\rangle - \frac{1}{\sqrt{3}}\,|m_s = 1/2, m_I = 0\rangle\,, \\
|F = 1/2, m_F = -1/2\rangle &= \frac{1}{\sqrt{3}}\,|m_s = -1/2, m_I = 0\rangle - \sqrt{\frac{2}{3}}\,|m_s = 1/2, m_I = -1\rangle\,.
\end{aligned} \tag{3.22}$$

Analogously follows the $2P_{1/2}$ set

$$\mathcal{D}_{I=1} \otimes \mathcal{D}_{j=1/2} = \mathcal{D}_{F=3/2} \otimes \mathcal{D}_{F=1/2}, \tag{3.23}$$

with the corresponding six states

$$
\begin{aligned}
&|F = 3/2, m_F = 3/2\rangle = |m_j = 1/2, m_I = 1\rangle \\
&= \sqrt{\frac{2}{3}}\,|m_l = 1, m_s = -1/2, m_I = 1\rangle - \frac{1}{\sqrt{3}}\,|m_l = 0, m_s = 1/2, m_I = 1\rangle\,, \\
&|F = 3/2, m_F = 1/2\rangle = \frac{1}{\sqrt{3}}\,|m_j = -1/2, m_I = 1\rangle + \sqrt{\frac{2}{3}}\,|m_j = 1/2, m_I = 0\rangle \\
&= \frac{1}{\sqrt{3}}\left(\frac{1}{\sqrt{3}}\,|m_l = 0, m_s = -1/2, m_I = 1\rangle - \sqrt{\frac{2}{3}}\,|m_l = -1, m_s = 1/2, m_I = 1\rangle\right) \\
&+ \sqrt{\frac{2}{3}}\left(\sqrt{\frac{2}{3}}\,|m_l = 1, m_s = -1/2, m_I = 0\rangle - \frac{1}{\sqrt{3}}\,|m_l = 0, m_s = 1/2, m_I = 0\rangle\right), \\
&|F = 3/2, m_F = -1/2\rangle = \sqrt{\frac{2}{3}}\,|m_j = -1/2, m_I = 0\rangle + \frac{1}{\sqrt{3}}\,|m_j = 1/2, m_I = -1\rangle \\
&= \sqrt{\frac{2}{3}}\left(\frac{1}{\sqrt{3}}\,|m_l = 0, m_s = -1/2, m_I = 0\rangle - \sqrt{\frac{2}{3}}\,|m_l = -1, m_s = 1/2, m_I = 0\rangle\right) \\
&+ \frac{1}{\sqrt{3}}\left(\sqrt{\frac{2}{3}}\,|m_l = 1, m_s = -1/2, m_I = -1\rangle - \frac{1}{\sqrt{3}}\,|m_l = 0, m_s = 1/2, m_I = -1\rangle\right), \\
&|F = 3/2, m_F = -3/2\rangle = |m_j = -1/2, m_I = -1\rangle \\
&= \frac{1}{\sqrt{3}}\,|m_l = 0, m_s = -1/2, m_I = -1\rangle - \sqrt{\frac{2}{3}}\,|m_l = -1, m_s = 1/2, m_I = -1\rangle\,, \\
&|F = 1/2, m_F = 1/2\rangle = \sqrt{\frac{2}{3}}\,|m_j = -1/2, m_I = 1\rangle - \frac{1}{\sqrt{3}}\,|m_j = 1/2, m_I = 0\rangle \\
&= \sqrt{\frac{2}{3}}\left(\frac{1}{\sqrt{3}}\,|m_l = 0, m_s = -1/2, m_I = 1\rangle - \sqrt{\frac{2}{3}}\,|m_l = -1, m_s = 1/2, m_I = 1\rangle\right) \\
&- \frac{1}{\sqrt{3}}\left(\sqrt{\frac{2}{3}}\,|m_l = 1, m_s = -1/2, m_I = 0\rangle - \frac{1}{\sqrt{3}}\,|m_l = 0, m_s = 1/2, m_I = 0\rangle\right), \\
&|F = 1/2, m_F = -1/2\rangle = \frac{1}{\sqrt{3}}\,|m_j = -1/2, m_I = 0\rangle - \sqrt{\frac{2}{3}}\,|m_j = 1/2, m_I = -1\rangle \\
&= \frac{1}{\sqrt{3}}\left(\frac{1}{\sqrt{3}}\,|m_l = 0, m_s = -1/2, m_I = 0\rangle - \sqrt{\frac{2}{3}}\,|m_l = -1, m_s = 1/2, m_I = 0\rangle\right) \\
&- \sqrt{\frac{2}{3}}\left(\sqrt{\frac{2}{3}}\,|m_l = 1, m_s = -1/2, m_I = -1\rangle - \frac{1}{\sqrt{3}}\,|m_l = 0, m_s = 1/2, m_I = -1\rangle\right).
\end{aligned}
\tag{3.24}
$$

Finally, the system for the $2P_{3/2}$ set is expressed as

$$
\mathcal{D}_{I=1} \otimes \mathcal{D}_{j=3/2} = \mathcal{D}_{F=5/2} \otimes \mathcal{D}_{F=3/2} \otimes \mathcal{D}_{F=1/2}, \tag{3.25}
$$

with the set of states

$$
\begin{aligned}
&|F = {}^5\!/_2, m_F = {}^5\!/_2\rangle = |m_j = {}^3\!/_2, m_I = 1\rangle = |m_l = 1, m_s = {}^1\!/_2, m_I = 1\rangle\,,\\
&|F = {}^5\!/_2, m_F = {}^3\!/_2\rangle = \sqrt{\frac{2}{5}}\,|m_j = {}^3\!/_2, m_I = 0\rangle + \sqrt{\frac{3}{5}}\,|m_j = {}^1\!/_2, m_I = 1\rangle\\
&= \sqrt{\frac{2}{5}}\,|m_l = 1, m_s = {}^1\!/_2, m_I = 0\rangle\\
&+ \sqrt{\frac{3}{5}}\left(\frac{1}{\sqrt{3}}\,|m_l = 1, m_s = -{}^1\!/_2, m_I = 1\rangle + \sqrt{\frac{2}{3}}\,|m_l = 0, m_s = {}^1\!/_2, m_I = 1\rangle\right),\\
&|F = {}^5\!/_2, m_F = {}^1\!/_2\rangle\\
&= \frac{1}{\sqrt{10}}\,|m_j = {}^3\!/_2, m_I = -1\rangle + \sqrt{\frac{3}{5}}\,|m_j = {}^1\!/_2, m_I = 0\rangle + \sqrt{\frac{3}{10}}\,|m_j = -{}^1\!/_2, m_I = 1\rangle\\
&= \frac{1}{\sqrt{10}}\,|m_l = 1, m_s = {}^1\!/_2, m_I = -1\rangle\\
&+ \sqrt{\frac{3}{5}}\left(\frac{1}{\sqrt{3}}\,|m_l = 1, m_s = -{}^1\!/_2, m_I = 0\rangle + \sqrt{\frac{2}{3}}\,|m_l = 0, m_s = {}^1\!/_2, m_I = 0\rangle\right)\\
&+ \sqrt{\frac{3}{10}}\left(\sqrt{\frac{2}{3}}\,|m_l = 0, m_s = -{}^1\!/_2, m_I = 1\rangle + \frac{1}{\sqrt{3}}\,|m_l = -1, m_s = {}^1\!/_2, m_I = 1\rangle\right),\\
&|F = {}^5\!/_2, m_F = -{}^1\!/_2\rangle\\
&= \sqrt{\frac{3}{10}}\,|m_j = {}^1\!/_2, m_I = -1\rangle + \sqrt{\frac{3}{5}}\,|m_j = -{}^1\!/_2, m_I = 0\rangle + \frac{1}{\sqrt{10}}\,|m_j = -{}^3\!/_2, m_I = 1\rangle\\
&= \sqrt{\frac{3}{10}}\left(\frac{1}{\sqrt{3}}\,|m_l = 1, m_s = -{}^1\!/_2, m_I = -1\rangle + \sqrt{\frac{2}{3}}\,|m_l = 0, m_s = {}^1\!/_2, m_I = -1\rangle\right)\\
&+ \sqrt{\frac{3}{5}}\left(\sqrt{\frac{2}{3}}\,|m_l = 0, m_s = -{}^1\!/_2, m_I = 0\rangle + \frac{1}{\sqrt{3}}\,|m_l = -1, m_s = {}^1\!/_2, m_I = 0\rangle\right)\\
&+ \frac{1}{\sqrt{10}}\,|m_l = -1, m_s = -{}^1\!/_2, m_I = 1\rangle\,,\\
&|F = {}^5\!/_2, m_F = -{}^3\!/_2\rangle = \sqrt{\frac{3}{5}}\,|m_j = -{}^1\!/_2, m_I = -1\rangle + \sqrt{\frac{2}{5}}\,|m_j = -{}^3\!/_2, m_I = 0\rangle\\
&= \sqrt{\frac{3}{5}}\left(\sqrt{\frac{2}{3}}\,|m_l = 0, m_s = -{}^1\!/_2, m_I = -1\rangle + \frac{1}{\sqrt{3}}\,|m_l = -1, m_s = {}^1\!/_2, m_I = -1\rangle\right)\\
&+ \sqrt{\frac{2}{5}}\,|m_l = -1, m_s = -{}^1\!/_2, m_I = 0\rangle\,,\\
&|F = {}^5\!/_2, m_F = -{}^5\!/_2\rangle = |m_j = -{}^3\!/_2, m_I = -1\rangle = |m_l = -1, m_s = -{}^1\!/_2, m_I = -1\rangle\,,\\
&|F = {}^3\!/_2, m_F = {}^3\!/_2\rangle = \sqrt{\frac{3}{5}}\,|m_j = {}^3\!/_2, m_I = 0\rangle - \sqrt{\frac{2}{5}}\,|m_j = {}^1\!/_2, m_I = 1\rangle\\
&= \sqrt{\frac{3}{5}}\,|m_l = 1, m_s = {}^1\!/_2, m_I = 0\rangle\\
&- \sqrt{\frac{2}{5}}\left(\frac{1}{\sqrt{3}}\,|m_l = 1, m_s = -{}^1\!/_2, m_I = 1\rangle + \sqrt{\frac{2}{3}}\,|m_l = 0, m_s = {}^1\!/_2, m_I = 1\rangle\right),\\
&|F = {}^3\!/_2, m_F = {}^1\!/_2\rangle\\
&= \sqrt{\frac{2}{5}}\,|m_j = {}^3\!/_2, m_I = -1\rangle + \frac{1}{\sqrt{15}}\,|m_j = {}^1\!/_2, m_I = 0\rangle - \sqrt{\frac{8}{15}}\,|m_j = -{}^1\!/_2, m_I = 1\rangle
\end{aligned}
\tag{3.26}
$$

$$
\begin{aligned}
&= \sqrt{\frac{2}{5}}\,|m_l = 1, m_s = {}^1\!/_2, m_I = -1\rangle \\
&+ \frac{1}{\sqrt{15}}\left(\frac{1}{\sqrt{3}}\,|m_l = 1, m_s = -{}^1\!/_2, m_I = 0\rangle + \sqrt{\frac{2}{3}}\,|m_l = 0, m_s = {}^1\!/_2, m_I = 0\rangle\right) \\
&- \sqrt{\frac{8}{15}}\left(\sqrt{\frac{2}{3}}\,|m_l = 0, m_s = -{}^1\!/_2, m_I = 1\rangle + \frac{1}{\sqrt{3}}\,|m_l = -1, m_s = {}^1\!/_2, m_I = 1\rangle\right), \\
&|F = {}^3\!/_2, m_F = -{}^1\!/_2\rangle \\
&= \sqrt{\frac{8}{15}}\,|m_j = {}^1\!/_2, m_I = -1\rangle - \frac{1}{\sqrt{15}}\,|m_j = -{}^1\!/_2, m_I = 0\rangle - \sqrt{\frac{2}{5}}\,|m_j = -{}^3\!/_2, m_I = 1\rangle \\
&= \sqrt{\frac{8}{15}}\left(\frac{1}{\sqrt{3}}\,|m_l = 1, m_s = -{}^1\!/_2, m_I = -1\rangle + \sqrt{\frac{2}{3}}\,|m_l = 0, m_s = {}^1\!/_2, m_I = -1\rangle\right) \\
&- \frac{1}{\sqrt{15}}\left(\sqrt{\frac{2}{3}}\,|m_l = 0, m_s = -{}^1\!/_2, m_I = 0\rangle + \frac{1}{\sqrt{3}}\,|m_l = -1, m_s = {}^1\!/_2, m_I = 0\rangle\right) \\
&- \sqrt{\frac{2}{5}}\,|m_l = -1, m_s = -{}^1\!/_2, m_I = 1\rangle\,, \\
&|F = {}^3\!/_2, m_F = -{}^3\!/_2\rangle = \sqrt{\frac{2}{5}}\,|m_j = -{}^1\!/_2, m_I = -1\rangle - \sqrt{\frac{3}{5}}\,|m_j = -{}^3\!/_2, m_I = 0\rangle \\
&= \sqrt{\frac{2}{5}}\left(\sqrt{\frac{2}{3}}\,|m_l = 0, m_s = -{}^1\!/_2, m_I = -1\rangle + \frac{1}{\sqrt{3}}\,|m_l = -1, m_s = {}^1\!/_2, m_I = -1\rangle\right) \\
&- \sqrt{\frac{3}{5}}\,|m_l = -1, m_s = -{}^1\!/_2, m_I = 0\rangle\,, \\
&|F = {}^1\!/_2, m_F = {}^1\!/_2\rangle \\
&= \frac{1}{\sqrt{2}}\,|m_j = {}^3\!/_2, m_I = -1\rangle - \frac{1}{\sqrt{3}}\,|m_j = {}^1\!/_2, m_I = 0\rangle + \frac{1}{\sqrt{6}}\,|m_j = -{}^1\!/_2, m_I = 1\rangle \\
&= \frac{1}{\sqrt{2}}\,|m_l = 1, m_s = {}^1\!/_2, m_I = -1\rangle \\
&- \frac{1}{\sqrt{3}}\left(\frac{1}{\sqrt{3}}\,|m_l = 1, m_s = -{}^1\!/_2, m_I = 0\rangle + \sqrt{\frac{2}{3}}\,|m_l = 0, m_s = {}^1\!/_2, m_I = 0\rangle\right) \\
&+ \frac{1}{\sqrt{6}}\left(\sqrt{\frac{2}{3}}\,|m_l = 0, m_s = -{}^1\!/_2, m_I = 1\rangle + \frac{1}{\sqrt{3}}\,|m_l = -1, m_s = {}^1\!/_2, m_I = 1\rangle\right), \\
&|F = {}^1\!/_2, m_F = -{}^1\!/_2\rangle \\
&= \frac{1}{\sqrt{6}}\,|m_j = {}^1\!/_2, m_I = -1\rangle - \frac{1}{\sqrt{3}}\,|m_j = -{}^1\!/_2, m_I = 0\rangle + \frac{1}{\sqrt{2}}\,|m_j = -{}^3\!/_2, m_I = 1\rangle \\
&= \frac{1}{\sqrt{6}}\left(\frac{1}{\sqrt{3}}\,|m_l = 1, m_s = -{}^1\!/_2, m_I = -1\rangle + \sqrt{\frac{2}{3}}\,|m_l = 0, m_s = {}^1\!/_2, m_I = -1\rangle\right) \\
&- \frac{1}{\sqrt{3}}\left(\sqrt{\frac{2}{3}}\,|m_l = 0, m_s = -{}^1\!/_2, m_I = 0\rangle + \frac{1}{\sqrt{3}}\,|m_l = -1, m_s = {}^1\!/_2, m_I = 0\rangle\right) \\
&+ \frac{1}{\sqrt{2}}\,|m_l = -1, m_s = -{}^1\!/_2, m_I = 1\rangle\,.
\end{aligned}
$$

In the next step the Breit-Rabi system of the metastable $2S_{1/2}$ set based on Sec. 2.4.3 is investigated. The eigenproblem of the Breit-Rabi Hamiltonian H_{BR} from Eq. (2.113) can be split into

four independent linear systems

$$
\begin{aligned}
&\langle F = 3/2, m_F = 3/2|H_{BR}|F = 3/2, m_F = 3/2\rangle = \frac{A_{2S_{1/2}}}{2} + \left(\frac{1}{2}g_s\mu_B - g_I\mu_k\right)B_z,\\
&\qquad\qquad\qquad |F = 3/2, m_F = 1/2\rangle \qquad\qquad |F = 1/2, m_F = 1/2\rangle\\
&H_{BR} = \begin{matrix}\langle F=3/2, m_F=1/2|\\ \langle F=1/2, m_F=1/2|\end{matrix}\begin{pmatrix} \frac{A_{2S_{1/2}}}{2} + \frac{1}{3}\left(\frac{1}{2}g_s\mu_B - g_I\mu_k\right)B_z & -\frac{\sqrt{2}}{3}\left(g_s\mu_B + g_I\mu_k\right)B_z \\ -\frac{\sqrt{2}}{3}\left(g_s\mu_B + g_I\mu_k\right)B_z & -A_{2S_{1/2}} - \frac{1}{3}\left(\frac{1}{2}g_s\mu_B + 2g_I\mu_k\right)B_z \end{pmatrix},\\
&\qquad\qquad\qquad |F = 3/2, m_F = -1/2\rangle \qquad\qquad |F = 1/2, m_F = -1/2\rangle\\
&H_{BR} = \begin{matrix}\langle F=3/2, m_F=-1/2|\\ \langle F=1/2, m_F=-1/2|\end{matrix}\begin{pmatrix} \frac{A_{2S_{1/2}}}{2} - \frac{1}{3}\left(\frac{1}{2}g_s\mu_B - g_I\mu_k\right)B_z & -\frac{\sqrt{2}}{3}\left(g_s\mu_B + g_I\mu_k\right)B_z \\ -\frac{\sqrt{2}}{3}\left(g_s\mu_B + g_I\mu_k\right)B_z & -A_{2S_{1/2}} + \frac{1}{3}\left(\frac{1}{2}g_s\mu_B + 2g_I\mu_k\right)B_z \end{pmatrix},\\
&\langle F = 3/2, m_F = -3/2|H_{BR}|F = 3/2, m_F = -3/2\rangle = \frac{A_{2S_{1/2}}}{2} - \left(\frac{1}{2}g_s\mu_B - g_I\mu_k\right)B_z.
\end{aligned}
\tag{3.27}
$$

The corresponding eigensystem is defined by

$$
\begin{aligned}
&E_{\alpha_1} = \frac{A_{2S_{1/2}}}{2} + \left(\frac{1}{2}g_s\mu_B - g_I\mu_k\right)B_z,\\
&|\alpha_1\rangle = |F = 3/2, m_F = 3/2\rangle,\\
&E_{\alpha_2} = -\frac{A_{2S_{1/2}}}{4} - \frac{1}{2}g_I\mu_k B_z + \sqrt{\frac{A_{2S_{1/2}}^2}{2} + \left(\frac{A_{2S_{1/2}}}{4} + \frac{1}{2}\left(g_s\mu_B + g_I\mu_k\right)B_z\right)^2},\\
&|\alpha_2\rangle = \frac{1}{\sqrt{1+\gamma_1^2(B_z)}}\left(\gamma_1(B_z)\,|F = 1/2, m_F = 1/2\rangle + |F = 3/2, m_F = 1/2\rangle\right),\\
&E_{\alpha_3} = -\frac{A_{2S_{1/2}}}{4} + \frac{1}{2}g_I\mu_k B_z + \sqrt{\frac{A_{2S_{1/2}}^2}{2} + \left(\frac{A_{2S_{1/2}}}{4} - \frac{1}{2}\left(g_s\mu_B + g_I\mu_k\right)B_z\right)^2},\\
&|\alpha_3\rangle = \frac{1}{\sqrt{1+\Gamma_1^2(B_z)}}\left(\Gamma_1(B_z)\,|F = 1/2, m_F = -1/2\rangle + |F = 3/2, m_F = -1/2\rangle\right),\\
&E_{\beta_4} = \frac{A_{2S_{1/2}}}{2} - \left(\frac{1}{2}g_s\mu_B - g_I\mu_k\right)B_z,\\
&|\beta_4\rangle = |F = 3/2, m_F = -3/2\rangle,\\
&E_{\beta_5} = -\frac{A_{2S_{1/2}}}{4} + \frac{1}{2}g_I\mu_k B_z - \sqrt{\frac{A_{2S_{1/2}}^2}{2} + \left(\frac{A_{2S_{1/2}}}{4} - \frac{1}{2}\left(g_s\mu_B + g_I\mu_k\right)B_z\right)^2},\\
&|\beta_5\rangle = \frac{1}{\sqrt{1+\Gamma_2^2(B_z)}}\left(|F = 1/2, m_F = -1/2\rangle + \Gamma_2(B_z)\,|F = 3/2, m_F = -1/2\rangle\right),\\
&E_{\beta_6} = -\frac{A_{2S_{1/2}}}{4} - \frac{1}{2}g_I\mu_k B_z - \sqrt{\frac{A_{2S_{1/2}}^2}{2} + \left(\frac{A_{2S_{1/2}}}{4} + \frac{1}{2}\left(g_s\mu_B + g_I\mu_k\right)B_z\right)^2},\\
&|\beta_6\rangle = \frac{1}{\sqrt{1+\gamma_2^2(B_z)}}\left(|F = 1/2, m_F = 1/2\rangle + \gamma_2(B_z)\,|F = 3/2, m_F = 1/2\rangle\right)
\end{aligned}
\tag{3.28}
$$

$$
\text{with}\quad \gamma_{1/2}(B_z) = \mp\frac{\sqrt{2}}{3}\frac{\left(g_s\mu_B + g_I\mu_k\right)B_z}{\frac{3A_{2S_{1/2}}}{4} + \frac{1}{6}\left(g_s\mu_B + g_I\mu_k\right)B_z + \sqrt{\frac{A_{2S_{1/2}}^2}{2} + \left(\frac{A_{2S_{1/2}}}{4} + \frac{1}{2}\left(g_s\mu_B + g_I\mu_k\right)B_z\right)^2}}
$$

$$
\text{and}\quad \Gamma_{1/2}(B_z) = \mp\frac{\sqrt{2}}{3}\frac{\left(g_s\mu_B + g_I\mu_k\right)B_z}{\frac{3A_{2S_{1/2}}}{4} - \frac{1}{6}\left(g_s\mu_B + g_I\mu_k\right)B_z + \sqrt{\frac{A_{2S_{1/2}}^2}{2} + \left(\frac{A_{2S_{1/2}}}{4} - \frac{1}{2}\left(g_s\mu_B + g_I\mu_k\right)B_z\right)^2}}.
$$

Analogously the Breit-Rabi system for the $2P_{1/2}$ set is presented as follows

$$
\begin{aligned}
E_{e_1} &= \frac{A_{2P_{1/2}}}{2} + \left(\frac{1}{2} g_j \mu_B - g_I \mu_k\right) B_z, \\
|e_1\rangle &= |F = 3/2, m_F = 3/2\rangle\,, \\
E_{e_2} &= -\frac{A_{2P_{1/2}}}{4} - \frac{1}{2} g_I \mu_k B_z + \sqrt{\frac{A_{2P_{1/2}}^2}{2} + \left(\frac{A_{2P_{1/2}}}{4} + \frac{1}{2}\left(g_j \mu_B + g_I \mu_k\right) B_z\right)^2}, \\
|e_2\rangle &= \frac{1}{\sqrt{1 + \tilde{\gamma}_1^2(B_z)}} \left(\tilde{\gamma}_1(B_z)\,|F = 1/2, m_F = 1/2\rangle + |F = 3/2, m_F = 1/2\rangle\right), \\
E_{e_3} &= -\frac{A_{2P_{1/2}}}{4} + \frac{1}{2} g_I \mu_k B_z + \sqrt{\frac{A_{2P_{1/2}}^2}{2} + \left(\frac{A_{2P_{1/2}}}{4} - \frac{1}{2}\left(g_j \mu_B + g_I \mu_k\right) B_z\right)^2}, \\
|e_3\rangle &= \frac{1}{\sqrt{1 + \tilde{\Gamma}_1^2(B_z)}} \left(\tilde{\Gamma}_1(B_z)\,|F = 1/2, m_F = -1/2\rangle + |F = 3/2, m_F = -1/2\rangle\right), \\
E_{f_4} &= \frac{A_{2P_{1/2}}}{2} - \left(\frac{1}{2} g_j \mu_B - g_I \mu_k\right) B_z, \\
|f_4\rangle &= |F = 3/2, m_F = -3/2\rangle\,, \\
E_{f_5} &= -\frac{A_{2P_{1/2}}}{4} + \frac{1}{2} g_I \mu_k B_z - \sqrt{\frac{A_{2P_{1/2}}^2}{2} + \left(\frac{A_{2P_{1/2}}}{4} - \frac{1}{2}\left(g_j \mu_B + g_I \mu_k\right) B_z\right)^2}, \\
|f_5\rangle &= \frac{1}{\sqrt{1 + \tilde{\Gamma}_2^2(B_z)}} \left(|F = 1/2, m_F = -1/2\rangle + \tilde{\Gamma}_2(B_z)\,|F = 3/2, m_F = -1/2\rangle\right), \\
E_{f_6} &= -\frac{A_{2P_{1/2}}}{4} - \frac{1}{2} g_I \mu_k B_z - \sqrt{\frac{A_{2P_{1/2}}^2}{2} + \left(\frac{A_{2P_{1/2}}}{4} + \frac{1}{2}\left(g_j \mu_B + g_I \mu_k\right) B_z\right)^2}, \\
|f_6\rangle &= \frac{1}{\sqrt{1 + \tilde{\gamma}_2^2(B_z)}} \left(|F = 1/2, m_F = 1/2\rangle + \tilde{\gamma}_2(B_z)\,|F = 3/2, m_F = 1/2\rangle\right)
\end{aligned}
\tag{3.29}
$$

with $\tilde{\gamma}_{1/2}(B_z) = \mp\frac{\sqrt{2}}{3} \dfrac{\left(g_j \mu_B + g_I \mu_k\right) B_z}{\frac{3A_{2P_{1/2}}}{4} + \frac{1}{6}\left(g_j \mu_B + g_I \mu_k\right) B_z + \sqrt{\frac{A_{2P_{1/2}}^2}{2} + \left(\frac{A_{2P_{1/2}}}{4} + \frac{1}{2}\left(g_j \mu_B + g_I \mu_k\right) B_z\right)^2}}$

and $\tilde{\Gamma}_{1/2}(B_z) = \mp\frac{\sqrt{2}}{3} \dfrac{\left(g_j \mu_B + g_I \mu_k\right) B_z}{\frac{3A_{2P_{1/2}}}{4} - \frac{1}{6}\left(g_j \mu_B + g_I \mu_k\right) B_z + \sqrt{\frac{A_{2P_{1/2}}^2}{2} + \left(\frac{A_{2P_{1/2}}}{4} - \frac{1}{2}\left(g_j \mu_B + g_I \mu_k\right) B_z\right)^2}}$.

Subsequently, the Hamiltonian H_{BR} from Eq. (2.113) can be split into six independent linear systems for the $2P_{3/2}$ set

$$\langle F = 5/2, m_F = 5/2|H_{BR}|F = 5/2, m_F = 5/2\rangle = \frac{3A_{2P_{3/2}}}{2} + \left(\frac{3}{2}g_j\mu_B - g_I\mu_k\right)B_z,$$

$$H_{BR} = \begin{matrix} \\ \langle F=5/2,m_F=3/2| \\ \langle F=3/2,m_F=3/2| \end{matrix} \begin{matrix} |F = 5/2, m_F = 3/2\rangle & |F = 3/2, m_F = 3/2\rangle \\ \end{matrix} \begin{pmatrix} \frac{3A_{2P_{3/2}}}{2} + \frac{3}{5}\left(\frac{3}{2}g_j\mu_B - g_I\mu_k\right)B_z & \frac{\sqrt{6}}{5}\left(g_j\mu_B + g_I\mu_k\right)B_z \\ \frac{\sqrt{6}}{5}\left(g_j\mu_B + g_I\mu_k\right)B_z & -A_{2P_{3/2}} + \left(\frac{11}{10}g_j\mu_B - \frac{2}{5}g_I\mu_k\right)B_z \end{pmatrix},$$

$$H_{BR} = \begin{matrix} \\ \langle F=5/2,m_F=1/2| \\ \langle F=3/2,m_F=1/2| \\ \langle F=1/2,m_F=1/2| \end{matrix} \begin{matrix} |F=5/2,m_F=1/2\rangle & |F=3/2,m_F=1/2\rangle & |F=1/2,m_F=1/2\rangle \\ \end{matrix} \begin{pmatrix} \frac{3A}{2}+\frac{1}{5}\left(\frac{3}{2}g_j\mu_B-g_I\mu_k\right)B_z & \frac{3}{5}(g_j\mu_B+g_I\mu_k)B_z & 0 \\ \frac{3}{5}(g_j\mu_B+g_I\mu_k)B_z & -A+\left(\frac{11}{30}g_j\mu_B-\frac{2}{15}g_I\mu_k\right)B_z & \frac{\sqrt{5}}{3}(g_j\mu_B+g_I\mu_k)B_z \\ 0 & \frac{\sqrt{5}}{3}(g_j\mu_B+g_I\mu_k)B_z & -\frac{5A}{2}+\left(\frac{5}{6}g_j\mu_B+\frac{1}{3}g_I\mu_k\right)B_z \end{pmatrix},$$

$$H_{BR} = \begin{matrix} \\ \langle F=5/2,m_F=-1/2| \\ \langle F=3/2,m_F=-1/2| \\ \langle F=1/2,m_F=-1/2| \end{matrix} \begin{matrix} |F=5/2,m_F=-1/2\rangle & |F=3/2,m_F=-1/2\rangle & |F=1/2,m_F=-1/2\rangle \\ \end{matrix} \begin{pmatrix} \frac{3A}{2}-\frac{1}{5}\left(\frac{3}{2}g_j\mu_B-g_I\mu_k\right)B_z & \frac{3}{5}(g_j\mu_B+g_I\mu_k)B_z & 0 \\ \frac{3}{5}(g_j\mu_B+g_I\mu_k)B_z & -A-\left(\frac{11}{30}g_j\mu_B-\frac{2}{15}g_I\mu_k\right)B_z & \frac{\sqrt{5}}{3}(g_j\mu_B+g_I\mu_k)B_z \\ 0 & \frac{\sqrt{5}}{3}(g_j\mu_B+g_I\mu_k)B_z & -\frac{5A}{2}-\left(\frac{5}{6}g_j\mu_B+\frac{1}{3}g_I\mu_k\right)B_z \end{pmatrix}, \tag{3.30}$$

$$H_{BR} = \begin{matrix} \\ \langle F=5/2,m_F=-3/2| \\ \langle F=3/2,m_F=-3/2| \end{matrix} \begin{matrix} |F = 5/2, m_F = -3/2\rangle & |F = 3/2, m_F = -3/2\rangle \\ \end{matrix} \begin{pmatrix} \frac{3A_{2P_{3/2}}}{2} - \frac{3}{5}\left(\frac{3}{2}g_j\mu_B - g_I\mu_k\right)B_z & \frac{\sqrt{6}}{5}\left(g_j\mu_B + g_I\mu_k\right)B_z \\ \frac{\sqrt{6}}{5}\left(g_j\mu_B + g_I\mu_k\right)B_z & -A_{2P_{3/2}} - \left(\frac{11}{10}g_j\mu_B - \frac{2}{5}g_I\mu_k\right)B_z \end{pmatrix},$$

$$\langle F = 5/2, m_F = -5/2|H_{BR}|F = 5/2, m_F = -5/2\rangle = \frac{3A_{2P_{3/2}}}{2} - \left(\frac{3}{2}g_j\mu_B - g_I\mu_k\right)B_z.$$

Finally, the $2P_{3/2}$ set can be expressed as

$$
\begin{aligned}
E_{g_1} &= \frac{3A_{2P_{3/2}}}{2} + \left(\frac{3}{2}g_j\mu_B - g_I\mu_k\right)B_z, \\
|g_1\rangle &= |F = 5/2, m_F = 5/2\rangle\,, \\
E_{g_2} &= \frac{A_{2P_{3/2}}}{4} + g_j\mu_B B_z - \frac{1}{2}g_I\mu_k B_z \\
&\quad + \sqrt{\frac{1}{4}\left(g_j\mu_B + g_I\mu_k\right)^2 B_z^2 - \frac{A_{2P_{3/2}}}{4}\left(g_j\mu_B + g_I\mu_k\right)B_z + \frac{25}{16}A_{2P_{3/2}}^2}, \\
|g_2\rangle &= \frac{1}{\sqrt{1+\theta_1^2(B_z)}}\left(|F = 5/2, m_F = 3/2\rangle + \theta_1(B_z)\,|F = 3/2, m_F = 3/2\rangle\right), \\
E_{g_3} &= \frac{1}{30}\Bigg[-20A_{2P_{3/2}} + 15g_j\mu_B B_z \\
&\quad + \frac{245A_{2P_{3/2}}^2 - 60A_{2P_{3/2}}(g_j\mu_B + g_I\mu_k)B_z + 60\left(g_j\mu_B + g_I\mu_k\right)^2 B_z^2}{C^{1/3}} + 5C^{1/3}\Bigg], \\
|g_3\rangle &= \frac{1}{\sqrt{1+\alpha_1^2(B_z)+\beta_1^2(B_z)}}\left(|F = 5/2, m_F = 1/2\rangle\right. \\
&\quad \left.+\alpha_1(B_z)\,|F = 3/2, m_F = 1/2\rangle + \beta_1(B_z)\,|F = 1/2, m_F = 1/2\rangle\right), \\
E_{g_4} &= \frac{1}{30}\Bigg[-5\left(4A_{2P_{3/2}} + 3g_j\mu_B B_z\right) \\
&\quad + \frac{245A_{2P_{3/2}}^2 + 60A_{2P_{3/2}}\left(g_j\mu_B + g_I\mu_k\right)B_z + 60\left(g_j\mu_B + g_I\mu_k\right)^2 B_z^2}{\tilde{C}^{1/3}} + 5\tilde{C}^{1/3}\Bigg], \\
|g_4\rangle &= \frac{1}{\sqrt{1+\tilde{\alpha}_1^2(B_z)+\tilde{\beta}_1^2(B_z)}}\left(|5/2, m_F = -1/2\rangle\right. \\
&\quad \left.+\tilde{\alpha}_1(B_z)\,|F = 3/2, m_F = -1/2\rangle + \tilde{\beta}_1(B_z)\,|F = 1/2, m_F = -1/2\rangle\right), \\
E_{g_5} &= \frac{A_{2P_{3/2}}}{4} - g_j\mu_B B_z + \frac{1}{2}g_I\mu_k B_z \\
&\quad + \sqrt{\frac{1}{4}\left(g_j\mu_B + g_I\mu_k\right)^2 B_z^2 + \frac{A_{2P_{3/2}}}{4}\left(g_j\mu_B + g_I\mu_k\right)B_z + \frac{25}{16}A_{2P_{3/2}}^2}, \\
|g_5\rangle &= \frac{1}{1+\phi_1^2(B_z)}\left(|F = 5/2, m_F = -3/2\rangle + \phi_1(B_z)\,|F = 3/2, m_F = -3/2\rangle\right), \\
E_{g_6} &= \frac{3A_{2P_{3/2}}}{2} - \left(\frac{3}{2}g_j\mu_B - g_I\mu_k\right)B_z, \\
|g_6\rangle &= |F = 5/2, m_F = -5/2\rangle\,, \\
E_{h_7} &= \frac{A_{2P_{3/2}}}{4} + g_j\mu_B B_z - \frac{1}{2}g_I\mu_k B_z \\
&\quad - \sqrt{\frac{1}{4}\left(g_j\mu_B + g_I\mu_k\right)^2 B_z^2 - \frac{A_{2P_{3/2}}}{4}\left(g_j\mu_B + g_I\mu_k\right)B_z + \frac{25}{16}A_{2P_{3/2}}^2}, \\
|h_7\rangle &= \frac{1}{\sqrt{1+\theta_2^2(B_z)}}\left(\theta_2(B_z)\,|F = 5/2, m_F = 3/2\rangle + |F = 3/2, m_F = 3/2\rangle\right), \\
E_{h_8} &= \frac{1}{12}\Bigg[-8A_{2P_{3/2}} + 6g_j\mu_B B_z + i\left(i - \sqrt{3}\right)C^{1/3} \\
&\quad + \frac{i\left(i+\sqrt{3}\right)\left(49A_{2P_{3/2}}^2 - 12A_{2P_{3/2}}(g_j\mu_B + g_I\mu_k)B_z + 12\left(g_j\mu_B + g_I\mu_k\right)^2 B_z^2\right)}{C^{1/3}}\Bigg],
\end{aligned}
\tag{3.31}
$$

$$
\begin{aligned}
|h_8\rangle &= \frac{1}{\sqrt{1+\alpha_3^2(B_z)+\beta_3^2(B_z)}}\left(\alpha_3(B_z)\,|F=5/2,m_F=1/2\rangle\right.\\
&\left.+\,|F=3/2,m_F=1/2\rangle+\beta_3(B_z)\,|F=1/2,m_F=1/2\rangle\right),\\
E_{h_9} &= \frac{1}{30}\left[-5\left(4A_{2P_{3/2}}+3g_j\mu_B B_z\right)-\frac{5}{2}i\left(-i+\sqrt{3}\right)\tilde{C}^{1/3}\right.\\
&\left.+\frac{5i\left(i+\sqrt{3}\right)\left(49A_{2P_{3/2}}^2+12A_{2P_{3/2}}\left(g_j\mu_B+g_I\mu_k\right)B_z+12\left(g_j\mu_B+g_I\mu_k\right)^2B_z^2\right)}{2\tilde{C}^{1/3}}\right],\\
|h_9\rangle &= \frac{1}{\sqrt{1+\tilde{\alpha}_3^2(B_z)+\tilde{\beta}_3^2(B_z)}}\left(\tilde{\alpha}_3(B_z)\,|F=5/2,m_F=-1/2\rangle\right.\\
&\left.+\,|F=3/2,m_F=-1/2\rangle+\tilde{\beta}_3(B_z)\,|F=1/2,m_F=-1/2\rangle\right),\\
E_{h_{10}} &= \frac{A_{2P_{3/2}}}{4}-g_j\mu_B B_z+\frac{1}{2}g_I\mu_k B_z\\
&-\sqrt{\frac{1}{4}\left(g_j\mu_B+g_I\mu_k\right)^2B_z^2+\frac{A_{2P_{3/2}}}{4}\left(g_j\mu_B+g_I\mu_k\right)B_z+\frac{25}{16}A_{2P_{3/2}}^2},\\
|h_{10}\rangle &= \frac{1}{\sqrt{1+\phi_2^2(B_z)}}\left(\phi_2(B_z)\,|F=5/2,m_F=-3/2\rangle+|F=3/2,m_F=-3/2\rangle\right),\\
E_{k_{11}} &= \frac{1}{12}\left[-8A_{2P_{3/2}}+6g_j\mu_B B_z+i\left(i+\sqrt{3}\right)C^{1/3}\right.\\
&\left.-\frac{i\left(-i+\sqrt{3}\right)\left(49A_{2P_{3/2}}^2-12A_{2P_{3/2}}(g_j\mu_B+g_I\mu_k)B_z+12\left(g_j\mu_B+g_I\mu_k\right)^2B_z^2\right)}{C^{1/3}}\right],\\
|k_{11}\rangle &= \frac{1}{\sqrt{1+\alpha_2^2(B_z)+\beta_2^2(B_z)}}\left(\beta_2(B_z)\,|F=5/2,m_F=1/2\rangle\right.\\
&\left.+\alpha_2(B_z)\,|F=3/2,m_F=1/2\rangle+|F=1/2,m_F=1/2\rangle\right),\\
E_{k_{12}} &= \frac{1}{30}\left[-5\left(4A_{2P_{3/2}}+3g_j\mu_B B_z\right)+\frac{5}{2}i\left(i+\sqrt{3}\right)\tilde{C}^{1/3}\right.\\
&\left.-\frac{5i\left(-i+\sqrt{3}\right)\left(49A_{2P_{3/2}}^2+12A_{2P_{3/2}}\left(g_j\mu_B+g_I\mu_k\right)B_z+12\left(g_j\mu_B+g_I\mu_k\right)^2B_z^2\right)}{2\tilde{C}^{1/3}}\right],\\
|k_{12}\rangle &= \frac{1}{\sqrt{1+\tilde{\alpha}_2^2(B_z)+\tilde{\beta}_2^2(B_z)}}\left(\tilde{\beta}_2(B_z)\,|F=5/2,m_F=-1/2\rangle\right.\\
&\left.+\tilde{\alpha}_2(B_z)\,|F=3/2,m_F=-1/2\rangle+|F=1/2,m_F=-1/2\rangle\right)
\end{aligned}
$$

with $\theta_{1/2}(B_z)=\pm\frac{\sqrt{6}}{5}\frac{\left(g_j\mu_B+g_I\mu_k\right)B_z}{\frac{5A_{2P_{3/2}}}{4}-\frac{1}{10}\left(g_j\mu_B+g_I\mu_k\right)B_z+\sqrt{\frac{1}{4}\left(g_j\mu_B+g_I\mu_k\right)^2B_z^2-\frac{A_{2P_{3/2}}}{4}\left(g_j\mu_B+g_I\mu_k\right)B_z+\frac{25}{16}A_{2P_{3/2}}^2}}$,

$$\phi_{1/2}(B_z)=\pm\frac{\sqrt{6}}{5}\frac{\left(g_j\mu_B+g_I\mu_k\right)B_z}{\frac{5A_{2P_{3/2}}}{4}+\frac{1}{10}\left(g_j\mu_B+g_I\mu_k\right)B_z+\sqrt{\frac{1}{4}\left(g_j\mu_B+g_I\mu_k\right)^2B_z^2+\frac{A_{2P_{3/2}}}{4}\left(g_j\mu_B+g_I\mu_k\right)B_z+\frac{25}{16}A_{2P_{3/2}}^2}},$$

$$\alpha_1/\tilde{\alpha}_1(B_z)=-\frac{3}{5}\frac{\left(g_j\mu_B+g_I\mu_k\right)B_z}{-A_{2P_{3/2}}+\left(\pm\frac{11}{30}g_j\mu_B\mp\frac{2}{15}g_I\mu_k\right)B_z-E_{g_3/g_4}-\frac{5}{9}\frac{\left(g_j\mu_B+g_I\mu_k\right)^2B_z^2}{-\frac{5A_{2P_{3/2}}}{2}\pm\left(\frac{5}{6}g_j\mu_B+\frac{1}{3}g_I\mu_k\right)B_z-E_{g_3/g_4}}},$$

$$\alpha_2/\tilde{\alpha}_2(B_z)=-\frac{\sqrt{5}}{3}\frac{\left(g_j\mu_B+g_I\mu_k\right)B_z}{-A_{2P_{3/2}}+\left(\pm\frac{11}{30}g_j\mu_B\mp\frac{2}{15}g_I\mu_k\right)B_z-E_{k_{11}/k_{12}}-\frac{9}{25}\frac{\left(g_j\mu_B+g_I\mu_k\right)^2B_z^2}{\frac{3A_{2P_{3/2}}}{2}\pm\frac{1}{5}\left(\frac{3}{2}g_j\mu_B-g_I\mu_k\right)B_z-E_{k_{11}/k_{12}}}},$$

$$\alpha_3/\tilde{\alpha}_3(B_z)=-\frac{3}{5}\frac{\left(g_j\mu_B+g_I\mu_k\right)B_z}{\frac{3A_{2P_{3/2}}}{2}\pm\frac{1}{5}\left(\frac{3}{2}g_j\mu_B-g_I\mu_k\right)B_z-E_{h_8/h_9}},$$

Table 3.2: The table contains all necessary values and parameters for the deuterium states. Energy values are displayed in units of frequency as given in the original sources. The values were measured with much higher precision, resulting in uncertainties that are several orders of magnitude smaller. Thus, the uncertainties are omitted.

	g_j[a]	g_I	A [MHz][b]	τ	ΔE [MHz]	Q [fm^2][c]
$2S_{1/2}$	2.002 [132]	0.857438 [133]	27.282969 [134]	$\frac{1}{8.23}$ s [127]		0.286 [135]
$2P_{1/2}$	0.666	0.857438 [133]	9.088927 [125]	1.6 ns [129]	1058.49 [136][d]	0.286 [135]
$2P_{3/2}$	1.334	0.857438 [133]	1.817671 [125]	1.6 ns [129]	9912.59 [137][e]	0.286 [135]

a: Based on Ch. 2.4.2
b: Deviations of the values from the sources are explained in the text
c: Definition given in App. C
d: Corresponds to the Lamb-shift
e: Corresponds to the fine splitting

$$\beta_1/\tilde{\beta}_1(B_z) = \frac{1}{\sqrt{5}} \frac{(g_j\mu_B + g_I\mu_k)^2 B_z^2}{\left(-\frac{5A_{2P_{3/2}}}{2} \pm \left(\frac{5}{6}g_j\mu_B + \frac{1}{3}g_I\mu_k\right)B_z - E_{g_3/g_4}\right)\left(-A_{2P_{3/2}} \pm \left(\frac{11}{30}g_j\mu_B - \frac{2}{15}g_I\mu_k\right)B_z - E_{g_3/g_4}\right) - \frac{5}{9}(g_j\mu_B + g_I\mu_k)^2 B_z^2},$$

$$\beta_2/\tilde{\beta}_2(B_z) = \frac{1}{\sqrt{5}} \frac{(g_j\mu_B + g_I\mu_k)^2 B_z^2}{\left(\frac{3A_{2P_{3/2}}}{2} \pm \frac{1}{5}\left(\frac{3}{2}g_j\mu_B - g_I\mu_k\right)B_z - E_{k_{11}/k_{12}}\right)\left(-A_{2P_{3/2}} \pm \left(\frac{11}{30}g_j\mu_B - \frac{2}{15}g_I\mu_k\right)B_z - E_{k_{11}/k_{12}}\right) - \frac{9}{25}(g_j\mu_B + g_I\mu_k)^2 B_z^2},$$

$$\beta_3/\tilde{\beta}_3(B_z) = -\frac{\sqrt{5}}{3}\frac{(g_j\mu_B + g_I\mu_k)B_z}{-\frac{5A_{2P_{3/2}}}{2} \pm \left(\frac{5}{6}g_j\mu_B + \frac{1}{3}g_I\mu_k\right)B_z - E_{h_8/h_9}},$$

$$\begin{aligned}
C &= 143A_{2P_{3/2}}^3 + 18A_{2P_{3/2}}^2(g_j\mu_B + g_I\mu_k)B_z - 72A_{2P_{3/2}}(g_j\mu_B + g_I\mu_k)^2 B_z^2 \\
&+ \Big[A_{2P_{3/2}}^2\left(143A_{2P_{3/2}}^2 + 18A_{2P_{3/2}}(g_j\mu_B + g_I\mu_k)B_z - 72(g_j\mu_B + g_I\mu_k)^2 B_z^2\right)^2 \\
&- \left(49A_{2P_{3/2}}^2 - 12A_{2P_{3/2}}(g_j\mu_B + g_I\mu_k)B_z + 12(g_j\mu_B + g_I\mu_k)^2 B_z^2\right)^3\Big]^{1/2}, \\
\tilde{C} &= 143A_{2P_{3/2}}^3 - 18A_{2P_{3/2}}^2(g_j\mu_B + g_I\mu_k)B_z - 72A_{2P_{3/2}}(g_j\mu_B + g_I\mu_k)^2 B_z^2 \\
&+ \Big[A_{2P_{3/2}}^2\left(-143A_{2P_{3/2}}^2 + 18A_{2P_{3/2}}(g_j\mu_B + g_I\mu_k)B_z + 72(g_j\mu_B + g_I\mu_k)^2 B_z^2\right)^2 \\
&- \left(49A_{2P_{3/2}}^2 + 12A_{2P_{3/2}}(g_j\mu_B + g_I\mu_k)B_z + 12(g_j\mu_B + g_I\mu_k)^2 B_z^2\right)^3\Big]^{1/2}.
\end{aligned}$$

Analogously to the explanation in Sec. 3.1 the experimentally measured values are summarized in Tab. 3.2. Also here the values of the hyperfine splitting constants vary from the entire hyperfine splitting quoted in the sources. Again the reason is that the sources show the entire energy difference, which is proportional to the hyperfine constant, e.g. $E_{HFS} = E_{\alpha_1}|_{B=0} - E_{\beta_6}|_{B=0} = 1.5\,A$. Furthermore, the deuteron has no longer a spherical shape, which gives rise to an electric quadrupole moment Q. Its effect is small in comparison to the magnetic dipole moment and the external fields. Therefore, it is neglected in the following calculations as well as all off diagonal elements for the magnetic dipole moment. The latter is motivated in Sec. 2.2.3. For the sake of completeness the theory for electric multipole is stated in App. C. Moreover, the Breit-Rabi energies of Eq. (3.28), Eq. (3.29) and Eq. (3.31) are displayed in Fig. 3.3a and Fig. 3.3b. Following the same steps as described in Sec. 3.1 the new lifetimes of the single states are displayed in Fig. 3.4 for a constant electric field flux $E_x = 10^3\,\mathrm{V/m}$ and as function of the external magnetic field. The necessary coupling constants can be found in App. D.

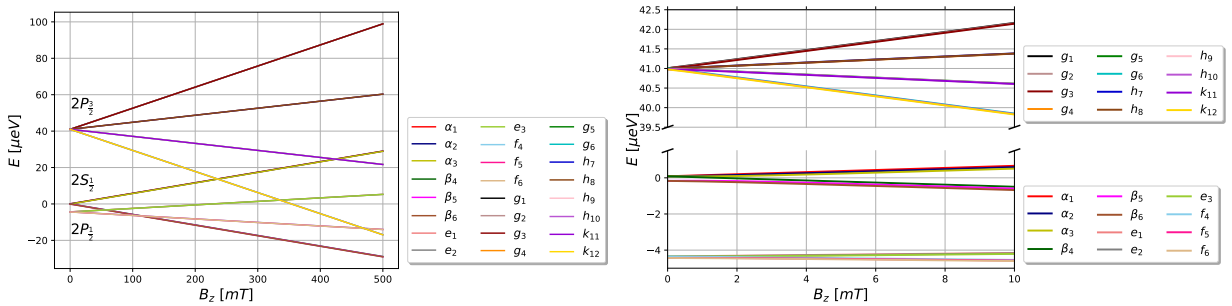

(a) (b)

Figure 3.3: The Breit-Rabi diagram for the excited deuterium states with $n = 2$ is depicted. The vertical axis describes the binding energy of the single states as function of the external magnetic field given on the horizontal axis. The zero-energy is defined by the binding energy excluding the hyperfine splitting of the metastable $2S_{1/2}$ set at zero magnetic field flux. Consequently, the $2P_{1/2}$ set differs by the Lamb-shift while the fine splitting separates the $2P_{3/2}$ set from the metastable $2S_{1/2}$ deuterium states. In Fig. 3.3a the evolution for large magnetic field fluxes is displayed while the eigenstates with the same electric quantum number m_j are better visible in Fig. 3.3b.

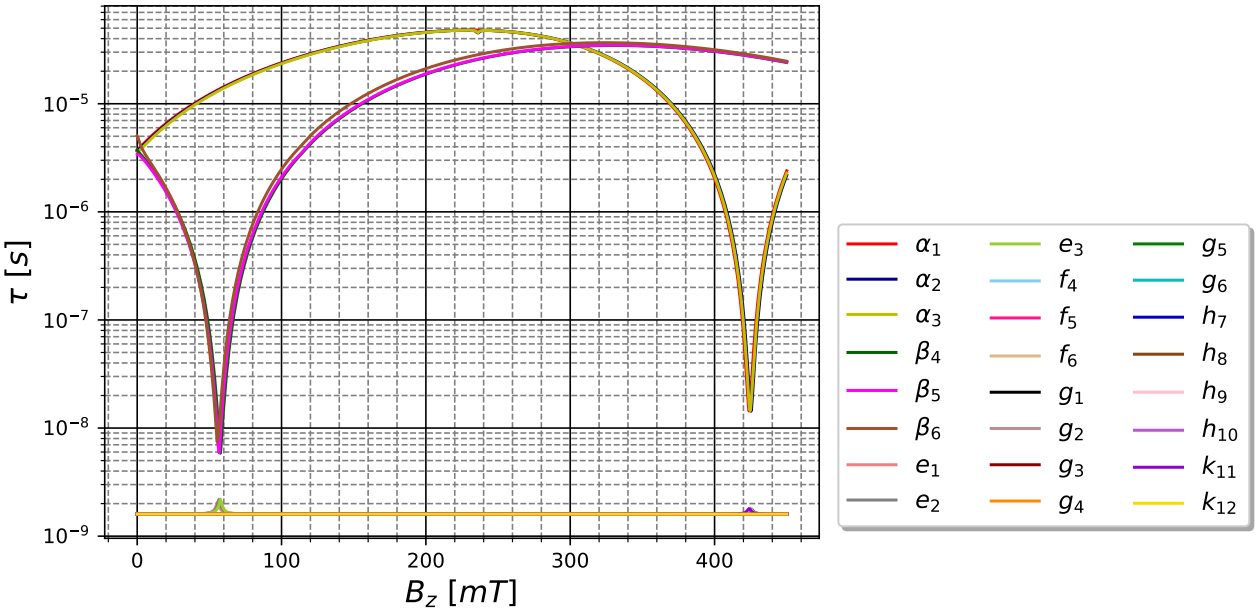

Figure 3.4: The evolution of the lifetime of metastable deuterium $2S_{1/2}$ as well as the short-living $2P_{1/2}$ and $2P_{3/2}$ states in the presence of an external electric field $\vec{E} = E_x \hat{e}_x$ and as function of a homogenous magnetic field $\vec{B} = B_z \hat{e}_z$ is displayed. The applied electric field flux is $E_x = 10^3\,\mathrm{V/m}$.

Table 3.3: The table contains all necessary values and parameters for the tritium states. Energy values are displayed in units of frequency as given in the original sources. The values were measured with much higher precision, resulting in uncertainties that are several orders of magnitude smaller. Thus, the uncertainties are omitted.

	g_j[a]	g_I	A [MHz][b]	τ	ΔE [MHz]
$2S_{1/2}$	2.002 [139]	5.957924931 [140]	189.594 [125]	$\frac{1}{8.23}$ s [127]	
$2P_{1/2}$	0.666	5.957924931 [140]	63.1724 [125]	1.6 ns [129]	1056.4 [125][c]
$2P_{3/2}$	1.334	5.957924931 [140]	12.62315 [125]	1.6 ns [129]	9920.8 [125][d]

a: Based on Ch. 2.4.2
b: Deviations of the values from the sources are explained in the text
c: Corresponds to the Lamb-shift
d: Corresponds to the fine splitting

3.3 Tritium

Triton is the heaviest naturally abundant isotope of hydrogen consisting of two neutrons and one proton. In addition, it is a spin $^1/_2$ particle. The triton is unstable and decays due to a β^- process with a half time of $T_{1/2} = 12.264 \pm 0.018$ yr [138]. Its decay reaction is given by

$$t \rightarrow {}^3_2\mathrm{He} + e^- + \bar{\nu}_e. \tag{3.32}$$

Nevertheless, the atom tritium has a similar structure and spin dynamics than hydrogen. Consequently, the binding energies and eigenstates equal those presented in Sec. 3.1. Also for the tritium the three excited sets $2S_{1/2}$, $2P_{1/2}$ and $2P_{3/2}$ are relevant. Therefore, the corresponding Breit-Rabi system is given by Eq. (3.15), Eq. (3.16) and Eq. (3.18). Moreover, the necessary tritium parameters are stated in Tab. 3.3 and the deviation for the hyperfine splitting constant is explained in Sec. 3.1. The Breit-Rabi diagram is displayed in Fig. 3.5a and Fig. 3.5b. Finally, the lifetime evolution of the excited tritium states in the presence of an external electric field is depicted in Fig. 3.6.

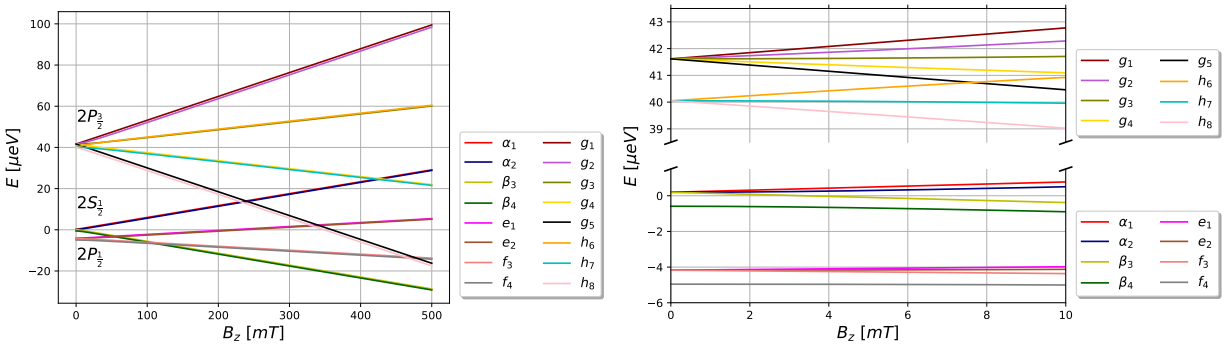

(a) (b)

Figure 3.5: The Breit-Rabi diagram for the excited tritium states with $n = 2$ is depicted. The vertical axis describes the binding energy of the single states as function of the external magnetic field given on the horizontal axis. The zero-energy is defined by the binding energy excluding the hyperfine splitting of the metastable $2S_{1/2}$ set at zero magnetic field flux. Consequently, the $2P_{1/2}$ set differs by the Lamb-shift while the fine splitting separates the $2P_{3/2}$ set from the metastable $2S_{1/2}$ tritium states. In Fig. 3.5a the evolution for large magnetic field fluxes is displayed while the eigenstates with the same electric quantum number m_j are better visible in Fig. 3.5b.

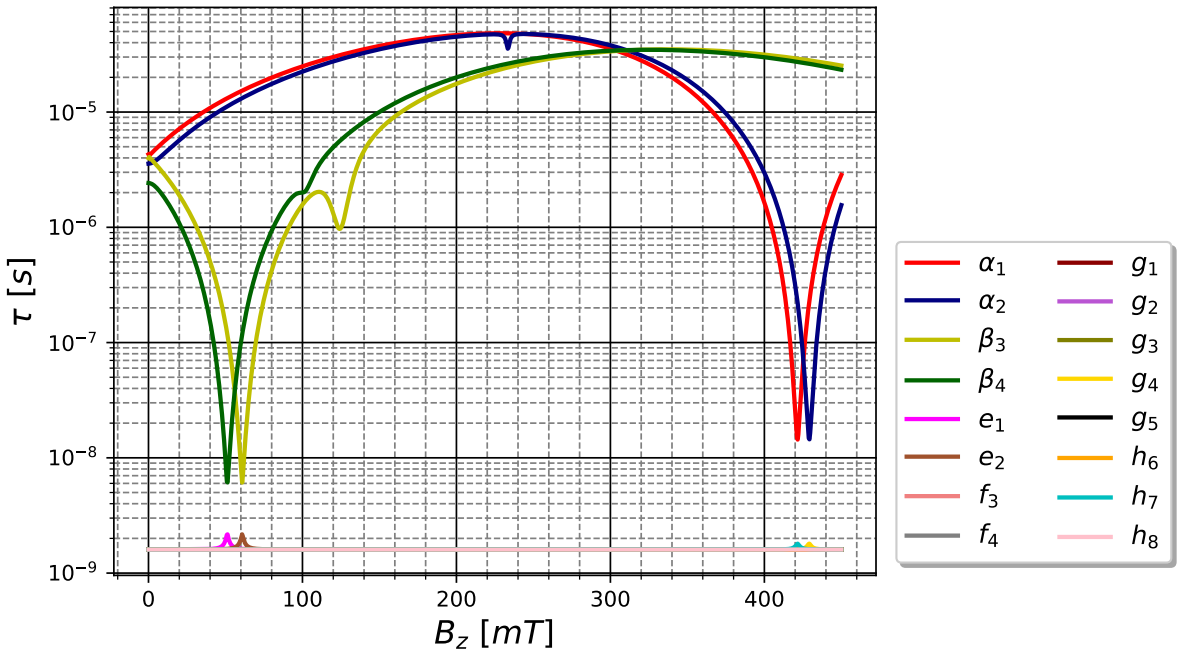

Figure 3.6: The evolution of the lifetime of metastable tritium $2S_{1/2}$ as well as the short-living $2P_{1/2}$ and $2P_{3/2}$ states in the presence of an external electric field $\vec{E} = E_x\hat{e}_x$ and as function of a homogenous magnetic field $\vec{B} = B_z\hat{e}_z$ is displayed. The applied electric field flux is $E_x = 10^3\,\mathrm{V/m}$.

3.4 Single ionized helium-3

Helium-3 is a stable isotope composed out of two protons and one neutron. Its nucleus is a spin $1/2$ particle. Consequently, the single ionized ${}^3_2\mathrm{He}^+$ has a hydrogen-like structure, but with a nuclear charge number of $Z = 2$. For the helium-3 ion only the metastable $2S_{1/2}$ and the short-living $2P_{1/2}$ set are important for the thesis. Due to the negative hyperfine splitting constants A the Breit-Rabi eigenstates differ slightly from those introduced in Sec. 3.1. The ones for the metastable $2S_{1/2}$ set

are stated as

$$
\begin{aligned}
E_{A_1} &= \frac{A_{2S_{1/2}}}{4} + \frac{1}{2}\left(g_s\mu_B - g_I\mu_k\right)B_z,\\
|A_1\rangle &= |F=1, m_F=1\rangle,\\
E_{A_2} &= -\frac{A_{2S_{1/2}}}{4} + \frac{1}{2}\sqrt{A_{2S_{1/2}}^2 + \left(g_s\mu_B + g_I\mu_k\right)^2 B_z^2},\\
|A_2\rangle &= \frac{1}{\sqrt{1+X^2(B_z)}}\left(|F=0, m_F=0\rangle + X(B_z)\,|F=1, m_F=0\rangle\right),\\
E_{B_3} &= \frac{A_{2S_{1/2}}}{4} - \frac{1}{2}\left(g_s\mu_B - g_I\mu_k\right)B_z,\\
|B_3\rangle &= |F=1, m_F=-1\rangle,\\
E_{B_4} &= -\frac{A_{2S_{1/2}}}{4} - \frac{1}{2}\sqrt{A_{2S_{1/2}}^2 + \left(g_s\mu_B + g_I\mu_k\right)^2 B_z^2},\\
|B_4\rangle &= \frac{1}{\sqrt{1+\Omega^2(B_z)}}\left(\Omega(B_z)\,|F=0, m_F=0\rangle + |F=1, m_F=0\rangle\right)\\
\text{with}\quad X(B_z) &= \frac{\left(g_s\mu_B + g_I\mu_k\right)B_z}{-A_{2S_{1/2}} + \sqrt{A_{2S_{1/2}}^2 + \left(g_s\mu_B + g_I\mu_k\right)^2 B_z^2}}\\
\text{and}\quad \Omega(B_z) &= \frac{-A_{2S_{1/2}} - \sqrt{A_{2S_{1/2}}^2 + \left(g_s\mu_B + g_I\mu_k\right)^2 B_z^2}}{\left(g_s\mu_B + g_I\mu_k\right)B_z}.
\end{aligned}
\tag{3.33}
$$

Analogue, the Breit-Rabi states for the $2P_{1/2}$ are expressed as

$$
\begin{aligned}
E_{E_1} &= \frac{A_{2P_{1/2}}}{4} + \frac{1}{2}\left(g_j\mu_B - g_I\mu_k\right)B_z,\\
|E_1\rangle &= |F=1, m_F=1\rangle,\\
E_{E_2} &= -\frac{A_{2P_{1/2}}}{4} + \frac{1}{2}\sqrt{A_{2P_{1/2}}^2 + \left(g_j\mu_B + g_I\mu_k\right)^2 B_z^2},\\
|E_2\rangle &= \frac{1}{\sqrt{1+Y^2(B_z)}}\left(|F=0, m_F=0\rangle + Y(B_z)\,|F=1, m_F=0\rangle\right),\\
E_{F_3} &= \frac{A_{2P_{1/2}}}{4} - \frac{1}{2}\left(g_j\mu_B - g_I\mu_k\right)B_z,\\
|F_3\rangle &= |F=1, m_F=-1\rangle,\\
E_{F_4} &= -\frac{A_{2P_{1/2}}}{4} - \frac{1}{2}\sqrt{A_{2P_{1/2}}^2 + \left(g_j\mu_B + g_I\mu_k\right)^2 B_z^2},\\
|F_4\rangle &= \frac{1}{\sqrt{1+Z^2(B_z)}}\left(Z(B_z)\,|F=0, m_F=0\rangle + |F=1, m_F=0\rangle\right)\\
\text{with}\quad Y(B_z) &= \frac{\left(g_j\mu_B + g_I\mu_k\right)B_z}{-A_{2P_{1/2}} + \sqrt{A_{2P_{1/2}}^2 + \left(g_j\mu_B + g_I\mu_k\right)^2 B_z^2}}\\
\text{and}\quad Z(B_z) &= \frac{-A_{2P_{1/2}} - \sqrt{A_{2P_{1/2}}^2 + \left(g_j\mu_B + g_I\mu_k\right)^2 B_z^2}}{\left(g_j\mu_B + g_I\mu_k\right)B_z}.
\end{aligned}
\tag{3.34}
$$

The Breit-Rabi diagram based on Eq. (3.33), Eq. (3.34) and the additional Lamb-shift is displayed in Fig. 3.7. The corresponding parameters are summarized in Tab. 3.4. Due to the charge number $Z = 2$ the Lamb-shift is much larger in comparison to the hydrogen. Consequently, the Zeeman

Table 3.4: The table contains all necessary values and parameters for the helium-3 states. Energy values are displayed in units of frequency as given in the original sources. The values were measured with much higher precision, resulting in uncertainties that are several orders of magnitude smaller. Thus, the uncertainties are omitted.

	g_j[a]	g_I	A [MHz]	τ	ΔE [MHz]
$2S_{1/2}$	2.002 [141]	−4.255 [141]	−1083.355 [142, 143]	$\frac{1}{525}$ s [144]	
$2P_{1/2}$	0.666	−4.255 [141]	−360.801[b]	1.6 ns [129]	14041.474 [145][c]

a: Based on Ch. 2.4.2
b: Calculated based on Ch. 2.2.3
c: Corresponds to the Lamb-shift

crossing points between the metastable $2S_{1/2}$ and the short-lived $2P_{1/2}$ sets appear only at much larger magnetic fields. Moreover, the evolution of the lifetimes in the presence of an external electric field in x-direction and as function of an external homogenous magnetic field is displayed in Fig. 3.8a and Fig. 3.8b. The Stark coupling is weaker as the internal electric potential is stronger due to the larger charge number.

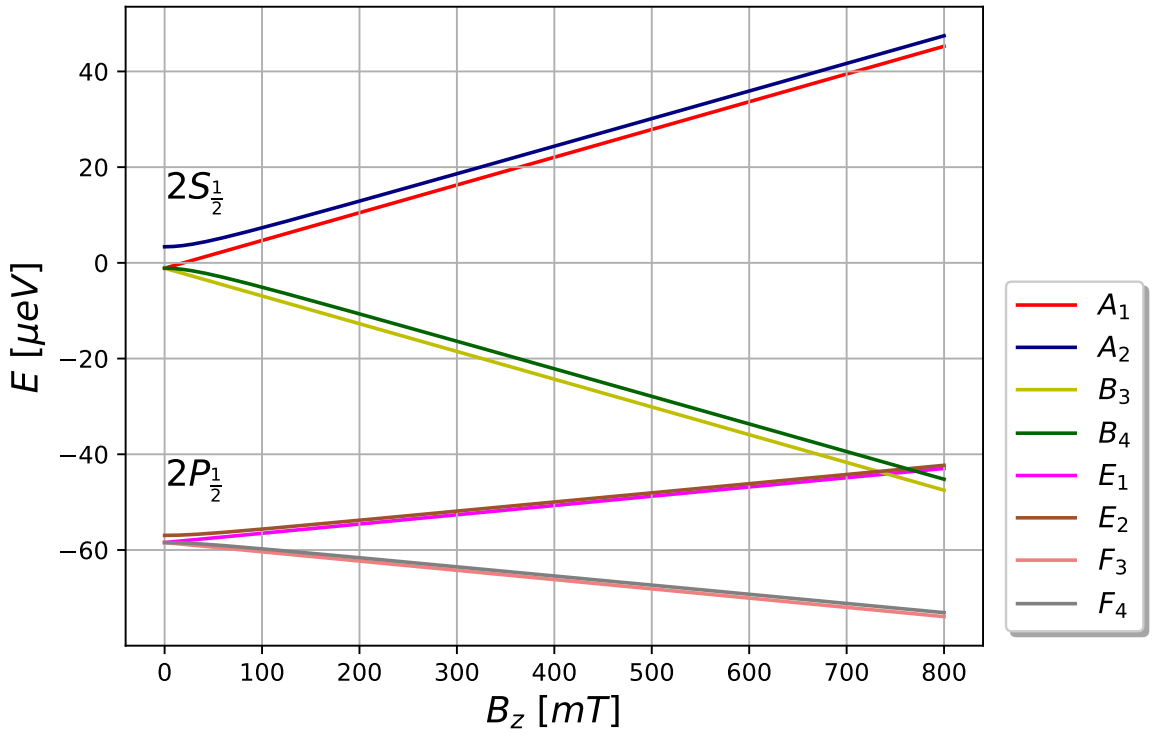

Figure 3.7: The Breit-Rabi diagram for the single ionized helium-3 metastable $2S_{1/2}$ and short-living $2P_{1/2}$ set is depicted. The vertical axis describes the binding energy of the single states as function of the external magnetic field given on the horizontal axis. The zero-energy is defined by the binding energy excluding the hyperfine splitting of the metastable $2S_{1/2}$ set at zero magnetic field flux. Consequently, the $2P_{1/2}$ set differs by the Lamb-shift.

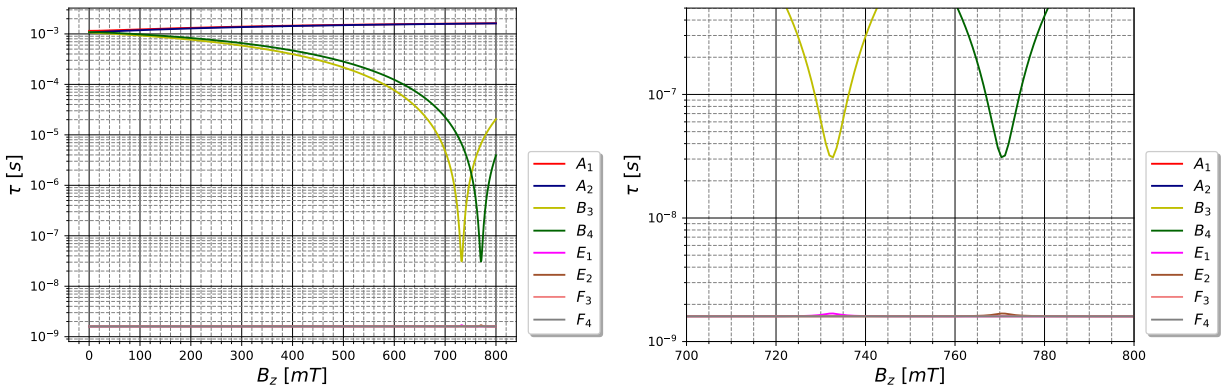

(a) (b)

Figure 3.8: The evolution of the lifetime of metastable helium-3 $2S_{1/2}$ and $2P_{1/2}$ states in the presence of an external electric field $\vec{E} = E_x\hat{e}_x$ and as function of a homogenous magnetic field $\vec{B} = B_z\hat{e}_z$ is displayed. The applied electric field flux is $E_x = 10^3\,{}^{\mathrm{V}}/_{\mathrm{m}}$.

3.5 The applied Lindblad master equation

Based on Sec. 2.5.1 a version of the Lindblad master equation is motivated to describe the time-dependent spin dynamics of the atomic and ionic systems. The Hamiltonians to model the external fields are introduced in Eq. (2.93) and Eq. (2.113). The potential from Eq. (2.118) describing the lifetime of excited atoms is not needed anymore as the decay is directly described by the Lindblad master equation itself. Therefore, the ladder operators L and $L^\dagger$, introduced in Sec. 2.5.1, have to connect the excited states with the ground states, while their lifetimes act as an inverse damping ratio. The entire Lindblad master equation is then expressed as

$$\dot{\rho}(t) = -\frac{i}{\hbar}\left[H(t), \rho(t)\right] + \sum_{i=1}^{N}\gamma_i\left(\sigma_i\rho(t)\sigma_i^\dagger - \frac{1}{2}\sigma_i^\dagger\sigma_i\rho(t) - \frac{1}{2}\rho(t)\sigma_i^\dagger\sigma_i\right), \tag{3.35}$$

with γ_i being the damping factors and σ_i the ladder operators. The sum runs over all necessary excited $n = 2$ states, which are coupled to the ground state by their lifetimes $\gamma_i = {}^1/_{\tau_i}$. In the following all hyperfine states of the ground state are combined into one artificial state called $|g\rangle$. Correspondingly, the ladder operator σ_i is defined as

$$\sigma_i = |g\rangle\langle i|\,. \tag{3.36}$$

Subsequently, for numerical applications the Lindblad master equation is transformed into a set of coupled differential equations. Therefore, a Hamiltonian is defined, based on the Stark effect and a modified Breit-Rabi Hamiltonian, which incorporates the energy corrections due to the Lamb-shift as well as the fine splitting

$$H = \tilde{H}_{BR} + H_{Stark}. \tag{3.37}$$

Consequently, the Lindblad master equation can be written in the Breit-Rabi basis as

$$\begin{aligned}\langle n_{BR}|\dot{\rho}\,(t)\,|m_{BR}\rangle = &\underbrace{-\frac{i}{\hbar}\langle n_{BR}|H(t)\rho(t)|m_{BR}\rangle}_{=I} + \underbrace{\frac{i}{\hbar}\langle n_{BR}|\rho(t)H(t)|m_{BR}\rangle}_{=II}\\ + \sum_{i=1}^{N}\gamma_i\Bigg(&\underbrace{\langle n_{BR}|\sigma_i\rho(t)\sigma_i^\dagger|m_{BR}\rangle}_{=III} - \frac{1}{2}\underbrace{\langle n_{BR}|\sigma_i^\dagger\sigma_i\rho(t)|m_{BR}\rangle}_{=IV} - \frac{1}{2}\underbrace{\langle n_{BR}|\rho(t)\sigma_i^\dagger\sigma_i|m_{BR}\rangle}_{=V}\Bigg),\end{aligned} \tag{3.38}$$

where $|n_{BR}\rangle$ are the relevant Breit-Rabi states. The first term from Eq. (3.38) can be rewritten as

$$\begin{aligned}
&-\frac{i}{\hbar}\langle n_{BR}|H(t)\rho(t)|m_{BR}\rangle = -\frac{i}{\hbar}\left(\langle n_{BR}|\tilde{H}_{BR}\rho(t)|m_{BR}\rangle + \langle n_{BR}|H_{Stark}\rho(t)|m_{BR}\rangle\right)\\
&= -\frac{i}{\hbar}\left(\langle m_{BR}|\left(\tilde{H}_{BR}\rho(t)\right)^{\dagger}|n_{BR}\rangle^{*} + \langle n_{BR}|H_{Stark}\mathbb{1}\rho(t)|m_{BR}\rangle\right)\\
&= -\frac{i}{\hbar}\left(\langle m_{BR}|\rho(t)^{\dagger}\tilde{H}_{BR}^{\dagger}|n_{BR}\rangle^{*} + \sum_{i_{BR}}\langle n_{BR}|H_{Stark}|i_{BR}\rangle\langle i_{BR}|\rho(t)|m_{BR}\rangle\right)\\
&= -\frac{i}{\hbar}\left(\langle m_{BR}|\rho(t)\tilde{H}_{BR}|n_{BR}\rangle^{*} + \sum_{i_{BR}}\langle n_{BR}|H_{Stark}|i_{BR}\rangle\langle i_{BR}|\rho(t)|m_{BR}\rangle\right)\\
&= -\frac{i}{\hbar}\left(E_{n_{BR}}\langle n_{BR}|\rho(t)|m_{BR}\rangle + \sum_{i_{BR}}\langle n_{BR}|H_{Stark}|i_{BR}\rangle\langle i_{BR}|\rho(t)|m_{BR}\rangle\right).
\end{aligned} \tag{3.39}$$

Here $E_{n_{BR}}$ denotes the Breit-Rabi eigenenergy in addition to possible energy corrections, due to the Lamb-shift or the fine structure, of the corresponding n_{BR} Breit-Rabi eigenstate. Furthermore, the non-vanishing matrix elements $\langle n_{BR}|H_{Stark}|i_{BR}\rangle$ are displayed in App. D. Subsequently, the second term of Eq. (3.38) can be expressed as

$$\begin{aligned}
&\frac{i}{\hbar}\langle n_{BR}|\rho(t)H(t)|m_{BR}\rangle = \frac{i}{\hbar}\left(\langle n_{BR}|\rho(t)\tilde{H}_{BR}|m_{BR}\rangle + \langle n_{BR}|\rho(t)H_{Stark}|m_{BR}\rangle\right)\\
&= \frac{i}{\hbar}\left(E_{m_{BR}}\langle n_{BR}|\rho(t)|m_{BR}\rangle + \sum_{i_{BR}}\langle n_{BR}|\rho(t)|i_{BR}\rangle\langle i_{BR}|H_{Stark}|m_{BR}\rangle\right).
\end{aligned} \tag{3.40}$$

The three last terms then take the following forms

$$\begin{aligned}
&\langle n_{BR}|\sigma_i\rho(t)\sigma_i^{\dagger}|m_{BR}\rangle = \langle n_{BR}|g\rangle\langle i_{BR}|\rho(t)|i_{BR}\rangle\langle g|m_{BR}\rangle = 0,\\
&\langle n_{BR}|\sigma_i^{\dagger}\sigma_i\rho(t)|m_{BR}\rangle = \langle n_{BR}|i_{BR}\rangle\langle g|g\rangle\langle i_{BR}|\rho(t)|m_{BR}\rangle = \langle i_{BR}|\rho(t)|m_{BR}\rangle\,\delta n_{BR},i_{BR},\\
&\langle n_{BR}|\rho(t)\sigma_i^{\dagger}\sigma_i|m_{BR}\rangle = \langle n_{BR}|\rho(t)|i_{BR}\rangle\langle g|g\rangle\langle i_{BR}|m_{BR}\rangle = \langle n_{BR}|\rho(t)|i_{BR}\rangle\,\delta m_{BR},i_{BR}.
\end{aligned} \tag{3.41}$$

Consequently, the Lindblad master equation is stated as

$$\begin{aligned}
&\langle n_{BR}|\dot{\rho}(t)|m_{BR}\rangle = -\frac{i}{\hbar}\left(E_{n_{BR}} - E_{m_{BR}}\right)\langle n_{BR}|\rho(t)|m_{BR}\rangle\\
&-\frac{i}{\hbar}\sum_{i_{BR}}\left(\langle n_{BR}|H_{Stark}|i_{BR}\rangle\langle i_{BR}|\rho(t)|m_{BR}\rangle - \langle n_{BR}|\rho(t)|i_{BR}\rangle\langle i_{BR}|H_{Stark}|m_{BR}\rangle\right)\\
&-\frac{1}{2}\left(\gamma_{n_{BR}} + \gamma_{m_{BR}}\right)\langle n_{BR}|\rho(t)|m_{BR}\rangle.
\end{aligned} \tag{3.42}$$

For the sake of completeness the artificial ground state $|g\rangle$ is addressed. The hydrogen-like ground state wave functions do not have any electric dipole interaction, which is explained in Sec. 2.4.1. Consequently, in first order they have no possible interference with the excited $n = 2$ states. In addition, their energy splitting to the next set of states is too large to play a major role in the spin dynamics of the excited $n = 2$ sets in the presence of weak external electromagnetic fields. This is also true for all sets of states with different main quantum number n as well as for helium-3 the $2P_{3/2}$ set, i.e. energy difference of approximately 526 μeV at 800 mT to the closest A state. Therefore, the artificial ground state is only there to ensure that the trace of the density operator is conserved at any time, but it has no further physical meaning for the following purposes. This is the reason for neglecting it for most of the further calculations performed in this thesis. Nevertheless, the full knowledge of the density operator can be used to calculate the entropy S as state function of the system [146]. Correspondingly, simulations incorporating the artificial ground state and resulting changes in the entropy are discussed in Sec. 4.1.1.

Chapter 4

Nuclear spin filter

The nuclear spin filter, developed in Los Alamos, is a device, which has been introduced first by McKibben et al. [6] and Ohlsen et al. [32]. Its purpose is to filter metastable atomic hydrogen, deuterium and tritium states by selective quenching. In Sec. 4.1 the developed framework from Ch. 3 is applied to model the already existing spin filter. Thereby, further knowledge is gained and the validation of the framework is established. In the second Sec. 4.2 the framework is extended and used to model a new design for an upgraded and improved nuclear spin filter beyond the known standards. Finally, in Sec. 4.3 a novel model for a nuclear spin filter based on helium-3 ions is established, which extends the usage of nuclear spin filter and the LSP beyond molecules and atoms based on hydrogen for the first time.

4.1 The old spin filter

In this section the functionality of the nuclear spin filter is discussed, based on the, in this work, introduced spin physics from Ch. 3. Thereby, the device has three key components to ensure that only one of the α states passes the spin filter, while all other metastable atoms are quenched into the ground state. A technical drawing of a spin filter is depicted in Fig. 4.1. The first important part is a homogenous magnetic field, which points into beam direction $\vec{B} = B_z \hat{e}_z$. Its purpose is to split the eigenenergies of the hyperfine states and to transform them into the Breit-Rabi states. Windings are placed carefully around a hollow iron cylinder guaranteeing such a homogenous field. A cylindrically shaped cavity with four isolated quadrants, is placed inside this cylinder. A picture of such a cavity is visible in Fig. 4.25. The second key factor is a static electric field $\vec{E} = E_x \hat{e}_x$, which is realized by applying voltages onto two opposite quadrants of the cavity. Its purpose is to utilize the Stark effect and thereby couple the metastable β states onto the short-living $2P_{1/2}$ e states. Therefore, the lifetimes of the β states are highly reduced once the external magnetic field reaches the critical area of roughly 60 mT, as it is visible in the lifetime diagrams, e.g. Fig. 3.2. For now the α states remain untouched. Through the other two cavity quadrants a resonance radio frequency is induced via antennas. This is the third and last component to ensure that only one α state remains stable. Its electric field component is thereby coupling the α states also to the e states. To increase the coupling strength, the frequency of the radio frequency needs to fill up the energy gap in between the states

$$E_\alpha|_{B=60\,\mathrm{mT}} - E_e|_{B=60\,\mathrm{mT}} \approx h f_{m,n,p}. \tag{4.1}$$

Consequently, the resonance frequency is often stated as $f_{m,n,p} = 1.60975$ GHz [6, 32]. Nevertheless, different frequency values may also be used, as long as they satisfy the upper condition Eq. (4.1). Subsequently, the $\mathrm{TM}_{0,1,0}$ mode, based on the theory for electromagnetic fields coupled into a cylindrically shaped cavity, introduced in Sec. 2.6, is used to accomplish the task. Eq. 2.173 connects the dimension of the cavity with the corresponding resonance frequency. In the case of

the $TM_{0,1,0}$ mode Eq. 2.173 takes the following form

$$f_{0,1,0} = \frac{1}{2\pi\sqrt{\mu_0\varepsilon_0}}\frac{x_{0,1}}{R}. \tag{4.2}$$

Consequently, the resonance frequency $f_{0,1,0}$ is independent of the length d of the cavity but needs to have a radius of $R = 71.3$ mm as the first root of $J_0(x)$ is at $x_{0,1} \approx 2.405$. In addition, it is visible in Fig. 4.1 and Fig. 4.25 that extensions are build onto the entry and exit of the cavity. These have two different reasons. The first and second reasons are that additional electric fields can be applied, which can be used to deflect ion beams and to ensure at the exit that all β states are removed from the beam by further stark quenching outside of the radio frequency area. Subsequently, two measurements of a metastable hydrogen beam are depicted in Fig. 4.2a and Fig. 4.2b. The signal is obtained in the quenching region, described in more detail in Sec. 5.3, as function of the electric current send through the spin filter to produce the magnetic field. The first peak decodes the population of the α_1 population, while the second peak gives us an insight of the α_2 population. For an ideal spectrum of an unpolarized beam, visible in Fig. 4.2a, both peaks should have the same peak height. Some background around the peaks occur due to different reasons, e.g. light with different wavelength is created due to ions hitting the wall or colliding with rest gas particles. To start the analysis process, the mentioned backgrounds are subtracted from the signals. Therefore, the background was fitted by a quadratic polynomial

$$f(I) = aI^2 + bI + c. \tag{4.3}$$

The corresponding fit parameters are summarized in Tab. 4.1. Moreover, the processed data is depicted in Fig. 4.3a and Fig. 4.3b. In addition, the peak structures are analyzed by fitting a Gauss function

$$f(I) = a' e^{-(I-b')^2/2c'^2}. \tag{4.4}$$

Again, the corresponding fit parameters for the four fits are combined in Tab. 4.2. The Gaussian curve (4.4) reaches its maximum, when the argument I equals the displacement value b' and its function value is a'. Therefore, a scaling factor V is introduced

$$V = \frac{a'_{\mathrm{Peak}_1\,\mathrm{unpol.}}}{a'_{\mathrm{Peak}_2\,\mathrm{unpol.}}} = 1.078 \pm (0.006)_{\mathrm{stat.}}\,, \tag{4.5}$$

to compensate the fact that the peaks have unequal peak heights even when the incoming beam is unpolarized. Its error is calculated via Gaussian law of propagation of uncertainty and propagates as systematic error into the polarized beam measurement. The reason for different peak structures and heights can originate from various reasons. One of them is that the increase in magnetic field changes the amplification factor in the photomultiplier tube (PMT), which is collecting the data. The detection process, utilizing the photomultiplier, is explained in detail later in Sec. 5.3. Finally, Eq. (2.128) is employed to determine the nuclear polarization of the incoming metastable hydrogen atoms. In the case of the amplification the equation takes the following form

$$P = \frac{a'_{\mathrm{Peak}_1} - V a'_{\mathrm{Peak}_2}}{a'_{\mathrm{Peak}_1} + V a'_{\mathrm{Peak}_2}} = 0.824 \pm (0.016)_{\mathrm{stat.}} \pm (0.001)_{\mathrm{syst.}}\,, \tag{4.6}$$

where $a'_{\mathrm{Peak}_{1/2}}$ are the fit parameters of Fig. 4.3b.

Table 4.1: The fit parameters for the background subtraction, visible in Fig. 4.2a and Fig. 4.2b, are presented in this table. The uncertainties originate all due to statistics.

Figure	$a\left[\frac{\mathrm{mV}}{\mathrm{A}^2}\right]$	$b\left[\frac{\mathrm{mV}}{\mathrm{A}}\right]$	c [mV]
4.2a	0.6094 ± 0.0029	-10.37 ± 0.05	42.98 ± 0.21
4.2b	0.5046 ± 0.0108	-8.27 ± 0.18	32.33 ± 0.79

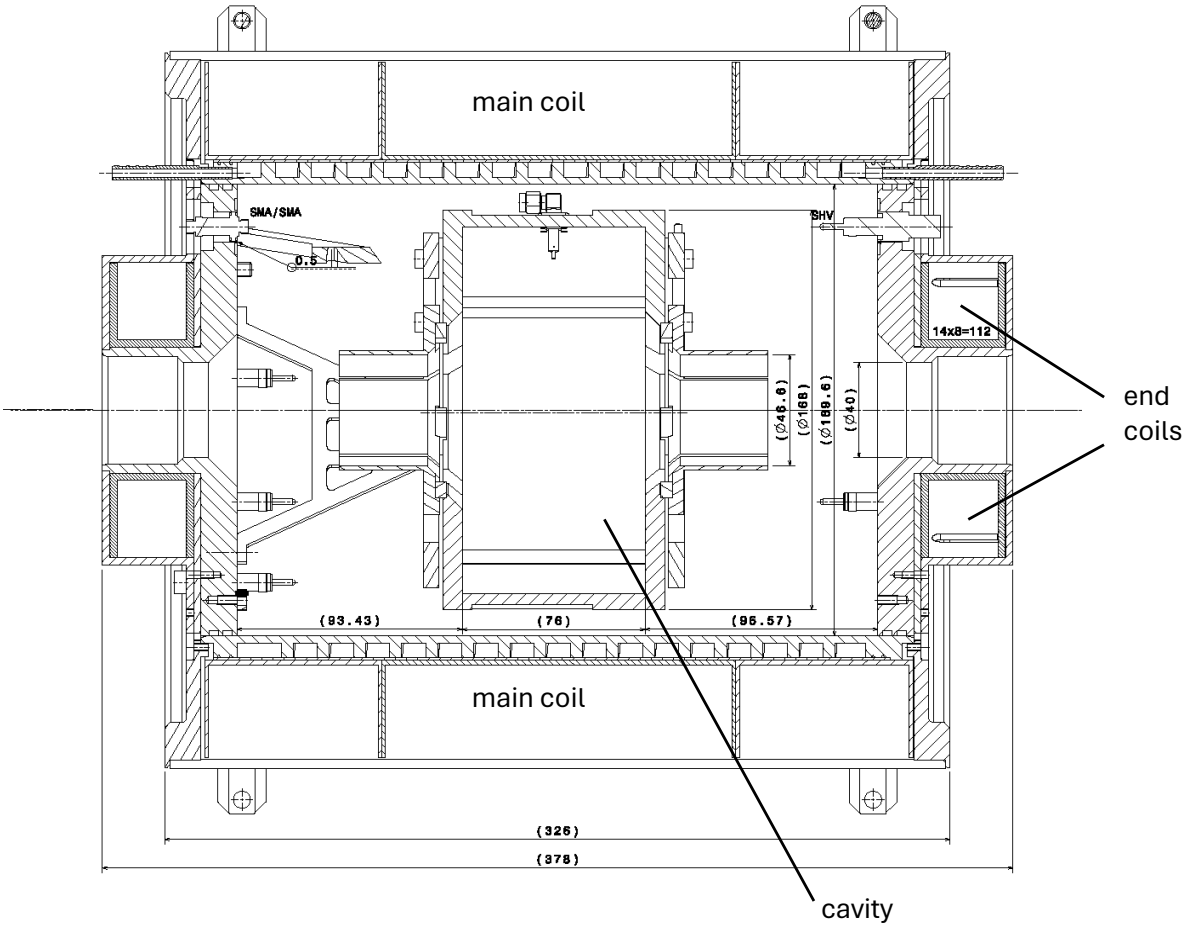

Figure 4.1: The realization of one of the nuclear spin filters, situated at the nuclear institute of Forschungszentrum Jülich (FZJ), is based on technical drawings, performed by the technical design department. The main components stated by the coils to produce the homogenous magnetic field in beam direction, as well as the cavity are marked.

Table 4.2: The fit parameters for the peak structure analysis in Fig. 4.3a and Fig. 4.3b are summarized in this table. The errors originate all due to statistics.

Figure	peak number	a' [mV]	b' [A]	c' [A]
4.3a	1	3.864 ± 0.016	8.0008 ± 0.0001	0.0270 ± 0.0001
4.3a	2	3.584 ± 0.015	8.9810 ± 0.0001	0.0276 ± 0.0001
4.3b	1	5.170 ± 0.047	8.0017 ± 0.0003	0.0280 ± 0.0003
4.3b	2	0.464 ± 0.046	8.9816 ± 0.0026	0.0229 ± 0.0026

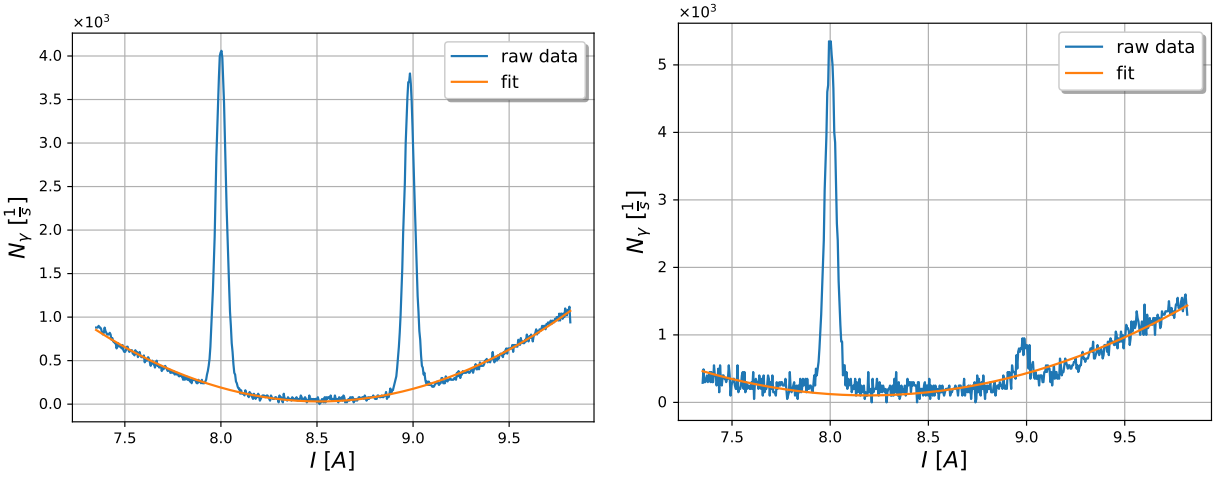

(a) (b)

Figure 4.2: The photomultiplier signal, represented as photon number N_γ, as a function of the electric current, used to ramp up the magnetic field inside the nuclear spin filter is shown. The signal is obtained in a quenching region, where the remaining metastable hydrogen atoms are quenched and the emitted Ly-α photons are detected by a photomultiplier. While Fig. 4.2a shows the result for an unpolarized hydrogen beam, Fig. 4.2b depicts the signal of an initial polarized beam. Moreover, a polynomial fit with Eq. (4.3) has been performed to describe the background, which is strongly beam dependent. Thus tiny changes in intensity and focusing can lead to different backgrounds. The corresponding fit parameters are summarized in Tab. 4.1.

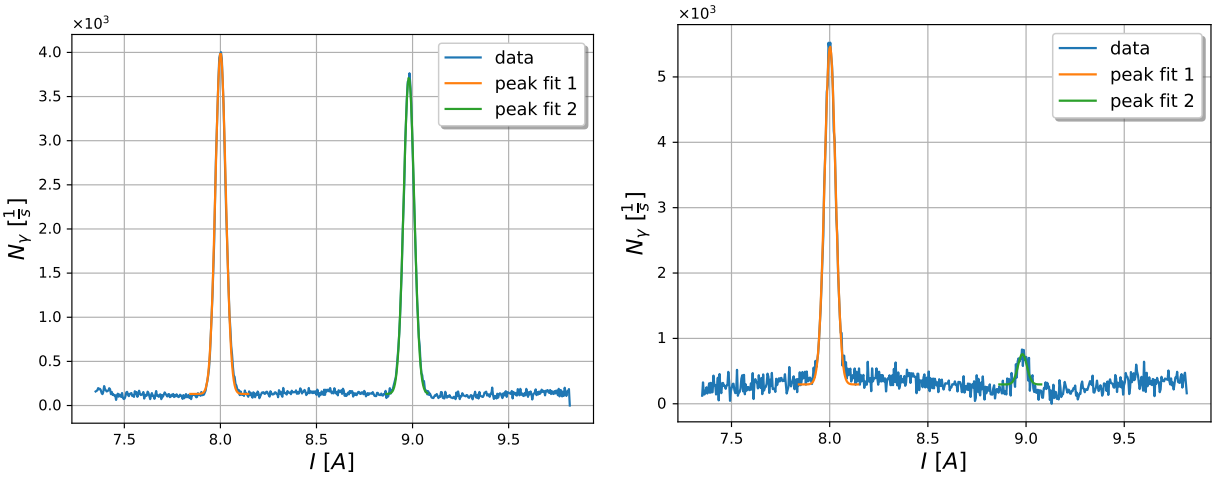

(a) (b)

Figure 4.3: The number of photons N_γ produced in the quenching process of metastable hydrogen atoms as function of the electric current, to ramp up the magnetic field inside the nuclear spin filter is shown. The raw data is subtracted from the background, which is visible in Fig. 4.2a and Fig. 4.2b. The signal is obtained in a quenching region, where the remaining metastable hydrogen atoms are quenched and the emitted Ly-α photons are detected by a photomultiplier. While Fig. 4.3a shows the result for an unpolarized hydrogen beam Fig. 4.3b depicts the signal of an initial polarized beam. In addition, the radio frequency power was too small to suppress the background on both sides entirely. Furthermore, fits based on Eq. (4.4) have been performed to analyze the nuclear spin polarization. The corresponding fit parameters are summarized in Tab. 4.2.

To get a better insight of different parameters effecting the signal, simulations are performed next. Therefore, the Lindblad master equation from Eq. 3.35 is solved numerically in the rest frame of the atom. Due to the small atomic velocities any relativistic corrections are neglected, e.g. the change of the time or additional electromagnetic field components due to the Lorentz transformation. The relativistic treatment for numerical simulations is described in App. I. Subsequently, the Hamiltonian for this system is expressed as

$$H(t) = \tilde{H}_{BR} + H_{Stark} + H_{RF}(t). \tag{4.7}$$

The first part $\tilde{H}_{BR}$ describes the internal energy splitting of the hydrogen-like system, as well as the coupling of their magnetic moments to the homogenous external magnetic field $\vec{B} = B_z \hat{e}_z$. The second term relates the electric dipole interaction due to the external static electric field $\vec{E} = E_x \hat{e}_x$ applied onto the quadrants of the cavity. Finally, the third Hamiltonian models the interaction of the radio frequency with the excited hydrogen-like atoms. Subsequently, the electromagnetic fields for the $\mathrm{TM}_{0,1,0}$ mode are expressed from Eq. (2.175) as

$$\begin{aligned} E_z &= E_0 J_0\left(\frac{2.405r}{R}\right)\cos\left(\omega_{0,1,0}t\right), \\ B_\varphi &= \frac{E_0}{c} J_1\left(\frac{2.405r}{R}\right)\sin\left(\omega_{0,1,0}t\right). \end{aligned} \tag{4.8}$$

First, the electric part is modelled also via an electric dipole interaction described by Eq. (2.93). The corresponding matrix elements are introduced again in the App. D and its substitution into the Lindblad master equation is analogue to the one made in Eq. (3.42). As introduced in Sec. 2.4.3 the external magnetic field couples to the magnetic moments of the atom. Consequently, the

magnetic part of the radio frequency is modelled by

$$\begin{aligned} H_{RF,B} &= \left(g_j\mu_B\frac{\vec{J}}{\hbar} - g_I\mu_k\frac{\vec{I}}{\hbar}\right)\cdot\vec{B} = \left(g_j\mu_B\frac{\vec{J}}{\hbar} - g_I\mu_k\frac{\vec{I}}{\hbar}\right)\cdot B_\varphi\hat{e}_\varphi \\ &= \left(g_j\mu_B\frac{\vec{J}}{\hbar} - g_I\mu_k\frac{\vec{I}}{\hbar}\right)\cdot B_\varphi\left(-\sin(\varphi)\,\hat{e}_x + \cos(\varphi)\,\hat{e}_y\right) \\ &= -g_j\mu_B B_\varphi\sin(\varphi)\frac{J_x}{\hbar} + g_j\mu_B B_\varphi\cos(\varphi)\frac{J_y}{\hbar} + g_I\mu_k B_\varphi\sin(\varphi)\frac{I_x}{\hbar} - g_I\mu_k B_\varphi\cos(\varphi)\frac{I_y}{\hbar} \\ &= \frac{iB_\varphi}{2\hbar}\left[g_j\mu_B\left(e^{i\varphi}J_- - e^{-i\varphi}J_+\right) + g_I\mu_k\left(e^{-i\varphi}I_+ - e^{i\varphi}I_-\right)\right]. \end{aligned} \tag{4.9}$$

Subsequently, it is advantageous to use the uncoupled representation $|m_j, m_I\rangle$ to calculate a general expression for the magnetic radio frequency part in the Lindblad master equation (3.38). Therefore, the additional matrix elements, in form of the commutator $[H_{RF,B}, \rho(t)]$, can be expressed by

$$\begin{aligned} &\langle m_j, m_I|H_{RF,B}\rho(t)|\tilde{m}_j, \tilde{m}_I\rangle = \langle\tilde{m}_j, \tilde{m}_I|\left(H_{RF,B}\rho(t)\right)^\dagger|m_j, m_I\rangle^* \\ &= \langle\tilde{m}_j, \tilde{m}_I|\rho(t)^\dagger H_{RF,B}^\dagger|m_j, m_I\rangle^* = \langle\tilde{m}_j, \tilde{m}_I|\rho(t)H_{RF,B}|m_j, m_I\rangle^* \\ &= \frac{iB_\varphi}{2}\Big[-g_j\mu_B e^{-i\varphi}\sqrt{j(j+1) - m_j(m_j-1)}\,\langle m_j - 1, m_I|\rho(t)|\tilde{m}_j, \tilde{m}_I\rangle \\ &+g_j\mu_B e^{i\varphi}\sqrt{j(j+1) - m_j(m_j+1)}\,\langle m_j + 1, m_I|\rho(t)|\tilde{m}_j, \tilde{m}_I\rangle \\ &-g_I\mu_k e^{i\varphi}\sqrt{I(I+1) - m_I(m_I+1)}\,\langle m_j, m_I + 1|\rho(t)|\tilde{m}_j, \tilde{m}_I\rangle \\ &+g_I\mu_k e^{-i\varphi}\sqrt{I(I+1) - m_I(m_I-1)}\,\langle m_j, m_I - 1|\rho(t)|\tilde{m}_j, \tilde{m}_I\rangle\Big], \end{aligned} \tag{4.10}$$

and

$$\begin{aligned} &\langle m_j, m_I|\rho(t)H_{RF,B}|\tilde{m}_j, \tilde{m}_I\rangle \\ &= \frac{iB_\varphi}{2}\Big[g_j\mu_B e^{i\varphi}\sqrt{j(j+1) - \tilde{m}_j(\tilde{m}_j-1)}\,\langle m_j, m_I|\rho(t)|\tilde{m}_j - 1, \tilde{m}_I\rangle \\ &-g_j\mu_B e^{-i\varphi}\sqrt{j(j+1) - \tilde{m}_j(\tilde{m}_j+1)}\,\langle m_j, m_I|\rho(t)|\tilde{m}_j + 1, \tilde{m}_I\rangle \\ &+g_I\mu_k e^{-i\varphi}\sqrt{I(I+1) - \tilde{m}_I(\tilde{m}_I+1)}\,\langle m_j, m_I|\rho(t)|\tilde{m}_j, \tilde{m}_I + 1\rangle \\ &-g_I\mu_k e^{i\varphi}\sqrt{I(I+1) - \tilde{m}_I(\tilde{m}_I-1)}\,\langle m_j, m_I|\rho(t)|\tilde{m}_j, \tilde{m}_I - 1\rangle\Big]. \end{aligned} \tag{4.11}$$

Finally, the commutator is stated as

$$\begin{aligned} &-\frac{i}{\hbar}\langle m_j, m_I|\left[H_{RF,B}, \rho(t)\right]|\tilde{m}_j, \tilde{m}_I\rangle \\ &= -\frac{B_\varphi}{2\hbar}\Big[g_j\mu_B e^{-i\varphi}\sqrt{j(j+1) - m_j(m_j-1)}\,\langle m_j - 1, m_I|\rho(t)|\tilde{m}_j, \tilde{m}_I\rangle \\ &-g_j\mu_B e^{i\varphi}\sqrt{j(j+1) - m_j(m_j+1)}\,\langle m_j + 1, m_I|\rho(t)|\tilde{m}_j, \tilde{m}_I\rangle \\ &+g_I\mu_k e^{i\varphi}\sqrt{I(I+1) - m_I(m_I+1)}\,\langle m_j, m_I + 1|\rho(t)|\tilde{m}_j, \tilde{m}_I\rangle \\ &-g_I\mu_k e^{-i\varphi}\sqrt{I(I+1) - m_I(m_I-1)}\,\langle m_j, m_I - 1|\rho(t)|\tilde{m}_j, \tilde{m}_I\rangle \\ &+g_j\mu_B e^{i\varphi}\sqrt{j(j+1) - \tilde{m}_j(\tilde{m}_j-1)}\,\langle m_j, m_I|\rho(t)|\tilde{m}_j - 1, \tilde{m}_I\rangle \\ &-g_j\mu_B e^{-i\varphi}\sqrt{j(j+1) - \tilde{m}_j(\tilde{m}_j+1)}\,\langle m_j, m_I|\rho(t)|\tilde{m}_j + 1, \tilde{m}_I\rangle \\ &+g_I\mu_k e^{-i\varphi}\sqrt{I(I+1) - \tilde{m}_I(\tilde{m}_I+1)}\,\langle m_j, m_I|\rho(t)|\tilde{m}_j, \tilde{m}_I + 1\rangle \\ &-g_I\mu_k e^{i\varphi}\sqrt{I(I+1) - \tilde{m}_I(\tilde{m}_I-1)}\,\langle m_j, m_I|\rho(t)|\tilde{m}_j, \tilde{m}_I - 1\rangle\Big]. \end{aligned} \tag{4.12}$$

From here a basis transformation to the Breit-Rabi basis, based on Ch. 3, needs to be performed. For an electric field flux of $E_0 \approx 10^3$ V/m, the magnetic field component has a flux in the order

of $E_0/c \approx 0.1$ μT. Numerical results of the Lindblad master equation Eq. (3.42) in the presence of the magnetic radio wave part is depicted in Fig. 4.4a, while Fig. 4.4b shows the result with $B_\varphi = 0$. By comparing Fig. 4.4a with Fig. 4.4b it is visible, that the magnetic field part of the radio frequency has no influence in the result. Therefore, from here on the magnetic part of the radio frequency is neglected to reduce computational time.

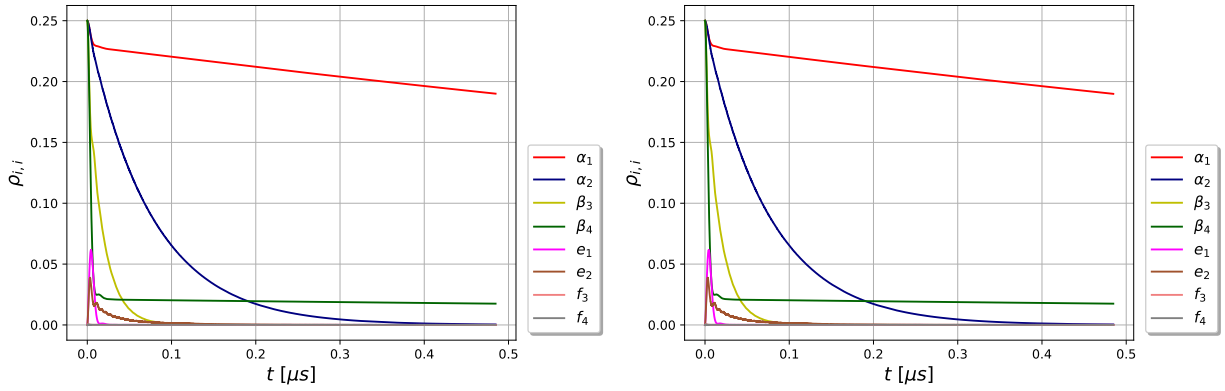

(a) (b)

Figure 4.4: The time evolution of an initially unpolarized metastable hydrogen beam entering the cavity of the nuclear spin filter is displayed. The simulation is performed for fixed parameters indicated in Tab. 4.5. Fig. 4.4a shows the spin dynamics including the magnetic radio frequency part B_φ, while Fig. 4.4b shows the result in its absence.

In addition, the simulations show the selective quenching process at the first Zeeman crossing point around $B_z = 54$ mT, as mainly the α_1 state has a large probability to be found at the extraction point of the cavity. To compare the simulation better with experimental results it is necessary to plot the final points in time of the probabilities $\rho_{i,i}$ as function of the magnetic field flux B_z. Meaning the Lindblad master equation is solved for a set of different magnetic field values B_z and for each of the simulations the values $\rho_{i,i}(t_{end})$ are extracted. The first result is depicted in Fig. 4.5.

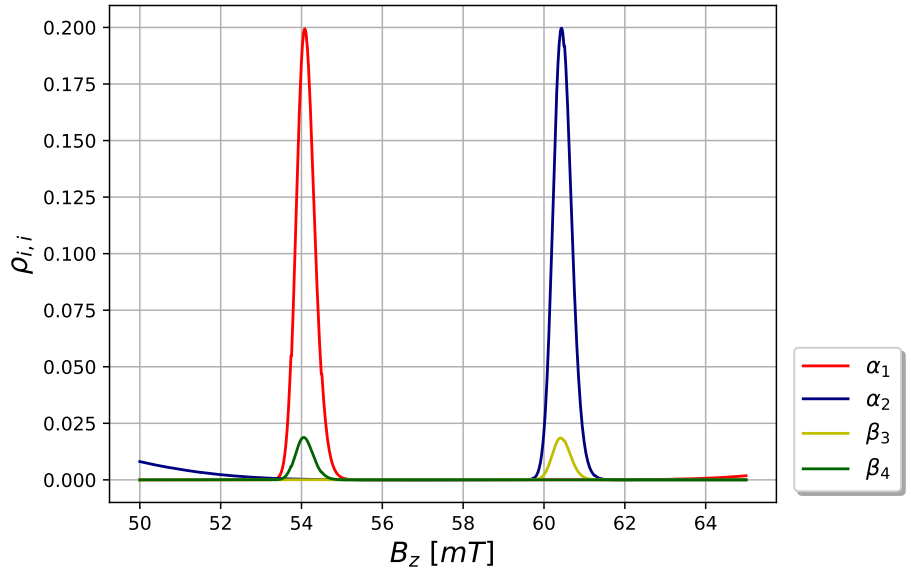

Figure 4.5: The single probabilities of the metastable hydrogen states as function of the homogenous magnetic field flux B_z, when leaving the system of the spin filter are displayed. The parameters to reproduce the simulation are stated in Tab. 4.5.

The result shows the two peaks for the corresponding α states at different magnetic field values B_z for an initially fully unpolarized beam, e.g. $\rho(t = 0) = \mathrm{diag}\,(1/4, 1/4, 1/4, 1/4)$. In addition, small amounts of β states are occupied which do not cause any problem. First of all the β state shares the same magnetic nuclear spin number m_I as the corresponding α state and thereby does not harm the determination of the nuclear spin polarization of the beam. In addition, the β states can be quenched easily by further applied static electric field behind the cavity, due to their reduced lifetime. The simulation parameters are stated at Tab. 4.5. Correspondingly, there are six individual variables E_x, E_0, $f_{m,n,p}$, v, r and Q. Starting with the static electric field E_x, the result for larger electric field fluxes is visible in Fig. 4.6. It shows that the survival probability for the α states is reduced, as larger electric fields reduce the total lifetime of excited states. In addition, the peaks get broader. The explanation is that the electric field flux goes linearly into the transition matrix elements for the β states into the e states. Consequently, the increasing transition values can bridge the energy gap earlier before reaching the Zeeman crossing points. Therefore, the repopulation of the α states, due to the radio frequency, can start for smaller magnetic field values B_z, leading to the broader peaks.

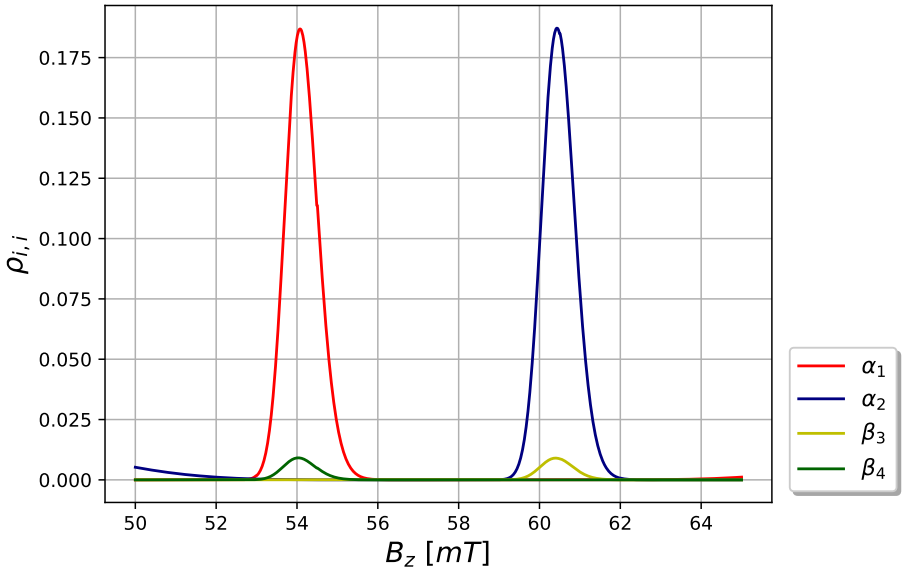

Figure 4.6: The single probabilities of the metastable hydrogen states as function of the homogenous magnetic field flux B_z, when leaving the system of the spin filter are displayed. The parameters to reproduce the simulation are stated in Tab. 4.5. In comparison to Fig. 4.5 the static electric field flux E_x is increased, resulting in broader and less intense peaks.

Furthermore, the electric field of the radio frequency E_0, i.e. directly related to the radio frequency power, is addressed in Fig. 4.7. Again, it is visible that the probabilities of the α peaks decrease. The explanation remains the same as before. With a larger electric field the lifetime of the metastable states are lowered. In addition, the population of the β states increases slightly as the coupling of the e states with the α states is proportional to the electric field of the radio frequency E_0. Consequently, there is a larger population of the e states, which can be transferred back to the β states due to the static electric field component E_x. Moreover, the peaks get more and more narrow. Due to the larger radio frequency field the transition between the short-lived e states and the α states is increased. Consequently, the population of the α states is suppressed when the magnetic field deviates from its value for the resonance condition, leading to narrow peaks.

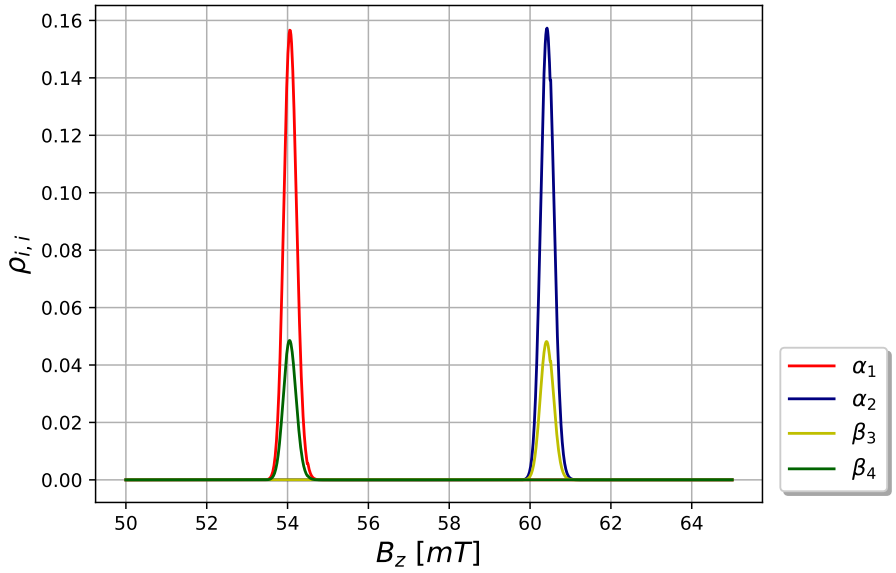

Figure 4.7: The single probabilities of the metastable hydrogen states as function of the homogenous magnetic field flux B_z, when leaving the system of the spin filter are displayed. The parameters to reproduce the simulation are stated in Tab. 4.5. In comparison to Fig. 4.5 the electric field flux E_0 for the radio frequency is increased, resulting in narrower and less intense peaks.

Corresponding measurements reflect the previously discussed effects due to the changing electric fields. In case of increasing voltages, producing the static electric field E_x, the peaks get broader, which is visible by comparing Fig. 4.8a, Fig.4.8b, Fig. 4.9a and Fig. 4.9b. The small peak in between the two α peaks in Fig. 4.9b is due to bad vacuum condition. At this point the radio frequency together with the static fields of the spin filter, ignite a plasma in the rest gas, which is detected by the photomultiplier. Furthermore, Fig. 4.10a, Fig. 4.8a and Fig. 4.10b show that the increase of the radio frequency power results in a flat background as well as even narrower peaks.

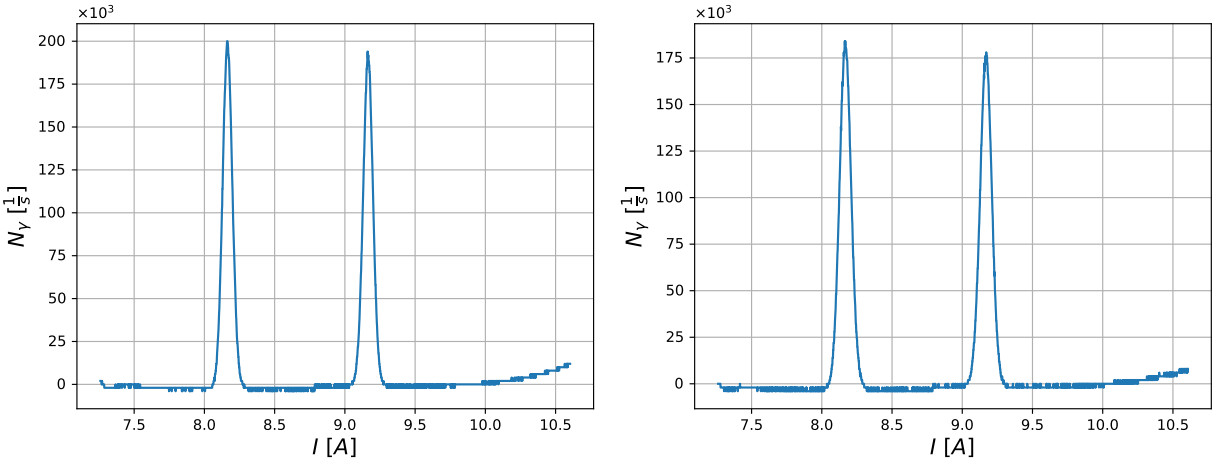

(a) (b)

Figure 4.8: The number of Ly-α photons N_γ per second as function of the current I sent into the coils of the nuclear spin filter is displayed. The photons are created due to the quenching process of remaining metastable hydrogen atoms in the quenching region. More explanations to the detection process are given in Sec. 5.3. The settings of the experimental parameters for the nuclear spin filter are summarized in Tab. 4.3. The measurement for Fig. 4.8b has utilized larger static electric fields in comparison to the measurement for Fig. 4.8a, resulting in broader less intense peaks.

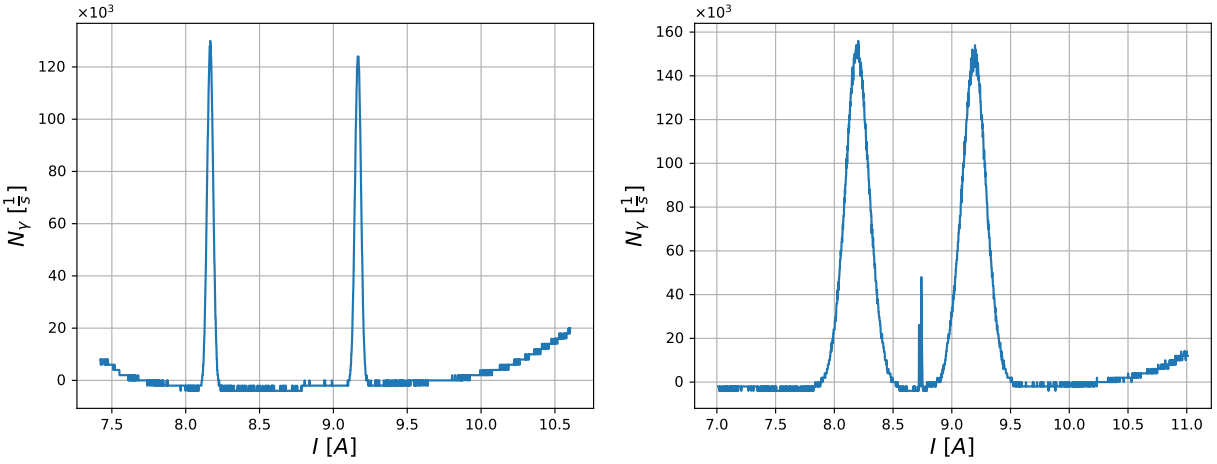

(a) (b)

Figure 4.9: The number of Ly-α photons N_γ per second as function of the current I sent into the coils of the nuclear spin filter is displayed. The photons are created due to the quenching process of remaining metastable hydrogen atoms in the quenching region. More explanations to the detection process are given in Sec. 5.3. The settings of the experimental parameters for the nuclear spin filter are summarized in Tab. 4.3. The measurement for Fig. 4.9a has utilized smaller static electric fields while the corresponding measurement for Fig. 4.9b used larger ones in comparison to the measurement for Fig. 4.8a. This leads to less intensive peaks. In addition, in Fig. 4.9b a small peak around $I \approx 8.7$ A due to a plasma ignition is visible.

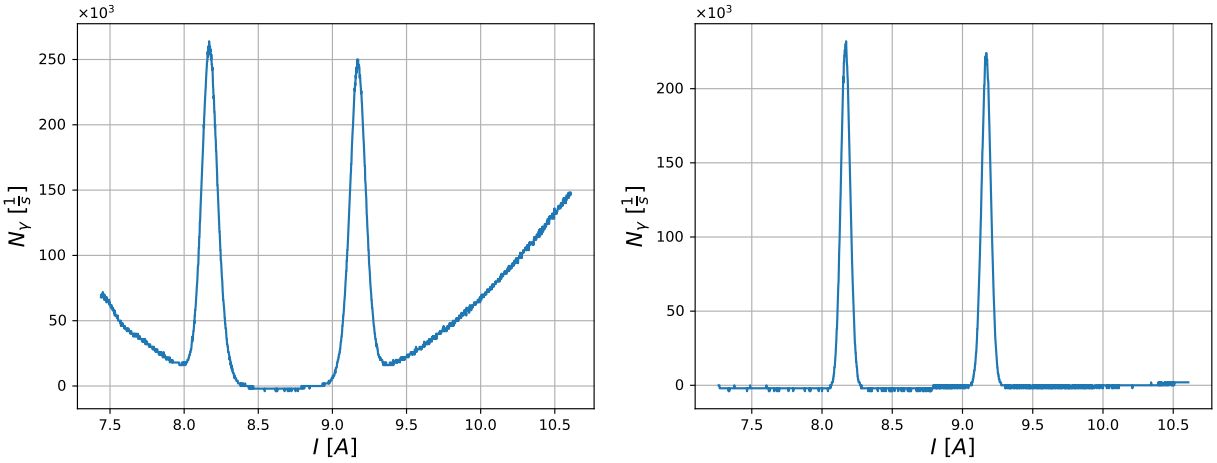

(a) (b)

Figure 4.10: The number of Ly-α photons N_γ per second as function of the current I sent into the coils of the nuclear spin filter is displayed. The photons are produced due to the quenching process of remaining metastable hydrogen atoms in the quenching region. More explanations to the detection process are given in Sec. 5.3. The settings of the experimental parameters for the nuclear spin filter are summarized in Tab. 4.3. The measurements for Fig. 4.10a and Fig. 4.10b utilize different radio frequency powers in comparison to the measurement for Fig. 4.8a.

Moreover, the resonance frequency $f_{m,n,p}$ is addressed. Simulations with different frequencies $f_{0,1,0}$ are displayed in Fig. 4.11a and Fig. 4.11b. The task of the resonance frequency is to overcome the energy gap between the α and the e states, as explained in the beginning of the chapter in Eq. (4.1). The optimal frequency would exactly fill up the energy from the Zeeman crossing point of the β and e states to the corresponding α state. Unfortunately, the energy differences are not perfectly equal at their Zeeman crossing points. Luckily, their values deviate only very little, which means that a frequency in the area of the Zeeman crossing points can be chosen such that the reinforcement of the coupling by the power of the radio frequency is sufficient. Consequently, the repopulation of the single α states works as long as the value of the resonance frequency corresponds to an energy gap in the Zeeman crossing point area, e.g. $B_z \approx 52$ mT to $B_z \approx 62$ mT. In Fig. 4.11a such a case is shown, while in Fig. 4.11b the resonance frequency has been chosen outside from the Zeeman crossing point area. Furthermore, it is visible that the peaks appear at different magnetic field values for Fig. 4.11a in comparison to Fig. 4.5 as the chosen frequency fills up the energy gap better at these points.

Table 4.3: The experimental settings for the single measurements are summarized in this table. The voltages $U_{\text{pos.}/\text{neg.}}$ are applied onto the single quadrants of the cavity, while $U_{\text{pos. s.}/\text{neg. s.}}$ are applied on the entrance and exit of the cavities to produce static external electric field. Moreover, the input radio frequency power is introduced in the units of dBm [147].

Figure	E_{kin} [keV]	$U_{\text{pos.}}$ [V]	$U_{\text{neg.}}$ [V]	$U_{\text{pos. s.}}$ [V]	$U_{\text{neg. s.}}$ [V]	P_{RF} [dBm]	$f_{0,1,0}$ [GHz]
4.8a	1	114	−107	41	−42	23	1.60991
4.8b	1	131	−126	41	−42	23	1.60991
4.9a	1	40	−40	41	−42	23	1.60991
4.9b	1	300	−234	41	−42	23	1.60991
4.10a	1	114	−107	41	−42	17	1.60991
4.10b	1	114	−107	41	−42	25	1.60991

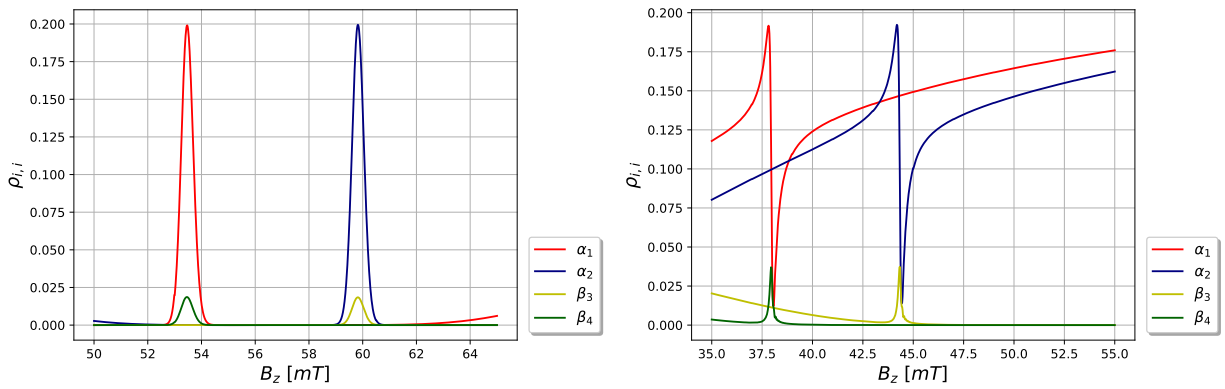

(a) (b)

Figure 4.11: The occupation numbers of the metastable hydrogen states as function of the magnetic field flux B_z are displayed. The necessary parameters are obtainable in Tab. 4.5. To produce Fig. 4.11a a resonance frequency of $f_{0,1,0}$ = 1.59229 GHz has been chosen, while for Fig. 4.11b the resonance frequency is $f_{0,1,0}$ = 1.15734 GHz.

The next parameter is the beam velocity in z-direction v. It is strongly limited due to the production cross section for metastable states, which is explained in more detail in Sec. 5.2. Furthermore, it is not directly influencing the spin dynamics but the time of flight through the cavity and therefore the interaction time. Moreover, the length d can compensate for any change in velocity as the $TM_{0,1,0}$ mode is not dependent on a specific value for d. This differs for the next two sections Sec. 4.2, Sec. 4.3.3 and is discussed there in more detail. Subsequently, the radius r in the xy-plane is discussed, which enters in the Bessel functions of the first kind $J_m(x)$ from Eq. (2.170). Some of the relevant Bessel functions for the radius R = 7.13 cm are presented in Fig. 4.12. Generally, apertures of 15 to 20 mm are limiting the beam size and are much smaller than the 7 cm radius of the cavity. Therefore, the change in the Bessel function is small, which impacts the spin dynamic only by a small degree. This is visible by comparing the two figures Fig. 4.32a and Fig. 4.32b. Therefore, in this case the beam profile is not of a great importance, which might change by employing a different mode as the number n dictates how many zero crossing are encountered by the Bessel function $J_m(x)$.

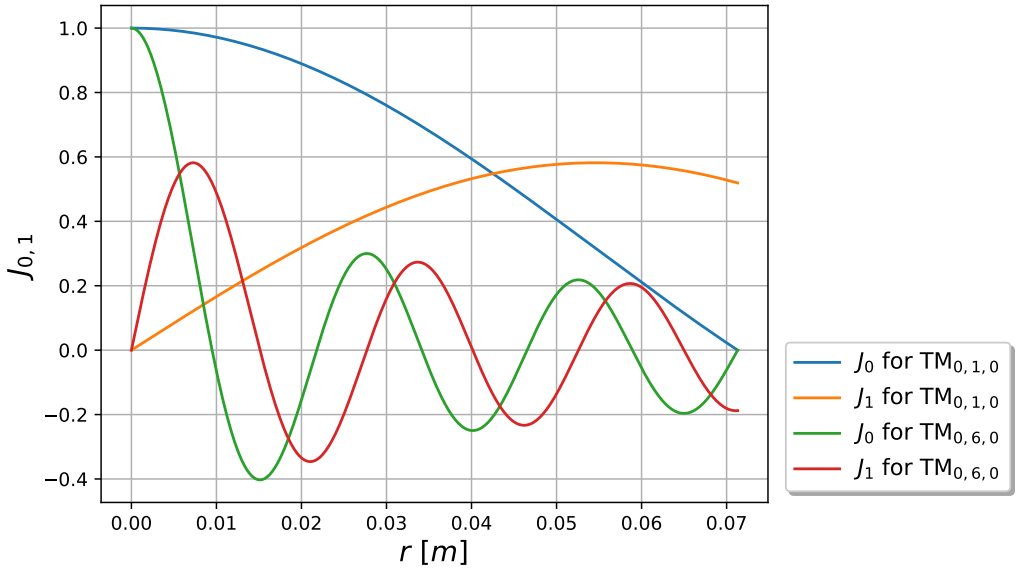

Figure 4.12: Some relevant Bessel functions of the first kind $J_m\left({}^{x_{m,n}r}/_{R}\right)$ are plotted as function of the radius r for a maximum radius $R = 7.13$ cm.

Finally, the quality factor Q is discussed. For now an ideal cavity has been addressed in which only one resonance frequency fits. In reality the electromagnetic waves can penetrate the surface of the cavity walls, as discussed in Sec. 2.6. This leads to a bunch of possible frequencies around the resonance frequency being created at the same time. The corresponding frequency spectrum is given by a Lorentz distribution

$$f\left(\omega, \omega_{m,n,p}, Q\right) = \frac{1}{\left(\omega - \omega_{m,n,p}\right)^2 + \frac{\omega_{m,n,p}^2}{4Q^2}}, \tag{4.13}$$

introduced in Eq. (2.191) and depicted in Fig. 4.13.

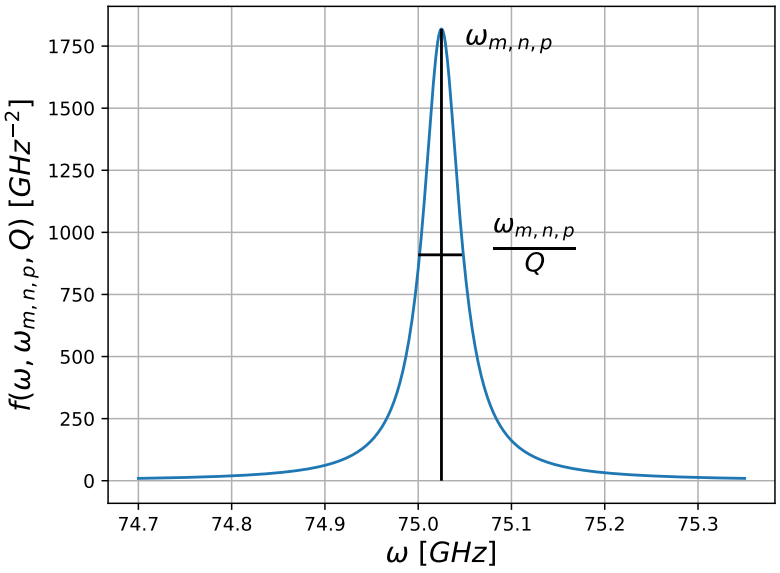

Figure 4.13: The Lorentz distribution introduced in Eq. (4.13) is depicted as function of circular frequencies, with a quality factor of $Q = 1600$ and a resonance frequency of $f_{m,n,p} = 11.94059$ GHz.

Subsequently, a measurement of the frequency band in a cylindrical cavity has been conducted.

Therefore, a frequency generator coupled the electromagnetic waves into the cavity, while the power output was extracted at the opposite wall of the cavity. By manually going through the frequency band and writing down the corresponding power output values, the resonance frequency distribution can be plotted. The data points are visible in Fig. 4.14, where an additional Lorentz fit is applied

$$F(f, A, Q, f_0) = \frac{A}{(f - f_0)^2 + \frac{f_0^2}{4Q^2}}. \tag{4.14}$$

The according fit parameters are stated in Tab. 4.4. The statistical uncertainty for the power output and the frequency generator have been determined by the last visible digit on the displays. Furthermore, Gaussian law of propagation of uncertainty has been applied to adjust the errors for the power output from dBm to watts [147]. Subtracting the fit values from the data, results in a residual plot, which is depicted in Fig. 4.15. In this plot, a symmetry is clearly observable, which explains the large deviation of the χ^2/ndf from one as the statistical errors are much smaller than the systematic ones. Its reasoning can origin from different sources, e.g. no constant temperature, no perfect setting of the step tuner. The latter is of great importance as the step tuner elongates the cable such that the electromagnetic wave corresponding to the resonance frequency enters with its maximal amplitude into the cavity. Small deviations in the optimal cable length create an asymmetry in the frequency band. Nevertheless, the value of the quality factor

$$Q = \frac{f_0}{\Delta f}, \tag{4.15}$$

as well as the resonance frequency f_0 are in good agreement to the data shown in Fig. 4.14.

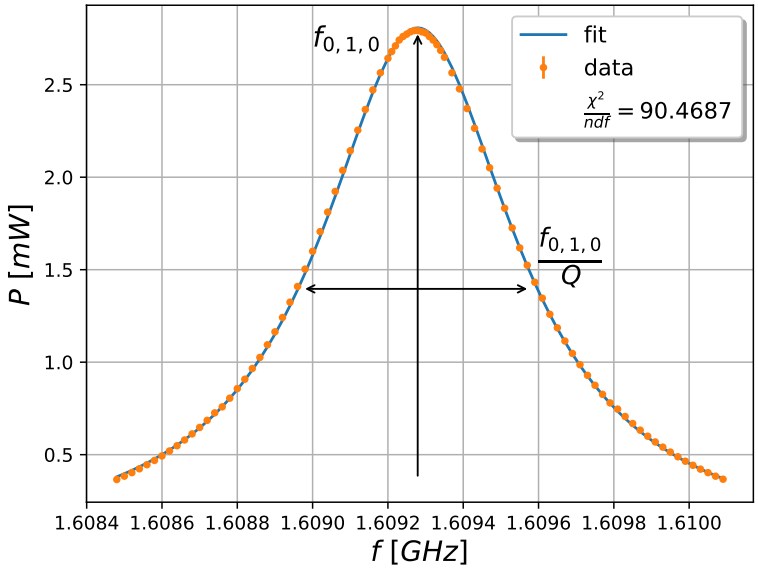

Figure 4.14: The power output of a resonance frequency f_0 inside the cavity is plotted as function of the induced frequency f. A corresponding Lorentz fit, based on Eq. (4.13), has been performed. The corresponding fit parameters are summarized in Tab. 4.4

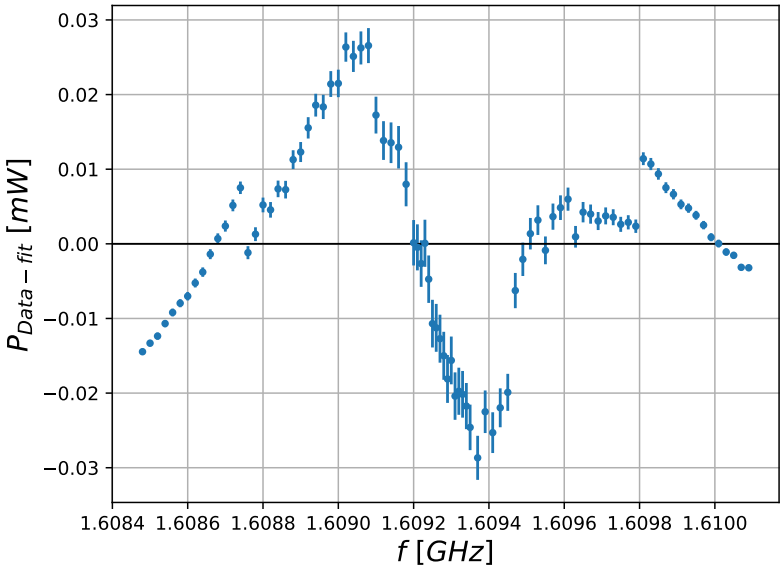

Figure 4.15: The data points are subtracted from the corresponding Lorentz fit, which is depict in Fig. 4.14, and then plotted as function of the applied frequency f.

To model the frequency band in the cavity the entire electric field produced by the radio frequencies is described by a sum of the individual frequency components

$$\vec{E}_{RF}(t) = \sum_k \vec{E}_{RF_k} \approx \sum_k E_{0,k} \cos(\omega_k t)\, J_0\left(\frac{x_{m,n} r}{R}\right) \hat{e}_z, \tag{4.16}$$

with

$$E_{0,k} = \frac{E_0 f(\omega_k, \omega_{m,n,p}, Q)}{\sum_k f(\omega_k, \omega_{m,n,p}, Q)}. \tag{4.17}$$

The amplitude $E_{0,k}$ guarantees the correct influence of each mode due to the Lorentz distribution. In addition, the denominator ensures convergence of the sum, while its value is proportional to the applied power. Subsequently, several simulations have been performed for different Q-values and the results are depicted in Fig. 4.16a, Fig. 4.16b and Fig. 4.17. If the Q value is too small, visible in Fig. 4.16a for $Q = 300$, the frequency band is larger and the power is distributed more equally over all modes. Subsequently, at different magnetic fields B_z frequencies can be found, which fill up the energy gap between the α and e states. As a result the peaks are not resolvable anymore and run into each other as the Zeeman crossing points are smeared out. Correspondingly, this sets a lower limit for the quality factor of the cylindrical cavity. Moreover, the results for a single resonance frequency are recovered by increasing the quality factor. This is visible by comparing Fig. 4.17 with Fig. 4.5.

Table 4.4: The fit parameters as well as the corresponding results of the χ^2-method are indicated for the frequency spectrum of the cylindrical cavity. The data and the according fit are shown in Fig. 4.14. The uncertainties are all statistical nature.

A [nW]	Q	$f_{0,1,0}$ [kHz]	χ^2	σ_f [Hz]	σ_P [dBm]
280.7 ± 0.6	2545 ± 5	1609279.1±0.4	7780.3090	0.05	0.005

Table 4.5: The necessary specifications to produce the numerical simulations in this Sec. 4.1 are introduced.

Figure	$E_x \left[\frac{\text{kV}}{\text{m}}\right]$	$E_0 \left[\frac{\text{kV}}{\text{m}}\right]$	$v \left[\frac{\text{m}}{\text{s}}\right]$	B_z [mT]	r [m]	d [m]	R [m]	Q
4.4	1.8	1.1	309500	54	0.01	0.15	0.0713	∞
4.5	1.8	1.1	309500	50 – 65	0	0.15	0.0713	∞
4.6	2.5	1.1	309500	50 – 65	0	0.15	0.0713	∞
4.7	1.8	2	309500	50 – 65	0	0.15	0.0713	∞
4.11a	1.8	1.1	309500	50 – 65	0	0.15	0.0721	∞
4.11b	1.8	1.1	309500	50 – 65	0	0.15	0.0992	∞
4.16a	1.8	1.1	309500	50 – 65	0	0.15	0.0713	300
4.16b	1.8	1.1	309500	50 – 65	0	0.15	0.0713	1600
4.17	1.8	1.1	309500	50 – 65	0	0.15	0.0713	6000
4.18	1.8	1.1	309500	50 – 65	0	0.15	0.0713	∞
4.19	1.8	1.1	309500	50 – 65	0	0.15	0.0713	∞
4.20	1.55	1.1	437694.72	50 – 65	0	0.15	0.072	2545

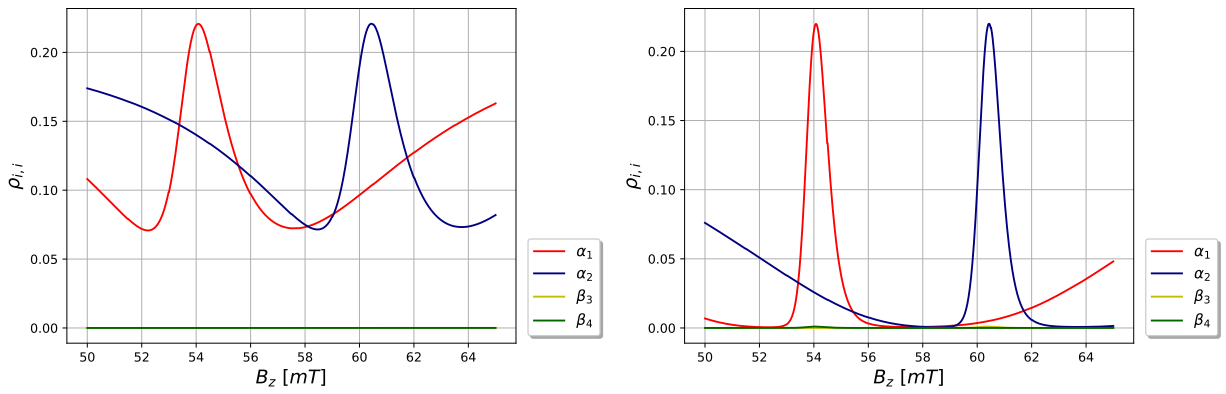

(a) (b)

Figure 4.16: The occupation numbers of the metastable hydrogen states as function of the magnetic field flux B_z are displayed. The necessary parameters are obtainable in Tab. 4.5. Fig. 4.16a shows the spin dynamics for a quality factor Q = 300, while Fig. 4.16b shows the result for Q = 1600.

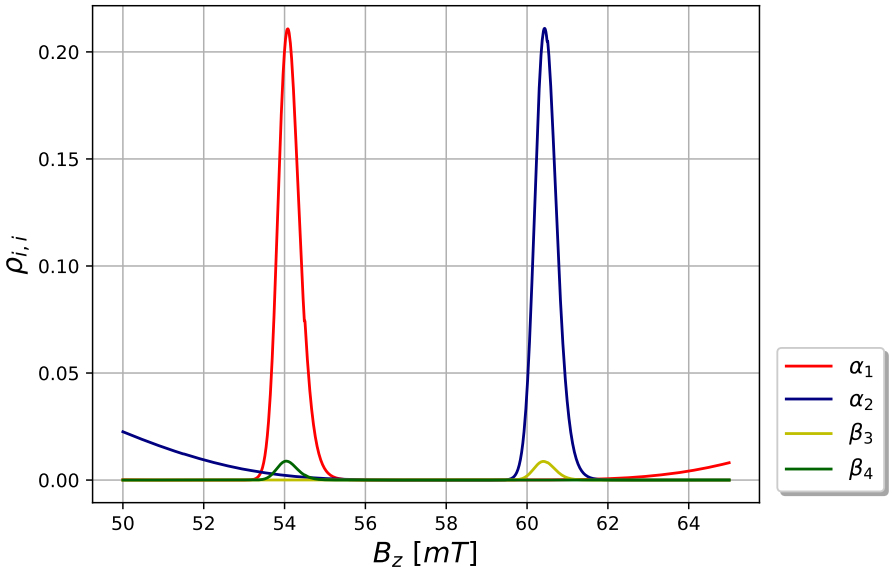

Figure 4.17: The simulation shows the occupation numbers for the metastable hydrogen states as function of the external magnetic field flux B_z for a quality factor of Q = 6000. The necessary parameters are summarized in Tab. 4.5.

Moreover, it is visible that the background created by the α_2 population is larger than the one produced by α_1, resulting in unequal peak heights even for an unpolarized spectra. This problem can be resolved by choosing a smaller resonance frequency. This is shown in Fig. 4.20, where a simulation is compared to the measurement shown first in Fig. **??**. Simulations for deuterium, visible in Fig. 4.18 show similar results with three distinguishable peaks, each representing one α state. Due to the fact that the nuclear g-factor g_I is much smaller than for hydrogen, the hyperfine splitting A is also reduced, which results in the small magnetic field area where the Zeeman crossing points between the β and e states happen in the Breit-Rabi diagram. Consequently, the three peaks are positioned very close to each other on the horizontal axis.

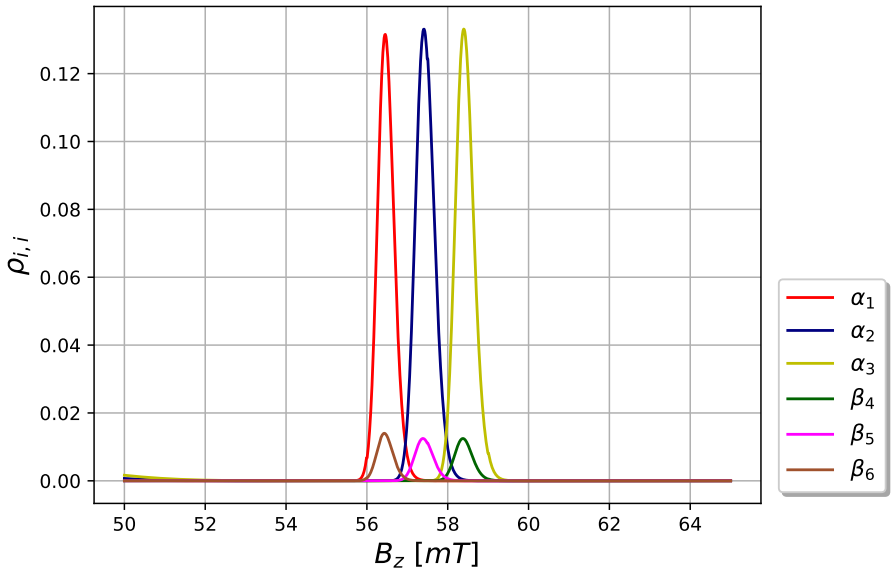

Figure 4.18: The simulation shows the occupation numbers for the metastable deuterium states as function of the external magnetic field flux B_z. The necessary parameters are given in Tab. 4.5.

Finally, a simulation is performed for the radioactive tritium, visible in Fig. 4.19. Due to the comparable hydrogen spin dynamics the result are very similar. Subsequently, the gap on the horizontal axis between the peaks increases slightly. The reason for it is the larger nuclear g-factor and correspondingly the more substantial hyperfine constant A.

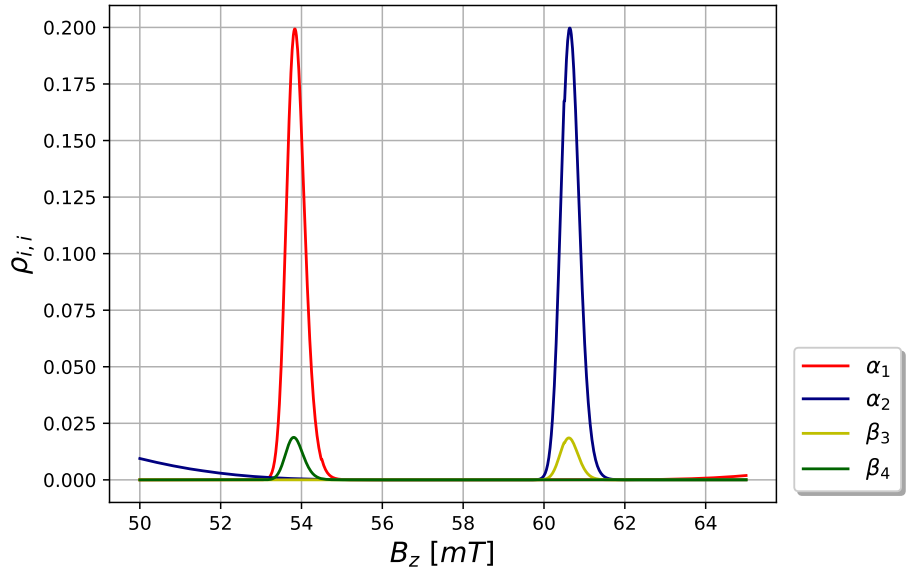

Figure 4.19: The simulation shows the occupation numbers for the metastable tritium states as function of the external magnetic field flux B_z. The necessary parameters are available in Tab. 4.5.

Finally, a full simulation is compared with a measurement resulting in an overall large agreement, visible in Fig. 4.20. Even for the most complex structures of measurements the simulation can reproduce the increase in the background very convincingly. The actual electric field flux E_0 of the radio frequency is difficult to be determined, therefore it is treated as a free parameter for the simulation. The reason is that the power supplied by the radio frequency generator is unequal to the power with which the standing wave builds up. In addition, it is visible that other parameters as the resonance frequency can vary slightly, which results in imperfections of the calibration of the frequency generator. In this case the frequency of the measurement $f_{\text{Measurement}} = 1.60991$ GHz has a discrepancy of about 1% to the frequency used in the simulation $f_{\text{Simulation}} \approx 1.59376$ GHz. Moreover, exact voltage values, to determine the static electric field E_x, are dependent on the resistance of cables from the power supplies to the cavity.

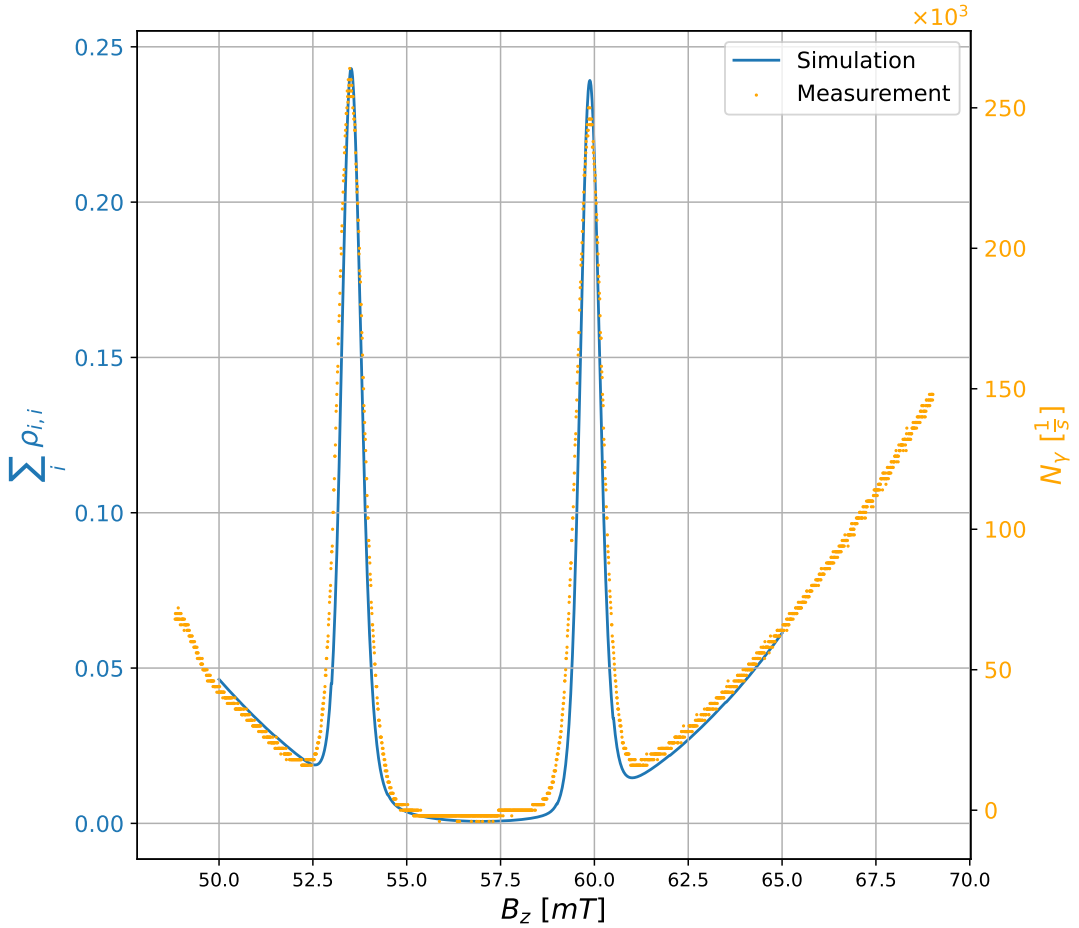

Figure 4.20: The measurement of Fig. 4.10a is compared to a corresponding simulation where its numeric parameter are summarized in Tab. 4.5.

4.1.1 The entropy of the system

In this section, the entropy S, as one of the state functions of this system, is introduced to visualize the change in polarization. Thereby, the focus lies only on the change of the occupation number of the original metastable atoms, while the far more abundant ground state atoms in the beam are not considered. Therefore, complete simulations for the old spin filter from Sec. 4.1 are shown, which include the artificial ground state g. Once full knowledge of the density operator ρ is obtained, it is possible to calculate the entropy of the system via the definition stated by von-Neumann [146]

$$S = -k_B \mathrm{Tr}\left(\rho \ln\left(\rho\right)\right). \tag{4.18}$$

Here, k_B stands for the Boltzmann constant. In the energy eigenbasis the density operator of the nuclear spin filter is stated as

$$\rho(t) = \sum_{i \epsilon \{2S_{1/2} \text{ and } 2P_{1/2}\}} p_i \left|i\right\rangle \left\langle i\right| + \sum_{\tilde{g}} p_{\tilde{g}} \left|\tilde{g}\right\rangle \left\langle \tilde{g}\right|, \tag{4.19}$$

where the first sum runs over all excited states while the second runs over the number of degenerated ground states $\tilde{g}$. It is a good assumption as the 10.2 eV energy gap between the $1S_{1/2}$ and the $2S_{1/2}$ states is much larger than the internal hyperfine and Zeeman energy splitting and, therefore, in average all four ground states will be equally populated. Thus, the entropy can be calculated

as

$$S(t) = -k_B \sum_j \langle j|\rho(t) \ln(\rho(t))\,|j\rangle = -k_B \left[\sum_{i\epsilon\{2S_{1/2} \text{ and } 2P_{1/2}\}} p_i \ln(p_i) + \sum_{\tilde{g}} p_{\tilde{g}} \ln(p_{\tilde{g}}) \right]. \tag{4.20}$$

In case of a fully initially polarized beam the density operator describes a pure state hence the entropy vanishes. This is visible in Fig. 4.23a and Fig. 4.24a at time $t = 0$. In case of a fully unpolarized metastable beam the ensemble is described by

$$\rho = \sum_{i\epsilon\{2S_{1/2}\}}^{\tilde{g}} p_i \,|i\rangle \langle i|\,, \tag{4.21}$$

where $p_i = p = 1/\tilde{g}$ as the number of ground and metastable states are equal. Therefore, the entropy is

$$S = -k_B \sum_{i\epsilon\{2S_{1/2}\}}^{\tilde{g}} p_i \ln(p_i) = k_B \ln(\tilde{g})\,. \tag{4.22}$$

In case of hydrogen $\tilde{g} = 4$ the entropy is equal to $S = k_B \ln(4) \approx 1.38\, k_B$, which is its value in Fig. 4.23b and Fig. 4.24b at $t = 0$. In addition, the entropy turns back to this value for $t \to \infty$ when all excited states decayed. This is well visible in Fig. 4.24b. At the beginning of the cavity the electromagnetic fields start repopulating the different states, which lets the entropy increase as the lack of information rises. When the states depopulate the probability to find the atom in the ground states increases and thereby the entropy moves exponentially towards the value of $k_B \ln(\tilde{g})$. Next, a derivation based on [146] is done to understand more where the change of the entropy originates from. A system with a fixed number of particles is assumed then the internal energy of the system is expressed as

$$E = \langle H \rangle = \mathrm{Tr}(\rho H)\,. \tag{4.23}$$

Consequently, the differential form is stated as

$$dE = \mathrm{Tr}(H d\rho + \rho dH)\,. \tag{4.24}$$

Analogue, the differential form of the entropy based on Eq. (4.18) is given by

$$dS = -k_B \mathrm{Tr}\left(\ln(\rho)\, d\rho + \rho \frac{d\rho}{\rho}\right) = -k_B \mathrm{Tr}(\ln(\rho)\, d\rho) \underbrace{-k_B \mathrm{Tr}(d\rho)}_{=0, \text{ because: } \mathrm{Tr}(\rho+d\rho)\approx \mathrm{Tr}(\rho)=1} \tag{4.25}$$

Inserting the density operator for the canonical ensemble

$$\begin{aligned} \rho &= \frac{1}{Z} e^{-H\beta}, \\ \text{with} \quad Z &= \mathrm{Tr}\left(e^{-H\beta}\right) \quad \text{and} \quad \beta = \frac{1}{k_B T}, \end{aligned} \tag{4.26}$$

in Eq. (4.25) leads to

$$dS = -k_B \mathrm{Tr}\left(\ln\left(\frac{1}{Z} e^{-H\beta}\right) d\rho\right) = k_B \underbrace{\mathrm{Tr}(\ln(Z)\, d\rho)}_{=0, \text{ as } \mathrm{Tr}(d\rho)=0} + \frac{1}{T} \mathrm{Tr}(H d\rho)\,. \tag{4.27}$$

Subsequently, inserting the result from Eq. (4.27) into Eq. (4.24) results in

$$dE = T dS + \mathrm{Tr}(\rho dH) = T dS + \left\langle \frac{\partial H}{\partial a} \right\rangle da = \delta Q + \delta W, \tag{4.28}$$

where a is any parameter in the Hamiltonian and δQ is an incremental change in the thermal energy and δW an incremental change in the work. By comparing the energy of a system in its eigenbasis with the last result the following relation is obtained

$$E = \sum_n p_n E_n \quad \Rightarrow \quad dE = \underbrace{\sum_n E_n dp_n}_{=\delta Q} + \underbrace{\sum_n p_n dE_n}_{=\delta W} . \tag{4.29}$$

Thus, changes in the entropy origin due to the change of the probabilities of given eigenenergies as it is observable in the figures below, while the external fields entering in the Hamiltonian change the eigenenergies as visible in the Breit-Rabi diagram in Ch. 3.

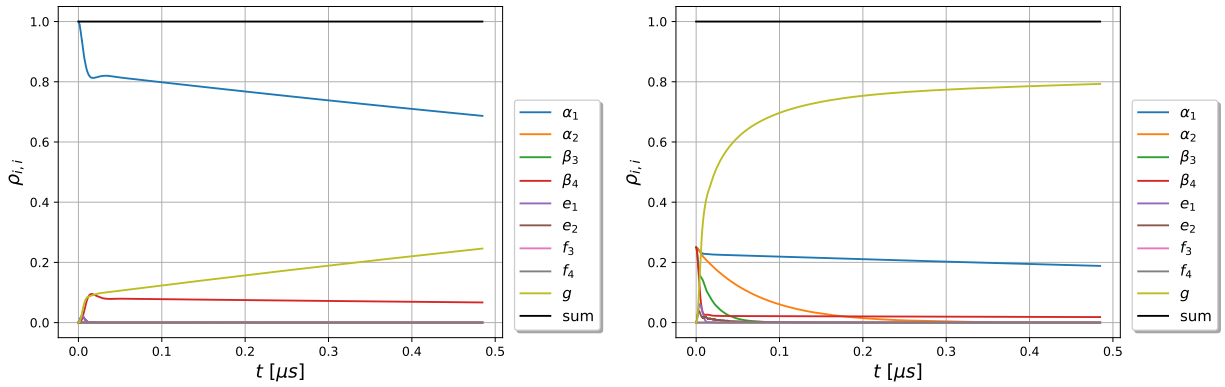

(a) (b)

Figure 4.21: The occupation numbers of the single Breit-Rabi states and the artificial ground state g as function of the time they travel through the cavity are displayed. For reproducibility the parameters are given in Tab. 4.6. In addition, the initial condition for Fig. 4.21a is a fully polarized α_1 state with $\rho(t=0) = \mathrm{diag}(1,0,0,0)$ while for Fig. 4.21b it is an unpolarized condition expressed as $\rho(t=0) = \mathrm{diag}(1/4, 1/4, 1/4, 1/4)$. Finally, the simulations are evaluated at a magnetic field $B = 54$ mT, where the resonance of α_1 is given.

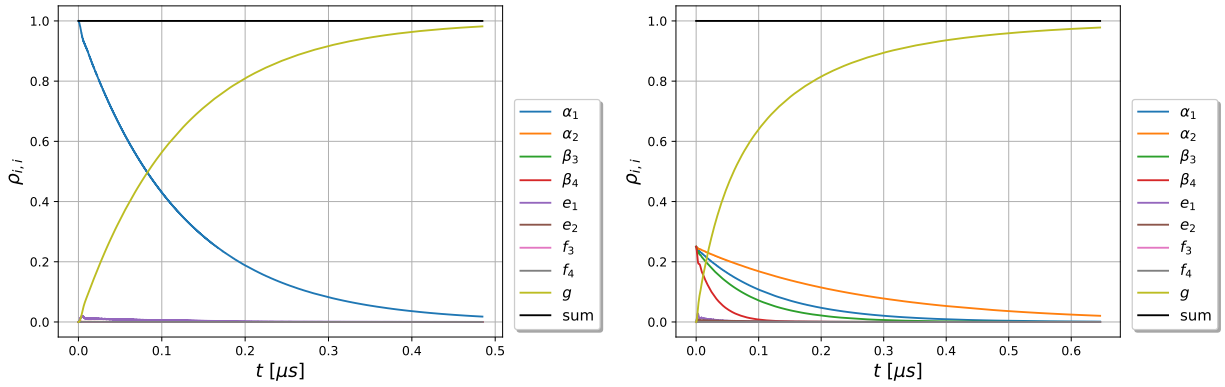

(a) (b)

Figure 4.22: The occupation numbers of the single Breit-Rabi states and the artificial ground state g as function of the time they travel through the cavity are displayed. For reproducibility the parameters are given in Tab. 4.6. In addition, the initial condition for Fig. 4.22a is a fully polarized α_1 state with $\rho(t=0) = \mathrm{diag}(1,0,0,0)$ while for Fig. 4.22b it is an unpolarized condition expressed as $\rho(t=0) = \mathrm{diag}(1/4, 1/4, 1/4, 1/4)$. In addition, a magnetic field value $B = 45$ mT is used for the simulations, for which all metastable states are eventually quenched.

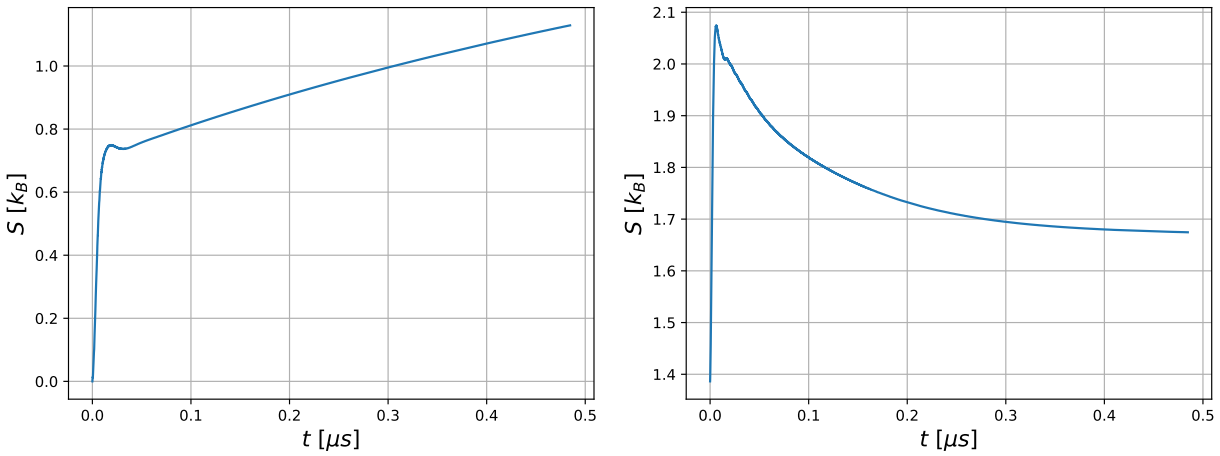

(a) (b)

Figure 4.23: The state function entropy S in units of k_B, the Boltzmann constant, as function of the time the atom needs to travel through the cavity is displayed. Fig. 4.23a is gained by the change of the density operator shown in Fig. 4.21a, while Fig. 4.23b shows the entropy for a density operator as given in Fig. 4.21b.

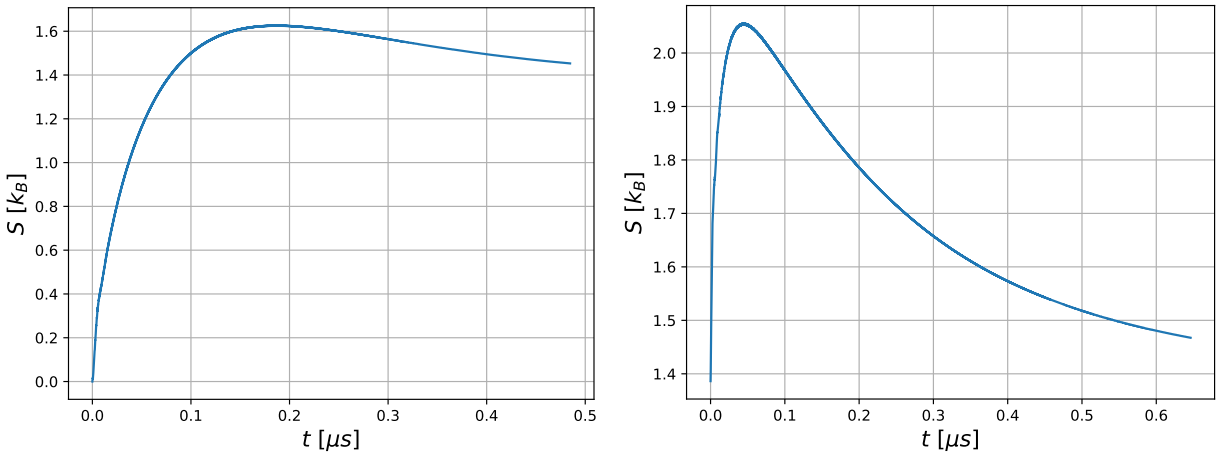

(a) (b)

Figure 4.24: The state function entropy S in units of k_B, the Boltzmann constant, as function of the time the atom needs to travel through the cavity is displayed. Fig. 4.24a is gained by the change of the density operator shown in Fig. 4.22a, while Fig. 4.24b shows the entropy for a density operator as given in Fig. 4.22b.

4.2 2nd generation spin filter

In Ch. 1 different experiments are motivated, where their success relies on detecting not only the α states but more importantly the β states. The nuclear spin filter, introduced in Sec. 4.1, is limited to the selection of α states. Consequently, either a new device needs to be designed or the nuclear spin filter needs to be upgraded, such that its functionality can be applied to all given hyperfine states. This upgrade is also discussed in [148]. To be capable of selecting single β states the α states need to be coupled to short-living states via the Stark effect. Therefore, a magnetic field regime needs to be found in which short-living states energetically cross the α states. For any magnetic field the $2P_{1/2}$ set is never crossing the α states. Thus another set of states is needed. The

Table 4.6: The parameters for the simulations introduced in this Sec. 4.1.1 are summarized.

Figure	$E_x \left[\frac{\text{kV}}{\text{m}}\right]$	$E_0 \left[\frac{\text{kV}}{\text{m}}\right]$	$v \left[\frac{\text{m}}{\text{s}}\right]$	B_z [mT]	r [m]	$\text{TM}_{m,n,p}$	Q
4.21a	1.8	1.1	309500	54	0	$0,1,0$	∞
4.21b	1.8	1.1	309500	54	0	$0,1,0$	∞
4.22a	1.8	1.1	309500	45	0	$0,1,0$	∞
4.22b	1.8	1.1	309500	45	0	$0,1,0$	∞

$2P_{3/2}$ set fulfills the requirements because it is energetically shifted by the fine structure. Suitable Zeeman crossings appear at magnetic fields around $B = 427$ mT. Consequently, the resonance frequency to couple the β states to the $2P_{3/2}$ set is increased significantly to $f = 11.94059$ GHz. To produce this frequency a different mode needs to be exploited. Different options are possible and are summarized in Tab. 4.7. The corresponding electromagnetic fields coupled into the cavity are, based on Eq. (2.175), expressed as

$$\begin{aligned}
\text{TM}_{0,6,0}: \quad E_z &= E_0 J_0\left(\frac{18.07106r}{R}\right)\cos\left(\omega_{0,6,0}t\right), \\
B_\varphi &= \frac{E_0}{c} J_1\left(\frac{18.07106r}{R}\right)\sin\left(\omega_{0,6,0}t\right), \\
\text{TM}_{0,1,p}: \quad E_r &= \frac{p\pi 2.405 E_0}{Rd\left(\frac{\omega_{0,1,p}^2}{c^2} - \frac{p^2\pi^2}{d^2}\right)} J_1\left(\frac{2.405r}{R}\right)\sin\left(\frac{p\pi z}{d}\right)\cos\left(\omega_{0,1,p}t\right), \\
E_z &= E_0 J_0\left(\frac{2.405r}{R}\right)\cos\left(\frac{p\pi z}{d}\right)\cos\left(\omega_{0,1,p}t\right), \\
B_\varphi &= \frac{2.405 E_0 \omega_{0,1,p}}{c^2 R\left(\frac{\omega_{0,1,p}^2}{c^2} - \frac{p^2\pi^2}{d^2}\right)} J_1\left(\frac{2.405r}{R}\right)\cos\left(\frac{p\pi z}{d}\right)\sin\left(\omega_{0,1,p}t\right).
\end{aligned} \tag{4.30}$$

The selection process for a special mode is based on several aspects. The most important fact is that the mode needs to have an electric field component parallel to the beam, i.e. E_z-component. Thus, all TE modes are not suitable. Next, it is necessary to remove as many different electromagnetic field components as possible to simplify the transition process. In addition, this assures that the lifetime of the surviving metastable state is not impacted by too many electric field components. Therefore, TM modes with $m = 0$ have been chosen. Lastly, the mode demands a cavity with specific proportions that must also be physically realizable. Subsequently, a device that filters all four metastable states individually requires a cavity with a radius fixed by the configuration described in Sec. 4.1, e.g. $R = 7.13$ cm. Due to the fact that the resonance frequency is roughly 10 times larger than the one for the already existing nuclear spin filter, the quality factor Q of the cylindrical cavity also needs to be 10 times larger. The direct proportionality of the resonance frequency to the quality factor Q is stated in Eq. (4.15). If its value is too low the peaks cannot be distinguished as they run into each other. This is also shown in simulations depicted in Fig. 4.34a and Fig. 4.34b. Building cylindrical cavities with significant quality factors is its own large research area, where it is predominately utilized in accelerator physics. Quality factors of orders 10^6 are realized at CERN (Conseil Européen pour la Recherche Nucléaire) [149, 150, 151]. So far cavities utilized in Sec. 4.1 are not made out of one piece of metal rather than out of four single quadrants isolated by the vacuum, which is depicted in Fig. 4.25.

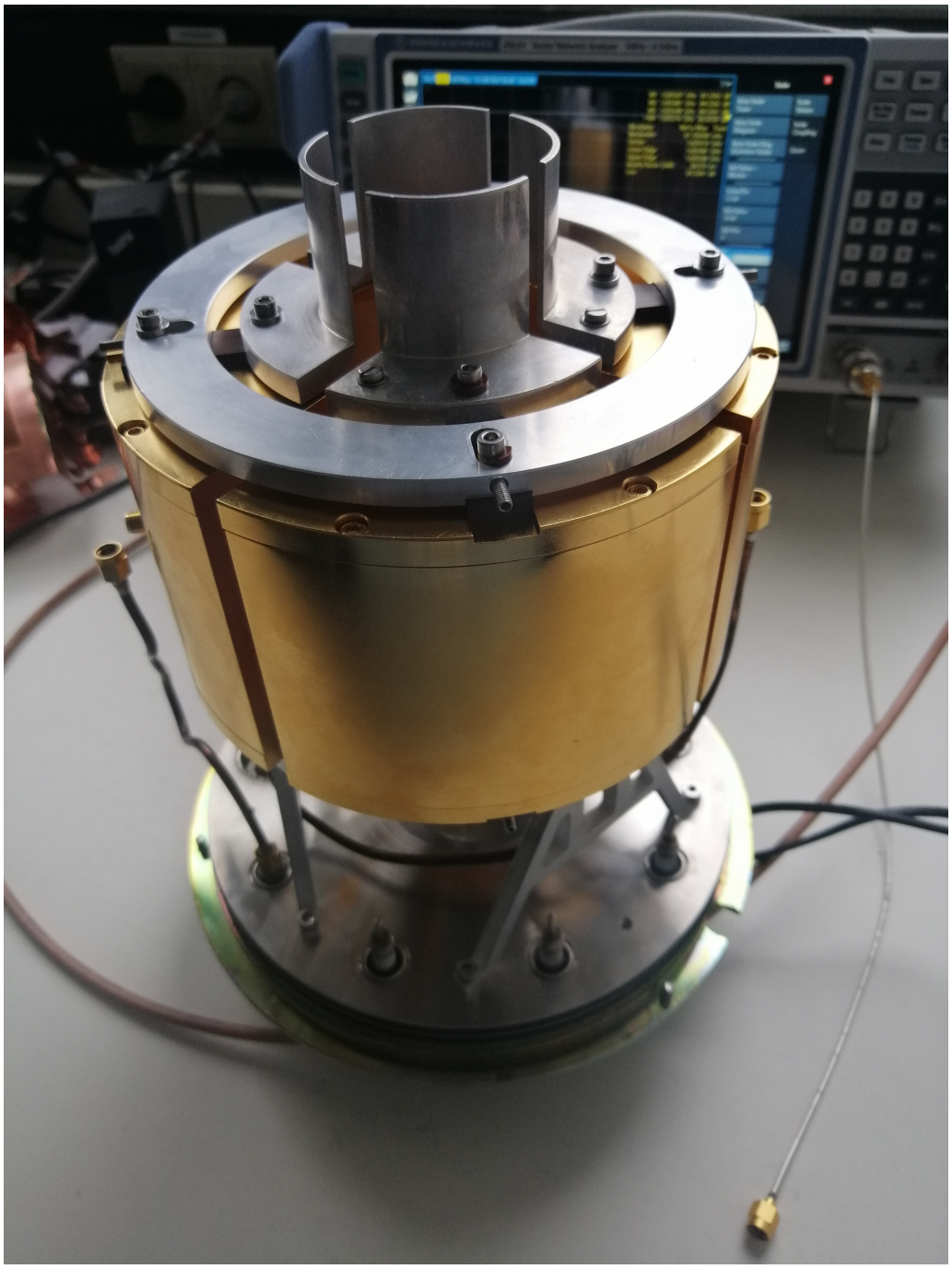

Figure 4.25: The gold layered cavity, which is utilized in the already existing spin filter from Sec. 4.1 is shown. It is mounted onto one of the flanges, which is standing on the table. This construction simplifies the extraction and reinstallation of the cavity.

Based on [152] the theoretical calculation of the quality factor due to the material, which has been used to built the cavity, is stated as

$$Q = 0.38 \frac{\lambda_0}{\delta} \frac{1}{1 + \frac{R}{d}}. \tag{4.31}$$

Here, λ_0 is the corresponding wavelength of the resonance frequency and δ is the skin depth

$$\delta = \sqrt{\frac{2\rho}{\omega_0 \mu}} \sqrt{\sqrt{1 + (\rho \omega_0 \varepsilon)^2} + \rho \omega_0 \varepsilon}, \tag{4.32}$$

where ρ stands for the electric resistivity of the material, while μ is the permeability and ε the permittivity. Silver is one of the best materials to build cavities because of its low resistivity. At low temperatures it reaches low values, e.g. $\rho = 10^{-11}\,\Omega$m [153]. Consequently, to improve the quality factor the spin filter would need to be cooled down to a few Kelvin. In addition, the cavity should be made of one solid cylinder with four separations made as thin as possible out of an isolating material. A design is shown in Fig. 4.26. To reach the necessary magnetic fields of 430 mT along the cavity superconducting coils are required for the solenoid. Thus, the cooling of the surrounding coils can be used to keep the cavity on these low temperatures. With additional values for the permeability μ [154] and permittivity ε [155] a value of roughly $Q \sim 420000$ can be reached theoretically. This means at low temperatures there is still more than an order of magnitude in between the theoretical value and the desired one $Q \approx 16000$. Therefore, losses due to the isolations of the four quadrants and imperfections in the fabrication process can be accounted.
In addition, it is important that other electromagnetic modes are not influencing the spin dynamics. Consequently, some resonance frequencies of different modes have been calculated for the dimensions $d = 5.068$ cm and $R = 7.13$ cm corresponding to the chosen $\mathrm{TM}_{0,1,4}$ mode. The necessary roots are summarized in App. G. Resonance frequencies have been calculated for $m = 0$ up to $m = 5$, $n = 1$ to $n = 6$ and $p = 0$ (respectively $p = 1$ for the TE mode) to $p = 99$. The resulting Lorentz distributions of the frequency spectrum with a Quality factor of $Q = 16000$ are depicted in Fig. 4.27.

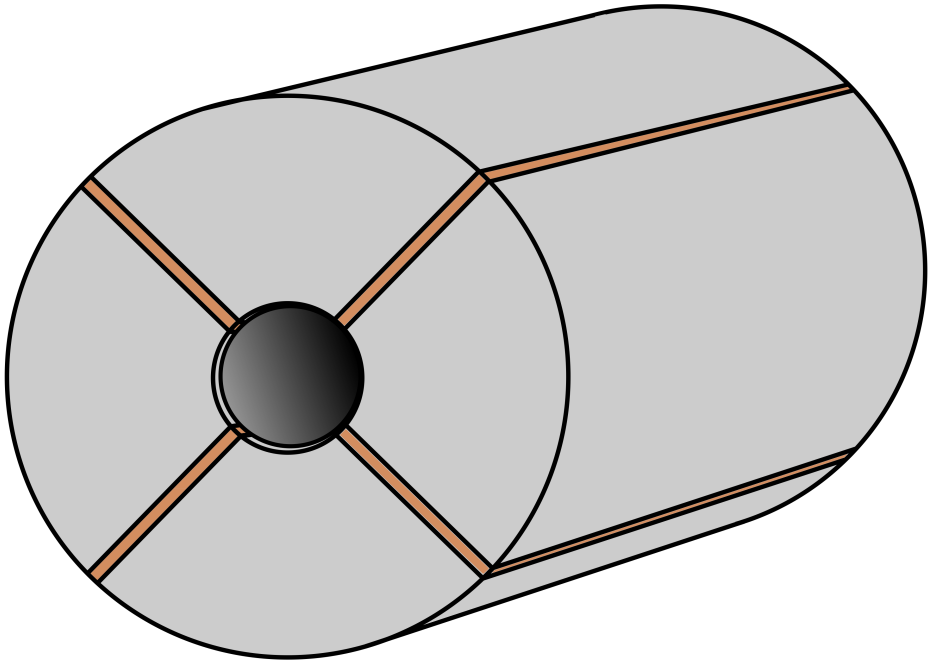

Figure 4.26: The design shows a cavity fabricated out of four quadrants of metal and having a silver layer. Thin isolation layers fix the single metal parts back to one cylinder.

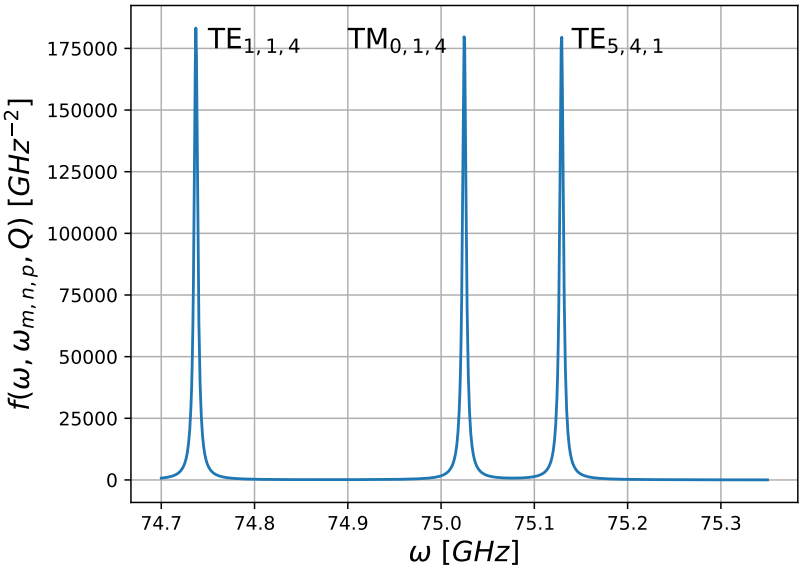

Figure 4.27: The Lorentz distributions are plotted as function of the angular frequency with a quality factor $Q = 16000$. The figure shows the $TE_{1,1,4}$, $TE_{5,4,1}$ as well as the $TM_{0,1,4}$ mode.

The $TM_{0,1,4}$ mode, for which the dimensions are fixed, has no interference with any other mode. The $TM_{0,6,0}$ has the advantage of being independent of the length d but has the disadvantage of having six roots. In the following the spin dynamics of the spin states is simulated by solving Eq. (3.35) numerically in the rest frame of the atom, as it is already done in the previous Sec. 4.1. Again any relativistic corrections due to the transformation into the rest frame are neglected. Due to the small velocity the Galilean transformation, as limit case of the Lorentz transformation, is utilized. Therefore, the position argument of the beam is replaced by $z = vt$. A more detailed relativistic treatment is compiled in App. I. Subsequently, corresponding simulation parameters are summarized in Tab. 4.8.

Fig. 4.28a shows the result of the numerical simulation for the $TM_{0,6,0}$ mode. It has perfect conditions but the mode itself has a disadvantage as it can be observed in Fig. 4.12. The Bessel function of the first kind $J_0\left(x_{0,6}r/R\right)$ has six roots in total, which makes its variation for different radii very relevant. Consequently, a small beam diameter needs to be chosen, when utilizing this mode, which would cost total intensity. In comparison, Fig. 4.28b shows the β peaks for the $TM_{0,1,1}$ mode. For this mode an experimental realization is quite challenging as the length of the cavity is only $d \approx 1.3$ cm. Due to the short time of flight the resultant peaks are much broader.

Table 4.7: The table introduces the different cavity modes exploited in this Sec. 4.2.

$TM_{m,n,p}$	$x_{m,n}$	d [m]	R [m]	$f_{m,n,p}$ [GHz]
$0, 6, 0$	18.07106	0.15	0.0722	11.94228
$0, 1, 1$	2.405	0.0126691095	0.0713	11.94059
$0, 1, 2$	2.405	0.025338219	0.0713	11.94059
$0, 1, 4$	2.405	0.050676438	0.0713	11.94059
$0, 1, 0$	2.405	0.050676438	0.0713	1.60941
$0, 1, 10$	2.405	0.126691095	0.0713	11.94059

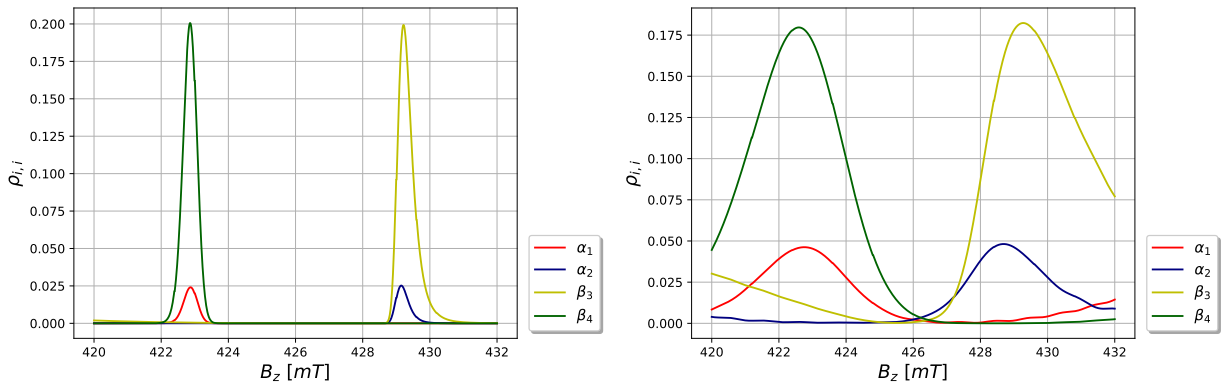

(a) (b)

Figure 4.28: The single probabilities of the metastable Breit-Rabi states of hydrogen as function of the magnetic field flux B_z are displayed. The necessary parameters for reproducibility are indicated in Tab. 4.8. Moreover, Fig. 4.28a is produced my modelling the $TM_{0,6,0}$ mode, while for Fig. 4.28b the $TM_{0,1,1}$ mode is utilized.

Furthermore, the $TM_{0,1,2}$ and $TM_{0,1,4}$ modes are investigated next in Fig. 4.29a and Fig. 4.29b. Similar results with broad but separable β peaks are visible. In comparison to larger p modes, shown in Fig. 4.31 for the $TM_{0,1,10}$, the $TM_{0,1,4}$ mode combines everything to be utilized for an experimental setting. It has a dimension of the cavity, which is experimentally realizable as well as relative large intensities. For each larger p value another zero crossing appears for the electrical component of the electromagnetic wave in Eq. (4.30), which reduces the intensity. Unfortunately, the $TM_{0,1,4}$ mode produces peaks, which are too broad to resolve the single β states for deuterium, which is depicted in Fig. 4.30b. In addition, the mode has the great advantage that the upgrade can be incorporated into the model of the old spin filter, discussed in Sec. 4.1, as it has the same radius of $R = 7.13$ cm. Only the length d changes. To compensate for the shorter time of flight, larger fields are utilized for the $TM_{0,1,0}$ mode. The results are visible for different radii in Fig. 4.32a and Fig. 4.32b. The deuterium β peaks however are well resolvable in the $TM_{0,6,0}$ mode depicted in Fig. 4.30a.

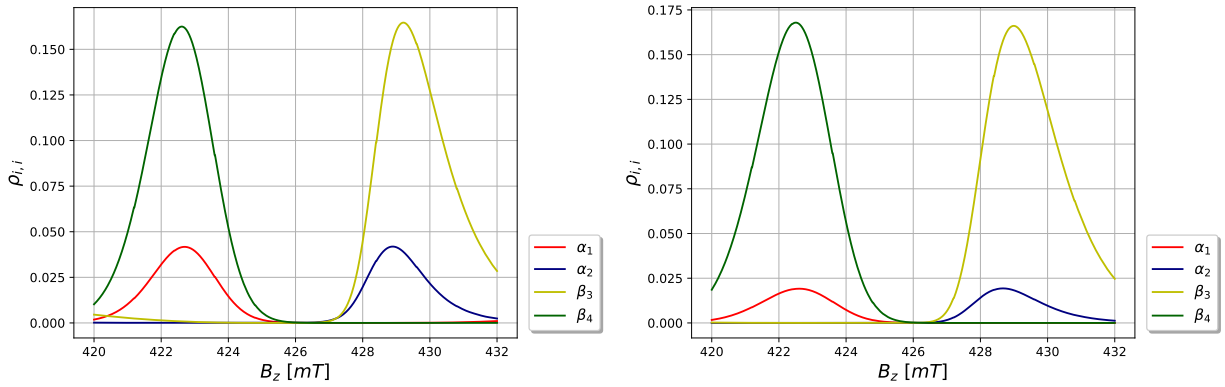

(a) (b)

Figure 4.29: The single probabilities of the metastable Breit-Rabi states of hydrogen as function of the magnetic field flux B_z are displayed. The necessary parameters for reproducibility are indicated in Tab. 4.8. Moreover, Fig. 4.29a is produced my modelling the $TM_{0,1,2}$ mode, while for Fig. 4.29b the $TM_{0,1,4}$ mode is utilized.

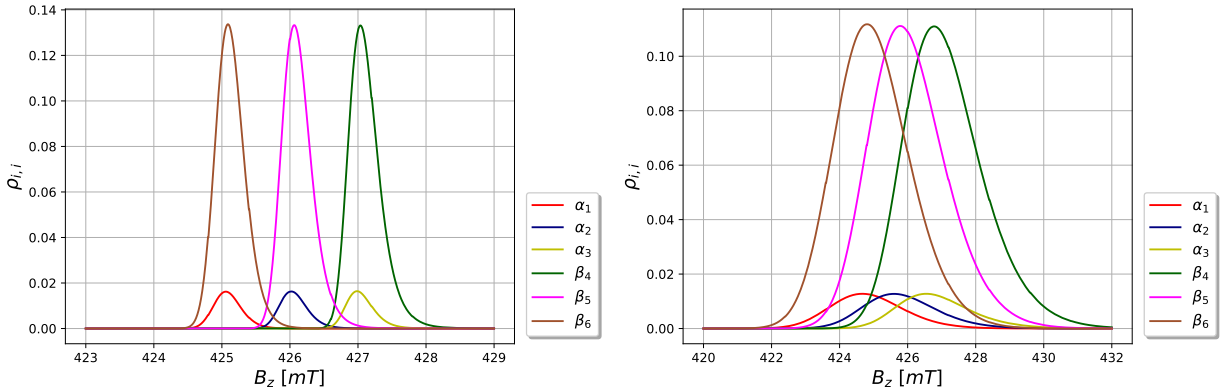

(a) (b)

Figure 4.30: The single probabilities of the metastable Breit-Rabi states of deuterium as function of the magnetic field flux B_z are displayed. The necessary parameters for reproducibility are indicated in Tab. 4.8. Moreover, Fig. 4.30a is produced my modelling the $TM_{0,6,0}$ mode, while for Fig. 4.30b the $TM_{0,1,4}$ mode is utilized.

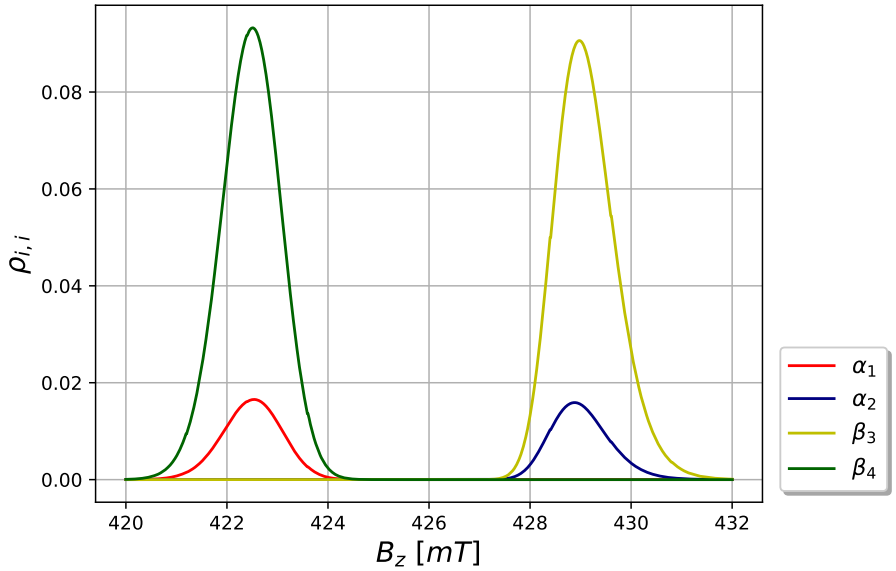

Figure 4.31: The single probabilities of the metastable Breit-Rabi states of hydrogen as function of the magnetic field flux B_z are displayed. The necessary parameters for reproducibility are indicated in Tab. 4.8. The $TM_{0,1,10}$ has been used to produce the simulation.

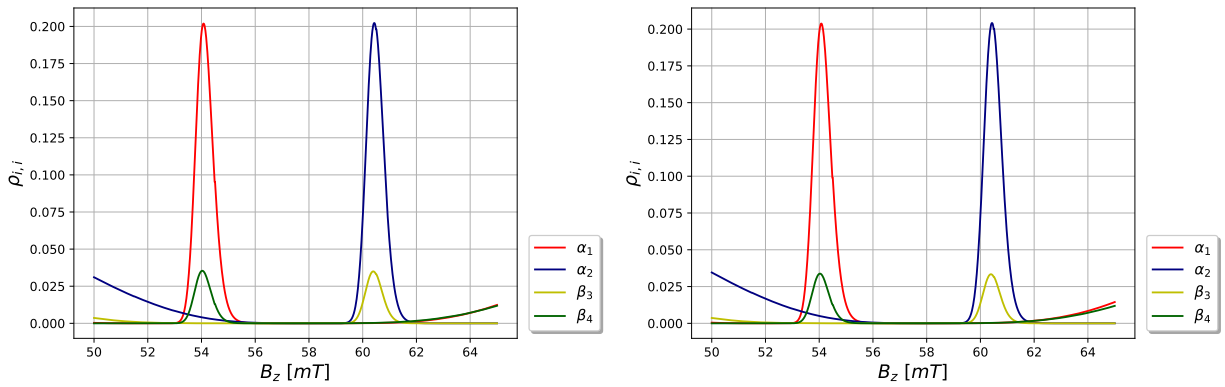

(a) (b)

Figure 4.32: The single probabilities of the metastable Breit-Rabi states of hydrogen as function of the magnetic field flux B_z are displayed. The necessary parameters for reproducibility are indicated in Tab. 4.8. Fig. 4.32a thereby shows the simulation of a hydrogen atom at fixed radius of $r = 1$ mm, while the radius to produce Fig. 4.32b is $r = 1$ cm.

Finally, a simulation for the tritium atom in the case of the $TM_{0,6,0}$ mode is illustrated in Fig. 4.33. Again the similarities to the hydrogen spin dynamics result in similar peak structures as explained in Sec. 4.1.

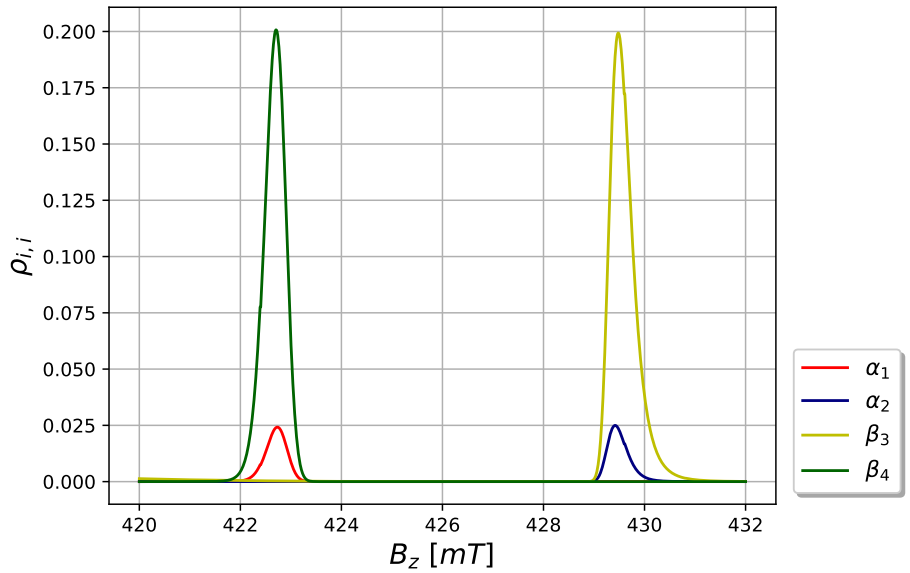

Figure 4.33: The single probabilities of the metastable Breit-Rabi states of tritium as function of the magnetic field flux B_z are displayed. The necessary parameters for reproducibility are indicated in Tab. 4.8. The $TM_{0,6,0}$ mode has been utilized to produce the simulation.

Table 4.8: The necessary specifications used for the numerical simulations in this Sec. 4.2 are presented. The dimensions of the cavity are introduced in Tab. 4.7.

Figure	E_x $\left[\frac{\text{kV}}{\text{m}}\right]$	E_0 $\left[\frac{\text{kV}}{\text{m}}\right]$	v $\left[\frac{\text{m}}{\text{s}}\right]$	B_z [mT]	r [m]	$\text{TM}_{m,n,p}$	Q
4.28a	2.6	0.9	309500	420 – 432	0	$0,6,0$	∞
4.28b	5	2.5	309500	420 – 432	0	$0,1,1$	∞
4.29a	5	2.5	309500	420 – 432	0	$0,1,2$	∞
4.29b	6	2	309500	420 – 432	0	$0,1,4$	∞
4.30a	2.6	0.9	309500	423 – 429	0	$0,6,0$	∞
4.30b	6	2	309500	420 – 432	0	$0,1,4$	∞
4.31	6	2.5	309500	420 – 432	0	$0,1,10$	∞
4.32a	1.8	1.5	309500	50 – 65	0.001	$0,1,0$	∞
4.32b	1.8	1.5	309500	50 – 65	0.01	$0,1,0$	∞
4.33	2.6	0.9	309500	420 – 432	0	$0,6,0$	∞
4.34a	2.6	0.9	309500	420 – 432	0	$0,6,0$	1600
4.34b	2.6	0.9	309500	420 – 432	0	$0,6,0$	16000

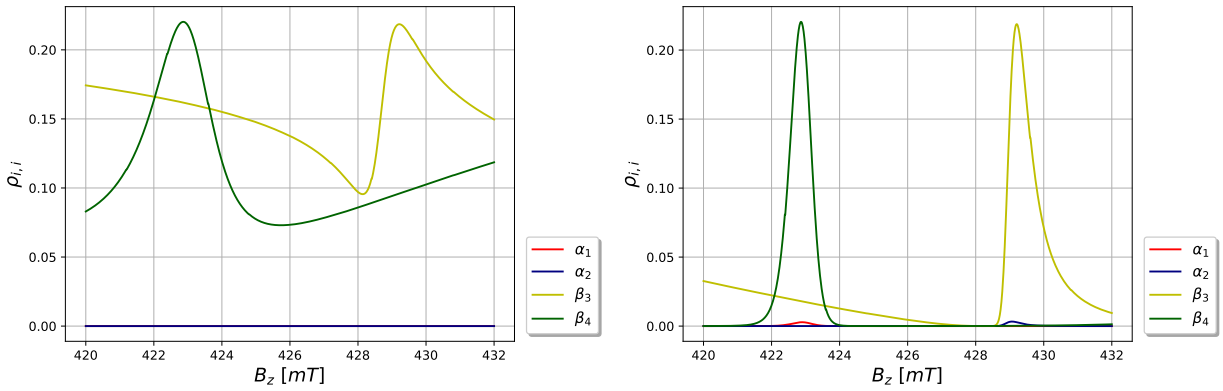

(a) (b)

Figure 4.34: The single probabilities of the metastable Breit-Rabi states of hydrogen as function of the magnetic field flux B_z are displayed. The necessary parameters for reproducibility are indicated in Tab. 4.8. For the production of Fig. 4.34a a quality factor of $Q = 1600$ is used, while for Fig. 4.34b $Q = 16000$ has been utilized.

Fig. 4.34a and Fig. 4.34b depict full numerical simulations including a Lorentz distribution for the frequency spectrum. The energy gap at the corresponding magnetic Zeeman crossing points is unequal, as already described in Sec. 4.1. In the case of the upgraded spin filter this energy difference is enlarged causing the peaks to be shaped differently as in comparison to Fig. 4.17. If the frequency is set equal to the energy gap for one Zeeman crossing point the corresponding peak takes a symmetric form while the other is even more deformed. Therefore, an average frequency has been chosen, leading to minor asymmetric deformation for both peaks. Nevertheless, the key aspect of individually filtering β states is accomplished.
Subsequently, a design draft is presented, which has been drawn by the design department of the nuclear institute at FZJ. In Fig. 4.35 the complete nuclear spin filter is shown from the outside. On the base areas two flanges are mounted such that the device can be implemented into a beam line. Connections for the static electric fields, the radio frequency power and the liquid helium cooling line for the cavity are depicted by the red connections. The purpose of the outer metal shell is to shield the magnetic coils, which produce the longitudinal 430 mT magnetic field. The corresponding liquid helium lines for the superconductivity and the electric connections are

represented by two tubes leaving the shell in the top middle.

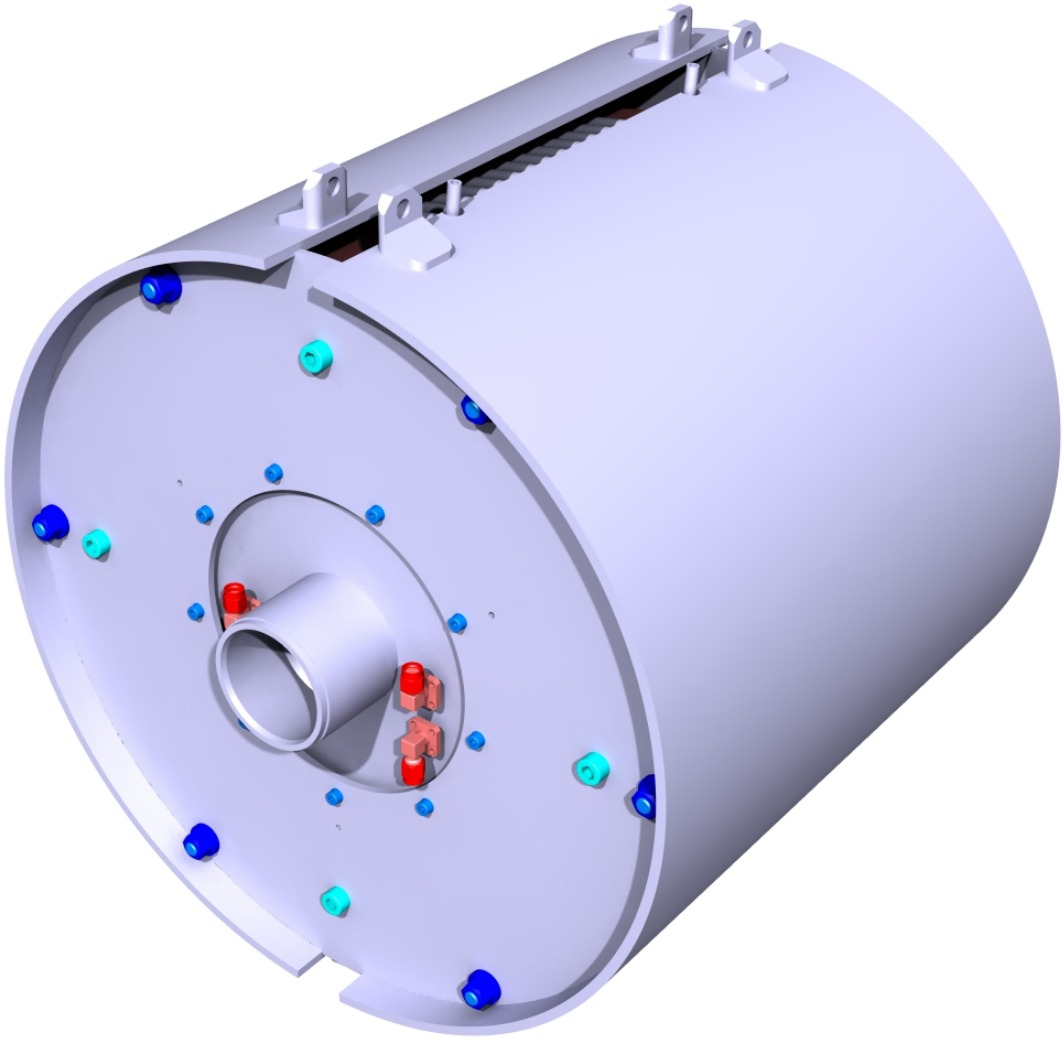

Figure 4.35: The outer shell design of a possible realization of the second generation of the nuclear spin filter is shown. The drawing, fabricated by the design department of the nuclear institute at FZJ (designer: Berthold Klimczok), shows the connection to the beam line with cylindrical shaped metal shielding of the magnetic field produced inside by superconductive windings.

Moreover, the connections are better visible in Fig. 4.36. Here, the liquid helium used for cooling, enters the red chamber through the front tube, while the backflow of the reheated helium gas takes place through the back one. To take full advantage of the liquid helium it is reused for cooling after turning gaseous. Therefore, some of the helium gas is extracted at the tee connection and flows another time around the red volume in the white tubes. Additionally, the electric connections for the windings enter through the exit point of the cooling helium gas. The red volume is a hollow metal cylinder, in which the magnetic coils are winded and the liquid helium is pumped in. The coils are shown in Fig. 4.37 as grey quadratic wires. Furthermore, the flanges and the red volume are mechanical fixed by the blue bars, while the sealing to the vacuum part of the beam line in turquoise is directly connected to the flanges. Subsequently, Fig. 4.38 shows the cavity, which is situated inside the vacuum tube. Mechanically it is fixed by the three sets of triangularly formed metal bar systems, which are connected directly to the front flange. Another cooling line is depicted in form of the orange tubes which are wired around the yellow shell of the cavity, which is better visible in Fig. 4.39.

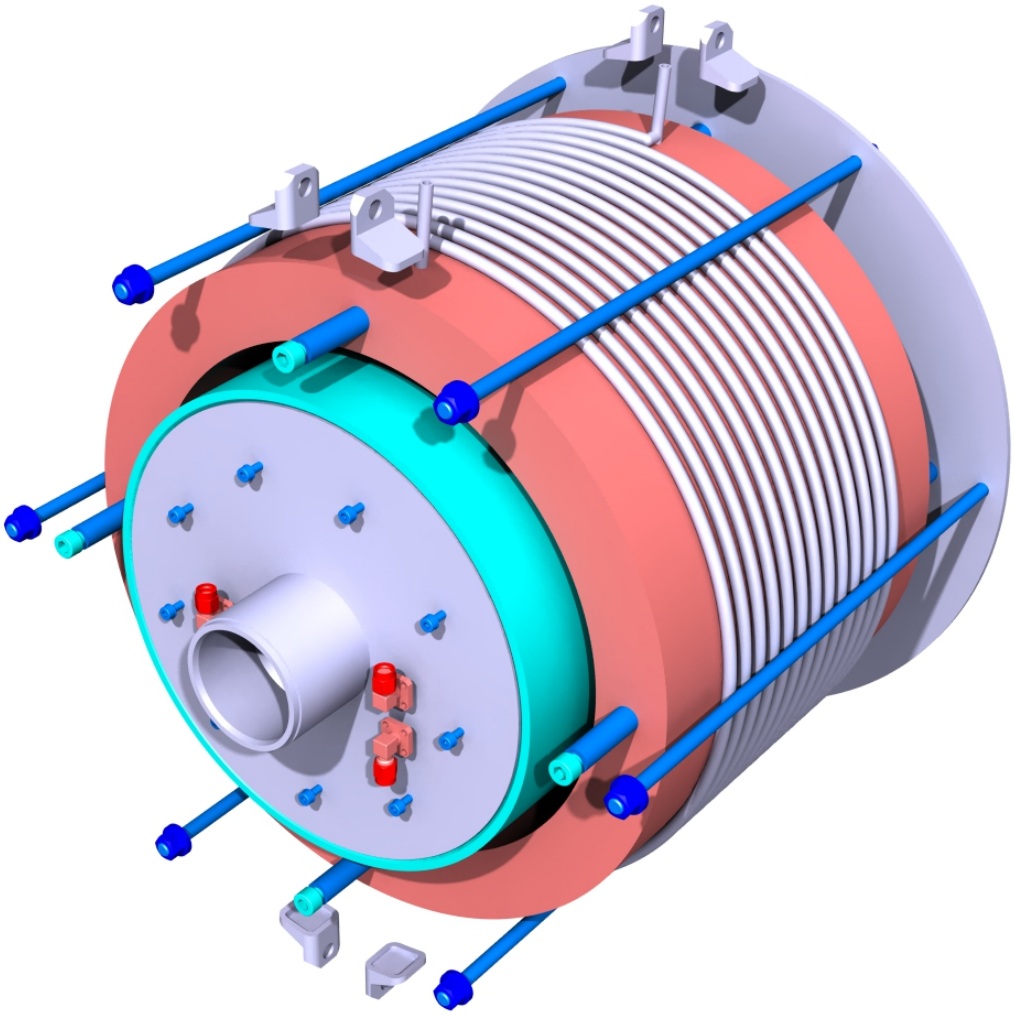

Figure 4.36: The drawing shows further internal structures based on Fig. 4.35 in the absence of the outer shell. The drawing, fabricated by the design department of the nuclear institute at FZJ (designer: Berthold Klimczok), shows the connection of the liquid helium, pumped through the red area in which the windings for the magnetic field are placed.

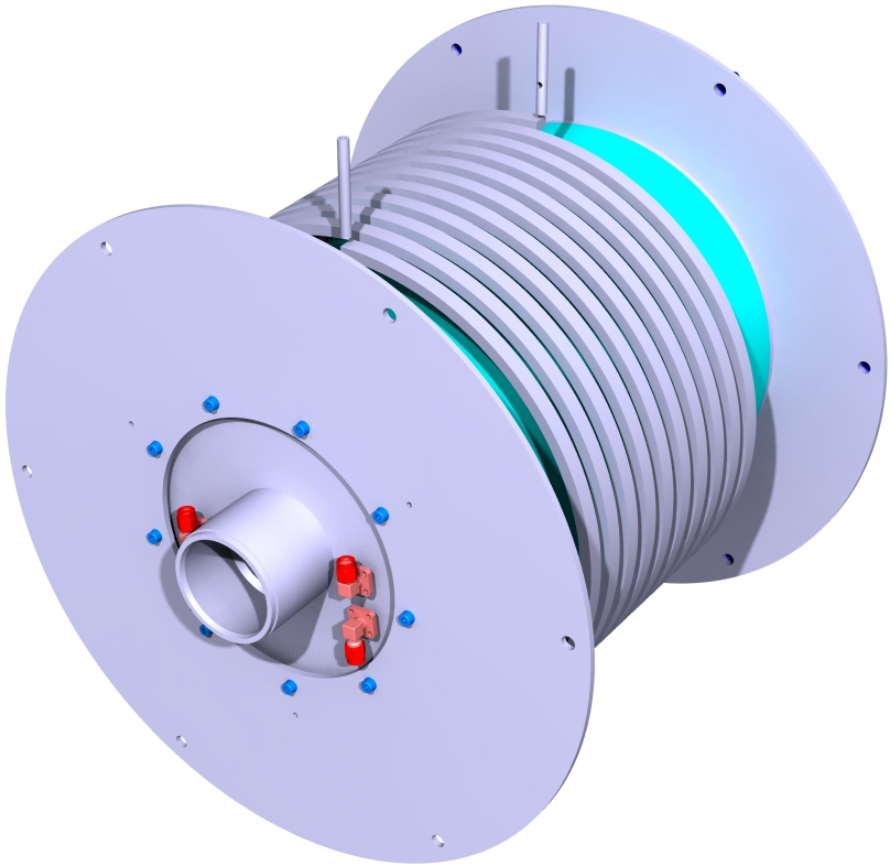

Figure 4.37: Continuing from Fig. 4.36 the figure, fabricated by the design department of the nuclear institute at FZJ (designer: Berthold Klimczok), shows the proposed configuration of the winding responsible for the homogenous magnetic field.

Due to the fact that a larger quality factor $Q \approx 16000$ is needed, a good cooling system is required. Therefore, a good heat conduction is necessary, which applies to materials with a high electric conductivity. Thus, the electric field is not applied directly onto the shell, since an electrical separation of the voltage would reduce the cooling efficiency. Instead the voltages are applied onto plates, which are placed inside the cavity. These plates and the inside of the cavity are visible in Fig. 4.40. The plates can be glued with an isolating material like ceramic onto the inner walls. Due to the fact that the applied voltages are relatively small the gap in between the plates and the shell surface can be minimized to keep the quality factor as good as possible.
Moreover, in the rest frame of the atom any non-parallel magnetic field to its motion $\vec{v} \nparallel \vec{B}$ produces also a corresponding electric field due to the Lorentz transformation. Consequently, to avoid unwanted quenching processes, also known as motional Stark effect, at the entrance and exit of the spin filter, permanent magnets can be placed. These need to produce a magnetic field in beam direction, which minimizes the magnetic field gradient from the stray fields. The optimal solution is keeping the magnetic field fixed from the point of creation of the metastable state until the detection point.

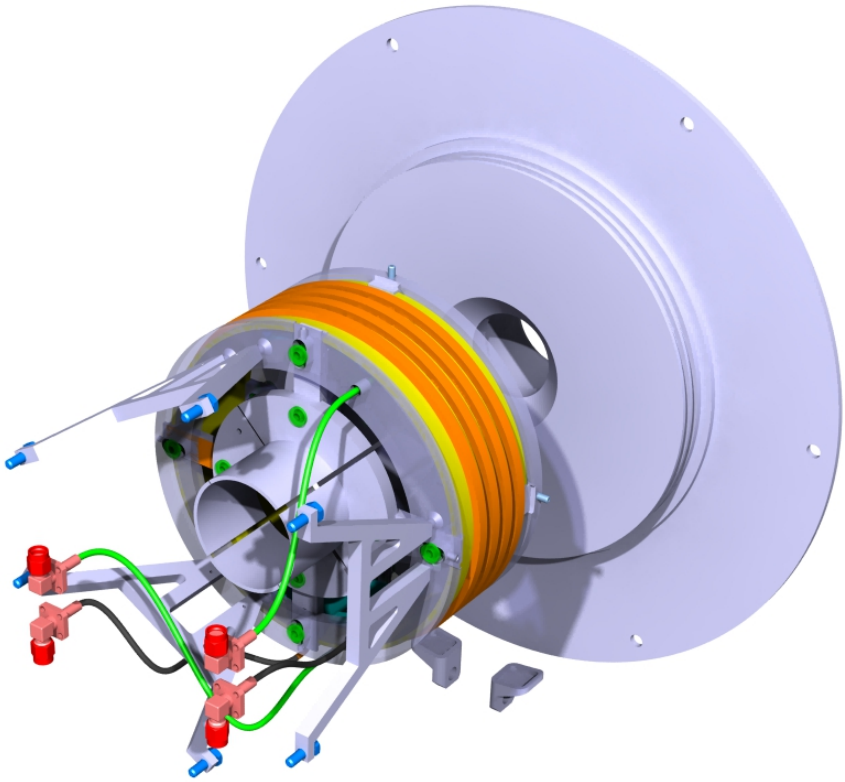

Figure 4.38: The figure, fabricated by the design department of the nuclear institute at FZJ (designer: Berthold Klimczok), gives a first look onto the cavity situated in the turquoise beam tube visible in Fig. 4.37. Again the orange tubes are representing the liquid helium cooling line, while the front structure is the mechanical rack to fix the cavity in the beam tube.

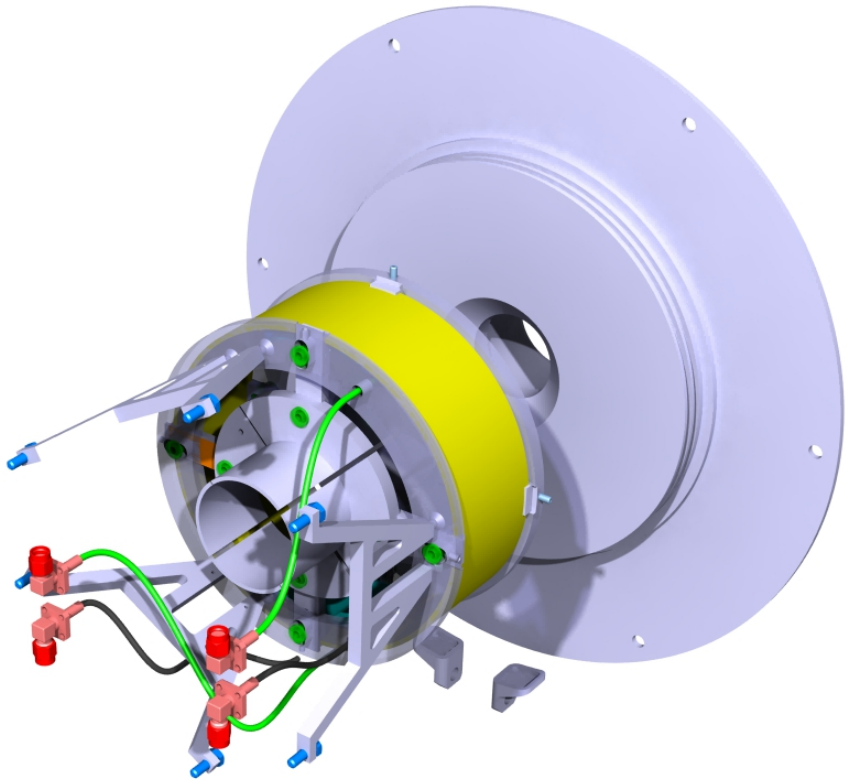

Figure 4.39: The figure, fabricated by the design department of the nuclear institute at FZJ (designer: Berthold Klimczok), shows the cavity without the liquid helium cooling tubes visible in Fig. 4.38.

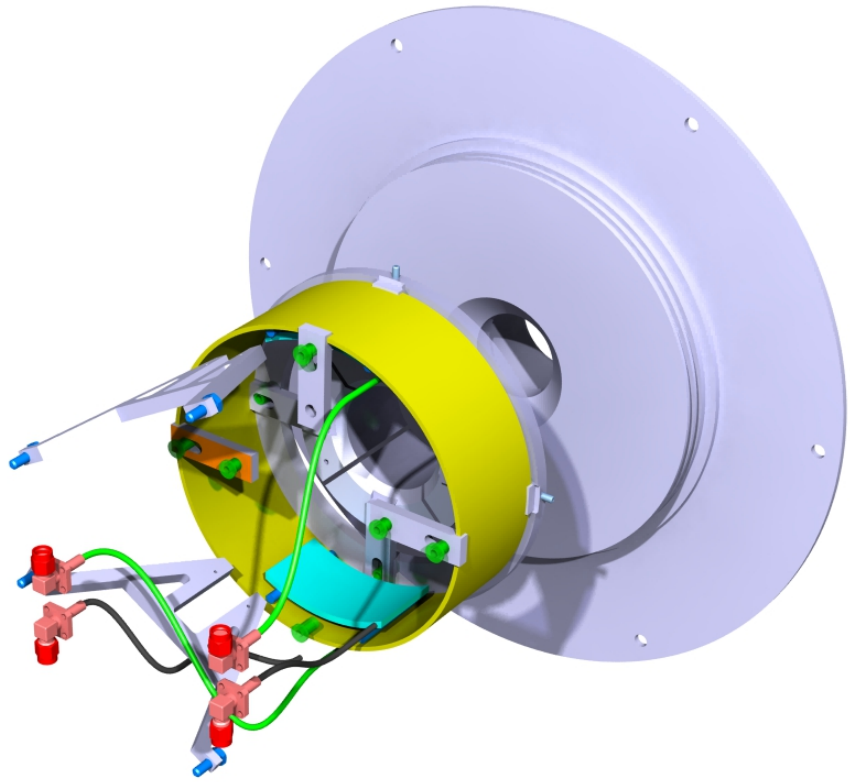

Figure 4.40: The figure, fabricated by the design department of the nuclear institute at FZJ (designer: Berthold Klimczok), shows the inside of the cavity. Moreover, one of the two turquoise electrical isolated plates for applying the static electric field is visible.

A more technical 2D drawing is provided in App. H.

4.3 Spin filter for single ionized helium-3

The previous sections are based on nuclear spin filters for hydrogen atoms and its isotopes. An atomic, ionic or molecular system needs to have metastable states, a hyperfine splitting and a reasonable energy gap to a short-living set of states such that a nuclear spin filter can be designed. The single ionized helium-3 ion fulfills all these conditions. In contrast to the hydrogen atom, the lifetime of the metastable state is reduced to $\tau \approx 0.002$ s and the Lamb-shift between the $2S_{1/2}$ and the $2P_{1/2}$ sets is increased by a factor of 10. The reason is the larger nuclear charge number $Z = 2$. This makes the spin dynamics and the corresponding realization of the device more challenging. In addition, the external fields now also change the trajectory of the incoming beam, which arises due to the fact that the helium-3 beam consist of ions. In the following both aspects are analyzed for one particle travelling through the cavity. This allows to estimate first settings for a design. But for an experimental realization the beam profile as well as the beam intensity need to be considered.

4.3.1 Mechanical dynamics

The nuclear spin filter, utilizing static and time dependent electromagnetic fields, manipulates the trajectories of charged particles. Such variations in the trajectories of helium-3 ions are investigated in this subsection. The mechanical dynamics is based on the textbook theory established in [156]. Moreover, field configurations are established for which the displacement of the beam is minimal, while the spin dynamics performs the separation of the A states. The latter is discussed in subsection 4.3.3. The single ionized helium-3 ions are deflected by external electromagnetic fields by the Lorentz force $\vec{F}_{Lor} = q\left(\vec{E} + \dot{\vec{r}} \times \vec{B}\right)$, where q is the electric charge of the particle, while $\vec{E}$ and $\vec{B}$ are the electric and the magnetic field, respectively. As long as the velocities of the particles do not exceed 1% of the speed of light c, the trajectories as well as the change in velocities are well described by solving the Newtonian equations of motion

$$m\ddot{\vec{r}} - q\left(\vec{E} + \dot{\vec{r}} \times \vec{B}\right) = 0. \tag{4.33}$$

The general solution to Eq. (4.33) is derived in App. E and is stated as

$$\begin{aligned} \dot{x}(t) &= c_1 e^{iqB_z t/m} + c_2 e^{-iqB_z t/m} \\ \dot{y}(t) &= ic_1 e^{iqB_z t/m} - ic_2 e^{-iqB_z t/m} - \frac{E_x}{B_z}. \end{aligned} \tag{4.34}$$

Integrating over time leaves us with the trajectories for the positions

$$\begin{aligned} x(t) &= \int \dot{x}(t)dt = -c_1 \frac{im}{qB_z} e^{iqB_z t/m} + c_2 \frac{im}{qB_z} e^{-iqB_z t/m} + x_0 \\ y(t) &= \int \dot{y}(t)dt = c_1 \frac{m}{qB_z} e^{iqB_z t/m} + c_2 \frac{m}{qB_z} e^{-iqB_z t/m} - \frac{E_x}{B_z} t + y_0, \end{aligned} \tag{4.35}$$

where x_0 and y_0 are some constants to be determined with initial conditions for the positions. In the next step, the fields of the electromagnetic wave of the $\mathrm{TM}_{0,1,10}$ mode are added. The fields are expressed by

$$\begin{aligned} E_r &= \frac{p\pi E_0 R}{dx_{0,1}} \sin\left(\frac{p\pi z}{d}\right) \cos\left(\omega_{0,1,10} t\right) J_1\left(\frac{x_{0,1} r}{R}\right), \\ E_z &= E_0 \cos\left(\frac{p\pi z}{d}\right) \cos\left(\omega_{0,1,10} t\right) J_0\left(\frac{x_{0,1} r}{R}\right), \\ B_\varphi &= \frac{\omega_{0,1,10} E_0 R}{c^2 x_{0,1}} \cos\left(\frac{p\pi z}{d}\right) \sin\left(\omega_{0,1,10} t\right) J_1\left(\frac{x_{0,1} r}{R}\right). \end{aligned} \tag{4.36}$$

Furthermore, cylindrical coordinates are a suitable choice of coordinates due to the field symmetries. Consequently, the Newtonian equation (4.33) is transformed to

$$m\left[\left(\ddot{r}-r\dot{\varphi}^2\right)\hat{e}_r+\left(2\dot{r}\dot{\varphi}+r\ddot{\varphi}\right)\hat{e}_\varphi+\ddot{z}\hat{e}_z\right]-q\left[\vec{E}+\left(\dot{r}\hat{e}_r+r\dot{\varphi}\hat{e}_\varphi+\dot{z}\hat{e}_z\right)\times\vec{B}\right]=0. \tag{4.37}$$

Moreover, the static fields are represented in cylindrical coordinates as follows

$$\begin{aligned}\vec{E}_{stat.}&=E_x\hat{e}_x=E_x\cos(\varphi)\,\hat{e}_r-E_x\sin(\varphi)\,\hat{e}_\varphi,\\ \vec{B}_{stat.}&=B_z\hat{e}_z.\end{aligned} \tag{4.38}$$

Therefore, Eq. (4.37) can be expressed as

$$\begin{aligned}&m\left[\left(\ddot{r}-r\dot{\varphi}^2\right)\hat{e}_r+\left(2\dot{r}\dot{\varphi}+r\ddot{\varphi}\right)\hat{e}_\varphi+\ddot{z}\hat{e}_z\right]\\ &=q\left[\left(E_r+E_x\cos(\varphi)\right)\hat{e}_r-E_x\sin(\varphi)\,\hat{e}_\varphi+E_z\hat{e}_z+\left(\dot{r}\hat{e}_r+r\dot{\varphi}\hat{e}_\varphi+\dot{z}\hat{e}_z\right)\times\left(B_\varphi\hat{e}_\varphi+B_z\hat{e}_z\right)\right]\\ &=q\left[\left(E_r+E_x\cos(\varphi)+r\dot{\varphi}B_z-\dot{z}B_\varphi\right)\hat{e}_r-\left(E_x\sin(\varphi)+\dot{r}B_z\right)\hat{e}_\varphi+\left(E_z+\dot{r}B_\varphi\right)\hat{e}_z\right].\end{aligned} \tag{4.39}$$

Subsequently, the three coupled differential equations are represented by

$$\begin{aligned}\ddot{r}&=\frac{q}{m}\left(E_r+E_x\cos(\varphi)+r\dot{\varphi}B_z-\dot{z}B_\varphi\right)+r\dot{\varphi}^2,\\ \ddot{\varphi}&=-\frac{q}{mr}\left(E_x\sin(\varphi)+\dot{r}B_z\right)-\frac{2\dot{r}\dot{\varphi}}{r},\\ \ddot{z}&=\frac{q}{m}\left(E_z+\dot{r}B_\varphi\right).\end{aligned} \tag{4.40}$$

Numerical results are depicted in Fig. 4.41a and Fig. 4.41b. In the latter it is visible that the effects of the electromagnetic wave are negligible. The reason is due to the fast oscillating frequency of $f = 21.06358806$ GHz, which changes the signs of the fields accordingly. In addition, the deflection of the beam is very small 0.3 mm, which is due to the change of the polarity of the static electric field and the large velocity. The high velocity is needed to maximize the cross section for the production of metastable helium-3, more on that in Sec. 5.2.

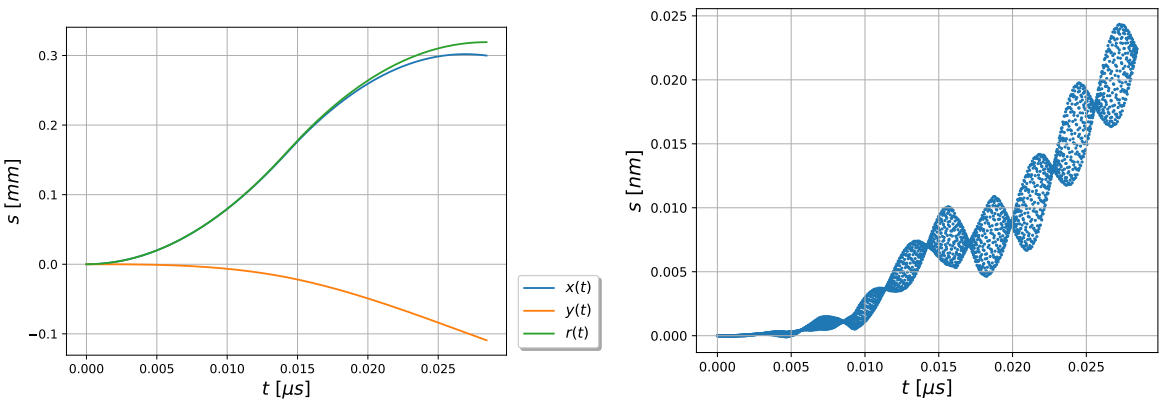

(a) (b)

Figure 4.41: The polar position coordinates as function of time are displayed. Thereby, s shows the amount of positional displacement perpendicular to the main beam velocity component v_z for the different coordinates $x(t)$, $y(t)$ and $r(t) = \sqrt{x^2(t)+y^2(t)}$. The static electric field switches its sign in the middle of the distance from positive to negative. While Fig. 4.41a shows the numerical results where the radio frequency fields are neglected, Fig. 4.41b shows the difference in the radial position $r(t)$ for both scenarios, e.g. $r(t) - r'(t)$. Furthermore, the additional parameters for reproducibility are indicated in Tab. 4.9.

Table 4.9: The table introduces the different parameters necessary to produce the simulations. The values for the single velocity components v_i represent the initial conditions for the numerical simulations at $t = 0$. Moreover, l denotes the length of the cavity in which the fields are acting.

Figure	$v_z \left[\frac{\mathrm{m}}{\mathrm{s}}\right]$	$v_x \left[\frac{\mathrm{m}}{\mathrm{s}}\right]$	$v_y \left[\frac{\mathrm{m}}{\mathrm{s}}\right]$	l [m]	B_z [mT]	$\lvert E_x\rvert \left[\frac{\mathrm{kV}}{\mathrm{m}}\right]$
4.41a	2526451	0	0	0.071833	770	50

4.3.2 Relativistic approach

For particle speeds in the relativistic regime the relativistic equation of motions need to be solved. The four-vector of the Lorentz force can be stated as

$$F^\mu = q\tilde{F}^\mu_\nu U^\nu \coloneqq q\begin{pmatrix} 0 & {}^{E_x}\!/_c & {}^{E_y}\!/_c & {}^{E_z}\!/_c \\ {}^{E_x}\!/_c & 0 & B_z & -B_y \\ {}^{E_y}\!/_c & -B_z & 0 & B_x \\ {}^{E_z}\!/_c & B_y & -B_x & 0 \end{pmatrix}\begin{pmatrix} \gamma c \\ \gamma v_x \\ \gamma v_y \\ \gamma v_z \end{pmatrix}, \tag{4.41}$$

where $\tilde{F}^\mu_\nu$ is the electromagnetic tensor, U^ν the four-velocity and $\gamma = \frac{1}{\sqrt{1-\frac{|\vec{v}|^2}{c^2}}}$ the Lorentz factor. The mechanical equation of motion is stated as

$$m\frac{dU^\mu}{d\tau} = F^\mu, \tag{4.42}$$

where τ is the proper time of the co-moving inertial system and is related to the laboratory time by

$$dt = \gamma d\tau. \tag{4.43}$$

Combining the results of Eq. (4.41) and Eq. (4.43) in the equation of motion Eq. (4.42) for the static fields introduced in 4.3.1 leads to the following differential equations

$$\begin{aligned} \frac{d}{dt}\left(\gamma mc^2\right) &= qv_xE_x, \\ \frac{d}{dt}\left(\gamma mv_x\right) &= qE_x + qv_yB_z, \\ \frac{d}{dt}\left(\gamma mv_y\right) &= -qv_xB_z, \\ \frac{d}{dt}\left(\gamma mv_z\right) &= 0. \end{aligned} \tag{4.44}$$

By using the product rule, the final version of the equations of motions are stated as

$$\begin{aligned} \frac{d}{dt}\gamma &= \frac{q\dot{x}E_x}{mc^2}, \\ \dot{x}\frac{d}{dt}\gamma + \gamma\ddot{x} &= \frac{q}{m}\left(E_x + \dot{y}B_z\right), \\ \dot{y}\frac{d}{dt}\gamma + \gamma\ddot{y} &= -\frac{q}{m}\dot{x}B_z, \\ \dot{z}\frac{d}{dt}\gamma + \gamma\ddot{z} &= 0. \end{aligned} \tag{4.45}$$

Inserting the first equation into the rest transforms the equations into a set of nonlinear coupled differential equations

$$\begin{aligned}\ddot{x} &= \frac{q}{\gamma m}\left(E_x + \dot{y}B_z - \frac{\dot{x}^2 E_x}{c^2}\right),\\ \ddot{y} &= -\frac{q}{\gamma m}\left(\dot{x}B_z + \frac{\dot{x}\dot{y}E_x}{c^2}\right),\\ \ddot{z} &= -\frac{q\dot{x}\dot{z}E_x}{\gamma m c^2}.\end{aligned} \tag{4.46}$$

Unfortunately, this systems has not an analytical solution and needs to be solved numerically. Nevertheless, in the limit $|\vec{v}| \ll c$ the equation of motions from classical mechanics, stated in Eq. (7.57), are recovered. For the sake of completeness, analogue to the classical treatment the electromagnetic wave, which is induced into the cavity, is addressed. Consequently, cylindrical coordinates should be applied. This has the result that the metric is changed and consequently Eq. (4.42) needs to be adjusted. The adaptation is stated in the geodesic equation from general relativity for heavy particles [157]

$$m\frac{dU^\mu}{d\tau} + m\Gamma^\mu_{\alpha\beta}U^\alpha U^\beta = F^\mu. \tag{4.47}$$

Here, F^μ represents any non-gravitational force, e.g. electromagnetic force. The $\Gamma^\alpha_{\beta\gamma}$ are Christoffel symbols, which are directly related to the metric $g_{\mu\nu}$ by

$$\Gamma^\mu_{\alpha\beta} = \frac{1}{2}g^{\mu\tilde{\beta}}\left(\frac{\partial g_{\tilde{\beta}\alpha}}{\partial x^\beta} + \frac{\partial g_{\tilde{\beta}\beta}}{\partial x^\alpha} - \frac{\partial g_{\alpha\beta}}{\partial x^{\tilde{\beta}}}\right). \tag{4.48}$$

In the following the four vectors in the cylindrical coordinate system are denoted by

$$\tilde{x}^{\tilde{\mu}} \coloneqq \begin{pmatrix} -ct \\ r \\ \varphi \\ z \end{pmatrix} \tag{4.49}$$

while the position vector in Cartesian coordinates remains x^μ. In the first step the metric in cylindrical coordinates is calculated by taking advantage of the Minkowski metric and its Lorentz invariance

$$\begin{aligned} ds^2 &= -c^2dt^2 + dx^2 + dy^2 + dz^2\\ &= -c^2dt^2 + \left(dr\cos(\varphi) - r\sin(\varphi)\,d\varphi\right)^2 + \left(dr\sin(\varphi) + r\cos(\varphi)\,d\varphi\right)^2 + dz^2\\ &= -c^2dt^2 + \cos^2(\varphi)\,dr^2 - 2r\sin(\varphi)\cos(\varphi)\,dr d\varphi + r^2\sin^2(\varphi)\,d\varphi^2\\ &+ \sin^2(\varphi)\,dr^2 + 2r\sin(\varphi)\cos(\varphi)\,dr d\varphi + r^2\cos^2(\varphi)\,d\varphi^2 + dz^2\\ &= -c^2dt^2 + dr^2 + r^2d\varphi^2 + dz^2. \end{aligned} \tag{4.50}$$

Consequently, the metric and its inverse are expressed as

$$g_{\mu\nu} \coloneqq \begin{pmatrix} -1 & 0 & 0 & 0\\ 0 & 1 & 0 & 0\\ 0 & 0 & r^2 & 0\\ 0 & 0 & 0 & 1 \end{pmatrix} \quad \text{and} \quad g^{\mu\nu} \coloneqq \begin{pmatrix} -1 & 0 & 0 & 0\\ 0 & 1 & 0 & 0\\ 0 & 0 & 1/r^2 & 0\\ 0 & 0 & 0 & 1 \end{pmatrix}. \tag{4.51}$$

In a next step the Christoffel symbols are calculated. The only non-vanishing elements are

$$\begin{aligned}\Gamma^r_{\varphi\varphi} &= -r,\\ \Gamma^\varphi_{\varphi r} &= \frac{1}{r},\\ \Gamma^\varphi_{r\varphi} &= \frac{1}{r}.\end{aligned} \tag{4.52}$$

Subsequently, the electromagnetic field tensor needs to be transformed into the new coordinate system

$$\begin{aligned}\tilde{F}^{\tilde{\mu}}_{\tilde{\nu}} &= \frac{\partial \tilde{x}^{\tilde{\mu}}}{\partial x^{\mu}} \frac{\partial x^{\nu}}{\partial \tilde{x}^{\tilde{\nu}}} F^{\mu}_{\nu} \\ &\coloneqq \begin{pmatrix} 0 & \frac{\cos(\varphi)E_x + \sin(\varphi)E_y}{c} & \frac{-r\sin(\varphi)E_x + r\cos(\varphi)E_y}{c} & E_z/c \\ \frac{\cos(\varphi)E_x + \sin(\varphi)E_y}{c} & 0 & rB_z & -\cos(\varphi)B_y + \sin(\varphi)B_x \\ \frac{-\sin(\varphi)E_x + \cos(\varphi)E_y}{rc} & -B_z/r & 0 & \frac{\sin(\varphi)B_y + \cos(\varphi)B_x}{r} \\ E_z/c & \cos(\varphi)B_y - \sin(\varphi)B_x & -r(\sin(\varphi)B_y + \cos(\varphi)B_x) & 0 \end{pmatrix}.\end{aligned} \tag{4.53}$$

Therefore, Eq. (4.47) takes in cylindrical coordinates the following form

$$m\gamma \frac{\tilde{U}^{\tilde{\mu}}}{dt} + m\Gamma^{\tilde{\mu}}_{\tilde{\alpha}\tilde{\beta}} \tilde{U}^{\tilde{\alpha}} \tilde{U}^{\tilde{\beta}} = \tilde{F}^{\tilde{\mu}}, \tag{4.54}$$

with

$$\tilde{U}^{\tilde{\mu}} \coloneqq \begin{pmatrix} \gamma c \\ \gamma \dot{r} \\ \gamma \dot{\varphi} \\ \gamma \dot{z} \end{pmatrix} \qquad \text{and} \qquad \tilde{F}^{\tilde{\mu}} = q\tilde{F}^{\tilde{\mu}}_{\tilde{\nu}} \tilde{U}^{\tilde{\nu}}. \tag{4.55}$$

At last, the system of coupled differential equations are stated as

$$\begin{aligned}\frac{d}{dt}(\gamma c) &= \frac{q}{mc}\left[\left(\cos(\varphi)E_x + \sin(\varphi)E_y\right)\dot{r} + r\left(-\sin(\varphi)E_x + \cos(\varphi)E_y\right)\dot{\varphi} + E_z\dot{z}\right], \\ \frac{d}{dt}(\gamma \dot{r}) &= \frac{q}{m}\left[\cos(\varphi)E_x + \sin(\varphi)E_y + rB_z\dot{\varphi} + \left(-\cos(\varphi)B_y + \sin(\varphi)B_x\right)\dot{z}\right] + r\gamma\dot{\varphi}^2, \\ \frac{d}{dt}(\gamma \dot{\varphi}) &= \frac{q}{m}\left[-\frac{\sin(\varphi)}{r}E_x + \frac{\cos(\varphi)}{r}E_y - \frac{B_z}{r}\dot{r} + \left(\frac{\sin(\varphi)}{r}B_y + \frac{\cos(\varphi)}{r}B_x\right)\dot{z}\right] - \frac{2\gamma\dot{r}\dot{\varphi}}{r}, \\ \frac{d}{dt}(\gamma \dot{z}) &= \frac{q}{m}\left[E_z + \left(\cos(\varphi)B_y - \sin(\varphi)B_x\right)\dot{r} - r\left(\sin(\varphi)B_y + \cos(\varphi)B_x\right)\dot{\varphi}\right].\end{aligned} \tag{4.56}$$

In the special case of the radio frequency mode $\mathrm{TM}_{0,1,10}$ the fields are expressed as

$$\begin{aligned}E_x &= E_{x,stat.} + E_{r,\mathrm{TM}}\cos(\varphi), \\ E_y &= E_{r,\mathrm{TM}}\sin(\varphi), \\ E_z &= E_{z,\mathrm{TM}}, \\ B_x &= -\sin(\varphi)B_{\varphi,\mathrm{TM}}, \\ B_y &= \cos(\varphi)B_{\varphi,\mathrm{TM}}, \\ B_z &= B_{z,stat.}.\end{aligned} \tag{4.57}$$

Subsequently, Eq. (4.56) reduces to

$$\begin{aligned}\frac{d}{dt}(\gamma c) &= \frac{q}{mc}\left[\cos(\varphi)E_{x,stat.}\dot{r} + E_{r,\mathrm{TM}}\dot{r} - r\sin(\varphi)E_{x,stat.}\dot{\varphi} + E_{z,\mathrm{TM}}\dot{z}\right], \\ \frac{d}{dt}(\gamma \dot{r}) &= \frac{q}{m}\left[\cos(\varphi)E_{x,stat.} + E_{r,\mathrm{TM}} + rB_{z,stat.}\dot{\varphi} - B_{\varphi,\mathrm{TM}}\dot{z}\right] + r\gamma\dot{\varphi}^2, \\ \frac{d}{dt}(\gamma \dot{\varphi}) &= -\frac{q}{mr}\left[\sin(\varphi)E_{x,stat.} + B_{z,stat.}\dot{r}\right] - \frac{2\gamma\dot{r}\dot{\varphi}}{r}, \\ \frac{d}{dt}(\gamma \dot{z}) &= \frac{q}{m}\left[E_{z,\mathrm{TM}} + B_{\varphi,\mathrm{TM}}\dot{r}\right].\end{aligned} \tag{4.58}$$

Again the classical equations Eq. (4.40) are recovered in the limit $|\vec{v}| \ll c$.

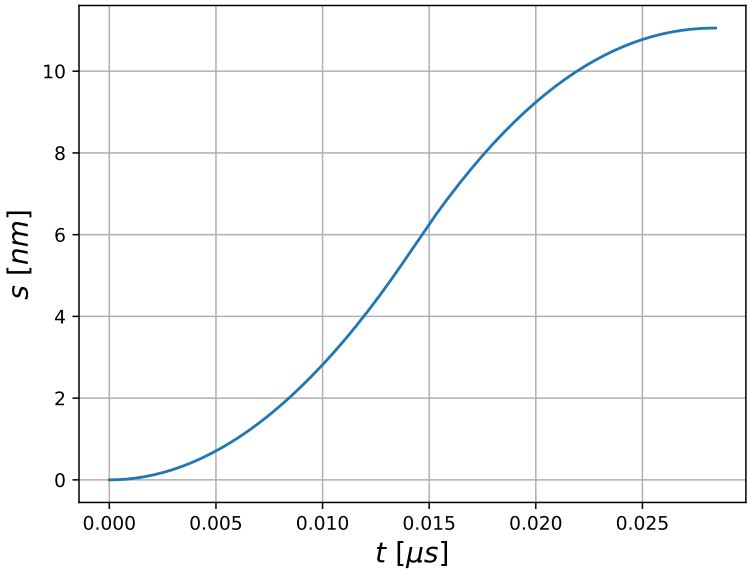

Figure 4.42: The difference between classical and relativistic treatment $s = r(t)_{\text{Classical}} - r(t)_{\text{Relativity}}$ for the radial positional change of the helium-3 ion beam is depicted as function of the time travelled through the cavity. Furthermore, the additional parameters for reproducibility are indicated in Tab. 4.9 and are the same as for Fig. 4.41a.

4.3.3 Spin dynamics

The Breit-Rabi diagram for singly ionized helium-3 is illustrated in Fig. 3.7, where Zeeman crossing points between the B and E states are visible at magnetic fields around $B \approx 750$ mT. Consequently, an even larger frequency, in comparison to the one stated in Ch. 4.2, is needed to bridge the energy gap between the A and E states at these Zeeman crossing points. The value of the frequency is $f = 21.063589$ GHz. Analogously to Sec. 4.2 a suitable electromagnetic mode needs to be chosen, which provides the resonance frequency with realistic dimensions for the cavity. The selected mode is the $\text{TM}_{0,1,10}$ mode. Its dimensions are summarized in Tab. 4.10 and the electromagnetic fields in Eq. (4.30). Subsequently, to distinguish the two individual peaks in the spin filter signal at least a quality factor of $Q = 16000$ is necessary. Moreover, the same amount of different resonance frequencies, as described in Sec. 4.2, have been calculated for the dimensions $d = 7.1833$ cm and $R = 4$ cm to search for interferences. The resulting frequency spectrum is illustrated in Fig. 4.43. It shows that the $\text{TM}_{0,1,10}$ mode is in first order separated from other resonance frequencies. To avoid that the influence of the neighbouring peaks is too large, the quality factor of the cavity can be improved to separate them even more. Furthermore, the process to create the metastable helium-3 ions $^3\text{He}^+$ is explained in more detail in Sec. 5.2. Nevertheless, the important point is that relevant cross sections increase at beam energies around 50 keV. Therefore, simulations based on Eq. (3.35) for corresponding beam velocities are performed in the rest frame of the helium ion and visible in Fig. 4.47a, Fig. 4.47b and Fig. 4.48. It shows that even for these large velocities, peak structures with decent intensity are resolved. As in the previous sections any relativistic adjustments due to the transformation into the rest frame are neglected. Even for the larger velocities the relativistic effects are minor as it can be seen in Fig. 4.42. The relativistic treatment is described in App. I. In addition, Fig. 4.48 shows that constant trajectories on larger radii do not change much in the structure rather a bit in the peak intensities. Therefore, in contradiction to the previous sections, constant trajectories for the single ions for the simulations of the spin dynamics are assumed to reduce the computational time. In addition, a change in the polarity in the middle of the cavity for the static electric field has been applied for these simulations. This helps the mechanical focusing towards the beam line as discussed in Sec. 4.3.1. For further

focusing more polarity changes for the static electric field might be applied in an experimental realization.

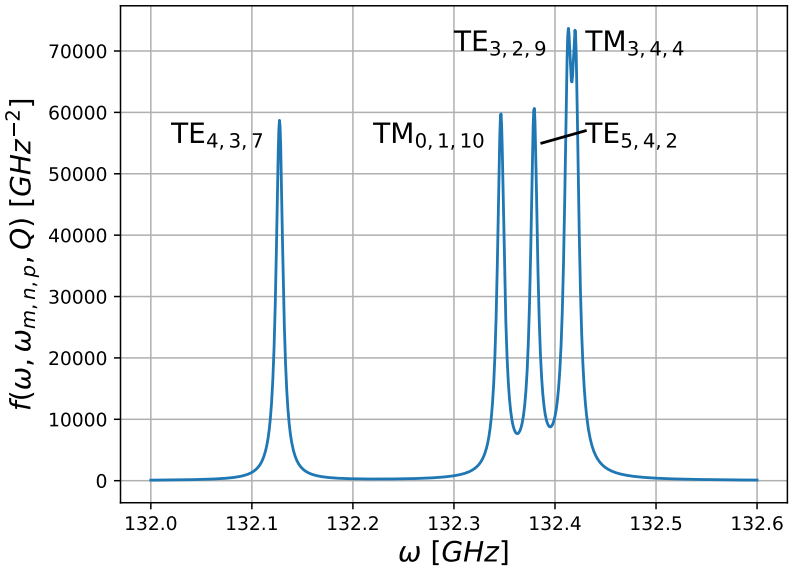

Figure 4.43: The Lorentz distributions are plotted as function of the angular frequency with a quality factor of $Q = 16000$. The figure shows the $TE_{4,3,7}$, $TM_{0,1,10}$, $TE_{5,4,2}$, $TE_{3,2,9}$ as well as the $TM_{3,4,4}$ mode.

In the following different spin dynamical simulations are discussed. In Fig. 4.44a a comparison to the hydrogen simulations in Sec. 4.1 can be done, while Fig. 4.44b exploits the new mode $TM_{0,1,10}$. Furthermore, Fig. 4.45a and Fig. 4.45b show the small difference in the probabilities due to the change of the polarity in the static electric field. Moreover, Fig. 4.46a depicts the result of a fully electron polarized helium-3 beam, while in Fig. 4.46b shows the result of a fully populated A_1 state as initial condition. As expected the structure of the single peaks does not change due to the initial condition but the probabilities increase drastically.

Table 4.10: The table introduces the different cavity modes exploited in this Sec. 4.3.3.

$TM_{m,n,p}$	$x_{m,n}$	d [m]	R [m]	$f_{m,n,p}$ [GHz]
$0, 1, 0$	2.405	0.15	0.00544783	21.06359
$0, 1, 10$	2.405	0.071833	0.04	21.06359

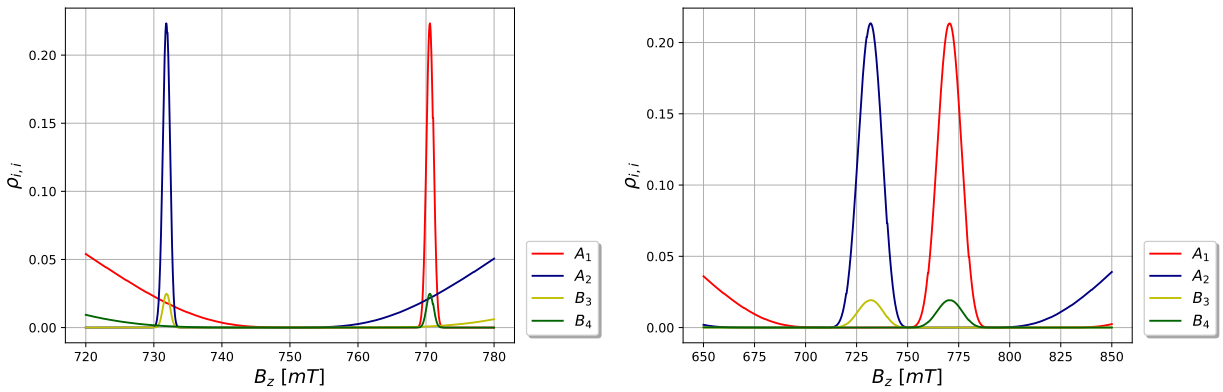

(a) (b)

Figure 4.44: The single probabilities of the metastable Breit-Rabi states of singly ionized helium-3 as function of the magnetic field flux B_z are displayed. The necessary parameters for reproducibility are indicated in Tab. 4.11. Moreover, Fig. 4.44a is produced my modelling the $TM_{0,1,0}$ mode, while for Fig. 4.44b the $TM_{0,1,10}$ mode is utilized.

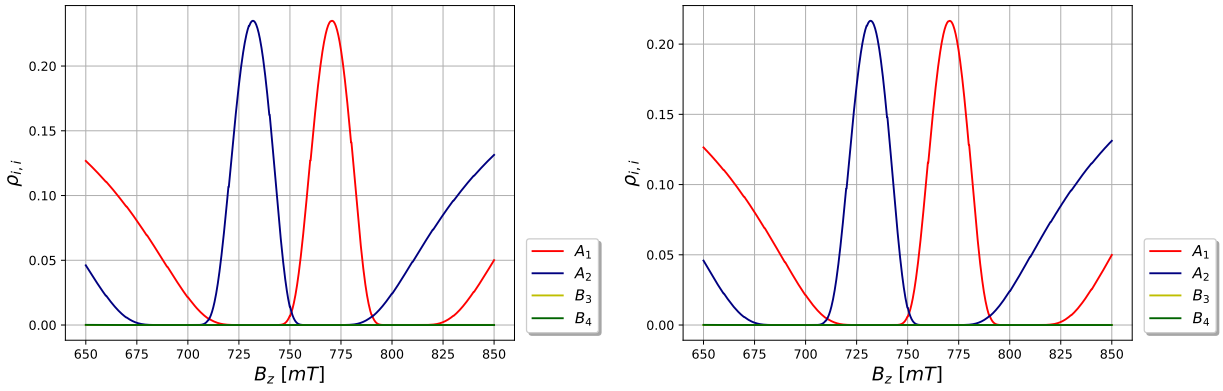

(a) (b)

Figure 4.45: The single probabilities of the metastable Breit-Rabi states of singly ionized helium-3 as function of the magnetic field flux B_z are displayed. The necessary parameters for reproducibility are indicated in Tab. 4.11. In comparison to the simulation in Fig. 4.44b, Fig. 4.45a has a frequency band with $Q = 16000$ and Fig. 4.45b has in addition a switch in polarity at the middle of the cavity for the static electric field.

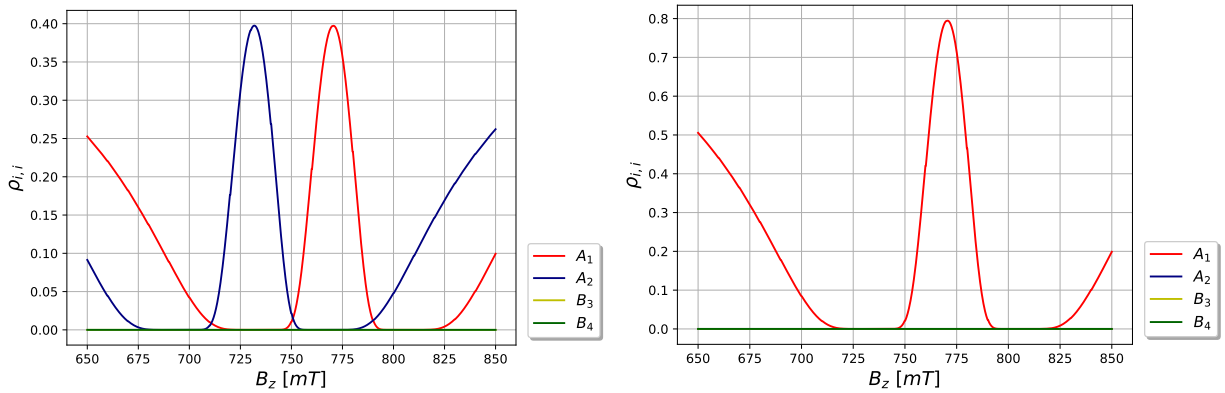

(a) (b)

Figure 4.46: The single probabilities of the metastable Breit-Rabi states of singly ionized helium-3 as function of the magnetic field flux B_z are displayed. The necessary parameters for reproducibility are indicated in Tab. 4.11. To produce Fig. 4.46a an initially full electron polarization is assumed $\rho(t = 0) = \mathrm{diag}\,(1/2, 1/2, 0, 0)$, while for Fig. 4.46b initially only the A_1 state is populated $\rho(t) = \mathrm{diag}\,(1, 0, 0, 0)$.

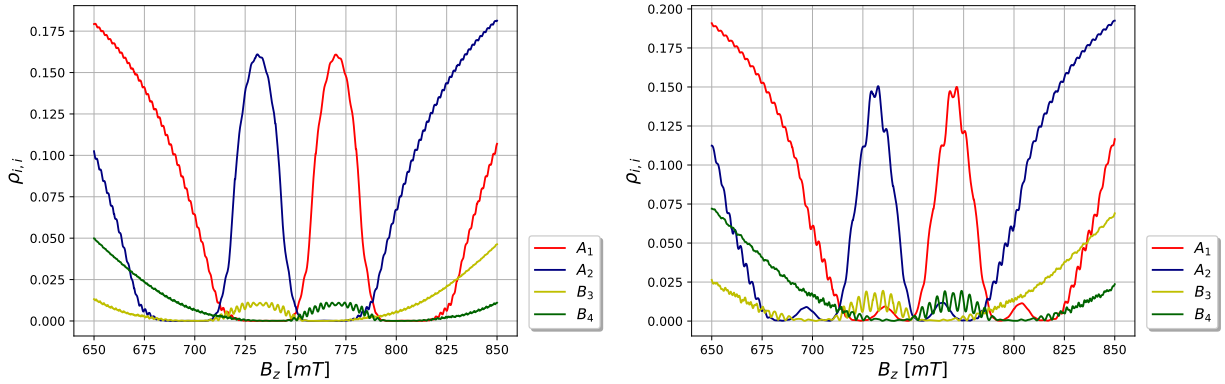

(a) (b)

Figure 4.47: The single probabilities of the metastable Breit-Rabi states of singly ionized helium-3 as function of the magnetic field flux B_z are displayed. The necessary parameters for reproducibility are indicated in Tab. 4.11. In comparison to Fig. 4.45b, the ion beam in Fig. 4.47a has a kinetic energy of $E_{\mathrm{kin}} \approx 50$ keV, while for Fig. 4.47b a kinetic energy of $E_{\mathrm{kin}} \approx 100$ keV has been used.

Finally, the same scheme from Sec. 4.2 for a possible realization of the design can be taken with small adaptations. Therefore, the plates inside the cavity, visible in Fig. 4.40, where the static electric field is applied need to be split to ensure a polarity switch, which is needed to focus the ion beam. In addition, the magnetic field coils need to be adjusted such that a larger magnetic field of roughly 750 mT is achieved.

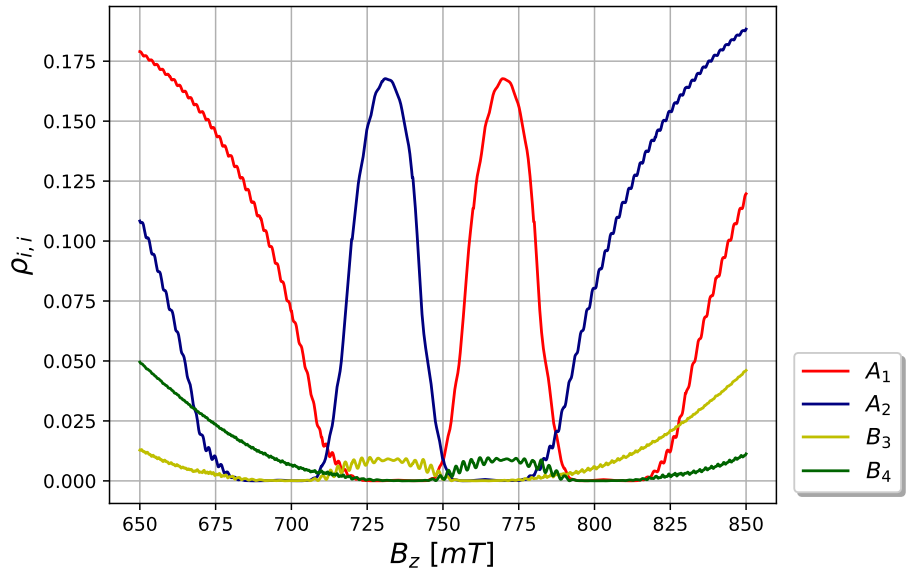

Figure 4.48: The single probabilities of the metastable Breit-Rabi states of the singly ionized helium-3 as function of the magnetic field flux B_z are displayed. The necessary parameters for reproducibility are indicated in Tab. 4.11. In comparison to Fig. 4.47a, the helium-3 ion beam travels at a fixed radius of $r = 1$ cm and fixed angle of $\varphi = 0$ for Fig. 4.48.

Table 4.11: The necessary specifications for the numerical simulations in this Sec. 4.3.3 are presented. The dimensions of the cavity are introduced in Tab. 4.10.

Figure	E_x $\left[\frac{\text{kV}}{\text{m}}\right]$	E_0 $\left[\frac{\text{kV}}{\text{m}}\right]$	v $\left[\frac{\text{m}}{\text{s}}\right]$	B_z [mT]	r [m]	$\text{TM}_{m,n,p}$	Q
4.44a	9	6	309500	720 – 780	0	$0,1,0$	∞
4.44b	50	30	309500	650 – 850	0	$0,1,10$	∞
4.45a	50	30	309500	650 – 850	0	$0,1,10$	16000
4.45b	50[a]	30	309500	650 – 850	0	$0,1,10$	16000
4.46a[b]	50[a]	30	309500	650 – 850	0	$0,1,10$	16000
4.46b[c]	50[a]	30	309500	650 – 850	0	$0,1,10$	16000
4.47a	50[a]	30	1786470	650 – 850	0	$0,1,10$	16000
4.47b	50[a]	30	2526451	650 – 850	0	$0,1,10$	16000
4.48	50[a]	30	1786470	650 – 850	0.01	$0,1,10$	16000

a: Electric field switches polarity at the middle of the cavity
b: Initial full electron polarization
c: Only A_1 is initially populated

Chapter 5

Lamb-shift polarimeter for helium-3

In the previous chapter 4 the nuclear spin filter is introduced. It is one of the main devices for the so-called Lamb-shift polarimeter [4, 5], which purpose is to deduce the nuclear spin polarization of an incoming particle beam. In Fig. 5.1 a sketch of an experimental setup for an LSP is stated. To date, it has only been effective for ions, atoms, or molecules consisting of hydrogen or its isotopes. Therefore, this chapter outlines the initial steps in modelling a detector system for helium-3 based on the LSP.

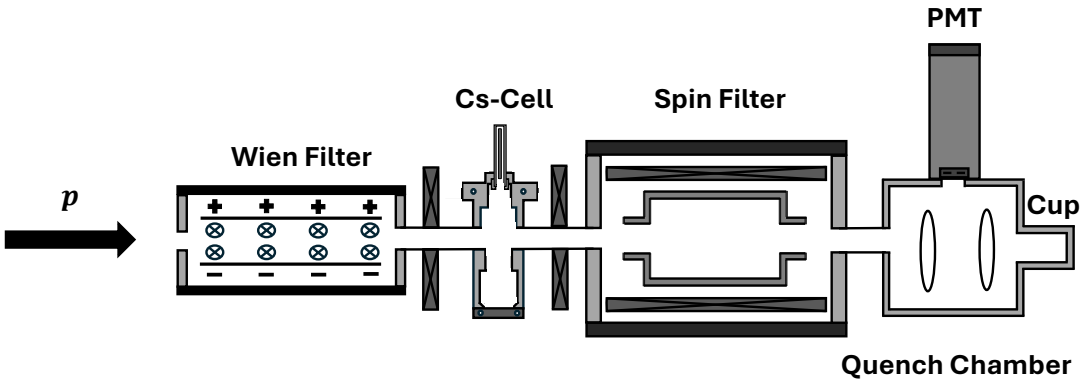

Figure 5.1: The sketch shows the experimental setup for a Lamb-shift polarimeter. It contains several components to determine the nuclear spin polarization of an incoming beam composed out of ions, molecules or atoms made of hydrogen or its isotopes.

5.1 Wien filter

The first device of an LSP is the Wien filter, which has multiple tasks. The primary and most simplest is that it sharpens the velocity distribution of an incoming ion beam. To fulfill this assignment it consists of a static homogenous electric $\vec{E} = E_x \hat{e}_x$ and magnetic field $\vec{B} = B_y \hat{e}_y$, which are both perpendicular to each other as well as to the incoming ion beam $\vec{v} = v_z \hat{e}_z$. Consequently, all ions are deflected due to the Lorentz force against the inner wall. The only exception are those which have a velocity, such that the forces cancel each other

$$\begin{aligned} & \vec{F}_{Elect.} = q\vec{E} = -q\vec{v} \times \vec{B} = -\vec{F}_{Mag.}, \\ \Rightarrow \quad & v_z = \frac{E_x}{B_y}. \end{aligned} \tag{5.1}$$

The dynamics of a charged particle inside electromagnetic fields are stated by Eq. (4.33). In case of the Wien filter the coupled differential equation is expressed as

$$\begin{aligned} \ddot{x} + \frac{q}{m}\left(-E_x + \dot{z}B_y\right) &= 0, \\ \ddot{y} &= 0, \\ \ddot{z} - \frac{q}{m}\dot{x}B_y &= 0. \end{aligned} \tag{5.2}$$

Following the same process as introduced in App. E results in the solutions

$$\begin{aligned} \dot{x}\left(t\right) &= c_1 e^{iqB_y t/m} + c_2 e^{-iqB_y t/m}, \\ \dot{y} &= v_{0,y}, \\ \dot{z}\left(t\right) &= -ic_1 e^{iqB_y t/m} + ic_2 e^{-iqB_y t/m} + \frac{E_x}{B_y}. \end{aligned} \tag{5.3}$$

The functions for the positions are obtained by integrating the velocities

$$\begin{aligned} x\left(t\right) &= -i\frac{m}{qB_y}c_1 e^{iqB_y t/m} + i\frac{m}{qB_y}c_2 e^{-iqB_y t/m} + x_0, \\ y\left(t\right) &= v_{0,y}t + y_0, \\ z\left(t\right) &= -\frac{m}{qB_y}c_1 e^{iqB_y t/m} - \frac{m}{qB_y}c_2 e^{-iqB_y t/m} + \frac{E_x}{B_y}t + z_0. \end{aligned} \tag{5.4}$$

For perfect initial conditions

$$\begin{aligned} \dot{x}\left(t=0\right) = \dot{y}\left(t=0\right) &= 0, \\ \dot{z}\left(t=0\right) &= v_{0,z} = v_z, \end{aligned} \tag{5.5}$$

the two constants c_1 and c_2 can be expressed by

$$\begin{aligned} c_1 &= \frac{i}{2}\left(v_z - \frac{E_x}{B_y}\right), \\ c_2 &= -\frac{i}{2}\left(v_z - \frac{E_x}{B_y}\right). \end{aligned} \tag{5.6}$$

In this case the condition for the external fields, obtained in the upper derivation Eq. (5.1), leaves $\dot{z}\left(t\right)$, $x\left(t\right)$ and $y\left(t\right)$ constant. For a fixed kinetic beam energy E_{kin} this relation allows also for filtering different charged masses

$$\begin{aligned} E_{kin} &= \frac{1}{2}mv^2, \\ \Rightarrow \quad m &= \frac{2E_{kin}B_y^2}{E_x^2}. \end{aligned} \tag{5.7}$$

Corresponding Wien filter mass spectra are provided in Fig. 5.2. The source is fed with helium-4, as its much cheaper in comparison to its helium-3 counter part, while a ramping generator is driving the current I inside the coils of the Wien filter to produce a corresponding magnetic field. In the meanwhile, the voltages producing the electric field are set to fixed values. The ions, which reach the end of the experimental setup, are detected in an ion cup, which produces the signal $\tilde{I}$ expressed at the y-axes. Fig. 5.2a and Fig. 5.2b show typical mass spectra with different residual gases. Thereby, the double peak structure arises due to a large inhomogeneous velocity distribution in the beam. After identifying the helium-4 peak the current is set such that its maximum value is reached.

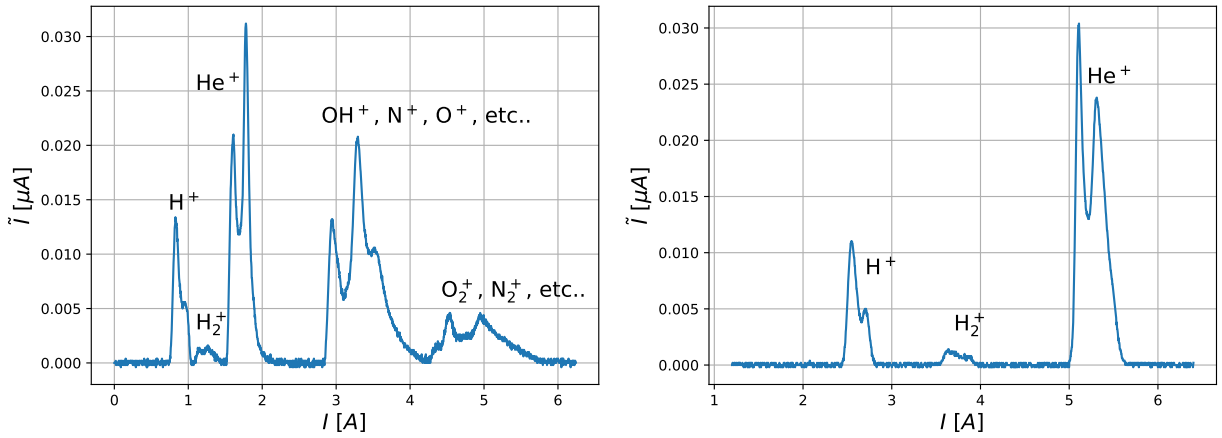

(a) (b)

Figure 5.2: The beam current registered at the ion cup is displayed at the vertical axis, while the horizontal axis represents the current generated by a ramping generator driving the power supply to produce the magnetic field in the Wien filter. To produce Fig. 5.2b larger static electric fields have been applied in comparison to Fig. 5.2a.

Therefore, the Wien filter is used to prepare the incoming beam, while selecting the desired ion specie.
An additional task is the rotation of the magnetic quantization axis as the LSP is only sensible in detecting a nuclear spin polarization aligned with the beam direction. Consequently, for a successful measurement the dominant magnetic field orientation needs to be rotated if the polarized beam has an alignment perpendicular to its momentum. The spin starts precessing around the magnetic field axis, while it reorientates itself towards the strongest magnetic field flux. This dynamic is known under the name Larmor precession. The corresponding frequency is proportional to the external magnetic field flux B as well as anti-proportional to the particle's mass

$$\omega_L = \frac{g_I q B}{2m}. \tag{5.8}$$

Here g_I denotes the nuclear g-factor, established in Sec. 2.2.3, while q is the particle's charge and m its mass. The particle's properties, with the dominant spin coupling towards the external magnetic field, drives the Larmor frequency. Examples are composed objects as molecules or ions, which still carry free electrons. If the electron is the dominant spin, then the Larmor frequency is 600 times larger than for a proton, which means the electron spin and consequently also the nuclear spin follow immediately the new orientation of the quantization axis. In case of spins from heavier particles the oscillation is well visible as function of the external magnetic field in the Wien filter. A so-called Wien filter curve is provided in [158].

5.2 Interaction region

The goal of this component is to produce as many metastable states as possible out of the incoming ion beam. In the already existing LSP a Cs-cell is utilized to use a charge exchange reaction to assemble as many atomic metastable $2S_{1/2}$ states as possible out of the incoming ion beam. In case of a proton beam the reaction can be stated as

$$p + {}^{133}_{55}\mathrm{Cs} \rightarrow \mathrm{H}_{2S_{1/2}} + {}^{133}_{55}\mathrm{Cs}^{+}. \tag{5.9}$$

The same treatment is possible for incoming deuteron and triton beams. The efficiency of producing metastable atomic states in the charge exchange reaction Eq. (5.9) depends on many different

parameters. The first one is the temperature, which is necessary to vaporize the cesium. The vaporized cesium then rises up and thereby passes the ion beam, until it reaches the top of the cell. At this point it condensates and drops back onto the bottom where the cycle restarts. The higher the temperature, the more cesium vapour is created, which increases the target density for the incoming beam. Therefore, an ideal temperature for efficient creation of metastable atomic states can be found. Such a temperature curve is shown in [5]. In addition, the cross section of producing metastable hydrogen atoms is depending on the beam energy of the incoming protons. This is the most critical condition, that the LSP is only efficient for low beam energies as the cross section decreases drastically for energies larger than 2 keV [159, 160, 161]. In conclusion, under optimal conditions, a theoretical maximum of 30% of all formed hydrogen atoms occupy metastable states.

For the helium-3 LSP analogue reactions need to be found, which enable an efficient production of metastable $^3He^+$. Shah and Gilbody measured in [162] the cross section for the creation of metastable $^3He^+$ ions from electron capture of a $^3He^{2+}$ beam in the beam energy range from $10-60$ keV. Six different gas targets $(Kr, N_2, H_2, Ar, O_2, He)$ have been employed. In a later publication [163] Shah and Gilbody measured the cross section for metastable $^3He^+$ production again for a $^3He^{2+}$ and a $^3He^+$ beam, respectively. This time they utilized H and H_2 as gas targets and covered the beam energy range of $4-343$ keV. The maximal cross section for an initially doubly ionized helium-3 beam on an atomic hydrogen target is in the range between 14 and 52 keV with a slow decrease in both directions. The population in the metastable state is about 13% but the cross sections 1.5 orders smaller than the charge exchange reaction for protons in cesium. The scattering cross sections for the molecular hydrogen target result in a bit smaller values, with a plateau at 26 to 67 keV but with the same percentage of producing metastable ions. The excitation cross sections for an initially singly ionized helium-3 ion beam for both targets are 1.5 orders smaller than for the double ionized helium-3 beam. In addition, the maximum values have a plateau at larger beam energies around 70 to 125 keV. Moreover, the charge exchange cross sections back into a neutral helium atom have been investigated in earlier papers [164, 165, 166, 167] for many different gas targets from few eV up to 200 keV. The result is a two order larger cross section value for the hydrogen gas target in comparison to the population into the metastable $^3He^+$ by the scattering process of an initially singly ionized helium-3 beam. Furthermore, Knopp et al. [168] have measured and calculated the cross section for producing excited singly ionized helium ions out of an incoming He^{2+} beam with a sodium target in a beam energy range of $2-13$ keV. The beam thereby scattered onto a sodium target and reached similar cross section values than for the molecular hydrogen target. In their paper they do not address the metastable $2S_{1/2}$ itself, but all excited states occupying the shell with $n = 2$. Here n stands for the main quantum number introduced in Sec. 2.1. Nevertheless, this sets an upper bound for the production of metastable helium states and provides also the magnitude. The initial helium beam needs to scatter on a gas target to produce the metastable singly ionized helium-3 ions. In the experiments in FZJ this gas target is introduced into the beam line by the argon cell. In the technical drawing Fig. 5.3 a cut through the beam line is depicted. This shows the connection of an external pin to the beam line tube from where the gas target is introduced into the beam line.

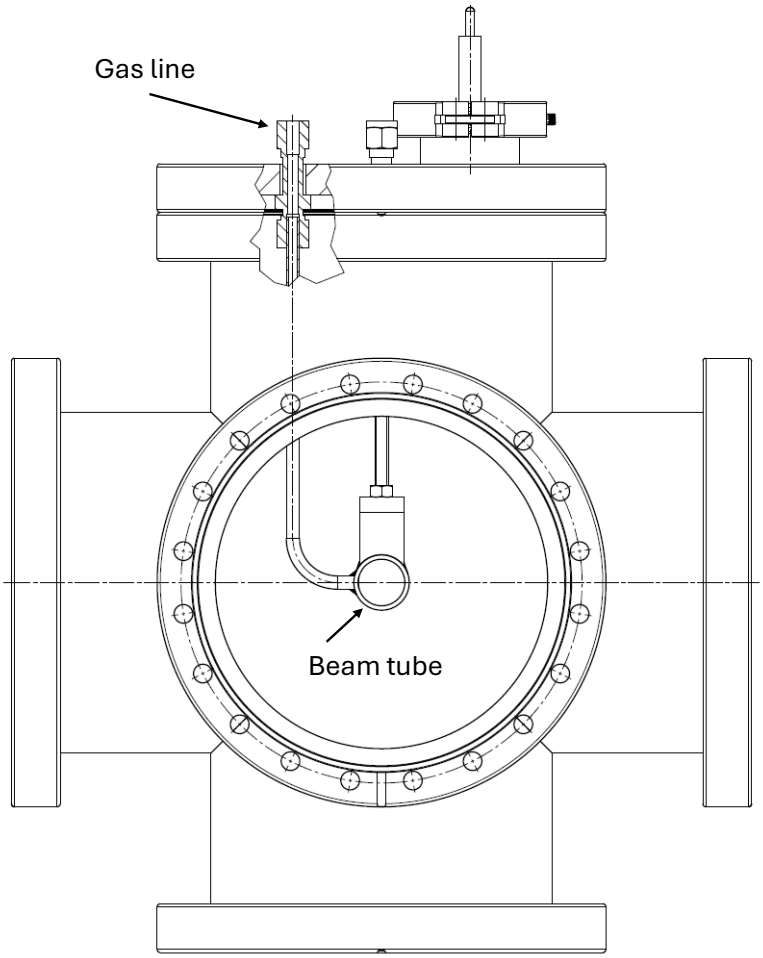

Figure 5.3: Technical drawing of the argon cell located at the nuclear institute at FZJ with a cut perpendicular to the beam line. Thereby, the drawings have been performed by the design department of the nuclear institute at FZJ. The gas line entering the beam line tube is connected to the outside by a Swagelok pin.

5.3 Quenching region

The data acquisition takes place in the last part of the experimental setup. Therefore, the remaining metastable atomic as well as ionic states are forced into the ground state due to strong external electric fields. The thereby released photons are then detected and transformed into a signal. For the metastable hydrogen atoms and its isotopes the photon energy corresponds to $E_\gamma \approx 10.2$ eV. The so-called Ly-α photons are detected by a photomultiplier [5]. To reduce the background a special MgF window is placed in front of the KBr photocathode. Therefore, the photomultiplier is sensitive within a wavelength range of 110 nm to 160 nm [169]. Monitoring the charged beam is done by a Faraday cup at the end of the quenching chamber.
The metastable helium-3 ions instead produce photons with energies of $E_\gamma \approx 40.8$ eV. Consequently, a different detector is needed as the corresponding photon wavelength is $\lambda_\gamma \approx 30.4$ nm. A charged-coupled device (CCD) camera would be suitable for this task. In the following an Andor CCD camera has been tested [170]. Thus the camera had an exposure time of 20 ms in

which the accumulated photons on each pixel were detected to create a single picture. The goal was to produce metastable helium-4 ions in a scattering process with different gas targets, which were introduced in the beam line through the argon cell, which is depicted in Fig. 5.3. Since the nucleus plays a minor role in the scattering process helium-4 has been chosen instead of helium-3, which is much more expensive. Moreover, the corresponding experimental setup is depicted in Fig. 5.4. Thereby, a mass flow controller has been employed to control the target gas flow into the beam tube of the argon cell. Furthermore, an electron cyclotron resonance (ECR) source was utilized [171]. First measurements, show a large background, which is correlated to the beam as it varies with the beam energy as well as with the quenching field and the gas target density. While Fig. 5.6, Fig. 5.8, Fig. 5.10 and Fig. 5.12 show the background without any gas target Fig. 5.5, Fig. 5.7, Fig. 5.9, Fig. 5.11 and Fig. 5.13 show the result for an employed N_2 target. The denser the gas target the more the beam spreads out. Consequently, more particles hit the walls of the chamber, thereby drastically increasing the background. In addition, the quenching potential defocuses parts of the beam, which also increase the background. Consequently, a shielding material needs to be placed in front of the camera to block unwanted background radiation. Data based on [172, 173] could be used to find an appropriate material, which only transmits light around the 30 nm. The transmission curve for the 1.2 μm thick aluminium foil is depicted in Fig. 5.14. In addition, Meidinger et al. [174] show that visible light is stopped due to the aluminium foil. Unfortunately, beam energies only up to 7 keV for a singly ionized helium beam were possible with the employed ECR source. Due to the fact that relevant cross sections for the production of metastable states occur at much larger beam energies, e.g. 100 keV, the experiments were stopped.

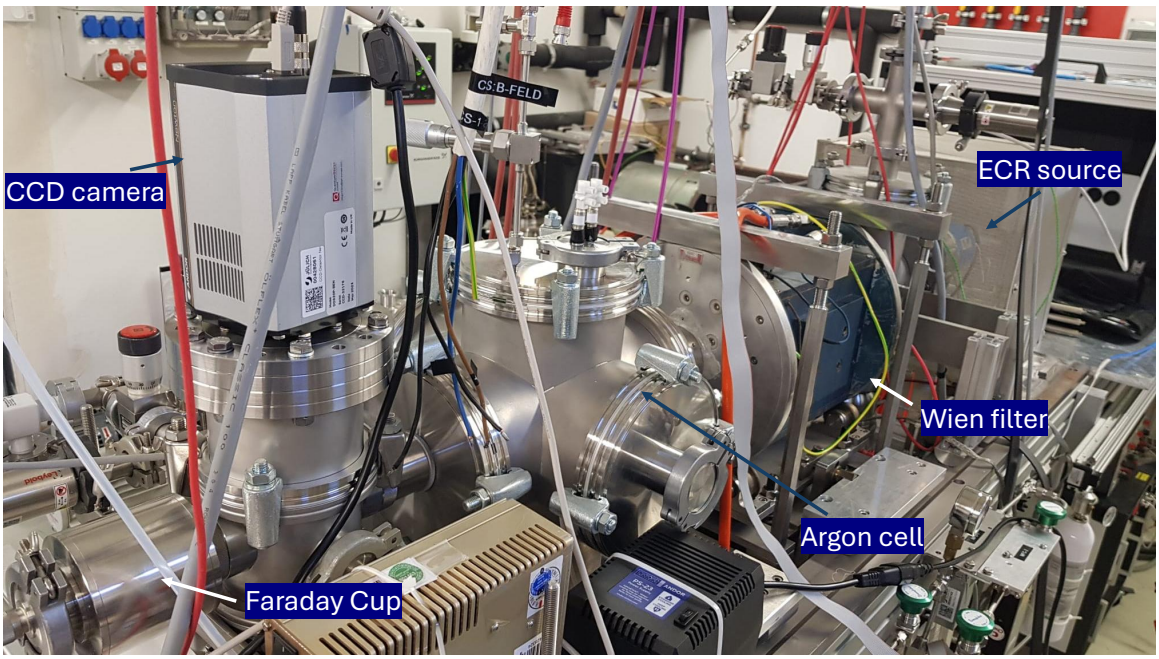

Figure 5.4: The experimental setup at the nuclear institute at FZJ to test a Andor Newton CCD camera [170] is shown. An ECR source [171] is utilized to produce a singly ionized helium beam, while a Wien filter selects mass number $A = 4$. The scattering process to produce metastable He^+ ions takes place in the argon cell. Electric fields are applied below the CCD camera to provide a quenching field for the metastable ions, while a Faraday cup monitors the charged beam.

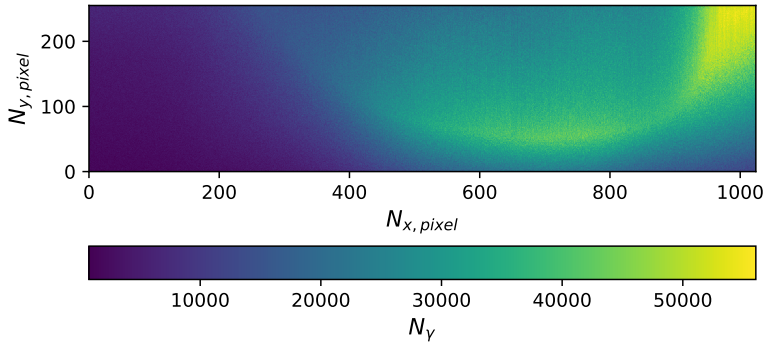

Figure 5.5: The number of photons detected onto the chip of the CCD camera subtracted from the background, which is visible in Fig. 5.6, is shown. The colorbar thereby connects the colors with the number of photons N_γ each pixel detected over an exposure time of 20 ms, while the x and y axis show the affected pixel on the chip. The corresponding experimental parameters are summarized in Tab. 5.1.

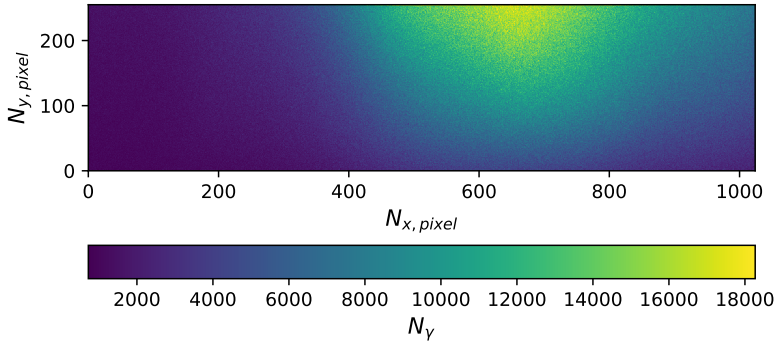

Figure 5.6: The number of photons detected onto the chip of the CCD camera is illustrated. The colorbar thereby connects the colors with the number of photons N_γ each pixel detected over an exposure time of 20 ms, while the x and y axis show the affected pixel on the chip. In addition this picture shows the background for Fig. 5.5 in absence of a gas target. Further experimental parameters are summarized in Tab. 5.1.

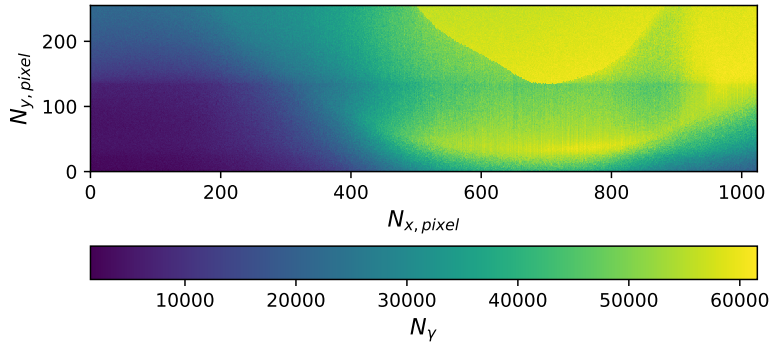

Figure 5.7: The number of photons detected onto the chip of the CCD camera subtracted from the background, which is visible in Fig. 5.8, is shown. The colorbar thereby connects the colors with the number of photons N_γ each pixel detected over an exposure time of 20 ms, while the x and y axis show the affected pixel on the chip. In comparison to Fig. 5.5 a larger electric quenching field is used, resulting in much larger number of detected photons. Further experimental parameters are summarized in Tab. 5.1.

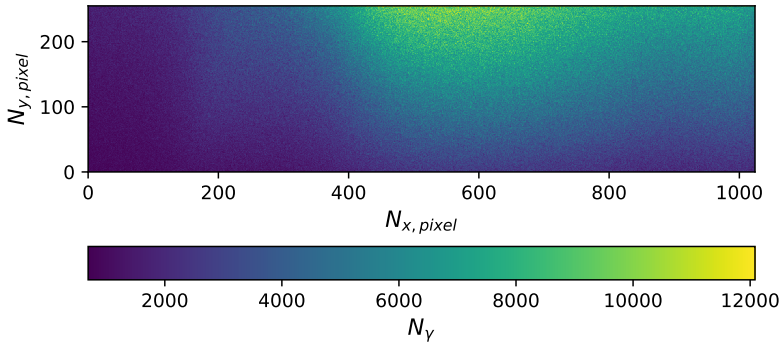

Figure 5.8: The number of photons detected onto the chip of the CCD camera is shown. The colorbar thereby connects the colors with the number of photons N_γ each pixel detected over an exposure time of 20 ms, while the x and y axis show the affected pixel on the chip. The plot is produced in the absence of a gas target, used as a background measurement for 5.7. Moreover, the corresponding experimental parameters are summarized in Tab. 5.1.

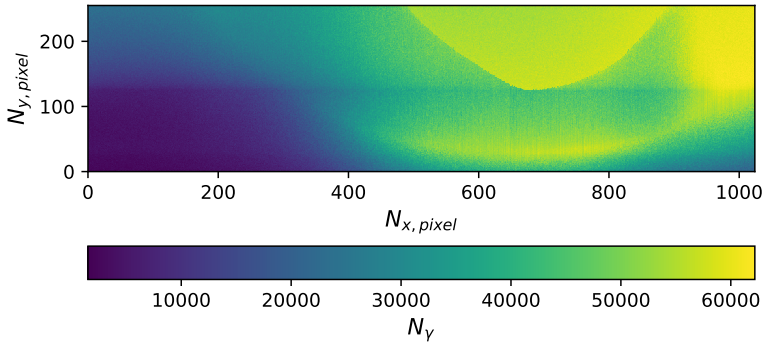

Figure 5.9: The number of photons detected onto the chip of the CCD camera subtracted from the background, which is visible in Fig. 5.10, is shown. The colorbar thereby connects the colors with the number of photons N_γ each pixel detected over an exposure time of 20 ms, while the x and y axis show the affected pixel on the chip. In comparison to Fig. 5.5 an increased electric quenching field has been utilized, resulting in a larger amount of detected photons. The corresponding experimental parameters are summarized in Tab. 5.1.

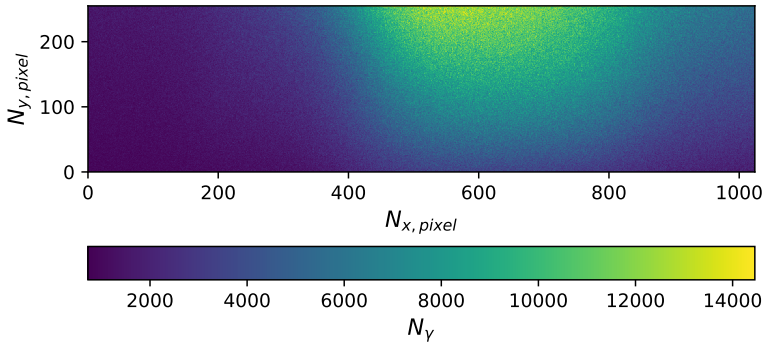

Figure 5.10: The number of photons detected onto the chip of the CCD camera is illustrated. The colorbar thereby connects the colors with the number of photons N_γ each pixel detected over an exposure time of 20 ms, while the x and y axis show the affected pixel on the chip. The plot is used a background measurement for Fig. 5.9 in the absence of a gas target. Further experimental parameters are summarized in Tab. 5.1.

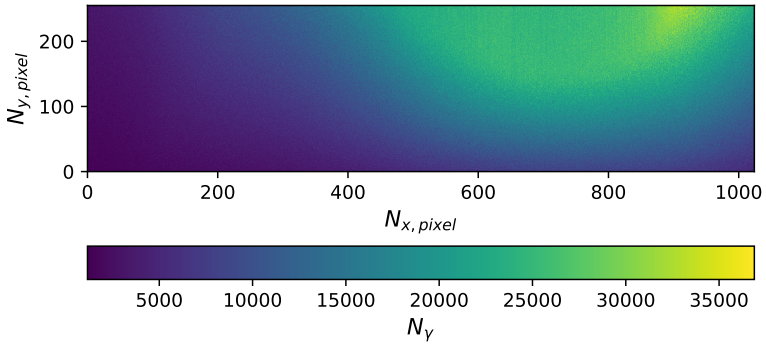

Figure 5.11: The number of photons detected onto the chip of the CCD camera subtracted from the background, which is visible in Fig. 5.12, is shown. The colorbar thereby connects the colors with the number of photons N_γ each pixel detected over an exposure time of 20 ms, while the x and y axis show the affected pixel on the chip. In comparison to Fig. 5.5 a larger beam energy but less strong electric quenching field and a less dense gas target have been used. As a result less photons are detected. The corresponding experimental parameters are summarized in Tab. 5.1.

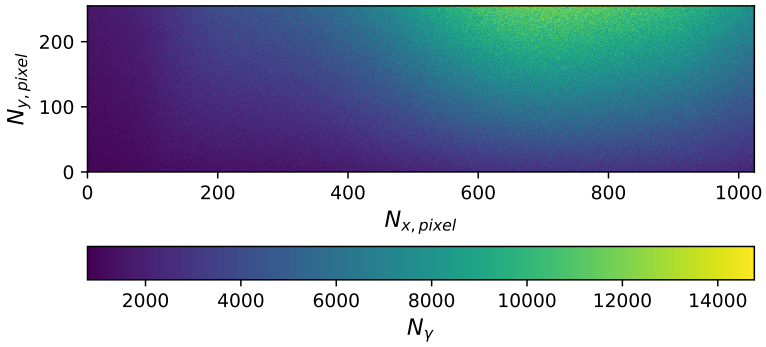

Figure 5.12: The number of photons detected onto the chip of the CCD camera is shown. The colorbar thereby connects the colors with the number of photons N_γ each pixel detected over an exposure time of 20 ms, while the x and y axis show the affected pixel on the chip. This measurement is used as a background measurement for Fig. 5.11 and Fig. 5.13. Further experimental parameters are summarized in Tab. 5.1.

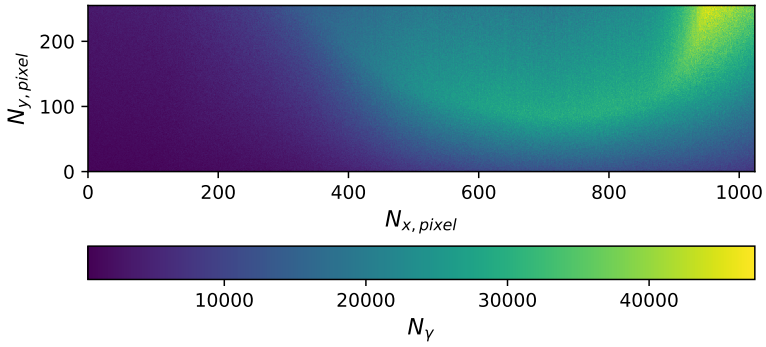

Figure 5.13: The number of photons detected onto the chip of the CCD camera subtracted from the background, which is visible in Fig. 5.12, is shown. The colorbar thereby connects the colors with the number of photons N_γ each pixel detected over an exposure time of 20 ms, while the x and y axis show the affected pixel on the chip. In comparison to Fig. 5.11 a denser gas target is used, resulting in a higher amount of detected photons. The corresponding experimental parameters are summarized in Tab. 5.1.

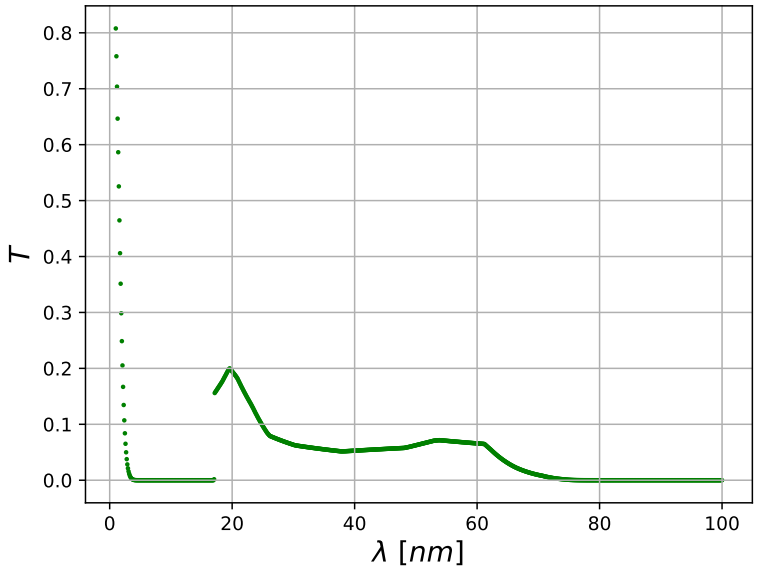

Figure 5.14: The transmission probability T for an incoming photon onto a 1.2 μm thick aluminium layer as function of the photon wavelength λ is displayed. The data was theoretically calculated by [172] based on [173].

Table 5.1: The experimental conditions for the different measurements with the CCD camera are summarized.

Figure	E_{kin} [keV]	gas target	U_{Quench} [kV]	Δp [mbar]
5.5	1.5	N_2	−5	$3.65 \cdot 10^{-5}$
5.6	1.5	–	−5	0
5.7	1.5	N_2	−6	$3.66 \cdot 10^{-5}$
5.8	1.5	–	−6	0
5.9	1.5	N_2	−5.5	$3.66 \cdot 10^{-5}$
5.10	1.5	–	−5.5	0
5.11	3	N_2	−4	$4.8 \cdot 10^{-6}$
5.12	3	–	−4	0
5.13	3	N_2	−4	$3.55 \cdot 10^{-5}$

Chapter 6

Possible applications

Finally, the experiments in the motivation section Ch. 1 are revisited and possible future setups discussed containing one of the modifications due to the models of this thesis.

6.1 TUM set-up for BoB

First the BoB experiment is reviewed for a possible realization in collaboration with the Technische Universität München (TUM). Based on the last publication [28] some adjustments are made, which are illustrated in Fig. 6.1. The experiment starts with a neutron source establishing a beam of protons, electrons and possible hydrogen atoms all created by neutron β decays. Starting at this point, a homogenous magnetic field parallel to the beam direction is established, which gently reaches towards the nuclear spin filter without large gradients to avoid any quenching of the metastable atoms due to motional Stark effect. Its tasks are focusing the beam and to establish a quantization axis, as well as guiding the beam to the spin filter. Then the beam reaches the nuclear spin filter of the second generation. Its assignments are to deflect all protons and electrons and to filter for both β states of the metastable hydrogen atoms. The last part of the setup has now to detect the residual metastable β atoms. Due to the very low branching ratio of the bound beta decay the most efficient detection process needs to be chosen. The quenching process, due to a single photomultiplier tube is discarded as its efficiency yields a loss of three orders in the signal. One order is lost as the Ly-α photons are isotropically radiated into all directions. Ideas to use mirrors or multiple photomultipliers to cover a larger solid angle are dismissed due to cost and efficiency in case of the mirrors [175]. Therefore, the idea to produce H^- ions out of metastable and ground state hydrogen atoms is proposed. When the H^- ion is produced from metastable $2S_{1/2}$ atoms, its kinetic energy is larger compared to those created by ground state atoms due to their excitation energy. Their difference in kinetic energy of 10.2 eV, which exactly equals the gap in the binding energy of both species, is then used to filter the H^- ions in a velocity filter. The advantage is that single H^- ions are detected with very little background. The charge exchange reaction with argon as gas target takes places in the argon cell directly behind the nuclear spin filter [33, 34]. Therefore, the metastable atoms also do not have any time to decay by any means. The MAC-E filter then selects the faster H^- ions created by metastable atoms. Finally, they are deflected into a CsI detector, where they are registered. The deflection reduces the background from all protons, which are also created in the argon cell in the reaction [33, 34]

$$\mathrm{H} + \mathrm{Ar} \rightarrow p + \mathrm{Ar} + e^-. \tag{6.1}$$

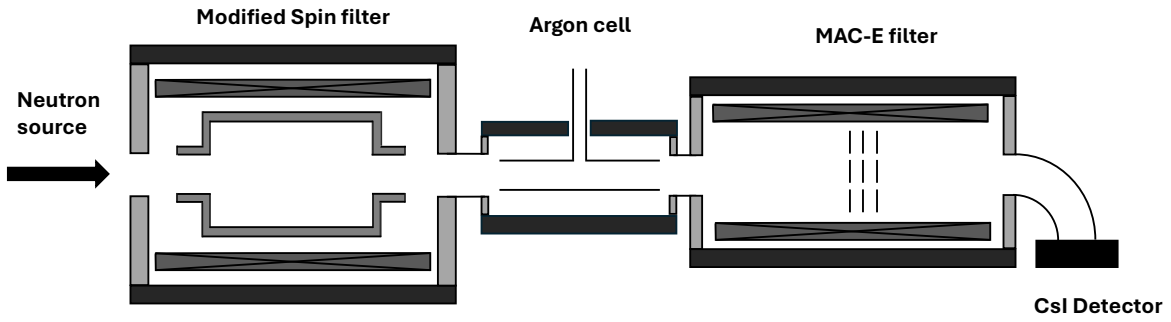

Figure 6.1: The setting for a possible detection of metastable hydrogen atoms created by the bound beta decay is sketched.

Based on this, first measurements to show the resolution of the kinetic energy of the H^- ions has been started by our group. The corresponding experimental setup is shown in Fig. 6.2. The ECR-source produces an ion beam, while the Wien filter allows only protons to pass through and sharpens the velocity of the beam. Then hydrogen atoms in metastable and ground states are produced in the Cs-cell. Subsequently, the spin filter is used to either quench all metastable atoms or to leave them unharmed. In the argon cell, argon is utilized as gas target to produce H^- ions with the hydrogen beam. Finally, three grids, visible in Fig. 6.3, are set to produce counter fields to stop the H^- ions before they reach the Faraday cup. The plan of the experiment is to measure the intensity of H^- ions as function of the counter field. The successful measurement would show a sharp step of the intensity loss, when the H^- created by the ground state hydrogen atoms do not reach the Faraday cup anymore. This step should then have a width of the 10.2 eV, when also the H^- ions created by metastable hydrogen atoms are stopped. Moreover, this step should vanish when metastable atoms are quenched in the spin filter before they reach the argon cell, where they react to H^- ions. The first successful test to show that H^- ions are produced by ground state and metastable atoms is illustrated in Fig. 6.4. Here, the larger cross section for metastable hydrogen atoms, in comparison to those for ground state atoms, into H^- ions at low beam energies [33] are used. Therefore, if metastable hydrogen atoms are in the beam the H^- intensity is increased. Subsequently, the nuclear spin filter can be used to show that both species produce H^- ions. By ramping through the magnetic field range single α states survive at the Zeeman crossing points, while at magnetic field values, which differ from this resonance condition, lead to the quenching of all metastable states. Consequently, a spin filter spectrum for H^- ions is depicted in Fig. 6.4. Thus, the H^- ions produced by ground state hydrogen atoms produce the linear background of roughly 0.28 nA, while the H^- ions created by metastable hydrogen atoms produce the resonances of approximately 0.03 nA.

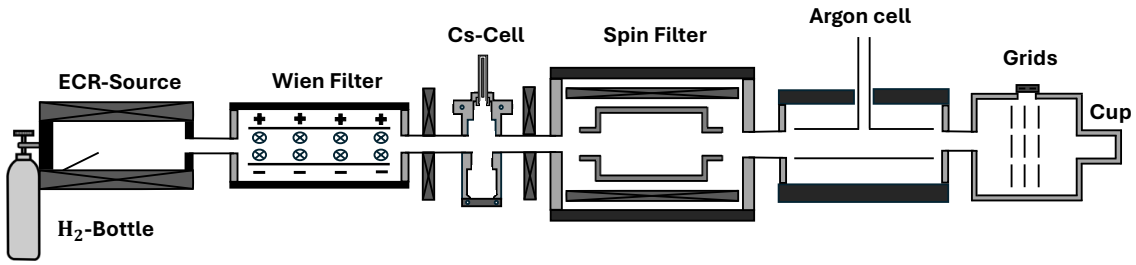

Figure 6.2: The setting at the institute for nuclear physics at FZJ to measure the difference in the kinetic energy of H^- ions is shown.



Figure 6.3: The grid system on which the electric voltages are applied to produce a counter field to stop the incoming ion beam is displayed.

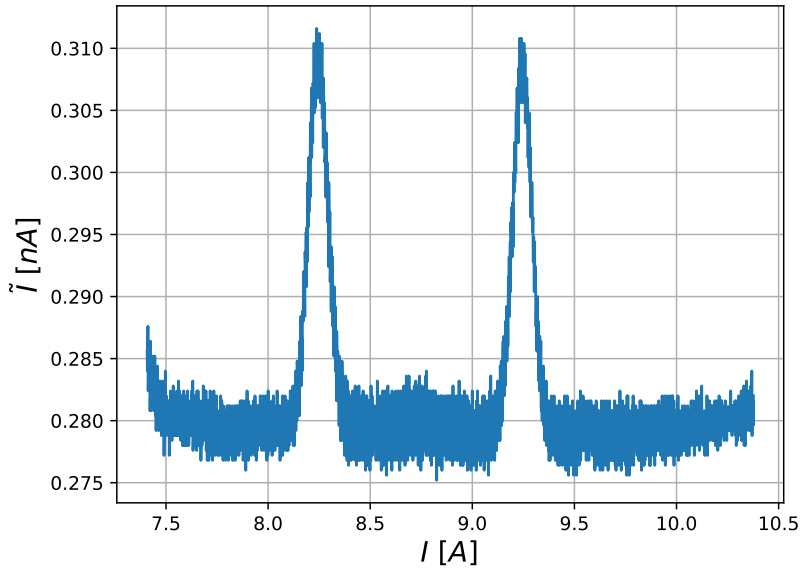

Figure 6.4: The beam intensity $\tilde{I}$, detected by the Faraday cup, is plotted on the vertical axis as function of the current I, which is producing the magnetic field in the nuclear spin filter. A positive electric counter field is applied on the middle grid in front of the cup to deflect all protons. The remaining H^- ions pass the grids and produce the signal in the Faraday cup. The parameters to reproduce the measurement are introduced in Tab. 6.1.

Table 6.1: The experimental conditions for the spin filter H^- measurement are shown. Therefore, the voltages produce external electric fields. $U_{\text{pos.}}/U_{\text{neg.}}$ are the main voltages creating the fields at the main part of the cavity, while $U_{\text{pos.s.}}/U_{\text{neg.s.}}$ are applied at the entrance and exit of the cavity. The radio frequency power input is also given in units of dBm.

Figure	E_{kin} [keV]	$U_{\text{pos.}}$ [V]	$U_{\text{neg.}}$ [V]	$U_{\text{pos.s.}}$ [V]	$U_{\text{neg.s.}}$ [V]	P_{RF} [dBm]	$f_{0,1,0}$ [GHz]
6.4	0.7	117	−140	41	−65	21	1.60991

6.2 Set-up for parity violation in metastable hydrogen

A possible setup for the investigation of the parity violation in metastable hydrogen, based on [176], is motivated and visible in Fig. 6.5. A high intensity low energy proton beam reaches the Cs-cell in which metastable hydrogen atoms are produced. Next, the beam enters the second generation spin filter in which one of the β states is selected, while all other metastable atoms are quenched. The specific selection of the β state depends on the crossing point, which is investigated. The crossing points are summarized in Tab. 1.2. Subsequently, the remaining β state enters the interaction region where the magnetic field scans the area of interest. In the meantime, a radio frequency is applied to transfer possible transitions from the β states into the short-lived $2P_{1/2}$ set, due to the weak force, back into a metastable α state. A second spin filter then scans for α states, therefore quenching all remaining β states. The surviving α state then radiates Ly-α light due to the quench process in the quench chamber. Subsequently, the light is detected by the photomultiplier tube as function of the magnetic field in the interaction region.
The experiment is challenging due to several conditions. First, any possible electric fields experienced by the beam produces a false signal in the α state population. The difference in the population needs to be distinguished from the signal of interest originating from the weak force. As guaranteeing zero fields is experimentally very challenging, due to several aspects, an additional electric field perpendicular to the beam direction might be applied. Before addressing the experiment itself, it is possible to measure the lifetime of the metastable atoms as function of the applied fields and comparing this with the theory. Therefore, an exact knowledge of the given fields can be gained. This needs a really stable beam to monitor the loss of population when the electric field is ramped. By doing so, the next challenging point is addressed too, which is the much larger magnetic field applied at the second generation spin filter. A small and steady decrease in the magnetic field needs to be done to get to the value of interest at the interaction region. Thereby, the produced motional Stark effect is then also investigated by measuring the lifetime of the beam. Moreover, the small interaction rate of the weak force leads to scanning for transition at least for a year resulting in a long-term experiment. An advantage is the possibility to reverse the electromagnetic components in the interaction region, which changes the asymmetry as defined in [176]. The great advantage with the setup is that all crossing points for protons as well as deuterons can be examined.

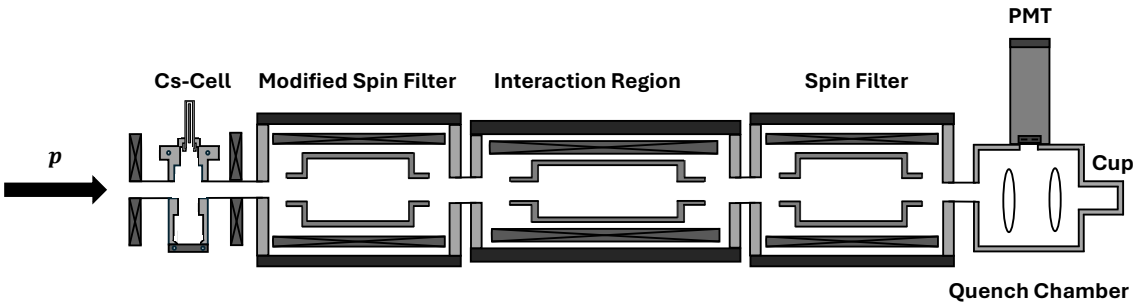

Figure 6.5: The sketch shows a possible setting for an experiment investigating the parity violation in metastable hydrogen atoms.

6.3 Set-up for probing dark matter axions

An experimental setup investigating dark matter axions is motivated, visible in Fig. 6.6. The setup is very comparable to the one investigating the parity violation. The only but main difference is that no cavity and electric field is needed in the interaction region. Again the idea of the setup is based on the theory paper by Yang and Dong [53]. Transitions in the hydrogen hyperfine states, created by the axion field, can be investigated by selecting a single β state as initial condition and to analyze the occupation numbers in a dedicated α state at the end. During the time of flight the hydrogen atoms in the β state have time to interact with the axion field. Therefore, the interaction region is used to ramp the magnetic field, which varies the energy difference between the single hyperfine states. By this, the mass range of the axions, which is proportional to their coupling strength, can be restricted. Limitations to external electric fields are less important as no crossing point with the low lived $2P_{1/2}$ and $2P_{3/2}$ is needed. Nevertheless, the magnetic field gradient from the second generation spin filter, preparing the initial beam in a dedicated β state, towards the interaction region should decrease slowly to avoid potential quenching. Due to the very low interaction of the axion field a very large beam intensity is needed. As this is very challenging an experimental setup utilizing an atomic beam source to produce dedicated ground state hydrogen hyperfine states might be more suitable but also much more expensive. To identify transitions in the ground states the authors Yang and Dong suggest using hydrogen maser [53].

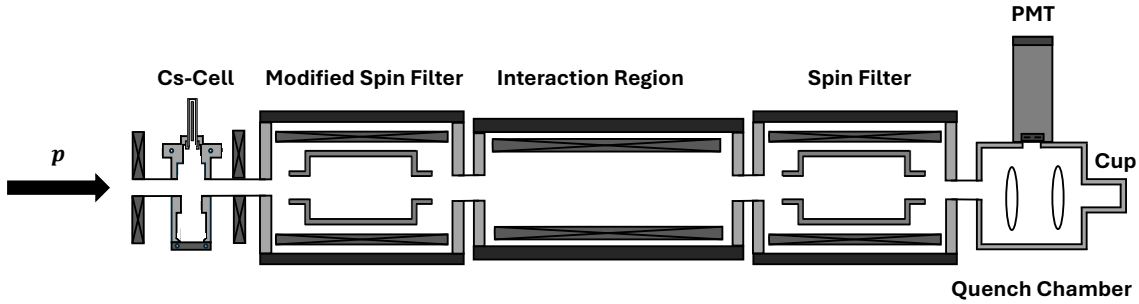

Figure 6.6: The sketch shows a possible setting for an experiment investigating the axion as a dark matter candidate.

6.4 Set-up for using a helium-3 LSP

The usage of a helium-3 Lamb-shift polarimeter for verifying the nuclear polarization of a polarized helium-3 source is motivated based on Fig. 6.7. So far the best method to produce nuclear polarized helium-3 is due to optical pumping methods [56]. Especially the method of metastability exchange

optical pumping (MEOP) is used very often, e.g. by the group from Jefferson Laboratory [177]. From here the idea is to pump the neutral nuclear polarized helium-3 atoms into a vacuum chamber surrounded by strong magnetic fields, to confine the polarization, where accelerated electrons fully ionize the atoms. The double ionized helium-3 ions can then be extracted and analyzed before entering the next acceleration stages from where they are introduced into storage rings. The extracted $^3He^{2+}$ ions first enter a Wien filter, which sharpens the velocity of the beam and rotates potentially the quantization axis. In addition, it deflects all other possible ions in the beam. Subsequently, the helium-3 ions enter the interaction region where a gas target is used to turn them into metastable $^3He^+$ ions. Magnetic fields should be established at this point to ensure that the nuclear polarization survives. This magnetic field can be combined with the one needed for the nuclear spin filter. The helium-3 spin filter then produces a single A state, which is finally identified by the CCD camera in the quench chamber. The nuclear polarization is then analyzed analogue to the measurement introduced in Sec. 4.1. In this measurement the photon intensity identified by the CCD camera is investigated as function of the magnetic field in the nuclear spin filter to see the difference in the population of the two A hyperfine substates.

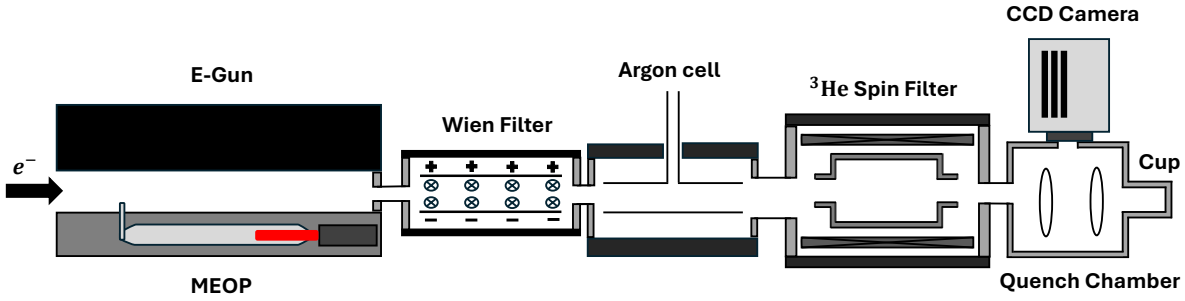

Figure 6.7: The sketch shows a possible setting for verifying the nuclear polarization of a polarized helium-3 source by utilizing a helium-3 Lamb-shift polarimeter.

6.5 Set-up to produce nuclear polarized fuel for nuclear fusion

A setup to produce nuclear polarized HD fuel for nuclear fusion facilities is described and visible in Fig. 6.8. The experiment is based on the article by Kannis and Rakitzis [94]. Cold HD is introduced into a system via a high pressure supersonic gas jet. Its task is to inject a high intensity beam with a sharp velocity distribution into the interaction chamber. Additionally, the beam is cooled such that nearly all molecules populate the states with zero molecular rotational angular momentum. From their infrared lasers are utilized to pump via a multiple step process the population into a polarized molecular rotational angular momentum. The rotational polarization is then transferred to the nucleus via the hyperfine beat. By repeating the laser excitation process large nuclear polarization values are expected. The nuclear polarized molecules then enter an ionizer where electrons are accelerated to strip an electron of the molecules and thereby transforming them to HD^+ ions. The process takes place at strong magnetic fields, preserving the nuclear polarization during the ionization process. The beam then enters the Wien filter where all ions, except HD^+, are deflected. Inside the Cs-cell the ions interact with cesium vapour to produce metastable H and D atoms. Also here a magnetic field is applied to confine the nuclear polarization in the reaction with the cesium. This process has been confirmed by Engels et al. in [14]. Subsequently, the metastable atoms enter the modified nuclear spin filter, which selects one of the four Breit-Rabi states. In case of the upgraded spin filter β states can be finally investigated as well. Finally, the population is identified by the photomultiplier tube in the quenching region. Again, the nuclear polarization is determined by comparing peak heights of the single Breit-Rabi states. With this method large amount of nuclear polarized DT should be generated to feed nuclear fusion reactors,

which then can take advantage of the polarized fuel. Due to radioactivity and rare abundance of tritium, hydrogen is used instead in the testing phase. Due to the similarity in their nuclear and atomic structure this is a valid approach.

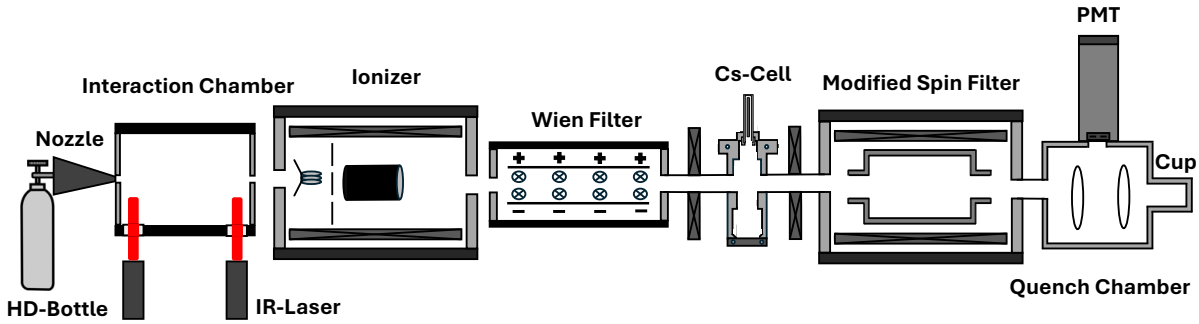

Figure 6.8: The sketch shows a possible setting to verify the production of nuclear polarized HD molecules as fuel for nuclear fusion reactors.

6.6 Spin filter as spin polarized beam source

Finally, the nuclear spin filter for helium-3 as well as second generation can also be used as a polarized source as it generates nuclear as well as electronic polarization. In the past a nuclear polarized H^-/D^- source based on the Lamb-shift was already utilized at the university of cologne [178] and correspondingly for $^3He^{2+}$ at Birmingham [179].

Summary and Conclusion

Nuclear polarized spin physics plays an important role in experimental research on fundamental particle physics as well as improvements in technologies. For the latter, medicine applications such as magnetic resonance tomography are based on natural nuclear polarizations, while hyperpolarized noble gas tracers are used for magnetic resonance imaging of the lung [57]. In addition, polarized nuclear fuel is estimated to improve the nuclear fusion in various aspects, e.g. 50% increased fusion rate. In particle physics famous experiments have shown that the preparation of specific nuclear spin states lead to new discoveries, e.g. revelation of the parity violation by the Wu experiment [40] or the discovery of a new resonance [180] at the cooler synchrotron COSY in Jülich. Realizations of nuclear polarized sources, targets and polarimetry establish the foundation to conduct polarized experiments.
An important polarimeter is the so-called Lamb-shift polarimeter, which is capable of measuring initial nuclear polarization of a low energy beam of charged atoms or molecules composed of hydrogen and its isotopes. Thereby, the measuring process is based on the creation of metastable hydrogen, deuterium or tritium atoms and the selective quenching of the metastable hyperfine states. Thus, the Lamb-shift polarimeter also enables the possibility to produce metastable hydrogen beams entirely composed of a single metastable hyperfine state with a large background of unpolarized ground state atoms. Its current disadvantage is that it can only address half of the hyperfine states, while the other half is always quenched in the ground state. Moreover, it is restricted to beams that can produce metastable hydrogen or its isotopes.
Thus, in this thesis a novel theoretical model is successfully developed to fully understand and upgrade the already existing Lamb-shift polarimeter, i.e. access the other half of hyperfine states, as well as creating a nuclear polarization detector system based on the Lamb-shift polarimeter for helium-3 ions. In addition, several possible applications for the upgraded nuclear spin filter and a Lamb-shift polarimeter for helium-3 are discussed, i.e. the preparation of large amount of nuclear polarized molecules to be used in fusion reactors or in medicine. The calculations for the model are based on the quantum mechanical density operator formalism and the atomic structure of hydrogen-like systems. This theoretical framework enables the simulations for hydrogen-like systems interacting with external electromagnetic fields. An application has been found in simulating the depolarization effects for deuterons in a confined plasma [181]. Subsequently, to validate the numerical results simulations for the already existing nuclear spin filter, a main component of the Lamb-shift polarimeter, are compared with experimental measurements showing a very good agreement in Fig. 4.20. By enabling a more complete theoretical description of the experimental data, this approach improves the systematic precision of polarization measurements. Based on the validation of the theoretical framework, further simulations have been performed to successfully proof the new concept of an upgraded nuclear spin filter for hydrogen and its isotopes as well as a nuclear spin filter for singly ionized helium-3. Moreover, different radio frequency modes have been utilized and discussed, which can be applied for various purposes. Furthermore, an experimental design has been motivated to set the path for an experimental realization of the device. In addition, helium-3 ion trajectories through the cavity of the spin filter are calculated without any intra-beam interactions in the relativistic as well as the non-relativistic regime.
Further developments for the different components of the detector system based on the Lamb-shift polarimeter have been taken into account, including the Wien filter, the interaction region and

the quench chamber. For the Wien filter, spectra are illustrated in Fig. 5.2 showing the mass separation and thereby also the sharpening of the beam velocity. Improvements in the velocity distribution comes with the cost of reducing intensity as the opening of the Wien filter needs to be limited by an aperture. Subsequently, main channels to produce metastable helium-3 ions are discussed, while the limitations by the ECR source to produce larger beam energies, limited further experimental investigations for different gas targets. Nevertheless, main results for the interaction region are that relevant cross sections to produce metastable $^3He^+$ states are expected at beam energies between 50 to 100 keV. Consequently, the applied static electric field in the cavity of the spin filter needs to change at least one time the polarity to focus the beam. Corresponding spin simulations show a positive result to this change and to the low time of flight through the device due to larger beam velocities. Finally, a detection method is presented to detected the 40.8 eV photons produced in the quenching process. The favored detector is a CCD camera developed by Andor [170]. To avoid as much background as possible a thin foil of aluminium could be utilized. This layer would theoretically only transfer light in the wavelength range between 20 to 70 nm. Again due to the lack of producing metastable helium-3 ions a future validation of the detector system would be necessary.

Hereafter, an experimental construction of an upgraded nuclear spin filter as well as an Lamb-shift polarimeter for helium-3 ions would help to bring this type of nuclear polarization detectors onto a new level. In a first step a cavity with a quality factor of at least Q = 16000 has to be constructed. In the meanwhile the outer parts, concerning the superconductive coil-system as well as the mechanical construction, can be prepared. In both cases the heat flow for the liquid helium needs to be monitored, which includes the placing of the plates at which static electric fields are applied at the cavity. In addition, their electric isolation to the cooled surface has to be guaranteed. Once this challenging step is successfully finalized the cavity can be implemented into the rest of the device. Furthermore, improved simulations, which include intra-beam scattering as well as a beam profile, would increase the understanding of the dynamics of the systems. The present quantum mechanical treatment neglects higher order corrections, e.g. electric, magnetic quadrupole transitions from external fields as well as from the nucleus. Hyperfine transitions into different sets of states by changing the main n and orbital quantum numbers l are also not taken into account. Furthermore, the magnetic part of the radio frequency as well as all electromagnetic fields originating from the Lorentz transformation into the rest system of the atomic beam are abandoned. Thus, the applied theoretical can be improved to identify even the smallest discrepancies between experiment and theory.

Concluding, the successful theoretical model for an upgraded nuclear spin filter enables the experimental investigation of several experiments, which are dependent on creating or measuring single β hyperfine states, e.g. the bound β decay experiment [28].

Chapter 7

Appendix

A Spherical harmonics

To show the different sign in the relation of Eq. (2.72) it is necessary to prove the relation for the definition of the spherical harmonics introduced in [111]

$$
\begin{aligned}
&\sqrt{\frac{(l-m+1)(l-m+2)}{(2l+1)(2l+3)}}Y_{l+1,m-1} - \sqrt{\frac{(l+m)(l+m-1)}{(2l+1)(2l-1)}}Y_{l-1,m-1} \\
&= \sqrt{\frac{(l-m+1)(l-m+2)}{(2l+1)(2l+3)}}\frac{1}{2^{l+1}(l+1)!}\sqrt{\frac{(2l+3)(l+m)!}{4\pi(l-m+2)!}}\times \\
&\times \frac{e^{i(m-1)\varphi}}{\sin^{m-1}(\theta)}\frac{d^{l-m+2}}{d(\cos(\theta))^{l-m+2}}\left[\cos^2(\theta)-1\right]^{l+1} \\
&- \sqrt{\frac{(l+m)(l+m-1)}{(2l+1)(2l-1)}}\frac{1}{2^{l-1}(l-1)!}\sqrt{\frac{(2l-1)(l+m-2)!}{4\pi(l-m)!}}\times \\
&\times \frac{e^{i(m-1)\varphi}}{\sin^{m-1}(\theta)}\frac{d^{l-m}}{d(\cos(\theta))^{l-m}}\left[\cos^2(\theta)-1\right]^{l-1} \\
&= \frac{1}{2^{l+1}(l+1)!}\sqrt{\frac{(l+m)!}{4\pi(2l+1)(l-m)!}}\frac{e^{i(m-1)\varphi}}{\sin^{m-1}(\theta)}\times \\
&\times \frac{d^{l-m}}{d(\cos(\theta))^{l-m}}\left[2(l+1)\left(\cos^2(\theta)-1\right)^{l} + 4l(l+1)\cos^2(\theta)\left(\cos^2(\theta)-1\right)^{l-1}\right] \qquad (7.1) \\
&- \frac{1}{2^{l-1}(l-1)!}\sqrt{\frac{(l+m)!}{4\pi(2l+1)(l-m)!}}\frac{e^{i(m-1)\varphi}}{\sin^{m-1}(\theta)}\frac{d^{l-m}}{d(\cos(\theta))^{l-m}}\left[\cos^2(\theta)-1\right]^{l-1} \\
&= \frac{1}{2^l l!}\sqrt{\frac{(l+m)!}{4\pi(2l+1)(l-m)!}}\frac{e^{i(m-1)\varphi}}{\sin^{m-1}(\theta)}\frac{d^{l-m}}{d(\cos(\theta))^{l-m}}\left[\left(\cos^2(\theta)-1\right)^{l}\right] \\
&+ \frac{1}{2^{l-1}(l-1)!}\sqrt{\frac{(l+m)!}{4\pi(2l+1)(l-m)!}}\frac{e^{i(m-1)\varphi}}{\sin^{m-1}(\theta)}\frac{d^{l-m}}{d(\cos(\theta))^{l-m}}\Big[\underbrace{\cos^2(\theta)\left(\cos^2(\theta)-1\right)^{l-1}}_{=(\cos^2(\theta)-1)^{l}+(\cos^2(\theta)-1)^{l-1}}\Big] \\
&- \frac{1}{2^{l-1}(l-1)!}\sqrt{\frac{(l+m)!}{4\pi(2l+1)(l-m)!}}\frac{e^{i(m-1)\varphi}}{\sin^{m-1}(\theta)}\frac{d^{l-m}}{d(\cos(\theta))^{l-m}}\left[\cos^2(\theta)-1\right]^{l-1} \\
&= \frac{1}{2^l l!}\sqrt{\frac{(2l+1)(l+m)!}{4\pi(l-m)!}}\frac{e^{i(m-1)\varphi}}{\sin^{m-1}(\theta)}\frac{d^{l-m}}{d(\cos(\theta))^{l-m}}\left[\cos^2(\theta)-1\right]^{l} \\
&= e^{-i\varphi}\sin(\theta)\,Y_{l,m}(\theta,\varphi)\,.
\end{aligned}
$$

The other relations are proven analogue. In addition, the mathematical induction can be used to show that the trigonometrical relation, used at the end of the proof, is correct

To proof: $\cos^2(\theta)\left(\cos^2(\theta)-1\right)^{l-1} = \left(\cos^2(\theta)-1\right)^{l} + \left(\cos^2(\theta)-1\right)^{l-1}$ for $\theta \in [0,\pi]$

Basis step (BS):

$l=1$ $\cos^2(\theta)\left(\cos^2(\theta)-1\right)^{0} = \cos^2(\theta) = \left(\cos^2(\theta)-1\right)^{1} + \left(\cos^2(\theta)-1\right)^{0}$

Inductive hypothesis (IH): Assume that the identity holds for some arbitrary but fixed number $l \in \mathbb{N}$.

Inductive step (IS): Show that the relation still holds for $l = n+1$

$$\cos^2(\theta)\left(\cos^2(\theta)-1\right)^{n} = \cos^2(\theta)\left(\cos^2(\theta)-1\right)^{n-1}\left(\cos^2(\theta)-1\right)$$
$$\overset{\text{IH}}{=} \left(\cos^2(\theta)-1\right)\left[\left(\cos^2(\theta)-1\right)^{n} + \left(\cos^2(\theta)-1\right)^{n-1}\right] = \left(\cos^2(\theta)-1\right)^{n+1} + \left(\cos^2(\theta)-1\right)^{n}.$$

The induction hypothesis is applied at the second equality.

Therefore, the relation holds for any $l \in \mathbb{N}$.

(7.2)

B Derivations for the general theory chapter

In this section derivations and calculations based on the associated Laguerre polynomials are introduced, which are relevant for Ch. 2. The first derivation from Sec. 2.2.1 is proven due to the fact that all terms of the polynomial are zero except the last one

$$\begin{aligned} L^1_{n-1}(0) &= \left[\frac{e^x x^{-1}}{(n-1)!}\frac{d^{n-1}}{dx^{n-1}}\left(e^{-x}x^n\right)\right]\Bigg|_{x=0} \\ &= \left[\frac{e^x x^{-1}}{(n-1)!}\left(\frac{d^{n-1}}{dx^{n-1}}\left(e^{-x}\right)x^n + \frac{d^{n-2}}{dx^{n-2}}\left(e^{-x}\right)\frac{d}{dx}\left(x^n\right) + \ldots + \underbrace{e^{-x}\frac{d^{n-1}}{dx^{n-1}}\left(x^n\right)}_{=e^{-x}n!x}\right)\right]\Bigg|_{x=0} \\ &= n. \end{aligned} \tag{7.3}$$

Next, the average values of r^{-1} and r^{-2} for the hydrogen atom are calculated. Starting with r^{-1} the result is obtained as

$$\begin{aligned} \left\langle\frac{1}{r}\right\rangle &= \langle\Psi_{n,l,m}|r^{-1}|\Psi_{n,l,m}\rangle = \int_0^\infty dr\, r|R_{n,l}|^2 \\ &= \int_0^\infty dr\, r\left(\frac{2Z}{na_0}\right)^3\frac{(n-l-1)!}{2n(n+l)!}e^{-\frac{2Zr}{na_0}}\left(\frac{2Zr}{na_0}\right)^{2l}\left(L^{2l+1}_{n-l-1}\left(\frac{2Zr}{na_0}\right)\right)^2 \\ &\overset{\text{use I}}{=} \frac{2Z}{na_0}\frac{(n-l-1)!}{2n(n+l)!}\underbrace{\int_0^\infty dx\, e^{-x}x^{2l+1}\left(L^{2l+1}_{n-l-1}(x)\right)^2}_{=\frac{(n+l)!}{(n-l-1)!}} \\ &= \frac{Z}{a_0 n^2}. \end{aligned} \tag{7.4}$$

Subsequently, the average value of r^{-2} is given by

$$\begin{aligned}
\left\langle \frac{1}{r^2} \right\rangle &= \langle \Psi_{n,l,m} | r^{-2} | \Psi_{n,l,m} \rangle = \int_0^\infty dr \, |R_{n,l}|^2 \\
&= \int_0^\infty dr \left(\frac{2Z}{na_0}\right)^3 \frac{(n-l-1)!}{2n\,(n+l)!} e^{-\frac{2Zr}{na_0}} \left(\frac{2Zr}{na_0}\right)^{2l} \left(L_{n-l-1}^{2l+1}\left(\frac{2Zr}{na_0}\right)\right)^2 \\
&= \left(\frac{2Z}{na_0}\right)^2 \frac{(n-l-1)!}{2n\,(n+l)!} \int_0^\infty dx\, e^{-x} x^{2l} \left(L_{n-l-1}^{2l+1}(x)\right)^2 \\
&= \left(\frac{2Z}{na_0}\right)^2 \frac{(n-l-1)!}{2n\,(n+l)!} \Bigg\{ \underbrace{\left[\frac{x^{2l+1}}{2l+1} e^{-x} \left(L_{n-l-1}^{2l+1}(x)\right)^2\right]\Big|_{x=0}^{\infty}}_{=0} \\
&\quad - \int_0^\infty dx \, \frac{x^{2l+1}}{2l+1} \frac{d}{dx} \left(e^{-x} \left(L_{n-l-1}^{2l+1}(x)\right)^2\right) \Bigg\} \\
&\overset{\text{use I}}{=} \left(\frac{2Z}{na_0}\right)^2 \frac{(n-l-1)!}{2n\,(n+l)!} \Bigg[\underbrace{\int_0^\infty dx \, \frac{x^{2l+1}}{2l+1} e^{-x} \left(L_{n-l-1}^{2l+1}(x)\right)^2}_{=\frac{(n+l)!}{(2l+1)(n-l-1)!}} \\
&\quad - \underbrace{\int_0^\infty dx \, \frac{2x^{2l+1}}{2l+1} e^{-x} L_{n-l-1}^{2l+1}(x) \frac{d}{dx} L_{n-l-1}^{2l+1}(x)}_{=0} \Bigg] \\
&= \frac{Z^2}{a_0^2 n^3 \,(l+1/2)}.
\end{aligned} \tag{7.5}$$

Moreover, the proof that the second integral is zero follows by

$$\begin{aligned}
\int_0^\infty dx\, x^{2l+1} e^{-x} L_{n-l-1}^{2l+1}(x) \frac{d}{dx} L_{n-l-1}^{2l+1}(x) &\overset{\text{use II}}{=} - \int_0^\infty dx\, x^{2l+1} e^{-x} L_{n-l-1}^{2l+1}(x) L_{n-l-2}^{2l+2}(x) \\
&\overset{\text{use III}}{=} - \int_0^\infty dx\, x^{2l+1} e^{-x} L_{n-l-1}^{2l+1}(x) \sum_{i=0}^{n-l-2} L_i^{2l+1}(x) \\
&\overset{\text{use I}}{=} 0,
\end{aligned} \tag{7.6}$$

where three properties are used for the associated Laguerre polynomial [102]

$$\begin{aligned}
&\text{I:} \quad \int_0^\infty dx\, e^{-x} x^k L_m^k(x) L_n^k(x) = \frac{\Gamma(n+k+1)}{n!} \delta_{m,n}, \\
&\text{II:} \quad \frac{d^\alpha}{dx^\alpha} L_n^k(x) = \begin{cases} (-1)^\alpha L_{n-\alpha}^{k+\alpha}(x) & \text{, if } \alpha \le n \\ 0 & \text{, else} \end{cases}, \\
&\text{III:} \quad L_n^{k+1}(x) = \sum_{i=0}^{n} L_i^k(x).
\end{aligned} \tag{7.7}$$

Next, the relations from Eq. (2.55) are proven by following the steps introduced in [105]. Specific commutator relations for $\vec{J}$ and $\vec{S}$ as well as other relations for arbitrary vectors $\vec{A}$, $\vec{B}$ and $\vec{C}$ are

stated next

$$\begin{aligned}
&\text{I:} \quad \left[\vec{A}\cdot\vec{B},\vec{C}\right] = \vec{A}\cdot\left[\vec{B},\vec{C}\right] - \left[\vec{C},\vec{A}\right]\cdot\vec{B},\\
&\text{II:} \quad \left[\vec{J},\vec{S}\right] = \left[\vec{S},\vec{J}\right] = -i\hbar\vec{S}\times\mathbb{1},\\
&\text{III:} \quad \vec{A}\cdot\vec{B}\times\vec{C} = \vec{A}\times\vec{B}\cdot\vec{C},\\
&\text{IV:} \quad \vec{A}\times\vec{B} = -\vec{B}\times\vec{A} + \left[\vec{A},\vec{B}\right]_x,\\
&\text{V:} \quad \left[\vec{C},\vec{A}\times\vec{B}\right] = \left[\vec{C},\vec{A}\right]\times\vec{B} - \left(\vec{A}\times\left[\vec{B},\vec{C}\right]_c\right),\\
&\text{VI:} \quad \left[\vec{B},\vec{A}\right] = -\left[\vec{A},\vec{B}\right]_c,\\
&\text{VII:} \quad \vec{A}\times\left(\vec{B}\times\vec{C}\right) = \vec{B}\left(\vec{A}\cdot\vec{C}\right) - \left(\vec{A}\cdot\vec{B}\right)\vec{C} - \left[\vec{B},\vec{A}\right]\cdot\vec{C}.
\end{aligned} \tag{7.8}$$

In addition, these commutator relations hold

$$\left[\vec{J}^2,\vec{S}\right] = \left[\vec{J}\cdot\vec{S},\vec{S}\right] = 0. \tag{7.9}$$

It is possible to take advantage of this by reformulating

$$\begin{aligned}
\left[\vec{J}^2,\vec{S}\right] &\overset{\text{use I}}{=} \vec{J}\cdot\left[\vec{J},\vec{S}\right] - \left[\vec{S},\vec{J}\right]\cdot\vec{J} \overset{\text{use II}}{=} -i\hbar\left(\vec{J}\cdot\vec{S}\times\mathbb{1} - \vec{S}\times\mathbb{1}\cdot\vec{J}\right)\\
&\overset{\text{use III}}{=} -i\hbar\left(\vec{J}\times\vec{S}\cdot\mathbb{1} - \vec{S}\times\mathbb{1}\cdot\vec{J}\right) = -i\hbar\left(\vec{J}\times\vec{S} - \vec{S}\times\vec{J}\right) \overset{\text{use IV}}{=} -2i\hbar\left(\vec{J}\times\vec{S} - i\hbar\vec{S}\right).
\end{aligned} \tag{7.10}$$

Next, this result is used to calculate

$$\begin{aligned}
\left[\vec{J}^2,\left[\vec{J}^2,\vec{S}\right]\right] &= -2i\hbar\left[\vec{J}^2,\left(\vec{J}\times\vec{S} - i\hbar\vec{S}\right)\right] \overset{\text{use V}}{=} -2i\hbar\left(-\vec{J}\times\left[\vec{S},\vec{J}^2\right]_c - i\hbar\left[\vec{J}^2,\vec{S}\right]\right)\\
&\overset{\text{use VI}}{=} -2i\hbar\left(\vec{J}\times\left[\vec{J}^2,\vec{S}\right] - i\hbar\left[\vec{J}^2,\vec{S}\right]\right)\\
&= -2i\hbar\left\{-2i\hbar\vec{J}\times\left(\vec{J}\times\vec{S} - i\hbar\vec{S}\right) - i\hbar\left(\vec{J}^2\vec{S} - \vec{S}\vec{J}^2\right)\right\}\\
&\overset{\text{use VII}}{=} -4\hbar^2\vec{J}\left(\vec{J}\cdot\vec{S}\right) + 4\hbar^2\left(\vec{J}\cdot\vec{J}\right)\vec{S} - 2\hbar^2\vec{J}^2\vec{S} + 2\hbar^2\vec{S}\vec{J}^2\\
&= -4\hbar^2\vec{J}\left(\vec{J}\cdot\vec{S}\right) + 2\hbar^2\left(\vec{J}^2\vec{S} + \vec{S}\vec{J}^2\right) = 0.
\end{aligned} \tag{7.11}$$

This concludes the proof of Eq. (2.55) with help of the commutator relations from Eq. (7.9).

C Electric multipole expansion

In this section the higher order corrections due to the electrostatic interaction between the electron and the nucleus are discussed. The derivation follows the steps of Ramsey in [110, 182].
The Coulomb interaction between the nucleus and the electron of a bound system depends on their charge densities ρ_e for the electron and ρ_n for the nucleus, respectively. Correspondingly, the Hamiltonian following the electric potential is stated as

$$H = \int_{V_e}\int_{V_n} \frac{\rho_e\rho_n dV_e dV_n}{4\pi\varepsilon_0 r}, \tag{7.12}$$

where V_e is the volume in which the electron charge is situated and V_n analogously for the nucleus. The vector $\vec{r}$ describes the relative position between both volumes. It is related to the vectors $\vec{r}_e$ and $\vec{r}_n$, which indicate the position of the volumes from the origin, by

$$\vec{r} = \vec{r}_e - \vec{r}_n. \tag{7.13}$$

Consequently, the absolute value squared of $\vec{r}$ can be expressed by

$$\begin{aligned}
|\vec{r}|^2 &= |\vec{r}_e|^2 + |\vec{r}_n|^2 - 2\vec{r}_e\cdot\vec{r}_n = |\vec{r}_e|^2 + |\vec{r}_n|^2 - 2|\vec{r}_e||\vec{r}_n|\cos(\theta)\\
&= |\vec{r}_e|^2\left(1 + \frac{|\vec{r}_n|^2}{|\vec{r}_e|^2} - 2\frac{|\vec{r}_n|}{|\vec{r}_e|}\cos(\theta)\right),
\end{aligned} \tag{7.14}$$

where θ is the angle enclosed by $\vec{r}_e$ and $\vec{r}_n$. Moreover, a Taylor expansion at $\frac{|\vec{r}_n|}{|\vec{r}_e|} = 0$ can be performed for $1/r$ by assuming that $\vec{r}_e \gg \vec{r}_n$. This leads to

$$\frac{1}{r} = \frac{1}{r_e} + \frac{\cos(\theta)}{r_e}\frac{r_n}{r_e} + \frac{\left(3\cos^2(\theta)-1\right)}{2r_e}\frac{r_n^2}{r_e^2} + \frac{3\cos(\theta)\left(5\cos^2(\theta)-3\right)}{6r_e}\frac{r_n^3}{r_e^3} + \mathcal{O}\left(\frac{r_n^4}{r_e^4}\right). \tag{7.15}$$

Furthermore, the result can be expressed in form of the Legendre polynomials $P_l(\cos(\theta)) = \frac{1}{2^l l!}\frac{d^l}{(d\cos(\theta))^l}\left(\cos^2(\theta)-1\right)^l$

$$\frac{1}{r} = \sum_l \frac{r_n^l}{r_e^{l+1}} P_l(\cos(\theta)). \tag{7.16}$$

To disentangle the two coordinate systems of the electron and the nucleus the following relation is used

$$P_l(\cos(\theta)) = \frac{4\pi}{2l+1}\sum_{m=-l}^{l}(-1)^m Y_{l,-m}(\theta_n,\varphi_n)\, Y_{l,m}(\theta_e,\varphi_e), \tag{7.17}$$

with $Y_{l,m}(\theta,\varphi)$ being the spherical harmonics. Combining the results the Hamiltonian can be expanded in orders of the spherical harmonics

$$\begin{aligned} H &= \sum_l H_l = \sum_l \sum_{m=-l}^{l} (-1)^m Q_{l,m} F_{l,-m}, \\ \text{with} \quad Q_{l,m} &= \sqrt{\frac{4\pi}{2l+1}} \int_{V_n} \rho_n r_n^l Y_{l,m}(\theta_n,\varphi_n)\, dV_n \\ \text{and} \quad F_{l,-m} &= \sqrt{\frac{4\pi}{2l+1}} \int_{V_e} \rho_e \frac{1}{4\pi\varepsilon_0 r_e^{l+1}} Y_{l,-m}(\theta_e,\varphi_e)\, dV_e. \end{aligned} \tag{7.18}$$

Consequently, by adding up the terms in l the higher correction orders are obtained.

C.1 Monopole

From Eq. (7.18) the Coulomb potential for a point-like charged nucleus is recaptured by the zeroth-order, also known as electrical monopole

$$\begin{aligned} Q_{0,0} &= \int_{V_n} \rho_n dV_n = Ze, \\ F_{0,0} &= \int_{V_e} \rho_e \frac{1}{4\pi\varepsilon_0 r_e} dV_e = -\frac{e}{4\pi\varepsilon_0 r_e} \coloneqq \phi(r_e), \\ H_0 &= -\frac{Ze^2}{4\pi\varepsilon_0 r}, \end{aligned} \tag{7.19}$$

with $\phi(r_e)$ being the electrostatic potential created by the electron. For a point-like particle, e.g. an electron, the charge density is given by $\rho_e = -e\delta^3(\vec{r}_e' - \vec{r}_e)$, which solves the upper integral, leading to the electrostatic potential. The result for the monopole is discussed in detail in Sec. 2.1.

C.2 Dipole

The dipole moment is obtained from Eq. (7.18) for $l = 1$. Consequently, the dipole Hamiltonian H_1 as well as the nuclear and electric part are stated as

$$
\begin{aligned}
H_1 &= Q_{1,0}F_{1,0} - Q_{1,-1}F_{1,1} - Q_{1,1}F_{1,-1},\\
Q_{1,0} &= \sqrt{\frac{4\pi}{3}}\int_{V_n}\rho_n r_n\sqrt{\frac{3}{4\pi}}\cos(\theta_n)\,dV_n = \int_{V_n}\rho_n z_n dV_n,\\
Q_{1,1} &= -\sqrt{\frac{4\pi}{3}}\int_{V_n}\rho_n r_n\sqrt{\frac{3}{8\pi}}\sin(\theta_n)\,e^{i\varphi_n}dV_n = -\frac{1}{\sqrt{2}}\int_{V_n}\rho_n\,(x_n + iy_n)\,dV_n,\\
Q_{1,-1} &= \sqrt{\frac{4\pi}{3}}\int_{V_n}\rho_n r_n\sqrt{\frac{3}{8\pi}}\sin(\theta_n)\,e^{-i\varphi_n}dV_n = \frac{1}{\sqrt{2}}\int_{V_n}\rho_n\,(x_n - iy_n)\,dV_n,\\
F_{1,0} &= \sqrt{\frac{4\pi}{3}}\int_{V_e}\frac{\rho_e}{4\pi\varepsilon_0 r_e^2}\sqrt{\frac{3}{4\pi}}\cos(\theta_e)\,dV_e = \int_{V_e}\frac{\rho_e}{4\pi\varepsilon_0 r_e^3}z_e dV_e = \frac{\partial\phi(r_e)}{\partial z_e},\\
F_{1,1} &= -\frac{1}{\sqrt{2}}\int_{V_e}\frac{\rho_e}{4\pi\varepsilon_0 r_e^3}\,(x_e + iy_e)\,dV_e = -\frac{1}{\sqrt{2}}\left(\frac{\partial\phi(r_e)}{\partial x_e} + i\frac{\partial\phi(r_e)}{\partial y_e}\right),\\
F_{1,-1} &= \frac{1}{\sqrt{2}}\int_{V_e}\frac{\rho_e}{4\pi\varepsilon_0 r_e^3}\,(x_e - iy_e)\,dV_e = \frac{1}{\sqrt{2}}\left(\frac{\partial\phi(r_e)}{\partial x_e} - i\frac{\partial\phi(r_e)}{\partial y_e}\right).
\end{aligned}
\tag{7.20}
$$

Moreover, the dipole moment is expressed as

$$
H_1 = \int_{V_n}\rho_n\left(z_n\frac{\partial\phi(r_e)}{\partial z_e} + y_n\frac{\partial\phi(r_e)}{\partial y_e} + x_n\frac{\partial\phi(r_e)}{\partial x_e}\right)dV_n. \tag{7.21}
$$

So far, no nuclear dipole moment has been experimentally observed in isolated atoms, although it plays an essential role in molecules.

C.3 Quadrupole

The next higher order is due to the electric quadrupole and is represented in Eq. (7.18) by the term with $l = 2$. The Hamiltonian and the $Q_{2,m}$ and $F_{2,m}$ terms are expressed as

$$
\begin{aligned}
H_2 &= Q_{2,0}F_{2,0} - Q_{2,1}F_{2,-1} - Q_{2,-1}F_{2,1} + Q_{2,2,}F_{2,-2} + Q_{2,-2}F_{2,2},\\
Q_{2,\pm2} &= \sqrt{\frac{4\pi}{5}}\int_{V_n}\rho_n r_n^2\sqrt{\frac{15}{32\pi}}\sin^2(\theta_n)\,e^{\pm2i\varphi_n}dV_n = \frac{\sqrt{6}}{4}\int_{V_n}\rho_n\left(x_n^2 - y_n^2 \pm 2ix_n y_n\right)dV_n,\\
Q_{2,\pm1} &= \mp\sqrt{\frac{4\pi}{5}}\int_{V_n}\rho_n r_n^2\sqrt{\frac{15}{8\pi}}\sin(\theta_n)\cos(\theta_n)\,e^{\pm i\varphi_n}dV_n = \mp\frac{\sqrt{6}}{2}\int_{V_n}\rho_n\,(x_n z_n \pm iy_n z_n)\,dV_n,\\
Q_{2,0} &= \frac{1}{2}\int_{V_n}\rho_n r_n^2\left(3\cos^2(\theta_n) - 1\right)dV_n = \frac{1}{2}\int_{V_n}\rho_n\left(2z_n^2 - x_n^2 - y_n^2\right)dV_n,\\
F_{2,\pm2} &= \frac{\sqrt{6}}{4}\int_{V_e}\frac{\rho_e}{4\pi\varepsilon_0 r_e^5}\left(x_e^2 - y_e^2 \pm 2ix_e y_e\right)dV_e = \frac{\sqrt{6}}{12}\left(-\frac{\partial^2\phi(r_e)}{\partial x_e^2} \mp 2i\frac{\partial^2\phi(r_e)}{\partial y\partial x} + \frac{\partial^2\phi(r_e)}{\partial^2 y_e}\right),\\
F_{2,\pm1} &= \mp\frac{\sqrt{6}}{2}\int_{V_e}\frac{\rho_e}{4\pi\varepsilon_0 r_e^5}\,(x_e z_e \pm iy_e z_e)\,dV_e = \mp\frac{1}{\sqrt{6}}\left(\frac{\partial^2\phi(r_e)}{\partial x\partial z} \pm i\frac{\partial^2\phi(r_e)}{\partial y\partial z}\right),\\
F_{2,0} &= \frac{1}{2}\int_{V_e}\frac{\rho_e}{4\pi\varepsilon_0 r_e^5}\left(2z_e^2 - x_e^2 - y_e^2\right)dV_e = \frac{1}{2}\frac{\partial^2\phi(r_e)}{\partial z_e^2}.
\end{aligned}
\tag{7.22}
$$

By adding all components for H_2 from Eq. (7.22) it is possible to rewrite the Hamiltonian to

$$
H_2 = \frac{1}{6}\sum_{i,j=1}^{3}\int_{V_n}\int_{V_e}\frac{\rho_n\rho_e}{4\pi\varepsilon_0 r_e^5}\left(3x_{n,i}x_{n,j} - \delta_{i,j}r_n^2\right)\left(3x_{e,i}x_{e,j} - \delta_{i,j}r_e^2\right)dV_n dV_e, \tag{7.23}
$$

where $x_1 = x$, $x_2 = y$ and $x_3 = z$. To bring the Hamiltonian into a form only depending on the angular momenta $\vec{I}$ and $\vec{J}$ the main quantum number n, as well as the total quantum number for the electron j is fixed. Consequently, the Hamiltonian is restricted to diagonal elements. With these assumptions it is possible to express the position variables by angular momentum quantum numbers

$$\sum_{i,j=1}^{3}\left(3x_ix_j-\delta_{i,j}r^2\right)=-\underbrace{\frac{2\left\langle r^2\right\rangle}{(2l+3)(2l-1)}}_{:=C}\frac{1}{\hbar^2}\sum_{i,j=1}^{3}\left(\frac{3\left(L_iL_j+L_jL_i\right)}{2}-\delta_{i,j}\vec{L}^2\right). \tag{7.24}$$

First the left side of Eq. (7.24) is investigated

$$\sum_{i,j=1}^{3}\left(3x_ix_j-\delta_{i,j}r^2\right)=6xy+6xz+6yz. \tag{7.25}$$

Hereafter the xy-term is calculated

$$\begin{aligned}
\langle l,m'|xy|l,m\rangle &= \int_0^\infty dr\int_0^{2\pi}d\varphi\int_0^{\pi}d\theta\, r^2\sin(\theta)\,xy|R_{n,l}|^2Y_{l,m}Y^*_{l,m'}\\
&= \frac{\left\langle r^2\right\rangle}{2\pi}\int_0^{2\pi}d\varphi\int_0^{\pi}d\theta\,(-1)^{m+m'}\sin^3(\theta)\cos(\varphi)\sin(\varphi)\,\mathcal{P}_{l,m}\mathcal{P}_{l,m'}e^{i(m-m')\varphi}\\
&\overset{\text{use I}}{=} -\frac{\left\langle r^2\right\rangle}{2\pi}(-1)^{m+m'}\left[\frac{2\sqrt{(l(l+1)-m(m-1))(l(l+1)-(m-1)(m-2))}}{(2l+3)(2l-1)}\right.\\
&\quad\left.\int_0^{2\pi}d\varphi\int_0^{\pi}d\theta\,\sin(\theta)\cos(\varphi)\sin(\varphi)\,\mathcal{P}_{l,m-2}\mathcal{P}_{l,m'}e^{i(m-m')\varphi}\right]\\
&= -\frac{\left\langle r^2\right\rangle}{2\pi}(-1)^{m+m'}\left[\frac{2\sqrt{(l(l+1)-m(m+1))(l(l+1)-(m+1)(m+2))}}{(2l+3)(2l-1)}\right.\\
&\quad\left.\int_0^{2\pi}d\varphi\int_0^{\pi}d\theta\,\sin(\theta)\cos(\varphi)\sin(\varphi)\,\mathcal{P}_{l,m+2}\mathcal{P}_{l,m'}e^{i(m-m')\varphi}\right],
\end{aligned} \tag{7.26}$$

where $\mathcal{P}_{l,m}$ are the normalized associated Legendre polynomials, which are related to the spherical harmonics in [46] by

$$Y_{l,m}(\varphi,\theta)=\frac{1}{\sqrt{2\pi}}e^{im\varphi}\mathcal{P}_{l,m}(\cos(\theta)). \tag{7.27}$$

To distinguish the possible m' values two orthogonal normalization relations are used [183]

$$\begin{aligned}
\int_0^{\pi}d\theta\,\sin(\theta)\,\mathcal{P}_{l,m}\mathcal{P}_{l',m} &= \delta_{l,l'},\\
\int_0^{\pi}d\theta\,\frac{\mathcal{P}_{l,m}\mathcal{P}_{l,m'}}{\sin(\theta)} &= \frac{2l+1}{2m}\delta_{m,m'}.
\end{aligned} \tag{7.28}$$

Starting with $m' \neq m \pm 2$ it is visible that the integrals vanish

$$\begin{aligned}
&\int_0^{2\pi}d\varphi\int_0^{\pi}d\theta\,(-1)^{m+m'}\sin(\theta)\cos(\varphi)\sin(\varphi)\,\mathcal{P}_{l,m\pm2}\mathcal{P}_{l,m'}e^{i(m-m')\varphi}\\
&= \int_0^{2\pi}d\varphi\int_0^{\pi}d\theta\,(-1)^{m+m'}\frac{\sin^2(\theta)}{\sin(\theta)}\cos(\varphi)\sin(\varphi)\,\mathcal{P}_{l,m\pm2}\mathcal{P}_{l,m'}e^{i(m-m')\varphi}\\
&\overset{\text{use I}}{=} (-1)^{m+m'+1}\frac{2\sqrt{(l\pm m'+2)(l\pm m'+1)(l\mp m')(l\mp m'-1)}}{(2l+3)(2l-1)}\\
&\int_0^{2\pi}d\varphi\int_0^{\pi}d\theta\,\frac{\cos(\varphi)\sin(\varphi)}{\sin(\theta)}\mathcal{P}_{l,m\pm2}\mathcal{P}_{l,m'\pm2}e^{i(m-m')\varphi}=0.
\end{aligned} \tag{7.29}$$

The second relation of Eq. (7.28) rules all options for any m' besides $m' = m, m \pm 4$ out. The integral for φ vanishes for the three other m' values. Subsequently, for $m' = m-2$ the first integral relation from Eq. (7.28) can be used to show

$$\begin{aligned}\langle l, m'|xy|l, m\rangle &= -\frac{\langle r^2\rangle\, i}{2\,(2l+3)\,(2l-1)\,\hbar^2}\,\langle l, m'|L_-^2 - L_+^2|l, m\rangle \\ &= -\frac{\langle r^2\rangle}{(2l+3)\,(2l-1)\,\hbar^2}\,\langle l, m'|L_xL_y + L_yL_x|l, m\rangle\,.\end{aligned} \tag{7.30}$$

Similar to this, the xz component

$$\begin{aligned}\langle l, m'|xz|l, m\rangle &= \frac{\langle r^2\rangle}{2\pi}\int_0^{2\pi} d\varphi \int_0^{\pi} d\theta\ (-1)^{m+m'}\sin^2(\theta)\cos(\theta)\cos(\varphi)\,\mathcal{P}_{l,m}\mathcal{P}_{l,m'}e^{i(m-m')\varphi} \\ &\overset{\text{use II}}{=} \frac{\langle r^2\rangle}{2\pi}\,(-1)^{m+m'}\left[\frac{(2m-1)\sqrt{l\,(l+1)-m\,(m-1)}}{(2l+3)\,(2l-1)}\right. \\ &\left.\int_0^{2\pi} d\varphi \int_0^{\pi} d\theta\,\sin(\theta)\cos(\varphi)\,\mathcal{P}_{l,m-1}\mathcal{P}_{l,m'}e^{i(m-m')\varphi}\right] \\ &= \frac{\langle r^2\rangle}{2\pi}\,(-1)^{m+m'}\left[\frac{(2m+1)\sqrt{l\,(l+1)-m\,(m+1)}}{(2l+3)\,(2l-1)}\right.\end{aligned} \tag{7.31}$$

$$\begin{aligned}&\left.\int_0^{2\pi} d\varphi \int_0^{\pi} d\theta\,\sin(\theta)\cos(\varphi)\,\mathcal{P}_{l,m+1}\mathcal{P}_{l,m'}e^{i(m-m')\varphi}\right] \\ &= -\frac{\langle r^2\rangle}{2\,(2l+3)\,(2l-1)\,\hbar^2}\,\langle l, m'|L_+L_z + L_-L_z + L_zL_+ + L_zL_-|l, m\rangle \\ &= -\frac{\langle r^2\rangle}{(2l+3)\,(2l-1)\,\hbar^2}\,\langle l, m'|L_xL_z + L_zL_x|l, m\rangle\end{aligned}$$

and the yz component are investigated

$$\begin{aligned}\langle l, m'|yz|l, m\rangle &= \frac{\langle r^2\rangle}{2\pi}\int_0^{2\pi} d\varphi \int_0^{\pi} d\theta\ (-1)^{m+m'}\sin^2(\theta)\cos(\theta)\sin(\varphi)\,\mathcal{P}_{l,m}\mathcal{P}_{l,m'}e^{i(m-m')\varphi} \\ &\overset{\text{use II}}{=} \frac{\langle r^2\rangle}{2\pi}\,(-1)^{m+m'}\left[\frac{(2m-1)\sqrt{l\,(l+1)-m\,(m-1)}}{(2l+3)\,(2l-1)}\right. \\ &\left.\int_0^{2\pi} d\varphi \int_0^{\pi} d\theta\,\sin(\theta)\sin(\varphi)\,\mathcal{P}_{l,m-1}\mathcal{P}_{l,m'}e^{i(m-m')\varphi}\right] \\ &= \frac{\langle r^2\rangle}{2\pi}\,(-1)^{m+m'}\left[\frac{(2m+1)\sqrt{l\,(l+1)-m\,(m+1)}}{(2l+3)\,(2l-1)}\right.\end{aligned} \tag{7.32}$$

$$\begin{aligned}&\left.\int_0^{2\pi} d\varphi \int_0^{\pi} d\theta\,\sin(\theta)\sin(\varphi)\,\mathcal{P}_{l,m+1}\mathcal{P}_{l,m'}e^{i(m-m')\varphi}\right] \\ &= -\frac{\langle r^2\rangle\, i}{2\,(2l+3)\,(2l-1)\,\hbar^2}\,\langle l, m'|L_-L_z - L_+L_z + L_zL_- - L_zL_+|l, m\rangle \\ &= -\frac{\langle r^2\rangle}{(2l+3)\,(2l-1)\,\hbar^2}\,\langle l, m'|L_yL_z + L_zL_y|l, m\rangle\,,\end{aligned}$$

where the following relations for the normalized associated Legendre polynomials are used from [46]

$$
\begin{aligned}
\text{I:}\quad \sin^2(\theta)\,\mathcal{P}_{l,m} &= \sqrt{\frac{(l+m+4)(l+m+3)(l+m+2)(l+m+1)}{(2l+5)(2l+3)^2(2l+1)}}\mathcal{P}_{l+2,m+2}\\
&- \frac{2\sqrt{(l+m+2)(l+m+1)(l-m)(l-m-1)}}{(2l+3)(2l-1)}\mathcal{P}_{l,m+2}\\
&+ \sqrt{\frac{(l-m)(l-m-1)(l-m-2)(l-m-3)}{(2l+1)(2l-1)^2(2l-3)}}\mathcal{P}_{l-2,m+2}\\
&= \sqrt{\frac{(l-m+4)(l-m+3)(l-m+2)(l-m+1)}{(2l+5)(2l+3)^2(2l+1)}}\mathcal{P}_{l+2,m-2}\\
&- \frac{2\sqrt{(l-m+2)(l-m+1)(l+m)(l+m-1)}}{(2l+3)(2l-1)}\mathcal{P}_{l,m-2}\\
&+ \sqrt{\frac{(l+m)(l+m-1)(l+m-2)(l+m-3)}{(2l+1)(2l-1)^2(2l-3)}}\mathcal{P}_{l-2,m-2},\\
\text{II:}\quad \cos(\theta)\sin(\theta)\,\mathcal{P}_{l,m} &= \sqrt{\frac{(l+m+3)(l+m+2)(l+m+1)(l-m+1)}{(2l+5)(2l+3)^2(2l+1)}}\mathcal{P}_{l+2,m+1}\\
&+ \frac{(2m+1)\sqrt{(l+m+1)(l-m)}}{(2l+3)(2l-1)}\mathcal{P}_{l,m+1}\\
&- \sqrt{\frac{(l+m)(l-m)(l-m-1)(l-m-2)}{(2l+1)(2l-1)^2(2l-3)}}\mathcal{P}_{l-2,m+1}\\
&= -\sqrt{\frac{(l-m+3)(l-m+2)(l-m+1)(l+m+1)}{(2l+5)(2l+3)^2(2l+1)}}\mathcal{P}_{l+2,m-1}\\
&+ \frac{(2m-1)\sqrt{(l-m+1)(l+m)}}{(2l+3)(2l-1)}\mathcal{P}_{l,m-1}\\
&+ \sqrt{\frac{(l+m)(l+m-1)(l+m-2)(l-m)}{(2l+1)(2l-1)^2(2l-3)}}\mathcal{P}_{l-2,m-1}.
\end{aligned}
\tag{7.33}
$$

For the sake of completeness and the proof of relation Eq. (2.53) the matrix elements for x^2 are computed next for $m' = m \mp 2$

$$
\begin{aligned}
\langle l,m'|x^2|l,m\rangle &= \frac{\langle r^2\rangle}{2\pi}\int_0^{2\pi}d\varphi\int_0^{\pi}d\theta\,(-1)^{m+m'}\sin^3(\theta)\cos^2(\varphi)\,\mathcal{P}_{l,m}\mathcal{P}_{l,m'}e^{i(m-m')\varphi}\\
&\overset{\text{use I}}{=} -\frac{\langle r^2\rangle}{2\pi}(-1)^{m+m'}\frac{2\sqrt{(l(l+1)-m(m-1))(l(l+1)-(m-1)(m-2))}}{(2l+3)(2l-1)}\\
&\int_0^{2\pi}d\varphi\int_0^{\pi}d\theta\,\sin(\theta)\cos^2(\varphi)\,\mathcal{P}_{l,m-2}\mathcal{P}_{l,m'}e^{i(m-m')\varphi}\\
&= -\frac{\langle r^2\rangle}{2\pi}(-1)^{m+m'}\frac{2\sqrt{(l(l+1)-m(m+1))(l(l+1)-(m+1)(m+2))}}{(2l+3)(2l-1)}\\
&\int_0^{2\pi}d\varphi\int_0^{\pi}d\theta\,\sin(\theta)\cos^2(\varphi)\,\mathcal{P}_{l,m+2}\mathcal{P}_{l,m'}e^{i(m-m')\varphi}\\
&= -\frac{\langle r^2\rangle}{2(2l+3)(2l-1)\hbar^2}\langle l,m'|L_-^2+L_+^2|l,m\rangle\,.
\end{aligned}
\tag{7.34}
$$

Subsequently, the case $m = m'$ is addressed

$$\begin{aligned}
\langle l,m|x^2|l,m\rangle &= \frac{\langle r^2\rangle}{2\pi}\int_0^{2\pi} d\varphi \int_0^{\pi} d\theta\, \sin^3(\theta)\cos^2(\varphi)\,\mathcal{P}_{l,m}\mathcal{P}_{l,m} \\
&\overset{\text{use }\tilde{\text{I}}}{=} \frac{\langle r^2\rangle}{2}\int_0^{\pi} d\theta\, \sin^2(\theta)\,\mathcal{P}_{l,m}\left[\sqrt{\frac{(l+m+1)(l+m+2)}{(2l+1)(2l+3)}}\mathcal{P}_{l+1,m+1}\right. \\
&\left. -\sqrt{\frac{(l-m)(l-m-1)}{(2l+1)(2l-1)}}\mathcal{P}_{l-1,m+1}\right] \\
&\overset{\text{use }\tilde{\text{II}}}{=} \frac{\langle r^2\rangle}{2(2l+1)}\int_0^{\pi} d\theta\, \sin(\theta)\,\mathcal{P}_{l,m}\left[\frac{(l+m+1)(l+m+2)}{(2l+3)}\mathcal{P}_{l,m}\right. \\
&\left. +\frac{(l-m-1)(l-m)}{(2l-1)}\mathcal{P}_{l,m}\right] \\
&= \frac{\langle r^2\rangle}{2(2l+1)}\left[\frac{(l+m+1)(l+m+2)}{(2l+3)}+\frac{(l-m-1)(l-m)}{(2l-1)}\right] \\
&= \langle r^2\rangle\,\frac{l^2+l-1+m^2}{(2l+3)(2l-1)} \\
&= \frac{\langle r^2\rangle}{3}-\frac{2\langle r^2\rangle}{(2l+3)(2l-1)\hbar^2}\left(\frac{L_+L_-+L_-L_+}{4}-\frac{1}{3}\vec{L}^2\right),
\end{aligned} \tag{7.35}$$

where two recursive relations for the associated Legendre polynomials are used [46]

$$\begin{aligned}
\tilde{\text{I}}: &\quad \sin(\theta)\,\mathcal{P}_{l,m} = \sqrt{\frac{(l+m+1)(l+m+2)}{(2l+1)(2l+3)}}\mathcal{P}_{l+1,m+1}-\sqrt{\frac{(l-m)(l-m-1)}{(2l+1)(2l-1)}}\mathcal{P}_{l-1,m+1}, \\
\tilde{\text{II}}: &\quad \sin(\theta)\,\mathcal{P}_{l,m} = -\sqrt{\frac{(l-m+1)(l-m+2)}{(2l+1)(2l+3)}}\mathcal{P}_{l+1,m-1}+\sqrt{\frac{(l+m)(l+m-1)}{(2l+1)(2l-1)}}\mathcal{P}_{l-1,m-1}.
\end{aligned} \tag{7.36}$$

Merging the results of Eq. (7.34) and Eq. (7.35) leads to

$$\langle l,m'|x^2|l,m\rangle = \frac{\langle r^2\rangle}{3}-\frac{2\langle r^2\rangle}{(2l+3)(2l-1)\hbar^2}\left[\langle l,m'|L_x^2|l,m\rangle-\frac{1}{3}\langle l,m'|\vec{L}^2|l,m\rangle\right]. \tag{7.37}$$

Likewise, the result for y^2 is obtained and stated as

$$\langle l,m'|y^2|l,m\rangle = \frac{\langle r^2\rangle}{3}-\frac{2\langle r^2\rangle}{(2l+3)(2l-1)\hbar^2}\left[\langle l,m'|L_y^2|l,m\rangle-\frac{1}{3}\langle l,m'|\vec{L}^2|l,m\rangle\right]. \tag{7.38}$$

Subsequently, the average value of z^2 is determined as

$$\begin{aligned}
\langle z^2\rangle &= \int_0^{\infty} dr\int_0^{2\pi} d\varphi\int_0^{\pi} d\theta\, r^4\sin(\theta)\cos^2(\theta)\,|R_{n,l}|^2 Y_{l,m}Y_{l,\tilde{m}}^* \\
&= \langle r^2\rangle\int_0^{2\pi} d\varphi\int_0^{\pi} d\theta\,\sin(\theta)\,\frac{2l^2+2l-1-2m^2}{(2l+3)(2l-1)}Y_{l,m}Y_{l,\tilde{m}}^* \\
&= \frac{2l^2+2l-1-2m^2}{(2l+3)(2l-1)}\langle r^2\rangle \\
&= \frac{\langle r^2\rangle}{3}-\frac{2\langle r^2\rangle}{(2l+3)(2l-1)\hbar^2}\left(\langle L_z^2\rangle-\frac{1}{3}\langle\vec{L}^2\rangle\right).
\end{aligned} \tag{7.39}$$

The property for the associated Legendre polynomial used in Eq. (7.39) is then

$$\begin{aligned}\cos^2(\theta)\,\mathcal{P}_{l,m}(\cos(\theta)) = &\sqrt{\frac{\left[(l+1)^2-m^2\right]\left[(l+2)^2-m^2\right]}{(2l+1)(2l+3)^2(2l+5)}}\mathcal{P}_{l+2,m}(\cos(\theta))\\ &+\frac{2l^2+2l-2m^2-1}{(2l+3)(2l-1)}\mathcal{P}_{l,m}(\cos(\theta))\\ &+\sqrt{\frac{\left[(l-1)^2-m^2\right](l^2-m^2)}{(2l+1)(2l-1)^2(2l-3)}}\mathcal{P}_{l-2,m}(\cos(\theta)).\end{aligned} \tag{7.40}$$

Finally, combining all these relations proves Eqs. (7.24) and (2.53). Before addressing the Hamiltonian the constant C from Eq. (7.24) is substituted by the scalar Q for the nuclear part as followed

$$\begin{aligned}Q &\coloneqq \frac{2}{e}\langle I, m_I = I|Q_{2,0}|I, m_I = I\rangle = -\frac{1}{e}\langle I, m_I = I|3z_n^2 - r_n^2|I, m_I = I\rangle\\ &= \langle I, m_I = I|\frac{C_n}{e}\left(3I_z^2 - \vec{I}^2\right)|I, m_I = I\rangle = \frac{C_n}{e}I(2I-1),\end{aligned} \tag{7.41}$$

where the relation from Eq. (7.39) is used. Analogously the electronic part can be transformed to

$$q_j \coloneqq \frac{2}{e}\langle j, m_j = j|F_{2,0}|j, m_j = j\rangle = \frac{C_e}{e}\langle j, m_j = j|3J_z^2 - \vec{J}^2|j, m_j = j\rangle = \frac{C_e}{e}j(2j-1). \tag{7.42}$$

Consequently, the Hamiltonian for the quadrupole can be expressed as

$$H_2 = \frac{1}{6}\frac{e^2 q_j Q}{I(2I-1)\,j(2j-1)\,\hbar^4}\sum_{i,j=1}^{3}\left[\frac{3(I_iI_j + I_jI_i)}{2} - \delta_{i,j}\vec{I}^2\right]\left[\frac{3(J_iJ_j + J_jJ_i)}{2} - \delta_{i,j}\vec{J}^2\right]. \tag{7.43}$$

To simplify the expression of Eq. (7.43) single terms are examined

$$\begin{aligned}&\text{I:}\quad \sum_{i,j=1}^{3} I_iI_jJ_iJ_j = \sum_{i=1}^{3} I_iJ_i\sum_{j=1}^{3} I_jJ_j = \left(\vec{I}\cdot\vec{J}\right)^2,\\ &\text{II:}\quad \sum_{i,j=1}^{3} I_iI_j\delta_{i,j}\vec{J}^2 = \sum_{j=1}^{3} I_j^2\vec{J}^2 = \vec{I}^2\vec{J}^2,\\ &\text{III:}\quad \sum_{i,j=1}^{3}\delta\vec{I}^2\vec{J}^2 = 3\vec{I}^2\vec{J}^2,\\ &\text{IV:}\quad \sum_{i,j=1}^{3} I_jI_iJ_iJ_j = \sum_{i,j=1}^{3}\left(I_iI_jJ_iJ_j + i\hbar\varepsilon_{j,i,k}I_kJ_iJ_j\right)\\ &= \left(\vec{I}\cdot\vec{J}\right)^2 + i\hbar\left(-I_3J_1J_2 + I_3J_2J_1 + I_2J_1J_3 - I_2J_3J_1 - I_1J_2J_3 + I_1J_3J_2\right)\\ &= \left(\vec{I}\cdot\vec{J}\right)^2 + i\hbar\left(-i\hbar I_3J_3 - i\hbar I_2J_2 - i\hbar I_1J_1\right) = \left(\vec{I}\cdot\vec{J}\right)^2 + \hbar^2\left(\vec{I}\cdot\vec{J}\right).\end{aligned} \tag{7.44}$$

Therefore, the Hamiltonian H_2 takes the form

$$H_2 = \frac{e^2 q_j Q}{2I(2I-1)\,j(2j-1)\,\hbar^4}\left[3\left(\vec{I}\cdot\vec{J}\right)^2 + \frac{3}{2}\hbar^2\left(\vec{I}\cdot\vec{J}\right) - \vec{I}^2\vec{J}^2\right]. \tag{7.45}$$

Furthermore, the Hamiltonian is applied for deuterium, the simplest atom carrying an electrical quadrupole moment. Therefore, the electronic part q_j is calculated first in the case of the

metastable states $j = s = 1/2$

$$\begin{aligned} q_{s=1/2} &= \frac{2}{e}\langle s, m_s = s|F_{2,0}|s, m_s = s\rangle = -\int \frac{3\cos^2(\theta)-1}{4\pi\varepsilon_0 r^3}|\Psi_{2,0,0}|^2 dV \\ &= -\int_0^\infty dr \int_0^{2\pi} d\varphi \int_0^\pi d\theta \frac{\sin(\theta)\left(3\cos^2(\theta)-1\right)}{(4\pi)^2\varepsilon_0 r}\frac{1}{8a_0^3}\left(-\frac{r}{a_0}+2\right)^2 e^{-r/a_0} = 0 \end{aligned} \tag{7.46}$$

because $\displaystyle\int_0^\pi \sin(\theta)\left(3\cos^2(\theta)-1\right)d\theta = 0.$

Likewise, the case $j = 1/2$ is calculated

$$\begin{aligned} q_{j=1/2} &= \frac{2}{e}\langle j, m_j = 1/2|F_{2,0}|j, m_j = 1/2\rangle = \frac{2}{e}\Bigg[\frac{2}{3}\langle m_l = 1, m_s = -1/2|F_{2,0}|m_l = 1, m_s = -1/2\rangle \\ &-\frac{\sqrt{2}}{3}\underbrace{\langle m_l = 1, m_s = -1/2|F_{2,0}|m_l = 0, m_s = 1/2\rangle}_{=0,\text{ due to the spin projection } m_s} - \frac{\sqrt{2}}{3}\underbrace{\langle m_l = 0, m_s = 1/2|F_{2,0}|m_l = 1, m_s = -1/2\rangle}_{=0} \\ &+\frac{1}{3}\langle m_l = 0, m_s = 1/2|F_{2,0}|m_l = 0, m_s = 1/2\rangle\Bigg]. \end{aligned} \tag{7.47}$$

Subsequently, the non-vanishing matrix elements are derived separately starting with

$$\begin{aligned} &\frac{2}{e}\langle m_l = 1, m_s = -1/2|F_{2,0}|m_l = 1, m_s = -1/2\rangle \\ &= -\int_0^\infty dr \int_0^{2\pi} d\varphi \int_0^\pi d\theta \frac{\sin(\theta)\left(3\cos^2(\theta)-1\right)}{4\pi\varepsilon_0 r}|\Psi_{2,1,1}|^2 \\ &= -\int_0^\infty dr \int_0^{2\pi} d\varphi \int_0^\pi d\theta \frac{3\sin^3(\theta)\left(3\cos^2(\theta)-1\right)}{32\pi^2\varepsilon_0 r}\frac{r^2}{24a_0^5}e^{-r/a_0} \\ &= \frac{1}{240\pi\varepsilon_0 a_0^3}, \end{aligned} \tag{7.48}$$

and next

$$\begin{aligned} &\frac{2}{e}\langle m_l = 0, m_s = 1/2|F_{2,0}|m_l = 0, m_s = 1/2\rangle \\ &= -\int_0^\infty dr \int_0^{2\pi} d\varphi \int_0^\pi d\theta \frac{\sin(\theta)\left(3\cos^2(\theta)-1\right)}{4\pi\varepsilon_0 r}|\Psi_{2,1,0}|^2 \\ &= -\int_0^\infty dr \int_0^{2\pi} d\varphi \int_0^\pi d\theta \frac{3\sin(\theta)\cos^2(\theta)\left(3\cos^2(\theta)-1\right)}{16\pi^2\varepsilon_0 r}\frac{r^2}{24a_0^5}e^{-r/a_0} \\ &= -\frac{1}{120\pi\varepsilon_0 a_0^3}. \end{aligned} \tag{7.49}$$

Therefore, the electronic part q_j also vanishes in the case $j = 1/2$. Finally, the case $j = 3/2$ is investigated

$$\begin{aligned} q_{j=3/2} &= \frac{2}{e}\langle j, m_j = 3/2|F_{2,0}|j, m_j = 3/2\rangle = \frac{2}{e}\langle m_l = 1, m_s = 1/2|F_{2,0}|m_l = 1, m_s = 1/2\rangle \\ &= \frac{1}{240\pi\varepsilon_0 a_0^3}. \end{aligned} \tag{7.50}$$

Furthermore, the hyperfine calculations from Sec. 3.2 are taken into account

$$\begin{aligned} \langle F = 5/2, m_F|\vec{I}\cdot\vec{J}|F = 5/2, m_F\rangle &= \frac{3\hbar^2}{2}, \\ \langle F = 3/2, m_F|\vec{I}\cdot\vec{J}|F = 3/2, m_F\rangle &= -\hbar^2, \\ \langle F = 1/2, m_F|\vec{I}\cdot\vec{J}|F = 1/2, m_F\rangle &= -\frac{5\hbar^2}{2}. \end{aligned} \tag{7.51}$$

As the quadrupole Hamiltonian Eq. (7.45) is diagonal in the basis $|F, m_F\rangle$ the non-vanishing matrix elements can be stated as

$$\begin{aligned}
\langle F = {}^5\!/_2, m_F|H_2|F = {}^5\!/_2, m_F\rangle &= \frac{e^2 Q}{960\pi\varepsilon_0 a_0^3} \approx 11.58 \text{ peV}, \\
\langle F = {}^3\!/_2, m_F|H_2|F = {}^3\!/_2, m_F\rangle &= -\frac{e^2 Q}{240\pi\varepsilon_0 a_0^3} \approx -46.32 \text{ peV}, \\
\langle F = {}^1\!/_2, m_F|H_2|F = {}^1\!/_2, m_F\rangle &= \frac{e^2 Q}{192\pi\varepsilon_0 a_0^3} \approx 57.90 \text{ peV},
\end{aligned} \tag{7.52}$$

where the nuclear quadrupole value $Q = 0.286$ fm^2 is used [135].

D Coupling constants

In this section the coupling constants, due to the first order Stark effect, are introduced in the Breit-Rabi basis. First, a static electric field pointing in x-direction $\vec{E} = \varepsilon_x \hat{e}_x$ is assumed, which interacts with the three excited ($2S_{1/2}$, $2P_{1/2}$ and $2P_{3/2}$) sets for hydrogen. The definitions of the Breit-Rabi states as well as the coupling conditions are shown in Sec. 3.1. Possible transitions and their coupling constants, caused by the Stark effect, are discussed in Sec. 2.4.1. Consequently, the

non-vanishing matrix elements are

$$
\begin{aligned}
\langle\alpha_1|H_{Stark}|e_2\rangle &= \frac{\delta}{\sqrt{3}\sqrt{1+y^2(B_z)}}\left(1-y(B_z)\right),\\
\langle\alpha_1|H_{Stark}|f_4\rangle &= \frac{\delta}{\sqrt{3}\sqrt{1+z^2(B_z)}}\left(z(B_z)-1\right),\\
\langle\alpha_1|H_{Stark}|g_1\rangle &= \delta,\\
\langle\alpha_1|H_{Strak}|g_3\rangle &= \frac{\delta}{\sqrt{6}\sqrt{1+\varepsilon_1^2(B_z)}}\left(\varepsilon_1(B_z)-1\right),\\
\langle\alpha_1|H_{Stark}|h_7\rangle &= \frac{\delta}{\sqrt{6}\sqrt{1+\varepsilon_2^2(B_z)}}\left(1-\varepsilon_2(B_z)\right),\\
\langle\alpha_2|H_{Stark}|e_1\rangle &= \frac{\delta}{\sqrt{3}\sqrt{1+x^2(B_z)}}\left(1-x(B_z)\right),\\
\langle\alpha_2|H_{Stark}|f_3\rangle &= \frac{\delta}{\sqrt{3}\sqrt{1+x^2(B_z)}}\left(1+x(B_z)\right),\\
\langle\alpha_2|H_{Stark}|g_2\rangle &= \frac{\delta}{\sqrt{1+x^2(B_z)}\sqrt{1+\chi_1^2(B_z)}}\left(\frac{1}{\sqrt{2}}+x(B_z)\chi_1(B_z)\sqrt{\frac{2}{3}}+\frac{1}{\sqrt{6}}\chi_1(B_z)\right),\\
\langle\alpha_2|H_{Stark}|g_4\rangle &= \frac{\delta}{\sqrt{1+x^2(B_z)}\sqrt{1+\kappa_1^2(B_z)}}\left(-\frac{1}{\sqrt{2}}-\sqrt{\frac{2}{3}}x(B_z)\kappa_1(B_z)+\frac{1}{\sqrt{6}}\kappa_1(B_z)\right),\\
\langle\alpha_2|H_{Stark}|h_6\rangle &= \frac{\delta}{\sqrt{1+x^2(B_z)}\sqrt{1+\chi_2^2(B_z)}}\left(\frac{1}{\sqrt{2}}\chi_2(B_z)+x(B_z)\sqrt{\frac{2}{3}}+\frac{1}{\sqrt{6}}\right),\\
\langle\alpha_2|H_{Stark}|h_8\rangle &= \frac{\delta}{\sqrt{1+x^2(B_z)}\sqrt{1+\kappa_2^2(B_z)}}\left(-\frac{1}{\sqrt{2}}\kappa_2(B_z)-\sqrt{\frac{2}{3}}x(B_z)+\frac{1}{\sqrt{6}}\right),\\
\langle\beta_3|H_{Stark}|e_2\rangle &= \frac{\delta}{\sqrt{3}\sqrt{1+y^2(B_z)}}\left(1+y(B_z)\right),\\
\langle\beta_3|H_{Stark}|f_4\rangle &= \frac{\delta}{\sqrt{3}\sqrt{1+z^2(B_z)}}\left(1+z(B_z)\right),\\
\langle\beta_3|H_{Stark}|g_3\rangle &= \frac{\delta}{\sqrt{6}\sqrt{1+\varepsilon_1^2(B_z)}}\left(1+\varepsilon_1(B_z)\right),\\
\langle\beta_3|H_{Stark}|g_5\rangle &= -\delta,\\
\langle\beta_3|H_{Stark}|h_7\rangle &= \frac{\delta}{\sqrt{6}\sqrt{1+\varepsilon_2^2(B_z)}}\left(1+\varepsilon_2(B_z)\right),\\
\langle\beta_4|H_{Stark}|e_1\rangle &= \frac{\delta}{\sqrt{3}\sqrt{1+\omega^2(B_z)}}\left(\omega(B_z)-1\right),\\
\langle\beta_4|H_{Stark}|f_3\rangle &= \frac{\delta}{\sqrt{3}\sqrt{1+\omega^2(B_z)}}\left(\omega(B_z)+1\right),\\
\langle\beta_4|H_{Stark}|g_2\rangle &= \frac{\delta}{\sqrt{1+\omega^2(B_z)}\sqrt{1+\chi_1^2(B_z)}}\left(\frac{\omega(B_z)}{\sqrt{2}}+\sqrt{\frac{2}{3}}\chi_1(B_z)+\frac{\omega(B_z)\chi_1(B_z)}{\sqrt{6}}\right),\\
\langle\beta_4|H_{Stark}|g_4\rangle &= \frac{\delta}{\sqrt{1+\omega^2(B_z)}\sqrt{1+\kappa_1^2(B_z)}}\left(-\frac{\omega(B_z)}{\sqrt{2}}-\sqrt{\frac{2}{3}}\kappa_1(B_z)+\frac{\omega(B_z)\kappa_1(B_z)}{\sqrt{6}}\right),\\
\langle\beta_4|H_{Stark}|h_6\rangle &= \frac{\delta}{\sqrt{1+\omega^2(B_z)}\sqrt{1+\chi_2^2(B_z)}}\left(\frac{1}{\sqrt{2}}\omega(B_z)\chi_2(B_z)+\sqrt{\frac{2}{3}}+\frac{1}{\sqrt{6}}\omega(B_z)\right),\\
\langle\beta_4|H_{Stark}|h_8\rangle &= \frac{\delta}{\sqrt{1+\omega^2(B_z)}\sqrt{1+\kappa_2^2(B_z)}}\left(-\frac{1}{\sqrt{2}}\omega(B_z)\kappa_2(B_z)-\sqrt{\frac{2}{3}}+\frac{1}{\sqrt{6}}\omega(B_z)\right).
\end{aligned}
\tag{7.53}
$$

Similarly, the coupling constant for a static electric field in z-direction $\vec{E} = \varepsilon_z \hat{e}_z$

$$
\begin{aligned}
\langle \alpha_1 | H_{Stark} | e_1 \rangle &= -\frac{1}{\sqrt{3}} \delta_z, \\
\langle \alpha_1 | H_{Stark} | g_2 \rangle &= \frac{\delta_z}{\sqrt{1+\chi_1^2(B_z)}} \left(\frac{1}{\sqrt{2}} - \frac{1}{\sqrt{6}} \chi_1(B_z) \right), \\
\langle \alpha_1 | H_{Stark} | h_6 \rangle &= \frac{\delta_z}{\sqrt{1+\chi_2^2(B_z)}} \left(\frac{1}{\sqrt{2}} \chi_2(B_z) - \frac{1}{\sqrt{6}} \right), \\
\langle \alpha_2 | H_{Stark} | e_2 \rangle &= -\frac{\delta_z \left(x(B_z) + y(B_z) \right)}{\sqrt{3}\sqrt{1+x^2(B_z)}\sqrt{1+y^2(B_z)}}, \\
\langle \alpha_2 | H_{Stark} | f_4 \rangle &= -\frac{\delta_z \left(1 + x(B_z) z(B_z) \right)}{\sqrt{3}\sqrt{1+x^2(B_z)}\sqrt{1+z^2(B_z)}}, \\
\langle \alpha_2 | H_{Stark} | g_3 \rangle &= \sqrt{\frac{2}{3}} \frac{\delta_z \left(1 + x(B_z) \varepsilon_1(B_z) \right)}{\sqrt{1+x^2(B_z)}\sqrt{1+\varepsilon_1^2(B_z)}}, \\
\langle \alpha_2 | H_{Stark} | h_7 \rangle &= \sqrt{\frac{2}{3}} \frac{\delta_z \left(x(B_z) + \varepsilon_2(B_z) \right)}{\sqrt{1+x^2(B_z)}\sqrt{1+\varepsilon_2^2(B_z)}}, \\
\langle \beta_3 | H_{Strak} | f_3 \rangle &= \frac{1}{\sqrt{3}} \delta_z, \\
\langle \beta_3 | H_{Stark} | g_4 \rangle &= \frac{\delta_z}{\sqrt{1+\kappa_1^2(B_z)}} \left(\frac{1}{\sqrt{2}} + \frac{1}{\sqrt{6}} \kappa_1(B_z) \right), \\
\langle \beta_3 | H_{Stark} | h_8 \rangle &= \frac{\delta_z}{\sqrt{1+\kappa_2^2(B_z)}} \left(\frac{1}{\sqrt{2}} \kappa_2(B_z) + \frac{1}{\sqrt{6}} \right), \\
\langle \beta_4 | H_{Stark} | e_2 \rangle &= -\frac{\delta_z \left(1 + \omega(B_z) y(B_z) \right)}{\sqrt{3}\sqrt{1+\omega^2(B_z)}\sqrt{1+y^2(B_z)}}, \\
\langle \beta_4 | H_{Stark} | f_4 \rangle &= -\frac{\delta_z \left(\omega(B_z) + z(B_z) \right)}{\sqrt{3}\sqrt{1+\omega^2(B_z)}\sqrt{1+z^2(B_z)}}, \\
\langle \beta_4 | H_{Stark} | g_3 \rangle &= \sqrt{\frac{2}{3}} \frac{\delta_z \left(\omega(B_z) + \varepsilon_1(B_z) \right)}{\sqrt{1+\omega^2(B_z)}\sqrt{1+\varepsilon_1^2(B_z)}}, \\
\langle \beta_4 | H_{Stark} | h_7 \rangle &= \sqrt{\frac{2}{3}} \frac{\delta_z \left(1 + \omega(B_z) \varepsilon_2(B_z) \right)}{\sqrt{1+\omega^2(B_z)}\sqrt{1+\varepsilon_2^2(B_z)}},
\end{aligned}
\tag{7.54}
$$

are obtained. Subsequently, the coupling constants for the deuterium atom follow for a static electric field in x-direction $\vec{E} = \varepsilon_x \hat{e}_x$. The definitions are obtainable in Sec. 3.2.

$$
\begin{aligned}
\langle \alpha_1 | H_{Stark} | e_2 \rangle &= \frac{\delta}{3\sqrt{1+\tilde{\gamma}_1^2(B_z)}} \left(2\tilde{\gamma}_1(B_z) + \sqrt{2} \right), \\
\langle \alpha_1 | H_{Stark} | f_6 \rangle &= \frac{\delta}{3\sqrt{1+\tilde{\gamma}_2^2(B_z)}} \left(2 + \sqrt{2}\tilde{\gamma}_2(B_z) \right), \\
\langle \alpha_1 | H_{Stark} | g_1 \rangle &= \delta, \\
\langle \alpha_1 | H_{Stark} | g_3 \rangle &= \frac{\delta}{\sqrt{1+\alpha_1^2(B_z)+\beta_1^2(B_z)}} \left(-\frac{1}{\sqrt{10}} + \frac{2\sqrt{10}}{15}\alpha_1(B_z) - \frac{\sqrt{2}}{6}\beta_1(B_z) \right), \\
\langle \alpha_1 | H_{Stark} | h_8 \rangle &= \frac{\delta}{\sqrt{1+\alpha_3^2(B_z)+\beta_3^2(B_z)}} \left(-\frac{1}{\sqrt{10}}\alpha_3(B_z) + \frac{2\sqrt{10}}{15} - \frac{\sqrt{2}}{6}\beta_3(B_z) \right), \\
\langle \alpha_1 | H_{Stark} | k_{11} \rangle &= \frac{\delta}{\sqrt{1+\alpha_2^2(B_z)+\beta_2^2(B_z)}} \left(-\frac{1}{\sqrt{10}}\beta_2(B_z) + \frac{2\sqrt{10}}{15}\alpha_2(B_z) - \frac{\sqrt{2}}{6} \right), \\
\langle \alpha_2 | H_{Stark} | e_1 \rangle &= \frac{\delta}{3\sqrt{1+\gamma_1^2(B_z)}} \left(2\gamma_1(B_z) + \sqrt{2} \right), \\
\langle \alpha_2 | H_{Stark} | e_3 \rangle &= \frac{\delta}{3\sqrt{3}\sqrt{1+\gamma_1^2(B_z)}\sqrt{1+\tilde{\Gamma}_1^2(B_z)}} \Big(-\sqrt{2}\gamma_1(B_z)\tilde{\Gamma}_1(B_z) \\
&\quad -2\gamma_1(B_z) + 2\tilde{\Gamma}_1(B_z) + 2\sqrt{2} \Big), \\
\langle \alpha_2 | H_{Stark} | f_5 \rangle &= \frac{\delta}{3\sqrt{3}\sqrt{1+\gamma_1^2(B_z)}\sqrt{1+\tilde{\Gamma}_2^2(B_z)}} \Big(-\sqrt{2}\gamma_1(B_z) \\
&\quad -2\gamma_1(B_z)\tilde{\Gamma}_2(B_z) + 2 + 2\sqrt{2}\tilde{\Gamma}_2(B_z) \Big), \\
\langle \alpha_2 | H_{Stark} | g_2 \rangle &= \frac{\delta}{\sqrt{1+\gamma_1^2(B_z)}\sqrt{1+\theta_1^2(B_z)}} \left(-\frac{\sqrt{5}}{3}\gamma_1(B_z)\theta_1(B_z) + \frac{\sqrt{15}}{5} + \frac{2\sqrt{10}}{15}\theta_1(B_z) \right), \\
\langle \alpha_2 | H_{Stark} | g_4 \rangle &= \frac{\delta}{\sqrt{1+\gamma_1^2(B_z)}\sqrt{1+\tilde{\alpha}_1^2(B_z)+\tilde{\beta}_1^2(B_z)}} \Big(\frac{\sqrt{15}}{9}\gamma_1(B_z)\tilde{\alpha}_1(B_z) \\
&\quad -\frac{4\sqrt{3}}{9}\gamma_1(B_z)\tilde{\beta}_1(B_z) - \frac{\sqrt{30}}{10} + \frac{4\sqrt{30}}{45}\tilde{\alpha}_1(B_z) - \frac{\sqrt{6}}{18}\tilde{\beta}_1(B_z) \Big), \\
\langle \alpha_2 | H_{Stark} | h_7 \rangle &= \frac{\delta}{\sqrt{1+\gamma_1^2(B_z)}\sqrt{1+\theta_2^2(B_z)}} \left(-\frac{\sqrt{5}}{3}\gamma_1(B_z) + \frac{\sqrt{15}}{5}\theta_2(B_z) + \frac{2\sqrt{10}}{15} \right), \\
\langle \alpha_2 | H_{Stark} | h_9 \rangle &= \frac{\delta}{\sqrt{1+\gamma_1^2(B_z)}\sqrt{1+\tilde{\alpha}_3^2(B_z)+\tilde{\beta}_3^2(B_z)}} \Big(\frac{\sqrt{15}}{9}\gamma_1(B_z) \\
&\quad -\frac{4\sqrt{3}}{9}\gamma_1(B_z)\tilde{\beta}_3(B_z) - \frac{\sqrt{30}}{10}\tilde{\alpha}_3(B_z) + \frac{4\sqrt{30}}{45} - \frac{\sqrt{6}}{18}\tilde{\beta}_3(B_z) \Big), \\
\langle \alpha_2 | H_{Stark} | k_{12} \rangle &= \frac{\delta}{\sqrt{1+\gamma_1^2(B_z)}\sqrt{1+\tilde{\alpha}_2^2(B_z)+\tilde{\beta}_2^2(B_z)}} \Big(\frac{\sqrt{15}}{9}\gamma_1(B_z)\tilde{\alpha}_2(B_z) \\
&\quad -\frac{4\sqrt{3}}{9}\gamma_1(B_z) - \frac{\sqrt{30}}{10}\tilde{\beta}_2(B_z) + \frac{4\sqrt{30}}{45}\tilde{\alpha}_2(B_z) - \frac{\sqrt{6}}{18} \Big), \\
\langle \alpha_3 | H_{Stark} | e_2 \rangle &= \frac{\delta}{3\sqrt{3}\sqrt{1+\Gamma_1^2(B_z)}\sqrt{1+\tilde{\gamma}_1^2(B_z)}} \Big(-\sqrt{2}\Gamma_1(B_z)\tilde{\gamma}_1(B_z) \\
&\quad +2\Gamma_1(B_z) - 2\tilde{\gamma}_1 + 2\sqrt{2} \Big),
\end{aligned}
\tag{7.55}
$$

$$\langle\alpha_3|H_{Stark}|f_4\rangle = \frac{\delta}{3\sqrt{1+\Gamma_1^2(B_z)}}\left(-2\Gamma_1(B_z)+\sqrt{2}\right),$$

$$\langle\alpha_3|H_{Stark}|f_6\rangle = \frac{\delta}{3\sqrt{3}\sqrt{1+\Gamma_1^2(B_z)}\sqrt{1+\tilde{\gamma}_2^2(B_z)}}\Big(-\sqrt{2}\Gamma_1(B_z) +2\Gamma_1(B_z)\tilde{\gamma}_2(B_z)-2+2\sqrt{2}\tilde{\gamma}_2(B_z)\Big),$$

$$\langle\alpha_3|H_{Stark}|g_3\rangle = \frac{\delta}{\sqrt{1+\Gamma_1^2(B_z)}\sqrt{1+\alpha_1^2(B_z)+\beta_1^2(B_z)}}\left(-\frac{\sqrt{15}}{9}\Gamma_1(B_z)\alpha_1(B_z) -\frac{4\sqrt{3}}{9}\Gamma_1(B_z)\beta_1(B_z)+\frac{\sqrt{30}}{10}+\frac{4\sqrt{30}}{45}\alpha_1(B_z)+\frac{\sqrt{6}}{18}\beta_1(B_z)\right),$$

$$\langle\alpha_3|H_{Stark}|g_5\rangle = \frac{\delta}{\sqrt{1+\Gamma_1^2(B_z)}\sqrt{1+\phi_1^2(B_z)}}\left(\frac{\sqrt{5}}{3}\Gamma_1(B_z)\phi_1(B_z)-\frac{\sqrt{15}}{5}+\frac{2\sqrt{10}}{15}\phi_1(B_z)\right),$$

$$\langle\alpha_3|H_{Stark}|h_8\rangle = \frac{\delta}{\sqrt{1+\Gamma_1^2(B_z)}\sqrt{1+\alpha_3^2(B_z)+\beta_3^2(B_z)}}\left(-\frac{\sqrt{15}}{9}\Gamma_1(B_z) -\frac{4\sqrt{3}}{9}\Gamma_1(B_z)\beta_3(B_z)+\frac{\sqrt{30}}{10}\alpha_3(B_z)+\frac{4\sqrt{30}}{45}+\frac{\sqrt{6}}{18}\beta_3(B_z)\right),$$

$$\langle\alpha_3|H_{Stark}|h_{10}\rangle = \frac{\delta}{\sqrt{1+\Gamma_1^2(B_z)}\sqrt{1+\phi_2^2(B_z)}}\left(\frac{\sqrt{5}}{3}\Gamma_1(B_z)-\frac{\sqrt{15}}{5}\phi_2(B_z)+\frac{2\sqrt{10}}{15}\right),$$

$$\langle\alpha_3|H_{Stark}|k_{11}\rangle = \frac{\delta}{\sqrt{1+\Gamma_1^2(B_z)}\sqrt{1+\alpha_2^2(B_z)+\beta_2^2(B_z)}}\left(-\frac{\sqrt{15}}{9}\Gamma_1(B_z)\alpha_2(B_z) -\frac{4\sqrt{3}}{9}\Gamma_1(B_z)+\frac{\sqrt{30}}{10}\beta_2(B_z)+\frac{4\sqrt{30}}{45}\alpha_2(B_z)+\frac{\sqrt{6}}{18}\right),$$

$$\langle\beta_4|H_{Stark}|e_3\rangle = \frac{\delta}{3\sqrt{1+\tilde{\Gamma}_1^2(B_z)}}\left(-2\tilde{\Gamma}_1(B_z)+\sqrt{2}\right),$$

$$\langle\beta_4|H_{Stark}|f_5\rangle = \frac{\delta}{3\sqrt{1+\tilde{\Gamma}_2^2(B_z)}}\left(-2+\sqrt{2}\tilde{\Gamma}_2(B_z)\right),$$

$$\langle\beta_4|H_{Stark}|g_4\rangle = \frac{\delta}{\sqrt{1+\tilde{\alpha}_1^2(B_z)+\tilde{\beta}_1^2(B_z)}}\left(\frac{1}{\sqrt{10}}+\frac{2\sqrt{10}}{15}\tilde{\alpha}_1(B_z)+\frac{\sqrt{2}}{6}\tilde{\beta}_1(B_z)\right),$$

$$\langle\beta_4|H_{Stark}|g_6\rangle = -\delta,$$

$$\langle\beta_4|H_{Stark}|h_9\rangle = \frac{\delta}{\sqrt{1+\tilde{\alpha}_3^2(B_z)+\tilde{\beta}_3^2(B_z)}}\left(\frac{1}{\sqrt{10}}\tilde{\alpha}_3(B_z)+\frac{2\sqrt{10}}{15}+\frac{\sqrt{2}}{6}\tilde{\beta}_3(B_z)\right),$$

$$\langle\beta_4|H_{Stark}|k_{12}\rangle = \frac{\delta}{\sqrt{1+\tilde{\alpha}_2^2(B_z)+\tilde{\beta}_2^2(B_z)}}\left(\frac{1}{\sqrt{10}}\tilde{\beta}_2(B_z)+\frac{2\sqrt{10}}{15}\tilde{\alpha}_2(B_z)+\frac{\sqrt{2}}{6}\right),$$

$$\langle\beta_5|H_{Stark}|e_2\rangle = \frac{\delta}{3\sqrt{3}\sqrt{1+\Gamma_2^2(B_z)}\sqrt{1+\tilde{\gamma}_1^2(B_z)}}\Big(-\sqrt{2}\tilde{\gamma}_1(B_z) -2\tilde{\gamma}_1(B_z)\Gamma_2(B_z)+2+2\sqrt{2}\Gamma_2(B_z)\Big),$$

$$\langle\beta_5|H_{Stark}|f_4\rangle = \frac{\delta}{3\sqrt{1+\Gamma_2^2(B_z)}}\left(-2+\sqrt{2}\Gamma_2(B_z)\right),$$

$$\langle\beta_5|H_{Stark}|f_6\rangle = \frac{\delta}{3\sqrt{3}\sqrt{1+\Gamma_2^2(B_z)}\sqrt{1+\tilde{\gamma}_2^2(B_z)}}\Big(-\sqrt{2} -2\Gamma_2(B_z)+2\tilde{\gamma}_2(B_z)+2\sqrt{2}\tilde{\gamma}_2(B_z)\Gamma_2(B_z)\Big),$$

$$\langle\beta_5|H_{Stark}|g_3\rangle = \frac{\delta}{\sqrt{1+\Gamma_2^2(B_z)}\sqrt{1+\alpha_1^2(B_z)+\beta_1^2(B_z)}}\Bigg(-\frac{\sqrt{15}}{9}\alpha_1(B_z) -\frac{4\sqrt{3}}{9}\beta_1(B_z)+\frac{\sqrt{30}}{10}\Gamma_2(B_z)+\frac{4\sqrt{30}}{45}\alpha_1(B_z)\Gamma_2(B_z)+\frac{\sqrt{6}}{18}\beta_1(B_z)\Gamma_2(B_z)\Bigg),$$

$$\langle\beta_5|H_{Stark}|g_5\rangle = \frac{\delta}{\sqrt{1+\Gamma_2^2(B_z)}\sqrt{1+\phi_1^2(B_z)}}\left(\frac{\sqrt{5}}{3}\phi_1(B_z)-\frac{\sqrt{15}}{5}\Gamma_2(B_z)+\frac{2\sqrt{10}}{15}\Gamma_2(B_z)\phi_1(B_z)\right),$$

$$\langle\beta_5|H_{Stark}|h_8\rangle = \frac{\delta}{\sqrt{1+\Gamma_2^2(B_z)}\sqrt{1+\alpha_3^2(B_z)+\beta_3^2(B_z)}}\Bigg(-\frac{\sqrt{15}}{9}-\frac{4\sqrt{3}}{9}\beta_3(B_z) +\frac{\sqrt{30}}{10}\alpha_3(B_z)\Gamma_2(B_z)+\frac{4\sqrt{30}}{45}\Gamma_2(B_z)+\frac{\sqrt{6}}{18}\beta_3(B_z)\Gamma_2(B_z)\Bigg),$$

$$\langle\beta_5|H_{Stark}|h_{10}\rangle = \frac{\delta}{\sqrt{1+\Gamma_2^2(B_z)}\sqrt{1+\phi_2^2(B_z)}}\left(\frac{\sqrt{5}}{3}-\frac{\sqrt{15}}{5}\Gamma_2(B_z)\phi_2(B_z)+\frac{2\sqrt{10}}{15}\Gamma_2(B_z)\right),$$

$$\langle\beta_5|H_{Stark}|k_{11}\rangle = \frac{\delta}{\sqrt{1+\Gamma_2^2(B_z)}\sqrt{1+\alpha_2^2(B_z)+\beta_2^2(B_z)}}\Bigg(-\frac{\sqrt{15}}{9}\alpha_2(B_z) -\frac{4\sqrt{3}}{9}+\frac{\sqrt{30}}{10}\beta_2(B_z)\Gamma_2(B_z)+\frac{4\sqrt{30}}{45}\alpha_2(B_z)\Gamma_2(B_z)+\frac{\sqrt{6}}{18}\Gamma_2(B_z)\Bigg),$$

$$\langle\beta_6|H_{Stark}|e_1\rangle = \frac{\delta}{3\sqrt{1+\gamma_2^2(B_z)}}\Big(2+\sqrt{2}\gamma_2(B_z)\Big),$$

$$\langle\beta_6|H_{Stark}|e_3\rangle = \frac{\delta}{3\sqrt{3}\sqrt{1+\gamma_2^2(B_z)}\sqrt{1+\tilde{\Gamma}_1^2(B_z)}}\Big(-\sqrt{2}\tilde{\Gamma}_1(B_z) -2+2\tilde{\Gamma}_1(B_z)\gamma_2(B_z)+2\sqrt{2}\gamma_2(B_z)\Big),$$

$$\langle\beta_6|H_{Stark}|f_5\rangle = \frac{\delta}{3\sqrt{3}\sqrt{1+\gamma_2^2(B_z)}\sqrt{1+\tilde{\Gamma}_2^2(B_z)}}\Big(-\sqrt{2} -2\tilde{\Gamma}_2(B_z)+2\gamma_2(B_z)+2\sqrt{2}\gamma_2(B_z)\tilde{\Gamma}_2(B_z)\Big),$$

$$\langle\beta_6|H_{Stark}|g_2\rangle = \frac{\delta}{\sqrt{1+\gamma_2^2(B_z)}\sqrt{1+\theta_1^2(B_z)}}\left(-\frac{\sqrt{5}}{3}\theta_1(B_z)+\frac{\sqrt{15}}{5}\gamma_2(B_z)+\frac{2\sqrt{10}}{15}\gamma_2(B_z)\theta_1(B_z)\right),$$

$$\langle\beta_6|H_{Stark}|g_4\rangle = \frac{\delta}{\sqrt{1+\gamma_2^2(B_z)}\sqrt{1+\tilde{\alpha}_1^2(B_z)+\tilde{\beta}_1^2(B_z)}}\Bigg(\frac{\sqrt{15}}{9}\tilde{\alpha}_1(B_z) -\frac{4\sqrt{3}}{9}\tilde{\beta}_1(B_z)-\frac{\sqrt{30}}{10}\gamma_2(B_z)+\frac{4\sqrt{30}}{45}\tilde{\alpha}_1(B_z)\gamma_2(B_z)-\frac{\sqrt{6}}{18}\tilde{\beta}_1(B_z)\gamma_2(B_z)\Bigg),$$

$$\langle\beta_6|H_{Stark}|h_7\rangle = \frac{\delta}{\sqrt{1+\gamma_2^2(B_z)}\sqrt{1+\theta_2^2(B_z)}}\left(-\frac{\sqrt{5}}{3}+\frac{\sqrt{15}}{5}\gamma_2(B_z)\theta_2(B_z)+\frac{2\sqrt{10}}{15}\gamma_2(B_z)\right),$$

$$\langle\beta_6|H_{Stark}|h_9\rangle = \frac{\delta}{\sqrt{1+\gamma_2^2(B_z)}\sqrt{1+\tilde{\alpha}_3^2(B_z)+\tilde{\beta}_3^2(B_z)}}\Bigg(\frac{\sqrt{15}}{9}-\frac{4\sqrt{3}}{9}\tilde{\beta}_3(B_z) -\frac{\sqrt{30}}{10}\tilde{\alpha}_3(B_z)\gamma_2(B_z)+\frac{4\sqrt{30}}{45}\gamma_2(B_z)-\frac{\sqrt{6}}{18}\tilde{\beta}_3(B_z)\gamma_2(B_z)\Bigg),$$

$$\langle\beta_6|H_{Stark}|k_{12}\rangle = \frac{\delta}{\sqrt{1+\gamma_2^2(B_z)}\sqrt{1+\tilde{\alpha}_2^2(B_z)+\tilde{\beta}_2^2(B_z)}}\Bigg(\frac{\sqrt{15}}{9}\tilde{\alpha}_2(B_z) -\frac{4\sqrt{3}}{9}-\frac{\sqrt{30}}{10}\tilde{\beta}_2(B_z)\gamma_2(B_z)+\frac{4\sqrt{30}}{45}\tilde{\alpha}_2(B_z)\gamma_2(B_z)-\frac{\sqrt{6}}{18}\gamma_2(B_z)\Bigg).$$

Similarly for the z-direction, $\vec{E} = E_z\hat{e}_z$ the coupling constants are

$$
\begin{aligned}
\langle\alpha_1|H_{Stark}|e_1\rangle &= -\frac{\delta_z}{\sqrt{3}},\\
\langle\alpha_1|H_{Stark}|g_2\rangle &= \frac{\delta_z}{\sqrt{1+\theta_1^2(B_z)}}\left(\sqrt{\frac{2}{5}} - \frac{2}{\sqrt{15}}\theta_1(B_z)\right),\\
\langle\alpha_1|H_{Stark}|h_7\rangle &= \frac{\delta_z}{\sqrt{1+\theta_2^2(B_z)}}\left(\sqrt{\frac{2}{5}}\theta_2(B_z) - \frac{2}{\sqrt{15}}\right),\\
\langle\alpha_2|H_{Stark}|e_2\rangle &= \frac{\delta_z}{9\sqrt{1+\gamma_1^2(B_z)}\sqrt{1+\tilde{\gamma}_1^2(B_z)}}\Big(\sqrt{3}\gamma_1(B_z)\tilde{\gamma}_1(B_z)\\
&\quad +2\sqrt{6}\gamma_1(B_z) + 2\sqrt{6}\tilde{\gamma}_1(B_z) - \sqrt{3}\Big),\\
\langle\alpha_2|H_{Stark}|f_6\rangle &= \frac{\delta_z}{9\sqrt{1+\gamma_1^2(B_z)}\sqrt{1+\tilde{\gamma}_2^2(B_z)}}\Big(\sqrt{3}\gamma_1(B_z)\\
&\quad +2\sqrt{6}\gamma_1(B_z)\tilde{\gamma}_2(B_z) + 2\sqrt{6} - \sqrt{3}\tilde{\gamma}_2(B_z)\Big),\\
\langle\alpha_2|H_{Stark}|g_3\rangle &= \frac{\delta_z}{\sqrt{1+\gamma_1^2(B_z)}\sqrt{1+\alpha_1^2(B_z)+\beta_1^2(B_z)}}\left(-\frac{\sqrt{30}}{9}\gamma_1(B_z)\alpha_1(B_z)\right.\\
&\quad \left.+\frac{2\sqrt{6}}{9}\gamma_1(B_z)\beta_1(B_z) + \frac{\sqrt{15}}{5} - \frac{2\sqrt{15}}{45}\alpha_1(B_z) - \frac{\sqrt{3}}{9}\beta_1(B_z)\right),\\
\langle\alpha_2|H_{Stark}|h_8\rangle &= \frac{\delta_z}{\sqrt{1+\gamma_1^2(B_z)}\sqrt{1+\alpha_3^2(B_z)+\beta_3^2(B_z)}}\left(-\frac{\sqrt{30}}{9}\gamma_1(B_z)\right.\\
&\quad \left.+\frac{2\sqrt{6}}{9}\gamma_1(B_z)\beta_3(B_z) + \frac{\sqrt{15}}{5}\alpha_3(B_z) - \frac{2\sqrt{15}}{45} - \frac{\sqrt{3}}{9}\beta_3(B_z)\right),\\
\langle\alpha_2|H_{Stark}|k_{11}\rangle &= \frac{\delta_z}{\sqrt{1+\gamma_1^2(B_z)}\sqrt{1+\alpha_2^2(B_z)+\beta_2^2(B_z)}}\left(-\frac{\sqrt{30}}{9}\gamma_1(B_z)\alpha_2(B_z)\right.\\
&\quad \left.+\frac{2\sqrt{6}}{9}\gamma_1(B_z) + \frac{\sqrt{15}}{5}\beta_2(B_z) - \frac{2\sqrt{15}}{45}\alpha_2(B_z) - \frac{\sqrt{3}}{9}\right),\\
\langle\alpha_3|H_{Stark}|e_3\rangle &= \frac{\delta_z}{9\sqrt{1+\Gamma_1^2(B_z)}\sqrt{1+\tilde{\Gamma}_1^2(B_z)}}\Big(-\sqrt{3}\Gamma_1(B_z)\tilde{\Gamma}_1(B_z)\\
&\quad +2\sqrt{6}\Gamma_1(B_z) + 2\sqrt{6}\tilde{\Gamma}_1(B_z) + \sqrt{3}\Big),\\
\langle\alpha_3|H_{Stark}|f_5\rangle &= \frac{\delta_z}{9\sqrt{1+\Gamma_1^2(B_z)}\sqrt{1+\tilde{\Gamma}_2^2(B_z)}}\Big(-\sqrt{3}\Gamma_1(B_z)\\
&\quad +2\sqrt{6}\Gamma_1(B_z)\tilde{\Gamma}_2(B_z) + 2\sqrt{6} + \sqrt{3}\tilde{\Gamma}_2(B_z)\Big),\\
\langle\alpha_3|H_{Stark}|g_4\rangle &= \frac{\delta_z}{\sqrt{1+\Gamma_1^2(B_z)}\sqrt{1+\tilde{\alpha}_1^2(B_z)+\tilde{\beta}_1^2(B_z)}}\left(-\frac{\sqrt{30}}{9}\Gamma_1(B_z)\tilde{\alpha}_1(B_z)\right.\\
&\quad \left.-\frac{2\sqrt{6}}{9}\Gamma_1(B_z)\tilde{\beta}_1(B_z) + \frac{\sqrt{15}}{5} + \frac{2\sqrt{15}}{45}\tilde{\alpha}_1(B_z) - \frac{\sqrt{3}}{9}\tilde{\beta}_1(B_z)\right),\\
\langle\alpha_3|H_{Stark}|h_9\rangle &= \frac{\delta_z}{\sqrt{1+\Gamma_1^2(B_z)}\sqrt{1+\tilde{\alpha}_3^2(B_z)+\tilde{\beta}_3^2(B_z)}}\left(-\frac{\sqrt{30}}{9}\Gamma_1(B_z)\right.\\
&\quad \left.-\frac{2\sqrt{6}}{9}\Gamma_1(B_z)\tilde{\beta}_3(B_z) + \frac{\sqrt{15}}{5}\tilde{\alpha}_3(B_z) + \frac{2\sqrt{15}}{45} - \frac{\sqrt{3}}{9}\tilde{\beta}_3(B_z)\right),
\end{aligned}
\tag{7.56}
$$

$$\langle \alpha_3|H_{Stark}|k_{12}\rangle = \frac{\delta_z}{\sqrt{1+\Gamma_1^2(B_z)}\sqrt{1+\tilde{\alpha}_2^2(B_z)+\tilde{\beta}_2^2(B_z)}}\left(-\frac{\sqrt{30}}{9}\Gamma_1(B_z)\tilde{\alpha}_2(B_z)\right.$$
$$\left.-\frac{2\sqrt{6}}{9}\Gamma_1(B_z)+\frac{\sqrt{15}}{5}\tilde{\beta}_2(B_z)+\frac{2\sqrt{15}}{45}\tilde{\alpha}_2(B_z)-\frac{\sqrt{3}}{9}\right),$$

$$\langle \beta_4|H_{Stark}|f_4\rangle = \frac{\delta_z}{\sqrt{3}},$$

$$\langle \beta_4|H_{Stark}|g_5\rangle = \frac{\delta_z}{\sqrt{1+\phi_1^2(B_z)}}\left(\sqrt{\frac{2}{5}}+\frac{2}{\sqrt{15}}\phi_1(B_z)\right),$$

$$\langle \beta_4|H_{Stark}|h_{10}\rangle = \frac{\delta_z}{\sqrt{1+\phi_2^2(B_z)}}\left(\sqrt{\frac{2}{5}}\phi_2(B_z)+\frac{2}{\sqrt{15}}\right),$$

$$\langle \beta_5|H_{Stark}|e_3\rangle = \frac{\delta_z}{9\sqrt{1+\Gamma_2^2(B_z)}\sqrt{1+\tilde{\Gamma}_1^2(B_z)}}\left(-\sqrt{3}\tilde{\Gamma}_1(B_z)\right.$$
$$\left.+2\sqrt{6}+2\sqrt{6}\Gamma_2(B_z)\tilde{\Gamma}_1(B_z)+\sqrt{3}\Gamma_2(B_z)\right),$$

$$\langle \beta_5|H_{Stark}|f_5\rangle = \frac{\delta_z}{9\sqrt{1+\Gamma_2^2(B_z)}\sqrt{1+\tilde{\Gamma}_2^2(B_z)}}\left(-\sqrt{3}\right.$$
$$\left.+2\sqrt{6}\tilde{\Gamma}_2(B_z)+2\sqrt{6}\Gamma_2(B_z)+\sqrt{3}\Gamma_2(B_z)\tilde{\Gamma}_2(B_z)\right),$$

$$\langle \beta_5|H_{Stark}|g_4\rangle = \frac{\delta_z}{\sqrt{1+\Gamma_2^2(B_z)}\sqrt{1+\tilde{\alpha}_1^2(B_z)+\tilde{\beta}_1^2(B_z)}}\left(-\frac{\sqrt{30}}{9}\tilde{\alpha}_1(B_z)\right.$$
$$\left.-\frac{2\sqrt{6}}{9}\tilde{\beta}_1(B_z)+\frac{\sqrt{15}}{5}\Gamma_2(B_z)+\frac{2\sqrt{15}}{45}\Gamma_2(B_z)\tilde{\alpha}_1(B_z)-\frac{\sqrt{3}}{9}\Gamma_2(B_z)\tilde{\beta}_1(B_z)\right),$$

$$\langle \beta_5|H_{Stark}|h_9\rangle = \frac{\delta_z}{\sqrt{1+\Gamma_2^2(B_z)}\sqrt{1+\tilde{\alpha}_3^2(B_z)+\tilde{\beta}_3^2(B_z)}}\left(-\frac{\sqrt{30}}{9}\right.$$
$$\left.-\frac{2\sqrt{6}}{9}\tilde{\beta}_3(B_z)+\frac{\sqrt{15}}{5}\Gamma_2(B_z)\tilde{\alpha}_3(B_z)+\frac{2\sqrt{15}}{45}\Gamma_2(B_z)-\frac{\sqrt{3}}{9}\Gamma_2(B_z)\tilde{\beta}_3(B_z)\right),$$

$$\langle \beta_5|H_{Stark}|k_{12}\rangle = \frac{\delta_z}{\sqrt{1+\Gamma_2^2(B_z)}\sqrt{1+\tilde{\alpha}_2^2(B_z)+\tilde{\beta}_2^2(B_z)}}\left(-\frac{\sqrt{30}}{9}\tilde{\alpha}_2(B_z)\right.$$
$$\left.-\frac{2\sqrt{6}}{9}+\frac{\sqrt{15}}{5}\Gamma_2(B_z)\tilde{\beta}_2(B_z)+\frac{2\sqrt{15}}{45}\Gamma_2(B_z)\tilde{\alpha}_2(B_z)-\frac{\sqrt{3}}{9}\Gamma_2(B_z)\right),$$

$$\langle \beta_6|H_{Stark}|e_2\rangle = \frac{\delta_z}{9\sqrt{1+\gamma_2^2(B_z)}\sqrt{1+\tilde{\gamma}_1^2(B_z)}}\left(\sqrt{3}\tilde{\gamma}_1(B_z)\right.$$
$$\left.+2\sqrt{6}+2\sqrt{6}\gamma_2(B_z)\tilde{\gamma}_1(B_z)-\sqrt{3}\gamma_2(B_z)\right),$$

$$\langle \beta_6|H_{Stark}|f_6\rangle = \frac{\delta_z}{9\sqrt{1+\gamma_2^2(B_z)}\sqrt{1+\tilde{\gamma}_2^2(B_z)}}\left(\sqrt{3}\right.$$
$$\left.+2\sqrt{6}\tilde{\gamma}_2(B_z)+2\sqrt{6}\gamma_2(B_z)-\sqrt{3}\gamma_2(B_z)\tilde{\gamma}_2(B_z)\right),$$

$$\langle \beta_6|H_{Stark}|g_3\rangle = \frac{\delta_z}{\sqrt{1+\gamma_2^2(B_z)}\sqrt{1+\alpha_1^2(B_z)+\beta_1^2(B_z)}}\left(-\frac{\sqrt{30}}{9}\alpha_1(B_z)\right.$$
$$\left.+\frac{2\sqrt{6}}{9}\beta_1(B_z)+\frac{\sqrt{15}}{5}\gamma_2(B_z)-\frac{2\sqrt{15}}{45}\gamma_2(B_z)\alpha_1(B_z)-\frac{\sqrt{3}}{9}\gamma_2(B_z)\beta_1(B_z)\right),$$

$$\langle\beta_6|H_{Stark}|h_8\rangle = \frac{\delta_z}{\sqrt{1+\gamma_2^2(B_z)}\sqrt{1+\alpha_3^2(B_z)+\beta_3^2(B_z)}}\left(-\frac{\sqrt{30}}{9}\right.$$
$$\left.+\frac{2\sqrt{6}}{9}\beta_3(B_z)+\frac{\sqrt{15}}{5}\gamma_2(B_z)\alpha_3(B_z)-\frac{2\sqrt{15}}{45}\gamma_2(B_z)-\frac{\sqrt{3}}{9}\gamma_2(B_z)\beta_3(B_z)\right),$$
$$\langle\beta_6|H_{Stark}|k_{11}\rangle = \frac{\delta_z}{\sqrt{1+\gamma_2^2(B_z)}\sqrt{1+\alpha_2^2(B_z)+\beta_2^2(B_z)}}\left(-\frac{\sqrt{30}}{9}\alpha_2(B_z)\right.$$
$$\left.+\frac{2\sqrt{6}}{9}+\frac{\sqrt{15}}{5}\gamma_2(B_z)\beta_2(B_z)-\frac{2\sqrt{15}}{45}\gamma_2(B_z)\alpha_2(B_z)-\frac{\sqrt{3}}{9}\gamma_2(B_z)\right).$$

E Derivation of the differential equation for the Lorentz force

In this section the derivation for the differential equation in Sec. 4.3.1 is introduced. Assuming constant homogenous fields expressed as $\vec{E} = E_x\hat{e}_x$ and $\vec{B} = B_z\hat{e}_z$ then this turns the Newtonian equation Eq. (4.33) into two coupled and one decoupled differential equations

$$\begin{aligned}\ddot{x} - \frac{q}{m}\left(E_x + \dot{y}B_z\right) &= 0,\\ \ddot{y} + \frac{q}{m}\dot{x}B_z &= 0,\\ \ddot{z} &= 0.\end{aligned} \tag{7.57}$$

The result for the z-component is directly stated as

$$\begin{aligned}\dot{z} &= v_{0,z},\\ z(t) &= v_{0,z}t + z_0,\end{aligned} \tag{7.58}$$

with two constants $v_{0,z}$ for the velocity and z_0 for the position, which are fixed by the initial conditions. To decouple the remaining two differential equations for x and y it is useful to express them in a linear equation

$$\underbrace{\begin{pmatrix}\ddot{x}\\ \ddot{y}\end{pmatrix}}_{=\ddot{\vec{x}}} = \underbrace{\begin{pmatrix}0 & \frac{qB_z}{m}\\ -\frac{qB_z}{m} & 0\end{pmatrix}}_{=A}\underbrace{\begin{pmatrix}\dot{x}\\ \dot{y}\end{pmatrix}}_{=\dot{\vec{x}}} + \underbrace{\begin{pmatrix}\frac{qE_x}{m}\\ 0\end{pmatrix}}_{=\vec{b}(t)}. \tag{7.59}$$

In the first step the homogenous solution is obtained before searching for the particular one. Therefore, the eigensystem of the matrix A is obtained to decouple the equations. Consequently, the eigenvalues are calculated

$$\begin{aligned}&\det\left(A - \lambda\mathbb{1}\right) = 0,\\ \Rightarrow\quad &\lambda_{1,2} = \pm i\frac{qB_z}{m}.\end{aligned} \tag{7.60}$$

The corresponding eigenvectors are given by

$$\vec{v}_{1,2} = \begin{pmatrix}1\\ \pm i\end{pmatrix}. \tag{7.61}$$

Subsequently, the diagonalized equations are stated as

$$\begin{pmatrix}\ddot{\tilde{x}}\\ \ddot{\tilde{y}}\end{pmatrix} = \begin{pmatrix}i\frac{qB_z}{m} & 0\\ 0 & -i\frac{qB_z}{m}\end{pmatrix}\begin{pmatrix}\dot{\tilde{x}}\\ \dot{\tilde{y}}\end{pmatrix}. \tag{7.62}$$

Consequently, the results for the velocities in the diagonalized vector space are

$$\begin{aligned}\dot{\tilde{x}} &= c_1(t)e^{iqB_zt/m},\\ \dot{\tilde{y}} &= c_2(t)e^{-iqB_zt/m}.\end{aligned} \tag{7.63}$$

Transforming back into the original system results in the velocities for the homogenous solution

$$\begin{aligned} \begin{pmatrix} \dot{x} \\ \dot{y} \end{pmatrix} &= \begin{pmatrix} 1 & 1 \\ i & -i \end{pmatrix} \begin{pmatrix} \dot{\tilde{x}} \\ \dot{\tilde{y}} \end{pmatrix}, \\ \Rightarrow \quad \dot{x} &= c_1(t) e^{iqB_z t/m} + c_2(t) e^{-iqB_z t/m}, \\ \dot{y} &= i c_1(t) e^{iqB_z t/m} - i c_2(t) e^{-iqB_z t/m}. \end{aligned} \tag{7.64}$$

In the next step the inhomogeneous solution is addressed. Theorem 9.6.1 from [184] is thereby used to obtain the corresponding particular solution. The theorem exploits the method of varying parameters. If a set of n homogenous solutions $\dot{\vec{x}}_n(t)$ to the differential equation $\ddot{\vec{x}} = A\dot{\vec{x}}$ exist then the particular solution can be expressed as

$$\dot{\vec{x}}_{\text{par.}} = X(t) \int X^{-1}(t) \vec{b}(t) dt, \tag{7.65}$$

with

$$X(t) = \left(\dot{\vec{x}}_1(t), ..., \dot{\vec{x}}_n(t) \right), \tag{7.66}$$

and $\vec{b}(t)$ the inhomogeneous part of Eq. (7.59). The proof of the theorem based on [184] is given in the App. F. In this case the homogenous solutions are

$$\dot{\vec{x}}_1(t) = e^{iqB_z t/m} \begin{pmatrix} 1 \\ i \end{pmatrix}, \quad \dot{\vec{x}}_2(t) = e^{-iqB_z t/m} \begin{pmatrix} 1 \\ -i \end{pmatrix}. \tag{7.67}$$

Subsequently, $X(t)$ can be written as

$$X(t) = \begin{pmatrix} e^{iqB_z t/m} & e^{-iqB_z t/m} \\ i e^{iqB_z t/m} & -i e^{-iqB_z t/m} \end{pmatrix}. \tag{7.68}$$

Utilizing the Gauss-Jordan algorithm the inverse matrix of $X(t)$ is calculated to

$$X^{-1}(t) = \frac{1}{2} \begin{pmatrix} e^{-iqB_z t/m} & -i e^{-iqB_z t/m} \\ e^{iqB_z t/m} & i e^{iqB_z t/m} \end{pmatrix}. \tag{7.69}$$

Moreover, by calculating Eq. (7.65) the particular solution results in

$$\dot{\vec{x}}_{\text{par.}} = \begin{pmatrix} 0 \\ -\frac{E_x}{B_z} \end{pmatrix}. \tag{7.70}$$

Finally, the general solution to Eq. (4.33) is stated as

$$\begin{aligned} \dot{x}(t) &= c_1 e^{iqB_z t/m} + c_2 e^{-iqB_z t/m} \\ \dot{y}(t) &= i c_1 e^{iqB_z t/m} - i c_2 e^{-iqB_z t/m} - \frac{E_x}{B_z}. \end{aligned} \tag{7.71}$$

F Proof of the variation method theorem

The proof shown here in this section follows the steps introduced in [184]. The inhomogeneous differential equation of interest has a form of

$$\dot{\vec{x}}(t) = A\vec{x}(t) + \vec{b}\,(t)\,. \tag{7.72}$$

Subsequently, suppose there exist n linear independent solutions $\vec{x}(t)_n$ to the homogenous first order linear differential equation

$$\dot{\vec{x}}(t) = A\vec{x}(t), \tag{7.73}$$

Table 7.1: Some roots $x_{m,n}$ of the Bessel function of the first kind $J_m(x)$ are summarized.

n	$x_{0,n}$	$x_{1,n}$	$x_{2,n}$	$x_{3,n}$	$x_{4,n}$	$x_{5,n}$
1	2.4048	3.8317	5.1356	6.3802	7.5883	8.7715
2	5.5201	7.0156	8.4172	9.7610	11.0647	12.3386
3	8.6537	10.1735	11.6198	13.0152	14.3725	15.7002
4	11.7915	13.3237	14.7960	16.2235	17.6160	18.9801
5	14.9309	16.4706	17.9598	19.4094	20.8269	22.2178
6	18.0711	19.6159	21.1170	22.5827	24.0190	25.4303

and an invertible matrix with the form $X(t) = (\vec{x}_1(t), ..., \vec{x}_n(t))$ then it is possible to express the particular solution by

$$\vec{x}_{\text{part.}}(t) = X(t)\vec{u}(t). \tag{7.74}$$

Inserting Eq. (7.74) of the particular solution back into the original differential equation Eq. (7.72) results in

$$\frac{d}{dt}\left(X(t)\vec{u}(t)\right) = \dot{X}(t)\vec{u}(t) + X(t)\dot{\vec{u}}(t) = AX(t)\vec{u}(t) + \vec{b}(t). \tag{7.75}$$

Next, $\dot{X}(t)$ is addressed

$$\dot{X}(t) = \frac{d}{dt}\left(\vec{x}_1(t), ..., \vec{x}_n(t)\right) = \left(\dot{\vec{x}}_1(t), ..., \dot{\vec{x}}_n(t)\right). \tag{7.76}$$

Since each $\vec{x}_m(t)$ is a solution to Eq. (7.73) each derivative satisfies

$$\dot{\vec{x}}_m(t) = A\vec{x}_m(t) \tag{7.77}$$

Consequently, $\dot{X}(t)$ follows the following relation

$$\dot{X}(t) = AX(t). \tag{7.78}$$

Consequently, Eq. (7.75) reduces to

$$X(t)\dot{\vec{u}}(t) = \vec{b}(t). \tag{7.79}$$

Due to the assumption that $X(t)$ is invertible Eq. (7.79) can be transformed to

$$\dot{\vec{u}}(t) = X^{-1}(t)\vec{b}(t). \tag{7.80}$$

Finally, by integrating over time $\vec{u}(t)$ is recovered

$$\vec{u}(t) = \int X^{-1}(t)\vec{b}(t)dt. \tag{7.81}$$

Inserting this result in Eq. (7.74) leaves us with the result, which needed to be proven

$$\vec{x}_{\text{part.}}(t) = X(t)\int X^{-1}(t)\vec{b}(t)dt. \tag{7.82}$$

G Complementary material on the Bessel function of the first kind

The Bessel function of first kind $J_m(x)$ is part of the solutions for the Maxwell equations for cylindrical cavities introduced in Eq. (2.170). Its roots play a major part in identifying the resonance frequencies of the TM and TE modes. These are calculated numerically due to the complexity of the Bessel function. Subsequently, some roots $x_{m,n}$ of $J_m(x)$ are stated in Tab. 7.1. Similar to this, roots $\tilde{x}_{m,n}$ of the derivative $\partial J_m(x)/\partial x$ are combined in Tab. 7.2. Moreover, the

Table 7.2: Some roots $\tilde{x}_{m,n}$ of the derivative of the Bessel function of the first kind $\partial J_m(x)/\partial x$ are introduced.

n	$\tilde{x}_{0,n}$	$\tilde{x}_{1,n}$	$\tilde{x}_{2,n}$	$\tilde{x}_{3,n}$	$\tilde{x}_{4,n}$	$\tilde{x}_{5,n}$
1	3.8317	1.8412	3.0542	4.2012	5.3176	6.4156
2	7.0156	5.3314	6.7061	8.0152	9.2824	10.5199
3	10.1735	8.5363	9.9695	11.3459	12.6819	13.9872
4	13.3237	11.7060	13.1704	14.5858	15.9641	17.3128
5	16.4706	14.8636	16.3475	17.7887	19.1960	20.5755
6	19.6159	18.0156	19.5129	20.9725	22.4010	23.8036

calculation of the derivative of the Bessel function is given by

$$\begin{aligned}
\frac{\partial}{\partial x} J_m(x) &= \frac{1}{2}\sum_{l=0}^{\infty} \frac{(-1)^l (2l+m)}{l!\Gamma(l+m+1)} \left(\frac{x}{2}\right)^{2l+m-1} \\
&= \frac{m}{2m!}\left(\frac{x}{2}\right)^{m-1} + \frac{1}{2}\sum_{l=1}^{\infty} \frac{(-1)^l (2l+m)}{l!\Gamma(l+m+1)} \left(\frac{x}{2}\right)^{2l+m-1} \\
&= \frac{m}{2m!}\left(\frac{x}{2}\right)^{m-1} + \frac{1}{2}\sum_{l=1}^{\infty} (-1)^l \left(\frac{l+m}{l!(l+m)!} + \frac{l}{l!(l+m)!}\right)\left(\frac{x}{2}\right)^{2l+m-1} \\
&= \frac{m}{2m!}\left(\frac{x}{2}\right)^{m-1} + \frac{1}{2}\sum_{l=1}^{\infty} (-1)^l \left(\frac{1}{l!(l+m-1)!} + \frac{1}{(l-1)!(l+m)!}\right)\left(\frac{x}{2}\right)^{2l+m-1} \\
&= \frac{m}{2m!}\left(\frac{x}{2}\right)^{m-1} + \frac{1}{2}\sum_{l=1}^{\infty} \left(\frac{(-1)^l}{l!\Gamma(l+m)} - \frac{(-1)^{l-1}}{(l-1)!\Gamma(l+m+1)}\right)\left(\frac{x}{2}\right)^{2l+m-1} \\
&= \frac{1}{2}\left[\sum_{l=0}^{\infty} \frac{(-1)^l}{l!\Gamma(l+m)} \left(\frac{x}{2}\right)^{2l+m-1} - \sum_{l=0}^{\infty} \frac{(-1)^l}{l!\Gamma(l+m+2)} \left(\frac{x}{2}\right)^{2l+m+1}\right] \\
&= \frac{1}{2}\left(J_{m-1}(x) - J_{m+1}(x)\right).
\end{aligned} \tag{7.83}$$

H Drawings and additional simulations

This section provides some more simulations as well as design sketches for the realization of the upgraded nuclear spin filter.

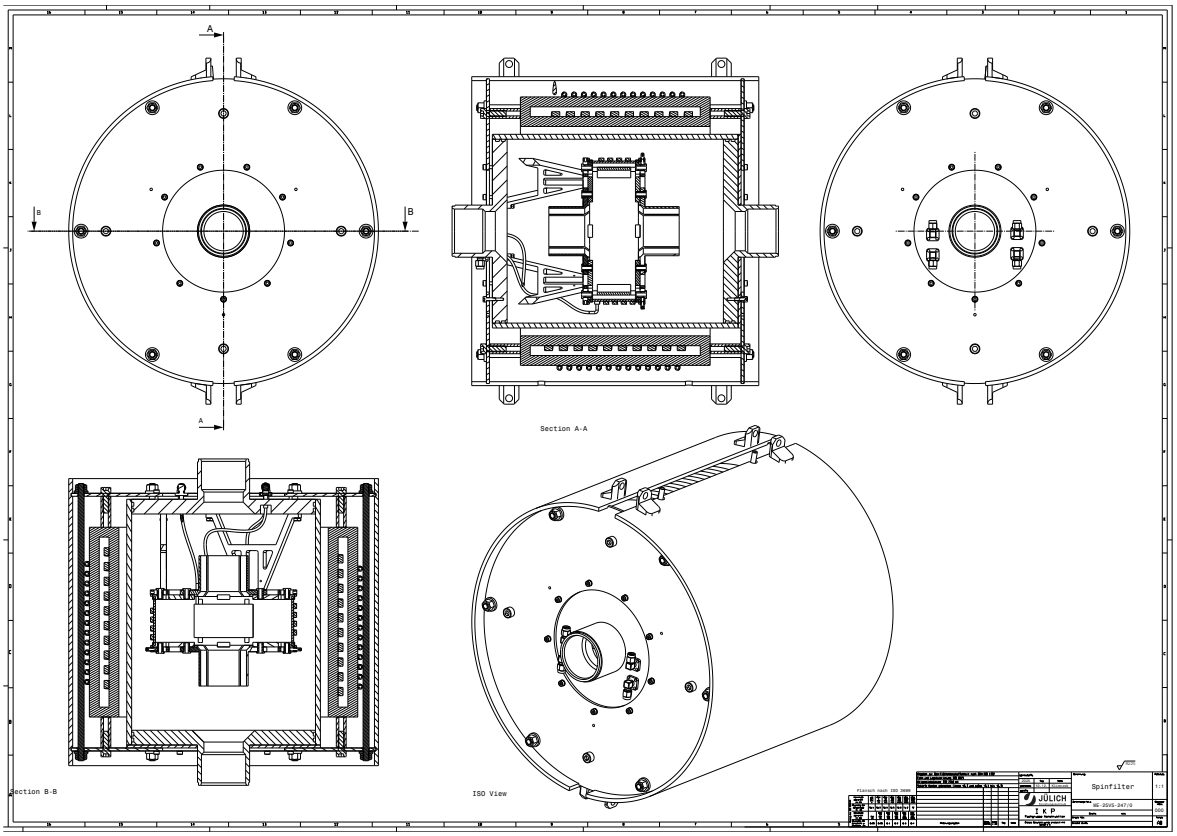

Figure 7.1: The figure, fabricated by the design department of the nuclear institute at FZJ (designer: Berthold Klimczok), shows more technial drawings for a possible realization of an upgraded nuclear spin filter.

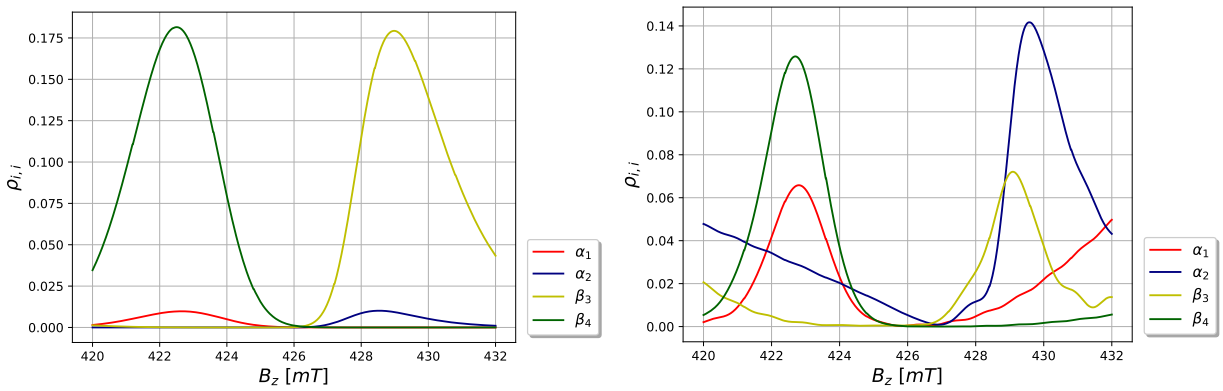

(a) (b)

Figure 7.2: The occupation numbers of the single Breit-Rabi states as function of the external magnetic field when leaving the cavity of the nuclear spin filter are displayed. For reproducibility the parameters are given in Tab. 7.3.

I Relativistic Simulations

In this section the proper relativistic treatment for the numerical spin dynamical simulation in the rest frame of the atom or ion is motivated. In case of an atom, which is at constant velocity v_z, the electromagnetic field tensor in the laboratory frame $F^{\mu\nu}$ can be transformed into the rest

Table 7.3: The parameters for the simulations introduced in this Sec. H are summarized.

Figure	$E_x\left[\frac{\mathrm{kV}}{\mathrm{m}}\right]$	$E_0\left[\frac{\mathrm{kV}}{\mathrm{m}}\right]$	$v\left[\frac{\mathrm{m}}{\mathrm{s}}\right]$	B_z [mT]	r [m]	$\mathrm{TM}_{m,n,p}$	Q
7.2a	6	2	309500	420 – 432	0	$0,1,4$	16000
7.2b	3.5	2.5	309500	420 – 432	0	$0,1,1$	∞

frame by a global transformation

$$\begin{aligned}\tilde{F}^{\mu\nu} &= \begin{pmatrix} \gamma & 0 & 0 & -\gamma\beta \\ 0 & 1 & 0 & 0 \\ 0 & 0 & 1 & 0 \\ -\gamma\beta & 0 & 0 & \gamma \end{pmatrix} \begin{pmatrix} 0 & {}^{E_x}\!/_c & {}^{E_y}\!/_c & {}^{E_z}\!/_c \\ -{}^{E_x}\!/_c & 0 & B_z & -B_y \\ -{}^{E_y}\!/_c & -B_z & 0 & B_x \\ -{}^{E_z}\!/_c & B_y & -B_x & 0 \end{pmatrix} \begin{pmatrix} \gamma & 0 & 0 & -\gamma\beta \\ 0 & 1 & 0 & 0 \\ 0 & 0 & 1 & 0 \\ -\gamma\beta & 0 & 0 & \gamma \end{pmatrix} \\ &= \begin{pmatrix} 0 & \gamma{}^{E_x}\!/_c - \gamma\beta B_y & \gamma{}^{E_y}\!/_c + \gamma\beta B_x & {}^{E_z}\!/_c \\ -\gamma{}^{E_x}\!/_c + \gamma\beta B_y & 0 & B_z & \gamma\beta{}^{E_x}\!/_c - \gamma B_y \\ -\gamma{}^{E_y}\!/_c - \gamma\beta B_x & -B_z & 0 & \gamma\beta{}^{E_y}\!/_c + \gamma B_x \\ -{}^{E_z}\!/_c & -\gamma\beta{}^{E_x}\!/_c + \gamma B_y & -\gamma\beta{}^{E_y}\!/_c - \gamma B_x & 0 \end{pmatrix}.\end{aligned} \tag{7.84}$$

Consequently, the electromagnetic components in the rest frame, denoted with a prime, can be expressed by the laboratory components as

$$\begin{aligned} \frac{E'_x}{c} &= \frac{\gamma E_x}{c} - \gamma\beta B_y \qquad & B'_x &= \frac{\gamma\beta E_y}{c} + \gamma B_x, \\ \frac{E'_y}{c} &= \frac{\gamma E_y}{c} + \gamma\beta B_x \qquad & B'_y &= -\frac{\gamma\beta E_x}{c} + \gamma B_y, \\ E'_z &= E_z & B'_z &= B_z. \end{aligned} \tag{7.85}$$

In case of the TM modes and the constant static fields, introduced in the thesis, the relevant laboratory electromagnetic components can be summarized by

$$\begin{aligned} &\vec{E}_x = E_x \hat{e}_x, \\ &\vec{E}_r\left(r,z,t\right) = E_r(r,z,t)\cos\left(\varphi\right)\hat{e}_x + E_r\left(r,z,t\right)\sin\left(\varphi\right)\hat{e}_y, \\ &\vec{E}_z\left(r,z,t\right) = E_z\left(r,z,t\right)\hat{e}_z, \\ &\vec{B}_\varphi\left(r,z,t\right) = -B_\varphi\left(r,z,t\right)\sin\left(\varphi\right)\hat{e}_x + B_\varphi\left(r,z,t\right)\cos\left(\varphi\right)\hat{e}_y, \\ &\vec{B}_z = B_z\hat{e}_z. \end{aligned} \tag{7.86}$$

Therefore, the corresponding fields in the rest frame are given as

$$\begin{aligned} & E'_x = \gamma E_x + \gamma E_r\cos\left(\varphi\right) - \gamma\beta c B_\varphi\cos\left(\varphi\right), \\ & E'_y = \gamma E_r\sin\left(\varphi\right) - \gamma\beta c B_\varphi\sin\left(\varphi\right), \\ \Rightarrow\quad & \vec{E}'_r = \left(\gamma E_r - \gamma\beta c B_\varphi\right)\hat{e}_r \quad \text{and} \quad \vec{E}'_x = \gamma E_x\hat{e}_x, \\ & B'_x = \frac{\gamma\beta E_r}{c}\sin\left(\varphi\right) - \gamma B_\varphi\sin\left(\varphi\right), \\ & B'_y = -\frac{\gamma\beta E_r}{c}\cos\left(\varphi\right) + \gamma B_\varphi\cos\left(\varphi\right), \\ \Rightarrow\quad & \vec{B}'_\varphi = \left(-\frac{\gamma\beta E_r}{c} + \gamma B_\varphi\right)\hat{e}_\varphi \quad \text{and} \quad \vec{B}'_z = B_z\hat{e}_z. \end{aligned} \tag{7.87}$$

In addition, the spatial and time coordinates need to be transformed into the rest frame, which results in

$$t' = \gamma t - \frac{\gamma\beta}{c}z \qquad z' = -\gamma\beta c t + \gamma z, \tag{7.88}$$

for a constant beam velocity v_z in z-direction. In the rest frame the particle is at a constant position for any time, which can be chosen to be $z' = 0$ without loss of generality. Consequently, the adjustment for the time is

$$t' = \gamma t - \gamma\beta^2 t = \frac{t}{\gamma}. \tag{7.89}$$

So far we treated the beam as if the electromagnetic fields do not change its constant velocity and have no effect on its trajectory whatsoever. In first order this is true for an atom but not for an ion. As the Lorentz force accelerates the ion the velocity and thereby the Lorentz factor is time-dependent. Therefore, it is not possible to perform a constant and global Lorentz transformation. The rest frame is now replaced by a co-moving inertial system and the proper time τ is connected to the laboratory time via

$$dt = \gamma d\tau. \tag{7.90}$$

To be able to determine the electromagnetic fields and their positional and time arguments it is necessary to solve the coupled differential equations from Eq. 4.45 at every point in time. Once the Lorentz factor $\gamma(t)$ is known the proper time τ can be evaluated via

$$\tau(t) = \int_0^t \frac{dt'}{\gamma(t')}. \tag{7.91}$$

Next, at every point in time a local Lorentz transformation as function of the proper time $\Lambda(\tau)$ can be performed. This changes the electromagnetic tensor such that the electromagnetic fields with the corresponding coordinates and times in the co-moving rest frame are obtained.

Bibliography

[1] W. Gerlach and O. Stern, "Der experimentelle Nachweis der Richtungsquantelung im Magnetfeld," *Z. Phys.*, vol. 9, pp. 349–352, Dec. 1922. [Online]. Available: https://doi.org/10.1007/BF01326983

[2] G. Clausnitzer, R. Fleischmann, and H. Schopper, "Erzeugung eines Wasserstoffatomstrahles mit gleichgerichteten Kernspins," *Z. Phys.*, vol. 144, no. 4, pp. 336–342, Aug. 1956. [Online]. Available: https://doi.org/10.1007/BF01340806

[3] M. Mikirtychyants, R. Engels, K. Grigoryev, H. Kleines, P. Kravtsov *et al.*, "The polarized H and D atomic beam source for ANKE at COSY-Jülich," *NIM-A*, vol. 721, pp. 83–98, Sep. 2013. [Online]. Available: https://www.sciencedirect.com/science/article/pii/S0168900213003483

[4] R. Engels, R. Emmerich, J. Ley, G. Tenckhoff, H. Paetz gen. Schieck *et al.*, "Precision Lamb-shift polarimeter for polarized atomic and ion beams," *Rev. Sci. Instrum.*, vol. 74, no. 11, pp. 4607–4615, Oct. 2003. [Online]. Available: https://doi.org/10.1063/1.1619550

[5] R. Engels, "Entwicklung eines universellen Lambshift-Polarimeters für polarisierte Atomstrahl-Targets wie an ANKE/COSY," Ph.D. dissertation, Universität zu Köln, Feb. 2002.

[6] J. L. McKibben, G. P. Lawrence, and G. G. Ohlsen, "Nuclear Spin Filter," *Phys. Rev. Lett.*, vol. 20, pp. 1180–1182, May 1968. [Online]. Available: https://link.aps.org/doi/10.1103/PhysRevLett.20.1180

[7] A. S. Belov, S. K. Esin, S. A. Kubalov, V. E. Kuzik, A. A. Stepanov *et al.*, "Pulsed high-intensity source of polarized protons," *NIM-A*, vol. 255, no. 3, pp. 442–459, Apr. 1987. [Online]. Available: https://www.sciencedirect.com/science/article/pii/0168900287912113

[8] S. K. Lemieux, T. B. Clegg, H. J. Karwowski, W. J. Thompson, and E. R. Crosson, "A spin-filter polarimeter for low energy hydrogen and deuterium ion beams," *NIM-A*, vol. 333, no. 2, pp. 434–442, Sep. 1993. [Online]. Available: https://www.sciencedirect.com/science/article/pii/016890029391188S

[9] H. R. Kremers, J. P. M. Beijers, N. Kalantar-Nayestanaki, and T. B. Clegg, "The KVI Lamb-shift polarimeter," *NIM-A*, vol. 516, no. 1, pp. 209–211, 2004. [Online]. Available: https://www.sciencedirect.com/science/article/pii/S016890020302299X

[10] A. Zelenski, "Polarimetry at RHIC: RHIC polarized beam in Run 2011," *BNL tech report*, Oct. 2013. [Online]. Available: https://technotes.bnl.gov/PDF?publicationId=34312

[11] C. Wilkin, "The legacy of the experimental hadron physics programme at COSY," *Eur. Phys. J. A*, vol. 53, no. 114, Jun. 2017. [Online]. Available: https://doi.org/10.1140/epja/i2017-12295-4

[12] A. Solovev, A. Andreyanov, L. Barion, G. Ciullo, R. Engels *et al.*, "Optimization and first tests of the experimental setup to investigate the double-polarized DD-fusion reactions," *J. Instrum.*, vol. 15, no. 08, p. C08003, Aug. 2020. [Online]. Available: https://doi.org/10.1088/1748-0221/15/08/C08003

[13] R. Engels, R. Gorski, K. Grigoryev, M. Mikirtychyants, F. Rathmann *et al.*, "Measurement of the nuclear polarization of hydrogen and deuterium molecules using a Lamb-shift polarimeter," *Rev. Sci. Instrum.*, Oct. 2014. [Online]. Available: https://pubmed.ncbi.nlm.nih.gov/25362391/

[14] R. Engels, K. Grigoryev, C. S. Kannis, Y. Michael, H. Ströher *et al.*, "Production of HD Molecules in Definite Hyperfine Substates," *Phys. Rev. Lett.*, vol. 124, p. 113003, Mar. 2020. [Online]. Available: https://link.aps.org/doi/10.1103/PhysRevLett.124.113003

[15] T. El-Kordy, R. Engels, N. Faatz, P. Costa Pinto, P. Di Nezza *et al.*, "Tests of amorphous carbon-coated storage cells for a polarized gas target at LHCb and further results*," *Chin. Phys. C*, vol. 49, no. 8, p. 084002, Aug. 2025. [Online]. Available: https://doi.org/10.1088/1674-1137/add70e

[16] H. Kleines, J. Sarkadi, K. Zwoll, R. Engels, K. Grigoryev *et al.*, "The control system of the polarized internal target of ANKE at COSY," *Nucl. Instrum. Methods Phys. Res. Section A: Accelerators, Spectrometers, Detectors and Associated Equipment*, vol. 560, no. 2, pp. 503–516, May 2006. [Online]. Available: https://www.sciencedirect.com/science/article/pii/S016890020502629X

[17] N. Faatz, B. Breitkreutz, R. W. Engels, R. Gebel, K. Grigoryev *et al.*, "Further development of a Lamb-shift polarimeter," *PoS*, vol. PSTP2024, p. 011, Jun. 2025. [Online]. Available: https://doi.org/10.22323/1.472.0011

[18] R. Weidmann, A. Glombik, H. Meyer, W. Kretschmer, M. Altmeier *et al.*, "The polarized ion source for COSY," *Rev. Sci. Instrum.*, vol. 67, no. 3, pp. 1357–1358, Mar. 1996. [Online]. Available: https://doi.org/10.1063/1.1146665

[19] E. Tiesinga, P. J. Mohr, D. B. Newell, and B. N. Taylor, "The 2022 CODATA Recommended Values of the Fundamental Physical Constants," *NIST*, 2025. [Online]. Available: https://physics.nist.gov/cgi-bin/cuu/Value?mnsmp

[20] A. N. Ivanov, R. Höllwieser, N. I. Troitskaya, M. Wellenzohn, and Y. A. Berdnikov, "Precision theoretical analysis of neutron radiative beta decay to order $O(\alpha^2/\pi^2)$," *Phys. Rev. D*, vol. 95, p. 113006, Jun. 2017. [Online]. Available: https://link.aps.org/doi/10.1103/PhysRevD.95.113006

[21] M. J. Bales, R. Alarcon, C. D. Bass, E. J. Beise, H. Breuer *et al.*, "Precision Measurement of the Radiative β Decay of the Free Neutron," *Phys. Rev. Lett.*, vol. 116, p. 242501, Jun. 2016. [Online]. Available: https://link.aps.org/doi/10.1103/PhysRevLett.116.242501

[22] R. Daudel, M. Jean, and M. Lecoin, "Sur la possibilité d'existence d'un type particulier de radioactivité phénomène de création e," *J. Phys. Radium*, vol. 8, pp. 238–243, Aug. 1947. [Online]. Available: https://doi.org/10.1051/jphysrad:0194700808023800

[23] M. Jung, F. Bosch, K. Beckert, H. Eickhoff, H. Folger *et al.*, "First observation of bound-state β^- decay," *Phys. Rev. Lett.*, vol. 69, pp. 2164–2167, Oct. 1992. [Online]. Available: https://link.aps.org/doi/10.1103/PhysRevLett.69.2164

[24] L. L. Nemenov and A. A. Ovchinnikova, "Effects of scalar and tensor interactions on the atomic decay of the neutron. $n \to H + \bar{\nu}_e$," *Sov. J. Nucl. Phys. (Engl. Transl.); (United States)*, vol. 31:5, May 1980. [Online]. Available: https://www.osti.gov/biblio/6491563

[25] J. Byrne, "Two-body decay of the neutron: A possible test for the existence of right-handed weak currents," *Europhys. Lett.*, vol. 56, no. 5, p. 633, Dec. 2001. [Online]. Available: https://dx.doi.org/10.1209/epl/i2001-00567-2

[26] W. Schott, T. Faestermann, P. Fierlinger, F. J. Hartmann, R. Hertenberger *et al.*, "An experiment to measure the bound-β-decay of the free neutron," *Hyperfine Interact.*, pp. 269–274, Sep. 2006. [Online]. Available: https://doi.org/10.1007/s10751-009-0011-z

[27] W. Schott, S. Paul, M. Berger, R. Emmerich, R. Engels *et al.*, "Neutron Bound β-Decay-BOB," *Phys. Procedia*, vol. 17, pp. 191–198, Aug. 2011, 2nd International Workshop on the Physics of fundamental Symmetries and Interactions - PSI2010. [Online]. Available: https://www.sciencedirect.com/science/article/pii/S1875389211003671

[28] J. McAndrew, S. Paul, J. Emmerich, P. Fierlinger, M. Gabriel *et al.*, "Neutron bound beta-decay: BOB," *Hyperfine Interact.*, vol. 210, no. 1-3, pp. 13–17, Apr. 2012. [Online]. Available: https://juser.fz-juelich.de/record/127474

[29] L. Nemenov, "Decay of the neutron into a hydrogen atom and an antineutrino," *Sov. J. Nucl. Phys. (Engl. Transl.)*, vol. 31, no. 1, p. 115–119, Jan. 1980. [Online]. Available: https://inis.iaea.org/records/9jqmy-30m47

[30] M. Faber, A. N. Ivanov, V. A. Ivanova, J. Marton, M. Pitschmann *et al.*, "Continuum-state and bound-state β^--decay rates of the neutron," *Phys. Rev. C*, vol. 80, p. 035503, Sep. 2009. [Online]. Available: https://link.aps.org/doi/10.1103/PhysRevC.80.035503

[31] F. M. Gonzalez, E. M. Fries, C. Cude-Woods, T. Bailey, M. Blatnik *et al.*, "Improved Neutron Lifetime Measurement with UCNτ," *Phys. Rev. Lett.*, vol. 127, p. 162501, Oct. 2021. [Online]. Available: https://link.aps.org/doi/10.1103/PhysRevLett.127.162501

[32] G. Ohlsen and J. McKibben, "Theory of a Radio-Frequency "Spin Filter" for a Metastable Hydrogen, Deuterium, or Tritium Atomic Beam," Los Alamos Scientific Laboratory of the University of California, Tech. Rep., Jan. 1967. [Online]. Available: https://doi.org/10.2172/4517131

[33] F. Roussel, P. Pradel, and G. Spiess, "Electron capture, electron loss, and deexcitation of fast H(2^2S) and H(1^2S) atoms in collisions with molecular hydrogen and inert gases," *Phys. Rev. A*, vol. 16, pp. 1854–1866, Nov. 1977. [Online]. Available: https://link.aps.org/doi/10.1103/PhysRevA.16.1854

[34] A. V. Phelps, "Collisions of H^+, H_2^+, H_3^+, ArH^+, H^-, H, and H_2 with Ar and of Ar^+ and ArH^+ with H_2 for Energies from 0.1 ev to 10 keV," *J. Phys. Chem. Ref. Data*, vol. 21, no. 4, pp. 883–897, Jul. 1992. [Online]. Available: https://doi.org/10.1063/1.555917

[35] A. Picard, H. Backe, H. Barth, J. Bonn, B. Degen *et al.*, "A solenoid retarding spectrometer with high resolution and transmission for keV electrons," *NIM-B*, vol. 63, no. 3, pp. 345–358, Feb. 1992. [Online]. Available: https://www.sciencedirect.com/science/article/pii/0168583X9295119C

[36] C. Cohen-Tannoudji, B. Diu, and F. Laloë, *Quantum mechanics volume 1*, 2nd ed. Wiley, 1977.

[37] R. H. Dalitz, "Decay of τ Mesons of Known Charge," *Phys. Rev.*, vol. 94, pp. 1046–1051, May 1954. [Online]. Available: https://link.aps.org/doi/10.1103/PhysRev.94.1046

[38] K. S. Krane, *Introductory nuclear physics*, 3rd ed. John Wiley & Sons, 1987.

[39] T. D. Lee and C. N. Yang, "Question of Parity Conservation in Weak Interactions," *Phys. Rev.*, vol. 104, pp. 254–258, Oct. 1956. [Online]. Available: https://link.aps.org/doi/10.1103/PhysRev.104.254

[40] C. S. Wu, E. Ambler, R. W. Hayward, D. D. Hoppes, and R. P. Hudson, "Experimental Test of Parity Conservation in Beta Decay," *Phys. Rev.*, vol. 105, pp. 1413–1415, Feb. 1957. [Online]. Available: https://link.aps.org/doi/10.1103/PhysRev.105.1413

[41] E. Ambler, M. A. Grace, H. Halban, N. Kurti, H. Durand *et al.*, "Nuclear polarization of cobalt 60," *Lond. Edinb. Dubl. Phil. Mag.*, vol. 44, no. 349, pp. 216–218, Jul. 1953. [Online]. Available: https://doi.org/10.1080/14786440208520296

[42] G. P. Zeller, K. S. McFarland, T. Adams, A. Alton, S. Avvakumov *et al.*, "Precise Determination of Electroweak Parameters in Neutrino-Nucleon Scattering," *Phys. Rev. Lett.*, vol. 88, p. 091802, Feb. 2002. [Online]. Available: https://link.aps.org/doi/10.1103/PhysRevLett.88.091802

[43] P. L. Anthony, R. G. Arnold, C. Arroyo, K. Baird, K. Bega *et al.*, "Observation of Parity Nonconservation in Møller Scattering," *Phys. Rev. Lett.*, vol. 92, p. 181602, May 2004. [Online]. Available: https://link.aps.org/doi/10.1103/PhysRevLett.92.181602

[44] R. W. Dunford and R. J. Holt, "Parity violation in hydrogen revisited," *J. Phys. G*, vol. 34, no. 10, pp. 2099–2118, Sep. 2007. [Online]. Available: https://doi.org/10.1088%2F0954-3899%2F34%2F10%2F001

[45] L. D. Landau and E. M. Lifschiz, *Band 3 Quantenmechanik*. Berlin, Boston: De Gruyter, 1988. [Online]. Available: https://doi.org/10.1515/9783112473603

[46] H. A. Bethe and E. E. Salpeter, *Quantum Mechanics of One- and Two-Electron Atoms*. Springer Berlin, Heidelberg, 1957. [Online]. Available: https://doi.org/10.1007/978-3-662-12869-5

[47] U. Le Verrier, "Recherches sur les mouvements d'Uranus," *C. r. hebd. séances Acad. sci.*, vol. 23, pp. 907–918, Jan. 1846. [Online]. Available: https://gallica.bnf.fr/ark:/12148/bpt6k29798/f911.item

[48] J. G. Galle, "Beobachtungen des Le Verrier'schen Planeten zu Berlin," *Astron. Nachr.*, vol. 25, no. 11, pp. 161–164, Jan. 1847. [Online]. Available: https://onlinelibrary.wiley.com/doi/abs/10.1002/asna.18470251103

[49] F. Zwicky, "Die Rotverschiebung extragalaktischer Nebeln," *Helv. Phys. acta*, vol. 6, pp. 110–127, Nov. 1933. [Online]. Available: https://www.e-periodica.ch/digbib/view?pid=hpa-001:1933:6#112

[50] V. C. Rubin and W. K. Ford, "Rotation of the Andromeda Nebula from a Spectroscopic Survey of Emission Regions," *ApJ.*, vol. 159, pp. 379–403, Feb. 1970. [Online]. Available: https://adsabs.harvard.edu/full/1970ApJ...159..379R?utm_source=chatgpt.com

[51] D. Clowe, M. Bradač, A. H. Gonzalez, M. Markevitch, S. W. Randall *et al.*, "A Direct Empirical Proof of the Existence of Dark Matter*," *ApJ.*, vol. 648, no. 2, p. L109, Aug. 2006. [Online]. Available: https://dx.doi.org/10.1086/508162

[52] S. Weinberg, "A New Light Boson?" *Phys. Rev. Lett.*, vol. 40, pp. 223–226, Jan. 1978. [Online]. Available: https://link.aps.org/doi/10.1103/PhysRevLett.40.223

[53] Q. Yang and S. Dong, "Probing dark matter axions using the hyperfine structure splitting of hydrogen atoms," *Phys. Lett. B*, vol. 843, p. 138004, Aug. 2023. [Online]. Available: https://www.sciencedirect.com/science/article/pii/S0370269323003386

[54] I. Alekseev, C. Allgower, M. Bai, Y. Batygin, L. Bozano *et al.*, "Polarized proton collider at RHIC," *NIM-A*, vol. 499, no. 2, pp. 392–414, Mar. 2003, the Relativistic Heavy Ion Collider Project: RHIC and its Detectors. [Online]. Available: https://www.sciencedirect.com/science/article/pii/S0168900202019460

[55] A. Cho, "Department of Energy picks New York over Virginia for site of new particle collider," *Science*, Jan. 2020. [Online]. Available: https://www.science.org/content/article/department-energy-picks-new-york-over-virginia-site-new-particle-collider

[56] J. Maxwell, C. Epstein, R. Milner, J. Alessi, E. Beebe *et al.*, "Development of a Polarized Helium-3 Source for RHIC and eRHIC," *Int. J. Mod. Phys. Conf. Ser.*, vol. 40, p. 1660102, Jan. 2016. [Online]. Available: https://doi.org/10.1142/S2010194516601022

[57] M. Ebert, T. Grossmann, W. Heil, W. E. Otten, R. Surkau *et al.*, "Nuclear magnetic resonance imaging with hyperpolarised helium-3," *Lancet*, vol. 347, pp. 1297–1299, May 1996. [Online]. Available: https://www.sciencedirect.com/science/article/pii/S014067369690940X

[58] M. Batz, S. Baeßler, W. Heil, E. W. Otten, D. Rudersdorf *et al.*, "^{3}He Spin Filter for Neutrons," *J. Res. Natl. Inst. Stand. Technol.*, vol. 110, pp. 293–298, Jun. 2005. [Online]. Available: https://pmc.ncbi.nlm.nih.gov/articles/PMC4849585/

[59] I. Engin, Z. M. Chitgar, O. Deppert, L. D. Lucchio, R. Engels *et al.*, "Laser-induced acceleration of Helium ions from unpolarized gas jets," *Plasma Phys. Control. Fusion*, vol. 61, no. 11, p. 115012, Oct. 2019. [Online]. Available: https://dx.doi.org/10.1088/1361-6587/ab4613

[60] M. Büscher, A. Hützen, L. Ji, and A. Lehrach, "Generation of polarized particle beams at relativistic laser intensities," *High Power Laser Sci. Eng.*, vol. 8, p. e36, Oct. 2020. [Online]. Available: https://www.cambridge.org/core/journals/high-power-laser-science-and-engineering/article/generation-of-polarized-particle-beams-at-relativistic-laser-intensities/073B4D5F1DBC59C5F761FBB73058BBEC

[61] P. Fedorets, C. Zheng, R. Engels, I. Engin, H. Feilbach *et al.*, "A High-Density Polarized ^{3}He Gas–Jet Target for Laser–Plasma Applications," *Instruments*, vol. 6, no. 2, Apr. 2022. [Online]. Available: https://www.mdpi.com/2410-390X/6/2/18

[62] Y. Avishai and M. Ripelle, "Electric Dipole Moment of ^{3}He," *Phys. Rev. Lett.*, vol. 56, pp. 2121–2123, Jun. 1986. [Online]. Available: https://www.sciencedirect.com/science/article/pii/0375947487901837

[63] R. Golub and S. K. Lamoreaux, "Neutron electric-dipole moment, ultracold neutrons and polarized ^{3}He," *Phys. Rep.*, vol. 237, no. 1, pp. 1–62, Feb. 1994. [Online]. Available: https://www.sciencedirect.com/science/article/pii/0370157394900841

[64] J. Krimmer, M. Distler, W. Heil, S. Karpuk, D. Kiselev *et al.*, "A highly polarized ^{3}He target for the electron beam at MAMI," *NIM-A*, vol. 611, no. 1, pp. 18–24, Nov. 2009. [Online]. Available: https://www.sciencedirect.com/science/article/pii/S0168900209018063

[65] J. L. Friar, B. F. Gibson, G. L. Payne, A. M. Bernstein, and T. E. Chupp, "Neutron polarization in polarized ^{3}He targets," *Phys. Rev. C*, vol. 42, pp. 2310–2314, Dec. 1990. [Online]. Available: https://link.aps.org/doi/10.1103/PhysRevC.42.2310

[66] M. T. Alley and L. D. Knutson, "Spin correlation measurements for p–^{3}He elastic scattering between 4.0 and 10.0 MeV," *Phys. Rev. C*, vol. 48, pp. 1890–1900, Oct. 1993. [Online]. Available: https://link.aps.org/doi/10.1103/PhysRevC.48.1890

[67] P. Grabmayr, "The structure of ^{3}He and the neutron electric form factor from polarization observables," *Prog. Part. Nucl. Phys.*, vol. 61, no. 1, pp. 113–119, Jul. 2008, quarks in Hadrons and Nuclei. [Online]. Available: https://www.sciencedirect.com/science/article/pii/S0146641007001032

[68] P. Mohanmurthy, F. Rathmann, and R. Milner, "Polarized ^{3}He ABS for an Absolute Polarimeter at the EIC," Talk, Sep. 2024, 20th International Workshop on Polarized Source, Targets, and Polarimetry (PSTP2024).

[69] A. Eddington, "The Internal Constitution of the Stars," *Nat.*, vol. 106, pp. 14–20, Sep. 1920. [Online]. Available: https://doi.org/10.1038/106014a0

[70] F. Hund, "Zur Deutung der Molekelspektren," *Z. Phys.*, vol. 40, pp. 742–764, Oct. 1927. [Online]. Available: https://doi.org/10.1007/BF01400234

[71] R. d. E. Atkinson and F. G. Houtermans, "Zur Frage der Aufbaumöglichkeit der Elemente in Sternen," *Z. Phys.*, vol. 54, pp. 656–665, Sep. 1929. [Online]. Available: https://doi.org/10.1007/BF01341595

[72] C. F. F. von Weizsäcker, *Über Elementumwandlungen im Inneren der Sterne. I.* S. Hirzel, 1937. [Online]. Available: https://books.google.de/books?id=NWpczgEACAAJ

[73] C. F. F. von Weizsäcker, *Über Elementumwandlungen im Inneren der Sterne. II.* S. Hirzel, 1938. [Online]. Available: https://books.google.de/books?id=SspdzgEACAAJ

[74] H. A. Bethe, "Energy Production in Stars," *Phys. Rev.*, vol. 55, pp. 103–103, Jan. 1939. [Online]. Available: https://link.aps.org/doi/10.1103/PhysRev.55.103

[75] H. A. Bethe, "Energy Production in Stars," *Phys. Rev.*, vol. 55, pp. 434–456, Mar. 1939. [Online]. Available: https://link.aps.org/doi/10.1103/PhysRev.55.434

[76] C. Iliadis, *Nuclear Physics of Stars*, 1st ed. Weinheim: WILEY-VCH, 2007.

[77] The Nobel Prize in Physics 1967. NobelPrize.org. Nobel Prize Outreach 2025, Feb. 2025. [Online]. Available: https://www.nobelprize.org/prizes/physics/1967/summary/

[78] B. T. Cleveland, T. Daily, R. Davis Jr., J. R. Distel, K. Lande *et al.*, "Measurement of the Solar Electron Neutrino Flux with the Homestake Chlorine Detector," *ApJ.*, vol. 496, no. 1, p. 505, Mar. 1998. [Online]. Available: https://dx.doi.org/10.1086/305343

[79] The Nobel Prize in Physics 2002. NobelPrize.org. Nobel Prize Outreach 2025, Feb. 2025. [Online]. Available: https://www.nobelprize.org/prizes/physics/2002/summary/

[80] Q. R. Ahmad, R. C. Allen, T. C. Andersen, J. D. Anglin, G. Bühler *et al.*, "Measurement of the Rate of $\nu_e + d \rightarrow p + p + e^-$ Interactions Produced by ^{8}B Solar Neutrinos at the Sudbury Neutrino Observatory," *Phys. Rev. Lett.*, vol. 87, p. 071301, Jul. 2001. [Online]. Available: https://link.aps.org/doi/10.1103/PhysRevLett.87.071301

[81] Y. Fukuda, T. Hayakawa, E. Ichihara, K. Inoue, K. Ishihara *et al.*, "Evidence for Oscillation of Atmospheric Neutrinos," *Phys. Rev. Lett.*, vol. 81, pp. 1562–1567, Aug. 1998. [Online]. Available: https://link.aps.org/doi/10.1103/PhysRevLett.81.1562

[82] The Nobel Prize in Physics 2015. NobelPrize.org. Nobel Prize Outreach 2025, Feb. 2025. [Online]. Available: https://www.nobelprize.org/prizes/physics/2015/summary/

[83] M. Agostini, K. Altenmüller, S. Appel, V. Atroshchenko, Z. Bagdasarian *et al.*, "Experimental evidence of neutrinos produced in the CNO fusion cycle in the Sun," *Nat.*, vol. 587, pp. 577–582, Nov. 2020. [Online]. Available: https://doi.org/10.1038/s41586-020-2934-0

[84] M. Agostini, K. Altenmüller, S. Appel, V. Atroshchenko, Z. Bagdasarian *et al.*, "Comprehensive measurements of *pp*-chain solar neutrinos," *Nat.*, vol. 562, pp. 505–510, Oct. 2018. [Online]. Available: https://doi.org/10.1038/s41586-018-0624-y

[85] M. Goldhaber, "On the probability of artificial nuclear transformations and its connection with the vector model of the nucleus," *Math. Proc. Camb. Phil. Soc.*, vol. 30, no. 4, p. 561–566, Oct. 1934. [Online]. Available: https://doi.org/10.1017/S0305004100012810

[86] R. M. Kulsrud, H. P. Furth, E. J. Valeo, and M. Goldhaber, "Fusion Reactor Plasmas with Polarized Nuclei," *Phys. Rev. Lett.*, vol. 49, pp. 1248–1251, Oct. 1982. [Online]. Available: https://link.aps.org/doi/10.1103/PhysRevLett.49.1248

[87] C. Zheng, Z. Fedorets, P. Chitgar, R. Engels, I. Engin, P. Gibbon *et al.*, "Preservation of ^{3}He ion polarization after laser-plasma acceleration," pp. 1–7, Apr. 2026. [Online]. Available: https://www.cambridge.org/core/journals/high-power-laser-science-and-engineering/article/preservation-of-3he-ion-polarization-after-laserdriven-acceleration-in-plasma/E6FC7622A7130299AF43998AC5B48A31

[88] W. Heidbrink, L. Baylor, M. Büscher, R. Engels, A. Garcia *et al.*, "A research program to measure the lifetime of spin polarized fuel," *Front. in Phys.*, vol. 12, p. 1355212., Jun. 2024. [Online]. Available: https://www.frontiersin.org/journals/physics/articles/10.3389/fphy.2024.1355212/full

[89] G. Ciullo, R. Engels, M. Büscher, and A. Vasilyev, *Nuclear Fusion with Polarized Fuel*, 1st ed., ser. Springer Proceedings in Physics. Switzerland: Springer, 2016, vol. 187. [Online]. Available: https://link.springer.com/book/10.1007/978-3-319-39471-8

[90] M. P. Rekalo and E. Tomasi-Gustafsson, "Polarization phenomena for low energy d+^{3}He collisions," *Phys. Rev. C*, vol. 57, pp. 2870–2879, Jun. 1998. [Online]. Available: https://link.aps.org/doi/10.1103/PhysRevC.57.2870

[91] C. Leemann, H. Bürgisser, P. Huber, U. Rohrer, H. Paetz gen Schieck *et al.*, "Investigation of the ^{3}He(d, p)^{4}He reaction with polarized beam and target at 430 keV," *Ann. Phys.*, vol. 66, no. 2, pp. 810–815, Aug. 1971. [Online]. Available: https://www.sciencedirect.com/science/article/pii/0003491671900832

[92] W. H. Geist, C. R. Brune, H. J. Karwowski, E. J. Ludwig, K. D. Veal *et al.*, "The ^{3}He($\vec{d}$,p)^{4}He reaction at low energies," *Phys. Rev. C*, vol. 60, p. 054003, Oct. 1999. [Online]. Available: https://link.aps.org/doi/10.1103/PhysRevC.60.054003

[93] A. Krauss, H. W. Becker, H. P. Trautvetter, C. Rolfs, and K. Brand, "Low-energy fusion cross sections of D + D and D +^{3} He reactions," *Nucl. Phys. A*, vol. 465, no. 1, pp. 150–172, Mar. 1987. [Online]. Available: https://www.sciencedirect.com/science/article/pii/0375947487903022

[94] C. S. Kannis and T. P. Rakitzis, "Production of spin-polarized molecular beams via microwave or infrared rotational excitation," *Chem. Phys.*, vol. 607, p. 113200, Aug. 2026. [Online]. Available: https://www.sciencedirect.com/science/article/pii/S0301010426001230

[95] T. P. Rakitzis, "Highly Spin-Polarized Atoms and Molecules from Rotationally State-Selected Molecules," *Phys. Rev. Lett.*, vol. 94, p. 083005, Mar. 2005. [Online]. Available: https://link.aps.org/doi/10.1103/PhysRevLett.94.083005

[96] D. Sofikitis, L. Rubio-Lago, M. R. Martin, D. J. A. Brown, N. C.-M. Bartlett *et al.*, "Preparation of highly polarized nuclei: Observation and control of time-dependent polarization transfer from $H^{35}Cl$ molecular rotation to ^{35}Cl nuclear spin," *Phys. Rev. A*, vol. 76, p. 012503, Jul. 2007. [Online]. Available: https://link.aps.org/doi/10.1103/PhysRevA.76.012503

[97] N. C.-M. Bartlett, D. J. Miller, R. N. Zare, A. J. Alexander, D. Sofikitis *et al.*, "Time-dependent depolarization of aligned HD molecules," *Phys. Chem. Chem. Phys.*, vol. 11, pp. 142–147, Nov. 2009. [Online]. Available: http://dx.doi.org/10.1039/B814133A

[98] R. Engels, M. Büscher, P. Buske, Y. Gan, and K. Grigoryev, "Direct observation of transitions between quantum states with energy differences below 10 neV employing a Sona unit," *EPJ D*, vol. 75, no. 9, p. 257, Sep. 2021. [Online]. Available: https://doi.org/10.1140/epjd/s10053-021-00268-4

[99] C. Kannis, "Theoretical and experimental investigation of Sona transitions," Ph.D. dissertation, Rheinisch-Westfälische Technische Hochschule Aachen, Mar. 2023.

[100] J. F. Parisi and A. Diallo, "Electric Power Enhancement using Spin-Polarized Fuel in Fusion Power Plants," Feb. 2025. [Online]. Available: https://arxiv.org/abs/2502.15941

[101] D. J. Griffiths and D. F. Schroeter, *Introduction to Quantum Mechanics*, 3rd ed. Cambridge University Press, 2018.

[102] G. Szegő, *Orthogonal Polynomials*, ser. American Math. Soc: Colloquium publ. American Mathematical Society, 1975. [Online]. Available: https://books.google.de/books?id=ZOhmnsXlcY0C

[103] A. Wachter, *Relativistische Quantenmechanik*, 1st ed., ser. Springer-Lehrbuch. Springer Berlin, Heidelberg, 2005.

[104] C. Cohen-Tannoudji, B. Diu, and F. Laloë, *Quantum mechanics volume 2*, 2nd ed. Wiley, 1978.

[105] E. U. Condon and G. H. Shortley, *The Theory of Atomic Spectra*, ser. Cambridge Univ.Pr.209. Cambridge University Press, 1935. [Online]. Available: https://books.google.de/books?id=hPyD-Nc_YmgC

[106] W. E. Lamb and R. C. Retherford, "Fine Structure of the Hydrogen Atom by a Microwave Method," *Phys. Rev.*, vol. 72, pp. 241–243, Aug. 1947. [Online]. Available: https://link.aps.org/doi/10.1103/PhysRev.72.241

[107] M. O. Scully and M. S. Zubairy, *Quantum Optics*, 1st ed. Cambridge University Press, 1997.

[108] S. Weinberg, *The Quantum Theory of Fields*. Cambridge University Press, 1995.

[109] L. Armstrong, *Theory of the Hyperfine Structure of Free Atoms*. Wiley-Interscience, 1971. [Online]. Available: https://books.google.de/books?id=Ytdr5nfo3J4C

[110] N. F. Ramsey, *Molecular Beams*, 1st ed., ser. Monographs on physics. Oxford University Press, 1990.

[111] J. J. Sakurai and J. Napolitano, *Modern Quantum Mechanics*, 3rd ed. Cambridge University Press, 2020.

[112] J. Stark, "Observation of the Separation of Spectral Lines by an Electric Field," *Nat.*, vol. 92, no. 401, Dec. 1913. [Online]. Available: https://doi.org/10.1038/092401b0

[113] P. S. Epstein, "The Stark Effect from the Point of View of Schroedinger's Quantum Theory," *Phys. Rev.*, vol. 28, pp. 695–710, Oct. 1926. [Online]. Available: https://link.aps.org/doi/10.1103/PhysRev.28.695

[114] X. Fan, T. G. Myers, B. A. D. Sukra, and G. Gabrielse, "Measurement of the Electron Magnetic Moment," *Phys. Rev. Lett.*, vol. 130, p. 071801, Feb. 2023. [Online]. Available: https://link.aps.org/doi/10.1103/PhysRevLett.130.071801

[115] P. Kusch and H. M. Foley, "The Magnetic Moment of the Electron," *Phys. Rev.*, vol. 74, pp. 250–263, Aug. 1948. [Online]. Available: https://link.aps.org/doi/10.1103/PhysRev.74.250

[116] M. D. Schwartz, *Quantum Field Theory and the Standard Model*, 1st ed. Cambridge University Press, 2013.

[117] D. P. Aguillard, T. Albahri, D. Allspach, J. Annala, K. Badgley *et al.*, "Measurement of the Positive Muon Anomalous Magnetic Moment to 127 ppb," *Phys. Rev. Lett.*, vol. 135, p. 101802, Sep. 2025. [Online]. Available: https://link.aps.org/doi/10.1103/7clf-sm2v

[118] H. Hellwig, R. Vessot, M. Levine, P. Zitzewitz, D. Allan *et al.*, "Measurement of the Unperturbed Hydrogen Hyperfine Transition Frequency," *IEEE Trans. Instrum. Meas.*, vol. 19, pp. 200 – 209, Dec. 1970. [Online]. Available: https://ieeexplore.ieee.org/document/4313902

[119] C. Smorra and A. Mooser, "Precision Measurements of the Fundamental Properties of the Proton and Antiproton," *J. Phys. Conf. Ser.*, vol. 1412, no. 3, p. 032001, Jan. 2020. [Online]. Available: https://dx.doi.org/10.1088/1742-6596/1412/3/032001

[120] W. Haeberli, "Sources of Polarized Ions," *Annu. Rev. Nucl. Part. Sci.*, vol. 17, pp. 373–426, Dec. 1967. [Online]. Available: https://www.annualreviews.org/content/journals/10.1146/annurev.ns.17.120167.002105

[121] H. Paetz gen Schieck, *Nuclear Physics with Polarized Particles*, 1st ed., ser. Lecture Notes in Physics. Heidelberg: Springer Berlin, 2012, vol. 842.

[122] G. Lindblad, "On the generators of quantum dynamical semigroups," *Commun. Math. Phys.*, vol. 48, pp. 119–130, Jun. 1976. [Online]. Available: https://doi.org/10.1007/BF01608499

[123] P. Pearle, "Simple derivation of the Lindblad equation," *Eur. J. Phys.*, vol. 33, no. 4, p. 805, Apr. 2012. [Online]. Available: https://dx.doi.org/10.1088/0143-0807/33/4/805

[124] J. D. Jackson, *Classical electrodynamics*, 2nd ed. New York, NY: Wiley, 1975.

[125] A. E. Kramida, "A critical compilation of experimental data on spectral lines and energy levels of hydrogen, deuterium, and tritium," *At. Data Nucl. Data Tables*, vol. 96, no. 6, pp. 586–644, Nov. 2010. [Online]. Available: https://www.sciencedirect.com/science/article/pii/S0092640X10000458

[126] N. Kolachevsky, M. Fischer, S. G. Karshenboim, and T. W. Hänsch, "High-Precision Optical Measurement of the 2S Hyperfine Interval in Atomic Hydrogen," *Phys. Rev. Lett.*, vol. 92, p. 033003, Jan. 2004. [Online]. Available: https://link.aps.org/doi/10.1103/PhysRevLett.92.033003

[127] S. Klarsfeld, "Radiative decay of metastable hydrogenic atoms," *Phys. Lett. A*, vol. 30, no. 7, pp. 382–383, Dec. 1969. [Online]. Available: https://www.sciencedirect.com/science/article/pii/0375960169907191

[128] S. R. Lundeen, P. E. Jessop, and F. M. Pipkin, "Measurement of the Hyperfine Structure of $2^2P_{\frac{1}{2}}$ State in Hydrogen," *Phys. Rev. Lett.*, vol. 34, pp. 377–380, Feb. 1975. [Online]. Available: https://link.aps.org/doi/10.1103/PhysRevLett.34.377

[129] W. S. Bickel and A. S. Goodman, "Mean Lives of the $2p$ and $3p$ Levels in Atomic Hydrogen," *Phys. Rev.*, vol. 148, pp. 1–4, Aug. 1966. [Online]. Available: https://link.aps.org/doi/10.1103/PhysRev.148.1

[130] C. Schwob, L. Jozefowski, B. de Beauvoir, L. Hilico, and F. Nez, "Optical Frequency Measurement of the $2S - 12D$ Transitions in Hydrogen and Deuterium: Rydberg Constant and Lamb Shift Determinations," *Phys. Rev. Lett.*, vol. 82, pp. 4960–4963, Jun. 1999. [Online]. Available: https://link.aps.org/doi/10.1103/PhysRevLett.82.4960

[131] E. W. Hagley and F. M. Pipkin, "Separated oscillatory field measurement of hydrogen $2S_{1/2}$-$2P_{3/2}$ fine structure interval," *Phys. Rev. Lett.*, vol. 72, pp. 1172–1175, Feb. 1994. [Online]. Available: https://link.aps.org/doi/10.1103/PhysRevLett.72.1172

[132] J. S. Geiger, V. W. Hughes, and H. E. Radford, "Electron g Value in the Ground State of Deuterium," *Phys. Rev.*, vol. 105, pp. 183–188, Jan. 1957. [Online]. Available: https://link.aps.org/doi/10.1103/PhysRev.105.183

[133] M. Puchalski, J. Komasa, and K. Pachucki, "Deuteron and triton magnetic moments from NMR spectra of the hydrogen molecule," *Phys. Rev. A*, vol. 92, p. 020501, Aug. 2015. [Online]. Available: https://link.aps.org/doi/10.1103/PhysRevA.92.020501

[134] N. Kolachevsky, P. Fendel, S. G. Karshenboim, and T. W. Hänsch, "$2S$ hyperfine structure of atomic deuterium," *Phys. Rev. A*, vol. 70, p. 062503, Dec. 2004. [Online]. Available: https://link.aps.org/doi/10.1103/PhysRevA.70.062503

[135] N. J. Stone, "Table of nuclear electric quadrupole moments," *Atomic Data and Nuclear Data Tables*, vol. 111-112, pp. 1–28, Sep.-Nov. 2016. [Online]. Available: https://www.sciencedirect.com/science/article/pii/S0092640X16000024

[136] E. E. Salpeter, "The Lamb Shift for Hydrogen and Deuterium," *Phys. Rev.*, vol. 89, pp. 92–97, Jan. 1953. [Online]. Available: https://link.aps.org/doi/10.1103/PhysRev.89.92

[137] E. S. Dayhoff, S. Triebwasser, and W. E. Lamb, "Fine Structure of the Hydrogen Atom. VI," *Phys. Rev.*, vol. 89, pp. 106–115, Jan. 1953. [Online]. Available: https://link.aps.org/doi/10.1103/PhysRev.89.106

[138] Y. A. Akulov and B. A. Mamyrin, "Difference between the triton beta decay constants in atomic and molecular tritium measured by the helium isotope method," *Phys. Lett. B*, vol. 600, no. 1, pp. 41–47, Oct. 2004. [Online]. Available: https://www.sciencedirect.com/science/article/pii/S0370269304012651

[139] D. J. Larson and N. F. Ramsey, "Measurement of the hydrogen-tritium g_J-factor ratio," *Phys. Rev. A*, vol. 9, pp. 1543–1548, Apr. 1974. [Online]. Available: https://link.aps.org/doi/10.1103/PhysRevA.9.1543

[140] M. Puchalski, J. Komasa, and K. Pachucki, "Deuteron and triton magnetic moments from NMR spectra of the hydrogen molecule," *Phys. Rev. A*, vol. 92, May 2015. [Online]. Available: https://doi.org/10.1103/PhysRevA.92.020501

[141] A. Schneider, B. Sikora, S. Dickopf, M. Müller, N. S. Oreshkina *et al.*, "Direct measurement of the $^3He^+$ magnetic moments," *Nat.*, vol. 606, pp. 878–883, Jun. 2022. [Online]. Available: https://doi.org/10.1038/s41586-022-04761-7

[142] R. Novick and E. D. Commins, "Hyperfine Structure of the Metastable State of Singly Ionized Helium-3," *Phys. Rev.*, vol. 111, pp. 822–840, Aug. 1958. [Online]. Available: https://link.aps.org/doi/10.1103/PhysRev.111.822

[143] S. G. Karshenboim and V. G. Ivanov, "Hyperfine structure in hydrogen and helium ion," *Phys. Lett. B*, vol. 524, no. 3, pp. 259–264, Jan. 2002. [Online]. Available: https://www.sciencedirect.com/science/article/pii/S0370269301013946

[144] E. A. Hinds, J. E. Clendenin, and R. Novick, "Decay rate of the $2^2s_{\frac{1}{2}}$ state of singly ionized helium," *Phys. Rev. A*, vol. 17, pp. 670–676, Feb. 1978. [Online]. Available: https://link.aps.org/doi/10.1103/PhysRevA.17.670

[145] U. D. Jentschura and G. W. F. Drake, "The $2S_{1/2}$-$2P_{1/2}$ Lamb shift in He^+," *Can. J. Phys.*, vol. 82, pp. 103–108, Feb. 2011. [Online]. Available: https://doi.org/10.1139/p03-114

[146] F. Schwabl, *Statistische Mechanik*, 3rd ed., ser. Springer-Lehrbuch. Springer Berlin, Heidelberg, 2006.

[147] U. Freyer, *Nachrichten-Übertragungstechnik: Grundlagen, Komponenten, Verfahren und Systeme der Telekommunikationstechnik*, 6th ed. Carl Hanser Verlag GmbH & Co. KG, 2009.

[148] N. Faatz, R. Engels, C. Kannis, B. Breitkreutz, and H. Soltner, "Development of a complete spin filter for metastable hydrogen atoms and its isotopes," *Phys. Open*, vol. 22, p. 100248, Feb. 2025. [Online]. Available: https://www.sciencedirect.com/science/article/pii/S2666032624000462

[149] P. Wang and A. Grudiev, "Single cylinder-based rf-cavity-system types for correction cavities in a klystron-based Compact Linear Collider," *Phys. Rev. Accel. Beams*, vol. 28, p. 032002, Mar. 2025. [Online]. Available: https://link.aps.org/doi/10.1103/PhysRevAccelBeams.28.032002

[150] R. Bossart, P. Brown, J. Mourier, I. Syratchev, and L. Tanner, "High-power Microwave Pulse Compression of Klystrons by Phase-Modulation of High-Q Storage Cavities," *CERN report*, Jan. 2004. [Online]. Available: https://cds.cern.ch/record/741401?ln=de

[151] P. Wang, A. Grudiev, B. Riffaud, E. Berthome, F. Motschmann *et al.*, "Design, fabrication and RF measurements of the storage and correction cavity prototypes of the RF pulse compression system for the klystron-based CLIC main linac," *CERN report*, p. 17, Sep. 2024. [Online]. Available: https://cds.cern.ch/record/2912954

[152] K. Lange and K.-H. Löcherer, *Taschenbuch der Hochfrequenztechnik*, 4th ed. Springer Berlin, Heidelberg, 1986.

[153] Z. Cheng, L. Liu, S. Xu, M. Lu, and X. Wang, "Temperature Dependence of Electrical and Thermal Conduction in Single Silver Nanowire," *Sci. Rep.*, vol. 5, p. 10718, Jun. 2015. [Online]. Available: https://doi.org/10.1038/srep10718

[154] S.-C. Su and T.-H. Chang, "Manipulating the permittivities and permeabilities of epoxy/silver nanocomposites over a wide bandwidth," *Appl. Phys. Lett.*, vol. 116, no. 20, p. 202904, May 2020. [Online]. Available: https://doi.org/10.1063/5.0006835

[155] M. Ferrera, M. Magnozzi, F. Bisio, and M. Canepa, "Temperature-dependent permittivity of silver and implications for thermoplasmonics," *Phys. Rev. Mater.*, vol. 3, p. 105201, Oct. 2019. [Online]. Available: https://link.aps.org/doi/10.1103/PhysRevMaterials.3.105201

[156] A. Wachter and H. Hoeber, *Repetitorium Theoretische Physik*, 2nd ed., ser. Springer-Lehrbuch. Springer Berlin, Heidelberg, 2004.

[157] B. Schutz, *A First Course in General Relativity*, 2nd ed. Cambridge University Press, 2009.

[158] T. El-Kordy, P. Costa Pinto, P. Di Nezza, R. Engels, M. Ferro-Luzzi *et al.*, "Amorphous carbon-coated storage cell tests for the polarized gas target at LHCb," *NIM-A*, vol. 1068, p. 169707, Nov. 2024. [Online]. Available: https://www.sciencedirect.com/science/article/pii/S0168900224006338

[159] P. Pradel, F. Roussel, A. S. Schlachter, G. Spiess, and A. Valance, "Formation of H($n = 2$) atoms by the nearly resonant process H^+ in Cs. Multiple collision processes," *Phys. Rev. A*, vol. 10, pp. 797–812, Sep. 1974. [Online]. Available: https://link.aps.org/doi/10.1103/PhysRevA.10.797

[160] I. A. Sellin and L. Granoff, "Energy dependence of H(2s) production in proton-alkali collisions from 2 to 30 keV," *Phys. Lett. A*, vol. 25, no. 6, pp. 484–485, Sep. 1967. [Online]. Available: https://www.sciencedirect.com/science/article/pii/0375960167900941

[161] F. W. Meyer, C. J. Anderson, and L. W. Anderson, "Total charge-transfer cross sections for H^+, H_2^+, H_3^+, He^+, N^+, N_2^+, Ne^+, Ar^+, Kr^+, and Xe^+ incident on Cs," *Phys. Rev. A*, vol. 15, pp. 455–462, Feb. 1977. [Online]. Available: https://link.aps.org/doi/10.1103/PhysRevA.15.455

[162] M. B. Shah and H. B. Gilbody, "Formation of $He^+(2S)$ metastable ions in passage of 10-60 keV $^3He^{2+}$ ions through gases," *J. Phys. B*, vol. 7, no. 2, p. 256, Feb. 1974. [Online]. Available: https://dx.doi.org/10.1088/0022-3700/7/2/011

[163] M. B. Shah and H. B. Gilbody, "Electron capture and $He^+(2s)$ formation in fast He^{2+}-H and He^+-H collisions," *J. Phys. B*, vol. 11, no. 1, p. 121, Jan. 1978. [Online]. Available: https://dx.doi.org/10.1088/0022-3700/11/1/016

[164] C. F. Barnett and P. M. Stier, "Charge Exchange Cross Sections for Helium Ions in Gases," *Phys. Rev.*, vol. 109, pp. 385–390, Jan. 1958. [Online]. Available: https://link.aps.org/doi/10.1103/PhysRev.109.385

[165] D. W. Koopman, "Measurement of Charge-Exchange Cross Sections for H^+, H_2^+, and He^+ Ions," *Phys. Rev.*, vol. 154, pp. 79–85, Feb. 1967. [Online]. Available: https://link.aps.org/doi/10.1103/PhysRev.154.79

[166] F. L. Eisele and S. W. Nagy, "Attenuation and single electron charge-exchange cross sections of He^+ on Ne and Ar in the 500–5000 eV energy range," *J. Chem. Phys.*, vol. 66, no. 3, pp. 883–885, Feb. 1977. [Online]. Available: https://doi.org/10.1063/1.433993

[167] T. Minami, T.-G. Lee, M. S. Pindzola, and D. R. Schultz, "Total and state-selective charge transfer in $He^{2+} + H$ collisions," *J. Phys. B*, vol. 41, no. 13, p. 135201, Jun. 2008. [Online]. Available: https://dx.doi.org/10.1088/0953-4075/41/13/135201

[168] S. Knoop, R. E. Olson, H. Ott, V. G. Hasan, R. Morgenstern *et al.*, "Single ionization and electron capture in $He^{2+} + Na$ collisions," *J. Phys. B*, vol. 38, no. 12, p. 1987, Jun. 2005. [Online]. Available: https://dx.doi.org/10.1088/0953-4075/38/12/013

[169] *51 mm (2") photomultiplier 9424B series data sheet*, ET Enterprises electron tubes, 45 Riverside Way Uxbridge UB8 2YF United Kingdom, Sep. 2010. [Online]. Available: https://et-enterprises.com/images/data_sheets/9424B.pdf

[170] *Andor Newton SO Series Direct Detection Spectroscopy*, Oxford Instruments. [Online]. Available: https://andor.oxinst.com/assets/uploads/products/andor/documents/andor-newton-so-specifications.pdf

[171] *M100 ECRIS system*, Pantechnik. [Online]. Available: https://www.pantechnik.com/wp-content/uploads/2020/07/monogan-M100.pdf

[172] E. Gullikson, "Cxro, the centre for x-ray optics," accessed 2025-10-22. [Online]. Available: https://henke.lbl.gov/optical_constants/

[173] B. L. Henke, E. M. Gullikson, and J. C. Davis, "X-Ray Interactions: Photoabsorption, Scattering, Transmission, and Reflection at E = 50-30,000 eV, Z = 1-92," *Atomic Data and Nuclear Data Tables*, vol. 54, no. 2, pp. 181–342, Jul. 1993. [Online]. Available: https://www.sciencedirect.com/science/article/pii/S0092640X83710132

[174] N. Meidinger, S. Bonerz, H. Braeuninger, R. Eckhardt, J. Englhauser *et al.*, "Frame store PN-CCD detector for the ROSITA mission," *P. Soc. Photo-Optical Instrum. Eng., 4851, 1040-1047 (2003)*, vol. 4851, Mar. 2003. [Online]. Available: https://www.spiedigitallibrary.org/conference-proceedings-of-spie/4851/1/Frame-store-PN-CCD-detector-for-the-ROSITA-mission/10.1117/12.461156.short

[175] R. Engels, "Internal discussion," 2026.

[176] L. P. Lévy and W. L. Williams, "Parity nonconservation in the hydrogen atom. III," *Phys. Rev. A*, vol. 30, pp. 220–238, Jul. 1984. [Online]. Available: https://link.aps.org/doi/10.1103/PhysRevA.30.220

[177] X. Li, J. D. Maxwell, D. Nguyen, J. Brock, C. D. Keith *et al.*, "Metastability exchange optical pumping of ^{3}He at low pressure and high magnetic field," *NIM-A*, vol. 1057, p. 168792, Dec. 2023. [Online]. Available: https://www.sciencedirect.com/science/article/pii/S0168900223007830

[178] V. Bechtold, L. Friedrich, P. Ziegler, R. Aniol, G. Latzel *et al.*, "The lamb shift polarized ion source at the FN tandem Van de Graaff accelerator of the university of cologne," *NIM*, vol. 150, no. 3, pp. 407–416, Apr. 1978. [Online]. Available: https://www.sciencedirect.com/science/article/pii/0029554X78901064

[179] W. E. Burcham, O. Karban, S. Oh, and W. B. Powell, "A source of polarized ^{3}He ions," *NIM*, vol. 116, no. 1, pp. 1–7, Mar. 1974. [Online]. Available: https://www.sciencedirect.com/science/article/pii/0029554X74905692

[180] P. Adlarson, W. Augustyniak, W. Bardan, M. Bashkanov, F. S. Bergmann *et al.*, "Evidence for a New Resonance from Polarized Neutron-Proton Scattering," *Phys. Rev. Lett.*, vol. 112, p. 202301, May 2014. [Online]. Available: https://link.aps.org/doi/10.1103/PhysRevLett.112.202301

[181] J. W. S. Cook, H. Ali, J. F. Parisi, A. Diallo, and N. Faatz, "Persistence of deuterium and tritium nuclear spin-polarization in presence of high-frequency plasma waves," *Nucl. Fusion*, Apr. 2026, accepted. [Online]. Available: http://iopscience.iop.org/article/10.1088/1741-4326/ae5ab8

[182] N. Ramsey, *Nuclear Moments*, ser. Experimental nuclear physics. Wiley, 1953. [Online]. Available: https://books.google.de/books?id=Zg8nAAAAMAAJ

[183] G. B. Arfken and H. J. Weber, *Mathematical methods for physicists*, 6th ed. Elsevier Academic Press, 2005.

[184] S. W. Goode and S. A. Annin, *Differential Equations and Linear Algebra*, 4th ed. Addison Wesley, 2016.

Acknowledgements

I would like to express my deepest gratitude to all those who have supported me throughout the journey of completing this PhD thesis.

First and foremost, I am profoundly grateful to my supervisor Dr. Ralf Engels for his assistance, broad knowledge and constructive feedback, which helped me to shape my thesis and to develop as a young researcher. His expertise in polarized sources, targets and polarimetry, especially in the Lamb-shift polarimeter, helped me to create own innovative concepts, which led to this thesis. In addition, he enabled me to thrive as a scientist by presenting and publishing results as well as by working in a large group.

I would also like to extend my sincere appreciation to Prof. Dr. Jörg Pretz and Prof. Dr. Christoph Hanhart for their supervision and discerning comments.

In addition, I am very grateful for the fruitful work together with Berthold Kimczok, which resulted in the new design for the upgraded spin filter.

Finally, I acknowledge all my collogues who inspired my thoughts by deep discussions and assistance in the laboratory. I am thankful for the great time and joy I had working with them together.

Fakultät für Mathematik und Naturwissenschaften | RWTH AACHEN UNIVERSITY

Declaration of Authorship

I, Nicolas Faatz

declare that this thesis and the work presented in it are my own and has been generated by me as the result of my own original research.

I do solemnely swear that:

1. This work was done wholly or mainly while in candidature for the doctoral degree at this faculty and university;

2. Where any part of this thesis has previously been submitted for a degree or any other qualification at this university or any other institution, this has been clearly stated;

3. Where I have consulted the published work of others or myself, this is always clearly attributed;

4. Where I have quoted from the work of others or myself, the source is always given. This thesis is entirely my own work, with the exception of such quotations;

5. I have acknowledged all major sources of assistance;

6. Where the thesis is based on work done by myself jointly with others, I have made clear exactly what was done by others and what I have contributed myself;

7. Parts of this work has been published before as:

    - Faatz, N. et al. (2026). Concept for a Lamb-shift polarimeter based on single ionized Helium-3 ions. (in preparation)
    - Kannis, C. S. et al. (2025). Spin manipulation and nuclear polarization enhancement in particle beams with static magnetic fields. Phys. Rev. A, 112 (1), 012801. https://doi.org/10.1103/4nr6-xt7m
    - Faatz, N. et al. (2025). Further development of a Lamb-shift polarimeter. PoS, PSTP2024, 011. https://doi.org/10.22323/1.472.0011
    - Faatz, N. et al. (2025). Development of a complete spin filter for metastable hydrogen atoms and its isotopes. Phys. Open, 22, 100248. https://doi.org/10.1016/j.physo.2024.100248

08.04.2026

